2008

DESIGN AND EVALUATION OF INFLATABLE WINGS FOR UAVs

Andrew D. Simpson
University of Kentucky, adsimpson@gmail.com

ABSTRACT OF DISSERTATION

Andrew D. Simpson

The Graduate School

University ofKentucky

2008

DESIGN AND EVALUATION OF INFLATABLE WINGS FOR UAVs

ABSTRACT OF DISSERTATION

A dissertation submitted in partial fulfillment of the
requirements for the degree of Doctor of Philosophy in the
College of Engineering
at the University of Kentucky

By

Andrew D. Simpson

Lexington, Kentucky

Co-Directors: Dr. Jamey D. Jacob, Associate Professors of Aerospace Engineering

and Dr. Suzanne Weaver Smith, Associate Professors of Mechanical Engineering

Stillwater, Oklahoma and Lexington, Kentucky

2008

ABSTRACT OF DISSERTATION

DESIGN AND EVALUATION OF INFLATABLE WINGS FOR UAVs

Performance of inflatable wings was investigated through laboratory, wind tunnel and flight-testing. Three airfoils were investigated, an inflatable-rigidazable wing, an inflatable polyurethane wing and a fabric wing restraint with a polyurethane bladder. The inflatable wings developed and used within this research had a unique outer airfoil profile. The airfoil surface consisted of a series of chord-wise "bumps." The effect of the bumps or "surface perturbations" on the performance of the wings was of concern and was investigated through smoke-wire flow visualization. Aerodynamic measurements and predictions were made to determine the performance of the wings at varying chord based Reynolds Numbers and angles of attack. The inflatable baffles were found to introduce turbulence into the free-stream boundary layer, which delayed separation and improved performance.

Another area of concern was aeroelasticity. The wings contain no solid structural members and thus rely exclusively on inflation pressure for stiffness. Inflation pressure was varied below the design pressure in order to examine the effect on wingtip twist and bending. This lead to investigations into wing deformation due to aerodynamic loading and an investigation of wing flutter. Photogrammetry and laser displacement sensors were used to determine the wing deflections. The inflatable wings exhibited wash-in deformation behavior. Alternately, as the wings do not contain structural members, the relationship between stiffness and inflation pressure was exploited to actively manipulate wing through wing warping. Several warping techniques were developed and employed within this research. The goal was to actively influence the shape of the inflatable wings to affect the flight dynamics of the vehicle employing them. Researchers have developed inflatable beam theory and models to analyze torsion and bending of inflatable beams and other inflatable structures. This research was used to model the inflatable wings to predict the performance of the inflatable wings during flight. Design elements of inflatable wings incorporated on the UAVs used within this research are also discussed. Finally, damage resistance of the inflatable wings is shown from results of flight tests.

KEYWORDS: Inflatable Wings, Aerodynamics, Aeroelasticity, Flight Testing, Unmanned Aerial Vehicle (UAV).

Andrew D. Simpson

02/22/2008

DESIGN AND EVALUATION OF INFLATABLE WINGS FOR UAVs

By

Andrew D. Simpson

Dr. Jamey D. Jacob
Co-Director of Thesis

Dr. Suzanne Weaver Smith
Co-Director of Thesis

Dr. L. Scott Stephens
Director of Graduate Studies

02/22/2008

RULES FOR THE USE OF DISSERTATIONS

Unpublished dissertations submitted for the Doctor's degree and deposited in the University of Kentucky Library are as a rule open for inspection, but are to be used only with due regard to the rights of the authors. Bibliographical references may be noted, but quotations or summaries of parts may be published only with the permission of the author, and with the usual scholarly acknowledgments.

Extensive copying or publication of the dissertation in whole or in part requires also the consent of the Dean of The Graduate School of the University of Kentucky.

A library which borrows this thesis for use by its patrons is expected to secure the signature of each user.

Name	Date

DISSERTATION

Andrew D. Simpson

The Graduate School

University of Kentucky

2008

DESIGN AND EVALUATION OF INFLATABLE WINGS FOR UAVs

DISSERTATION

A dissertation submitted in partial fulfillment of the
requirements for the degree of Doctor of Philosophy
in the College of Engineering
at the University of Kentucky

By

Andrew D. Simpson

Lexington, Kentucky

Co-Directors: Dr. Jamey D. Jacob, Associate Professors of Aerospace Engineering

and Dr. Suzanne Weaver Smith, Associate Professors of Mechanical Engineering

Stillwater, Oklahoma and Lexington, Kentucky

2008

ACKNOWLEDGEMENTS

I would first like to thank my wife, Colleen. You were my principle motivation for beginning this journey; and certainly the reason I am now completing it. I could not have done this without you. Thanks to my parents and brother (Mom, Dad and Rob) for all you have done. All of you have molded me into who I am today. You have always been my rocks to lean on in difficult times. I love you all so much.

I would like to thank my dissertation committee members; Dr. Michael Seigler, Dr. Raymond LeBeau (for your patience, advise and instruction "I always seemed able to focus better when to brought your baseball bat to class"), and Dr. Tim Stombaugh (for guiding me through my Masters degree and without whom I would not have come to the US). My outside committee member, Dr. Kamyar Mahboub for your time, commitment, and outside perspective. I would particularly like to thank Dr. Suzanne Smith and Dr. Jamey Jacob.

Dr. Smith, I cannot thank you enough for the countless opportunities that you have given me during the last four years; the travel, exciting projects and the opportunities to teach and talk with everybody form kinder gardeners to high school students to world-renowned researchers to old men ("sorry Ed") in the local flying club. Thank you for all the instruction and coaching I received.

Dr. JDJ (Jamey), you are a friend who is my mentor. You have opened so many doors for me, encouraged and challenged me, taken me on some wild and fun adventures, always with a smile and a witty comment. I hope one day I will be in a position to repay you. Thank you for all the lunches, dinners and beers you sponsored along the way. I hope you know my home will always be open to you and fridge will always be stocked with beers. Working with you has been fun and will always remain one of my fondest memories!

I've had some fantastic lab mates over the last few years. You guys have made life in the basement fun, thank you to Dr. Jennie Campbell, Mr. John Rowe, Dr. Arvind Santhanakrishnan, Dr. Nan Jou Pern, Mr Karthik Ramakumar, Mr. Jeff Gagel, Mrs. Kathy Warren, Ms. Michiko Usui, Dr. Jon Black, Mr David Munday, Dr. Rahul Bharadwajh, Ms. Lavanya Rangubhotla, Dr. Mark McQuilling, Mr. Tim Brown and Dr. Jody Purswell. Thanks to all of you, going to work everyday was a pleasant experience.

I'd like to thank the entire South African community in Lexington. I've singled out a few here but the list is much longer. The Snr de Beers, for feeding a starving grad student, and opening your home to me (and Fred for your standard question "so what are you going to do with the rest of your life? ... *awkward pause – I realizes he's not kidding – I stumble through an answer – which he follows with* ... Have you thought about a Ph.D.?"). The

Steyns for your friendship, Wehan for the fun on the rugby field and golf course. The Dorflings for you support encouragement, friendship, food and beer. You guys "are" family. Last but by no means least the Jnr DeBeers and my mother-in-law – Jan, Lauren, Idalia, Louisa, and Evelyn. Thank you for all that you have done for me... you have nourished me, housed me, clothed me, and married me off to your daughter (and sister). Jan I would not be here today had I not met you on my second day in the US... guaranteed.

I'd like to acknowledge the BIG BLUE team of over +-200 undergraduate, graduate, and high school students students in Mechanical and in Electrical and Computer Engineering at the University of Kentucky who conceived, designed, fabricated, tested, launched, recovered and evaluated many cool experiments some of which were directly related to this research. Thanks also to the men of the LMAC (especially Mr. Ed King), for sharing you runway with me, giving me helpful advice, and having a good laugh with me on Wednesday mornings. Without all of your help this project would not have been possible.

I'm very grateful for numerous discussions and support from ILC Dover, Inc. under the direction of Dave Cadogan and including Matt Mackusick, Stephen Scarborough, Frank Uhlesky, Tim Smith, and Ryan Lee, and Bobby Jones. Your support was greatly appreciated. This project was partially funded ILC Dover and Kentucky NASA EPSCoR under the auspices of Drs. Richard and Karen Hackney at Western Kentucky University. The BIG BLUE project was supported by a NASA Workforce Development grant from the NASA Kentucky Space Grant Consortium, directed by Dr. Richard Hackney.

TABLE OF CONTENTS

LIST OF TABLES

LIST OF FIGURES

LIST OF FILES

DISSERTATION-ADS.pdf, $\approx$ 9.5MB, PDF File

Chapter 1

INTRODUCTION

The research included herein emphasizes recent developments in the design, aerodynamic control, and aeroelasticity of inflatable wings. The goal was to determine performance benefits of inflatable winged aircraft over traditional fixed winged aircraft, and to examine concerns that emerge when designing inflatable wing vehicles.

1.1 The Inflatable Wing

The inflatable wings used within this research were manufactured by ILC Dover, Inc. Three variations of the wing were developed; Three variations of the wing were developed and tested over the course of 4 years: a S/E glass wing impregnated with epoxy that hardens under exposure to a catalyst, a vectran wing with a polyurethane bladder and a polyurethane coated nylon wing. These wings can be seen in Fig. 1.1. The primary focus of this dissertation is on the latter two designs; the rigidizable wing is discussed elsewhere.[21]

(a) S/E glass rigidizable wing.

(b) Vectran wing.

(c) Nylon wing.

Figure 1.1: Inflatable wing variations examined within this research.

Each of the inflatable wings shown in Fig. 1.1 were constructed in two semi-span pieces such that they could be mounted externally to a fuselage or plenum. The wings typically had a semi-span of 0.9 m (3 ft) and a chord length of between 0.3 m and 0.5 m (11 to 20 in). Inflation pressures varied substantially between wings. The S/E glass wings had a nominal design inflation pressure of 48.3 kPa (7 psi), the Vectran wings had a design inflation pressure of 186 kPa (27 psi) and the nylon wings had a design inflation pressure of 42.4 kPa (6 psi). This variation was due to the wing material and the original design mission of the UAV using the wings. The wing inflation pressures were substantially lower than other

inflatable wing UAVs [19] of this size. This was due the the unique shape of the inflatable wings which did not rely on pressurized circular tubes. The upper and lower wing surfaces were tied together with internal baffles and an end cap sealed the wing. High stiffness was achieved with low inflation pressure by maximizing the inflated sectional moment of inertia. As a consequence of the design, the wing surface was "bumpy" in the chord wise direction. The aerodynamic implications of the chord wise bumps were investigated. It is important to not that the wings developed in this research are entirely inflatable and thus do not contain any solid structural elements, including ailerons. Thus, vehicles employing these inflatable wings must generate a roll moment by other means and counteract any adverse aeroelastic effects.

1.2 Collaboration with ILC Dover

Throughout this dissertation, wing design and manufacture has been accomplished in partnership with ILC Dover. ILC has been instrumental to this research. Three variations of inflatable wings have been designed, developed, and tested at the University of Kentucky in collaboration with ILC. ILC has a rich history in the design and manufacture of engineered soft-goods such as space suits, airships, mars landing bags, and gas masks. One thrust of ILC has been to merge inflatable design and advanced materials to develop robust, engineered shapes for aerospace applications. Since the mid-seventies ILC has been designing and building inflatable wings for small to medium scale UAVs [18]. The inflatable wings described in this research were designed in partnership with ILC, manufactured by ILC, and tunnel and flight tested at the University of Kentucky.

1.3 Research Outline

A wide range of topics important to this research needs to be discussed in order to understand inflatable wings. These topics all play a role in the design and performance of the inflatable wings. Much of the background information needed for this research is detailed in Chapter 2. The inflatable wings developed within this research have a unique outer airfoil profile as highlighted above. The airfoil surface consists of a series of chord-wise "bumps." The affect of the bumps or "surface roughness" on the performance of the wings was of concern and was investigated. Aerodynamic measurements and predictions were made to determine the performance of the wings. This included both analytical analysis and tunnel testing. Many of the theoretical analytical techniques were derived and explained in Chapter 2. This includes a history of UAVs, aeroelasticity, morphing, and an introduction

to early inflatable wings.

Another area of concern was aeroelasticity or "flutter" and this is extensively investigated within this research. Inflatable wings have no structural members and thus rely exclusively on inflation pressure for stiffness. This lead to an investigation of wing deformation due to aerodynamic loading. Photogrammetry was used as the primary tool to investigate this deformation. Nodal analysis and vibration of the inflatable wings was examined and analyzed. Due to the fact that the wings do not contain structural members, the relationship between stiffness and inflation pressure could be exploited to actively manipulate wing through wing warping. Several warping techniques were developed and employed in this research. The goal was to actively influence the shape of the inflatable wings to affect the flight dynamics of the vehicle employing them. Finally, inflatable beam theory and models were used to analyze torsion and bending of the inflatable wings. This research was used to predict the performance of the inflatable wings during flight.

Aerodynamics, flight control and modeling of the inflatable wings was investigated. The aerodynamic performance of the "bumpy" wing profile was investigated through wake surveys. This investigation obtained direct measurements of the lift and drag form the bumpy profile at different Reynolds numbers. The impact of wing warping was investigated through particle image velocimetry (PIV), lifting line analysis and other modeling techniques. Performance of the wing in different warped configurations was examined. Substantial flight testing of the inflatable wings was done throughout this research. This included flight testing of the inflatable wings shown in Fig. 1.1 and flight testing of the wings using different wing warping arrangements.

1.4 Goals

The goal was to develop and validate inflatable wing technologies. The development of technology solutions to expand mission capabilities through concepts such as morphing, and to develop technologies for small vehicles which would allow them to be integrated into controlled airspace (low impact damage potential from flying airbag). Inflatable wing technologies have the potential to enhance survivability and thus; foster remote operations use, ease pilot skill burden (open the user range), expand the weather envelope for flight, decrease time out of service for repair, and reduce the logistics chain and life-cycle costs for small aircraft.

In order to achieve these goals, some fundamental questions relating to inflatable wings need to be answered. The goal of the dissertation is to answer these questions;

- Do these wings fly?
- Do the wings deform during flight?
- What are the aeroelastic concerns?
- What are the aerodynamic implications of the "bumpy" wing profile?
- Can we actively manipulate the wing shape (and if so, what forces are required)?
- Do the wings buckle at high loading factors?
- Can we predict the aerodynamic performance and wing buckling?

Research efforts have been focused on warping the Vectran and nylon inflatable wings to provide roll control through wing warping; examining the aeroelastic effects of the wings while changing the inflation pressure and varying the dynamic pressure; and investigating the warping and aeroelasticity of the wing as it effects the aerodynamic performance.

Chapter 2

PREVIOUS WORK

Currently most aircraft are designed for a single mission such as reconnaissance or attack. The geometry of an aircraft is dictated by the vehicles primary mission and is non-optimal for other mission segments and roles. This results in reduced range, loiter, and the inability to operate from some airfields. The ability to change wing shape and vehicle geometry substantially while in flight would allow a single vehicle to perform missions that are beyond current capabilities or to perform multiple tasks, including those done by separate aircraft operating as a large system.

The ability to change wing shape or morph combines optimal performance into a single system. Performance benefits may include a low turning radius, long endurance, increased payload, and high speed tasks that cannot be efficiently combined into a single vehicle. These new vehicles offer the potential of radically different flight regimes. Unmanned aerial vehicles or "UAVs" are the ideal platform to examine this new technology as pilot safety is not a concern.

2.1 A Brief History of UAVs

Unmanned aircraft have been under development since the beginning of flight. The Wright brothers tested heavier than air unmanned gliders over the dunes of Kitty Hawk, North Carolina, preceding the first powered flight. On May 6, 1896, Samuel Langley's Aerodrome made the first successful flight of an un-piloted, engine-driven, heavier-than-air craft [33]. The aircraft was launched from a spring-actuated catapult mounted on top of a houseboat on the Potomac River in Virginia. Two flights were made, one of 1,005 m (3,300 ft) and a second of 700 m (2,300 ft), at a speed of approximately 25 miles per hour. On November 28, another successful flight was made with a similar model. It flew a distance of approximately 1,460 m (4,790 ft). These aircraft were structurally weak and had minimal control systems.

Further UAV developments were made during World War I [34]. The Curtiss/Sperry Aerial Torpedo, seen in Fig. 2.1*a*, made its first successful flight on 6 March 1918 at Copiague, Long Island, NY. The 431 kg (950 lb) UAV flew 914 m (1000 yards) after being launched by a falling-weight catapult, it then dived at a preset distance from the launch

site into the water. The UAV was then recovered and re-flown. A total of six Torpedos were built and several made repeated flights. The vehicle had a wingspan 6.7 m (22 ft), an empty weight of 680 kg (1500 lb), a range of 80 km (50 miles), a top speed of 113 km/h (70 mph), and it was designed to carry a payload of 450 kg (1000 lb) of high-explosives.

Inspired by the successes of the Aerial Torpedo, the 530 lb Wright Liberty Eagle (a.k.a. Kettering Bug), seen in Fig. 2.1*b*, made its first successful flight in October 1918. The vehicle was half the size of the Curtiss Sperry Aerial Torpedo. The vehicle had a range of 50 miles, after which the ignition was cut and the vehicle entered a steep dive, delivering its 200 lb payload to the target. Orville Wright acted as the Kettering Bug's technical consultant and added dihedral to the vehicle's wings to improve its gust response. Forty were built; however, production was cut short by the end of World War I. Both these vehicles were forerunners of today's cruise missiles.

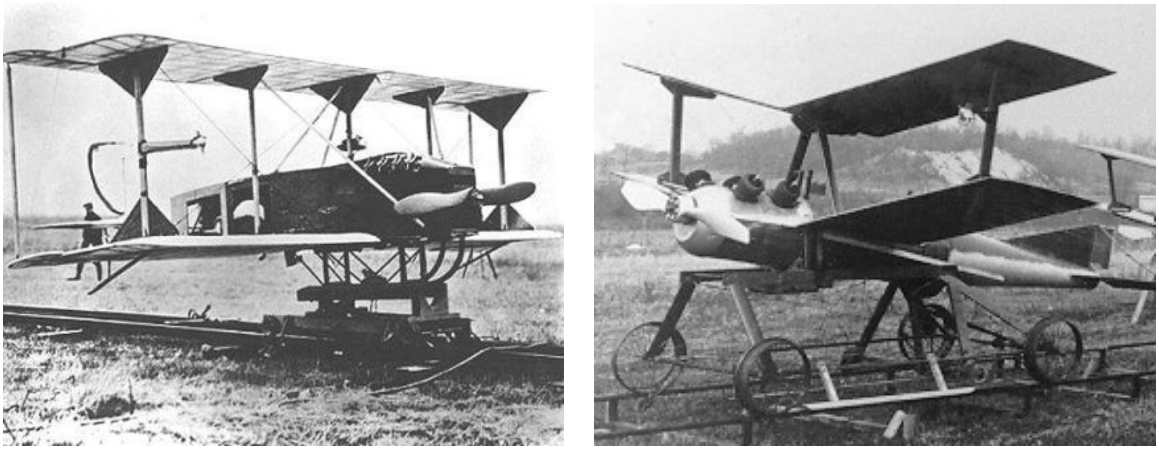

(a) Curtiss/Sperry – "Aerial Torpedo". (b) Wright Liberty Eagle – "Kettering Bug".

Figure 2.1: Early UAVs [1].

The British RAE 1921 Target made the world's first successful radio controlled flight without a pilot on board on 3 September 1924 [34]. A subsequent flight was made and had duration of 39 minutes during which 43 separate flight commands were executed. This was followed just 12 days later on 15 September by a modified U.S. Navy N-9. This flight lasted for 40 minutes, during which it executed 50 commands, then landed successfully.

Target drones were introduced in the 1930s in both the U.S. and in Britain as a spin-off of these early cruise missile efforts. By the end of the decade, hundreds were regularly being flown in both countries to train anti-aircraft gunners. However, these UAVs were little more than full-sized remote controlled airplanes.

Reconnaissance drones burst on to the military scene in the 1950s [34]. Cameras were added to target drones and the drones were used as the first tactical reconnaissance UAVs. Between 1959 and 1966, the United States Army operated 1,455 of these UAVs and spread the vehicle to other NATO countries. The US Marine Corps tested a two-man Bikini UAV for small units in the 1960s. This is a forerunner of the Pointer and later Dragon Eye mini-UAVs. By the time of the Cuban Missile Crisis, the Air Force had modified a number of target drones to carry cameras, a capability which was used extensively during the Vietnam conflict. The 1950s also saw the maturation of inertial navigation systems[34], the key technology in the development of unmanned flight.

In the last two decades, interest in UAVs has increased substantially. UAVs are currently being used in various roles, including reconnaissance and intelligence-gathering, and in more challenging roles, combat missions. Currently, 32 nations are developing or manufacturing more than 250 models of UAVs, and 41 countries operate 80 types of UAVs, primarily for reconnaissance [5, 35, 36, 37].

UAVs hold allure because they offer cheaper, capable vehicles that do not place aircrews at risk. Among the advantages of UAVs are their suitability to perform missions considered "dull, dirty, dark, or dangerous." These missions include orbiting a point for communications relay or jamming, collecting air samples to measure pollution, and flying reconnaissance over hostile air defenses. Repetitive, long duration and high- risk missions are the most suitable for UAVs.

2.2 Vehicle Terminology

For the purposes of this dissertation research, the term "Unmanned Aerial Vehicle" or "UAV" will be used to describe the aircraft designed, built and tested for this research. The term UAV is used to describe all aircraft without a pilot on-board. The UAV is a powered aircraft that does not carry a human operator. The vehicle uses aerodynamic forces to provide lift and can fly autonomously or be piloted by remote control. Additionally, unlike missiles or other projectiles, UAVs can be recovered for repeated flights. Thus, expendable autonomous projectiles like cruise missiles are not considered UAVs.

Many terms have been used to describe aircraft without a pilot on-board. The term "drone" (*Dictionary.com: "a remote control mechanism, such as a radio-controlled airplane or boat"*) was used in the 1940s and 1950s when describing vehicles used predominantly as an aerial target. This gave way to "Remotely Piloted Vehicle" (RPV) in the Vietnam era to distinguish the vehicles' new role as a reconnaissance asset due to the on-board

camera equipment. The RPV then evolved to "Unmanned Aerial Vehicle" (UAV) in the 1980s, the name change was used to distinguish the vehicles (due to their new technology) from the Vietnam era vehicles. With efforts to develop rules integrating UAVs into the National Airspace System (NAS), and realizing that Federal Aviation Administration (FAA) rule-making authority applied only to "aircraft." The term "Remotely Operated Aircraft" (ROA) was coined in 1997.

To further complicate things, the U.S. Air Force refers to its UAV aircraft as "Remotely Piloted Aircraft" (RPA) because they are unique in having a pilot with a stick and rudder flying them from a ground station. The FAA (and Department of Defense (DoD)) adopted the more inclusive term "Unmanned Aircraft System"(UAS) in 2004. The term "Micro Aerial Vehicle" or "μAVs" has also become prevalent over the last decade. The term μAVs, describes a class of aircraft whose size is of the order of magnitude of small birds. These vehicles have a maximum dimension of less than 15 cm (6 in) in any direction.

The length scales of UAVs pose challenging problems for engineers. The smaller vehicle sizes create aerodynamic concerns not encountered in larger vehicles. Designers are investigating new vehicle control and drag reduction techniques in morphing aircraft. The aerodynamics and aeroelasticity of these vehicles is of primary interest.

2.3 Aerodynamics

Aerodynamics is the study of the motion of gas moving around objects and the forces created by this interaction. The shape of the object and the speed at which gas flows over it determine the magnitude of the forces created. The principle non-dimensional relation of concern is the "Reynolds Number" (Re), seen in equation 2.1.

$$\mathrm{Re} = \frac{\rho U c}{\mu} = \frac{U c}{\nu} \tag{2.1}$$

in which ρ denotes density, c denotes a length scale (normally chord length), U denotes velocity, μ denotes dynamic viscosity, and ν denotes the fluid's kinematic viscosity.

The aerodynamic characteristics of low Re airfoils are fundamentally different from those seen in typical aviation applications. Subsonic aerodynamics, not a major area of study until the recent past, promises tremendous potential in the development of small, robust and high performance UAVs. For a given wing, we are principally interested in maximizing the airfoil lift L and minimizing the drag D, or alternatively, maximizing the lift-to-drag ratio, L/D (also written as the ratio of lift coefficient C_l to drag coefficient C_d, or C_l/C_d, defined below). This is taken as a measure of the wings overall efficiency.

This ratio is dependent upon the wing geometry and the flow conditions in which the wing is immersed. These flow conditions are typically expressed as dimensionless parameters such as the Re and Mach number (M). A given airfoil profile will have vastly different lift and drag characteristics over the possible ranges of Re and M. Thus, airfoils are typically designed for a narrow range of flight conditions for optimum performance, as seen in Fig. 2.2. This figure depicts several classes of air vehicles that fit into this Re and M number space. Note that each class of vehicle has a fairly narrow bandwidth in both Re and M space. The sole exceptions in this graph are UAVs and "Lighter-Than-Air" vehicles (LTAs), both of which cover a large category of aircraft built for a variety of purposes. An alternative is to design an airfoil that adequately operates over a wide range of flow conditions but does not perform well in any.

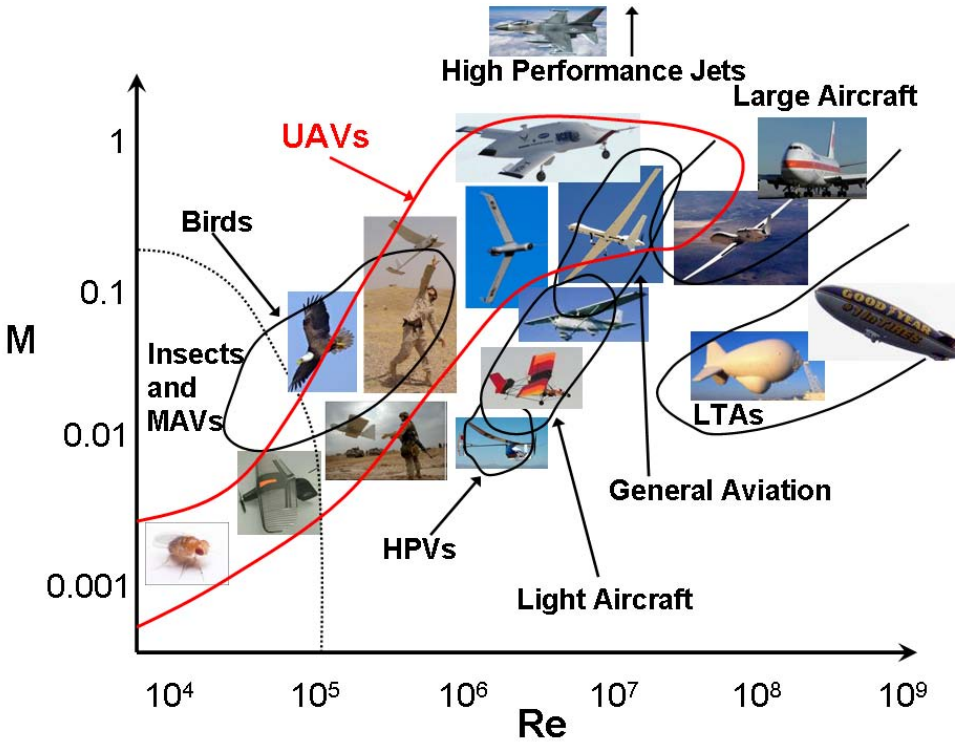

Figure 2.2: M versus Re for a wide range of airborne objects (adapted from Lissaman [2]).

Small UAVs have airfoils with relatively low chord lengths. Low chord lengths and flight velocities directly impact Re. This means that the Re of the flow surrounding small UAV airfoils remains low, and in extreme circumstances laminar. Typical Re values range from 50,000 to 500,000 for small UAVs. Fig. 2.2, adapted from Lissaman [2] illustrates the

Re and M envelope of aerial vehicles, both natural and man-made. The horizontal axis shows Re on a log-scale while the vertical axis shows M on a log scale. The balloon shapes indicate operating regimes of airborne objects. As seen, UAVs, RPVs, and μAVs operate in a large Re – M range. UAVs operate in a much lower Re –M range than conventional aircraft because these vehicles can be operated at high altitudes, have extremely low chord lengths, or operate at low flight velocities. At high altitudes, the kinematic viscosity is sufficiently increased by the low ambient density to lower the Re.

The same trend can be seen in Fig. 2.3a which charts the relationship between total *mass* and the chord Re [3] and Fig. 2.3b, in which the relationship between *wingspan* and *mass* for numerous flying bodies can be seen. Fig. 2.3a and b, have been adapted from Mueller and DeLaurier[3], and include current inflatable wing vehicles (details pertaining to the inflatable wing vehicles appear later). The small UAV flight regime, which includes μAVs is well below conventional aircraft. As in Fig. 2.2 and 2.3, this is the same flight regime occupied by birds and insects. These vehicles require efficient low Re airfoils that are not overly sensitive to wind shear, gusts, and the roughness produced by precipitation[3].

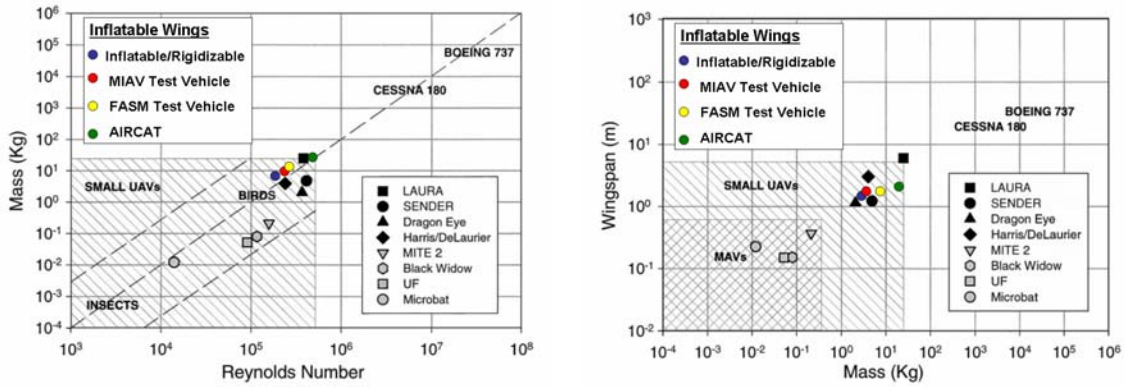

(a) Mass versus Re for a range of flying bodies.

(b) Wing span versus Mass for a range of flying bodies.

Figure 2.3: Characteristics of a range of aircraft[3].

Differences in operational range can clearly be seen in Fig. 2.4. This is "The Great Flight Diagram" that compares wing loading and cruising speeds of the largest and fastest airliners to the smallest insects. The diagram plots insects, birds and aircraft (human powered, ultralights, sailplanes, small engine powered airplanes and large commercial airliners). The smallest engine powered airplane in this diagram is the Piper Warrior, with a wing span 3.5 times larger than the albatross. The Boeing 747-400 has a wing span of 65m (21 times

greater than the albatross) and a cruising speed that is almost 10 times that of the albatross [4]. Fig. 2.5, shows the relationship between *wingspan* and *mass* for current operational UAVs.

UAVs are frequently required to perform at Re values below 500,000. The predominance of viscous effects in this regime causes the production of high drag forces and limits the maximum lift coefficient. The largest contribution to the total drag is from the pressure or form drag component, which arise due to the viscous influence of the boundary layer on the primarily inviscid pressure field. The drag problem is compounded when the flow separates, as the form drag increases significantly.

2.3.1 Surface Roughness

Surface roughness can be used to control separation and increase performance at low Re numbers. Experimental observations have shown that a "rough" airfoil surface will perform better than a "smooth" airfoil surface at low Re values, as shown in Fig. 2.6, adapted from McMasters and Henderson [38]. This is why small birds and insects have "rough" wing surfaces. Flow over the surface of an airfoil at low Re numbers (40–50,000) was laminar and remains laminar over the airfoil. Laminar fluid moves in layers and follows the curved surface of an airfoil. The closer the fluid layers are to the airfoil surface, the slower they move. Generally, the static pressure increases as the flow moves across a surface, small disturbances in the laminar flow are amplified and the flow turns turbulent. Static pressure decreases over the surface, disturbances in laminar flow are damped out and the flow remains laminar. Over an airfoil, the static pressure decreases from the leading edge to the point of maximum thickness. Thus, in this region, laminar flow was encouraged. However, the static pressure increases toward the trailing edge and laminar flow is hindered. In this laminar flow regime the airflow separates from the surface of the airfoil due to the unfavorable pressure gradients in the flow field. This causes a loss in performance of the airfoil, and the airfoil was said to "stall", causing loss of lift and a large increase in drag. In contrast at higher Re numbers, the airflow is turbulent. Turbulent flow over the same airfoils was shown to resist separation[39]. This provides a good reason for separation control by means of encouraging a transition from laminar to turbulent flow.

As seen in Fig. 2.6, surface roughness affects a body in a flow field. Surface roughness can cause the flow near the body to go from laminar to turbulent. The Re number and surface roughness both contribute to the determination of the laminar to turbulent transition. Low Re number flow will be laminar even on a rough surface and a very high Re number

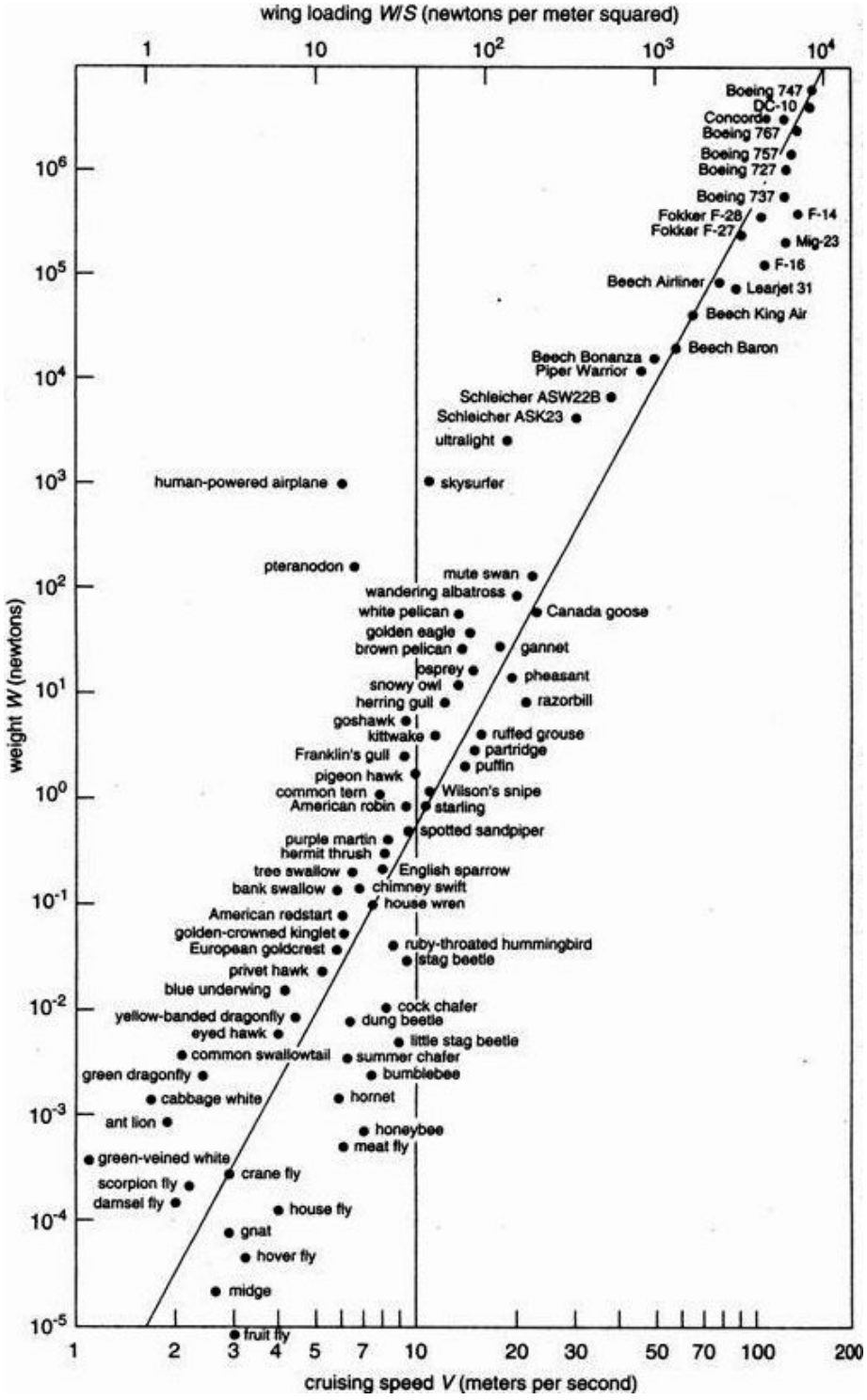

Figure 2.4: "The Great Flight Diagram [4]".

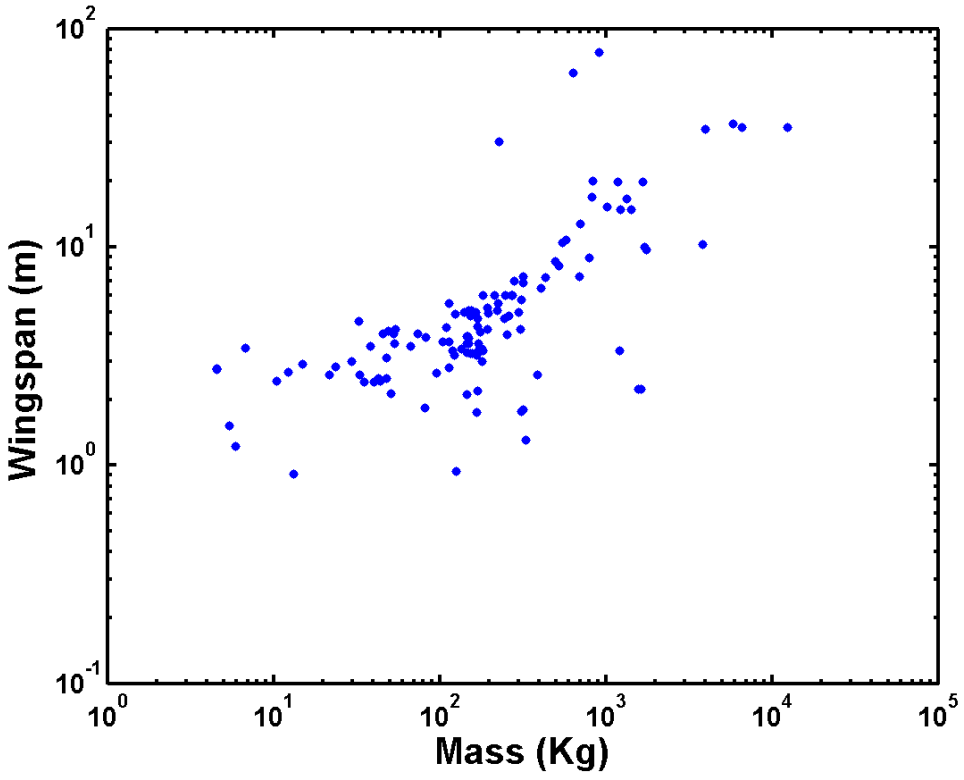

Figure 2.5: Wing span versus Mass for current operation UAVs (data obtained from [5]).

flow will be turbulent even on a smooth surface. This prompted research into devices which generated turbulence and hence aided in the transition from laminar to turbulent flow. The turbulence promoting devices ranged from static mechanical roughness elements such as strips and bumps to dynamic methods such as acoustic excitation and surface vibration. The methods disturb the flow and are generally hard to analyze[40].

The NACA reports[41, 42] are some of the earliest research studies on the effects of surface roughness on airfoil performance. The research placed protuberances of different shapes and sizes in a range of chord-wise locations. The reports observed that the loss of lift was directly proportional to the height of protuberances. At higher angles of attack, the protuberances had an adverse effect, especially when moved closer to the leading edge. Other work examined the effects of ice on the surface of wings[43, 44]. It was observed that bigger protuberances showed slightly better performance than thinner protuberances, and simple 2D protuberances provided the same benefits as 3D protuberances.

The effects of large distributed surface roughness on airfoil boundary layer development and transition to turbulence has been investigated for Re values of 0.5, 1.25 and 2.25 million by Kerho *et al.* [45]. They observed that the roughness promoted the growth of a transitional boundary layer, which required substantial chordwise extent (downstream of the roughness) to become fully turbulent. The fluctuating streamwise velocity and turbulence intensity in the roughness-induced boundary layer was found to be lower than the smooth case. In general, the longer the chordwise extent of the roughness and larger the roughness dimensions, the more the length of the transitional region was found to decrease.

Fig.2.6 shows the variation in L/D performance for various airfoils versus Re as determined by McMasters and Henderson [38]. Note that at low Re (in the range of birds, insects, μAVs, and UAVs), "smooth" airfoils perform worse than "rough" airfoils. However, the performance of smooth airfoils greatly improves at $Re \sim 10^5$ and exceeds that of rough airfoils. This is primarily due to the difference in the underlying physics at low and high Re and needs to be discussed further here.[3, 4, 46]

The variation in the L/D ratio with respect to Re for rough and smooth airfoils is described. However, the effect of the transition location with respect to L/D ratio is not described. As noted earlier, surface roughness and Re affect boundary layer development and the transition to turbulence. The effect of changing the initial trip location on L/D was examined. By altering the location of the transition point we can examine the effect of surface perturbations' positions on the performance of the airfoil. The location of the perturbations or the transition point, the Re number, and the characteristics of the airfoil and set-up affect the airfoils' performance.

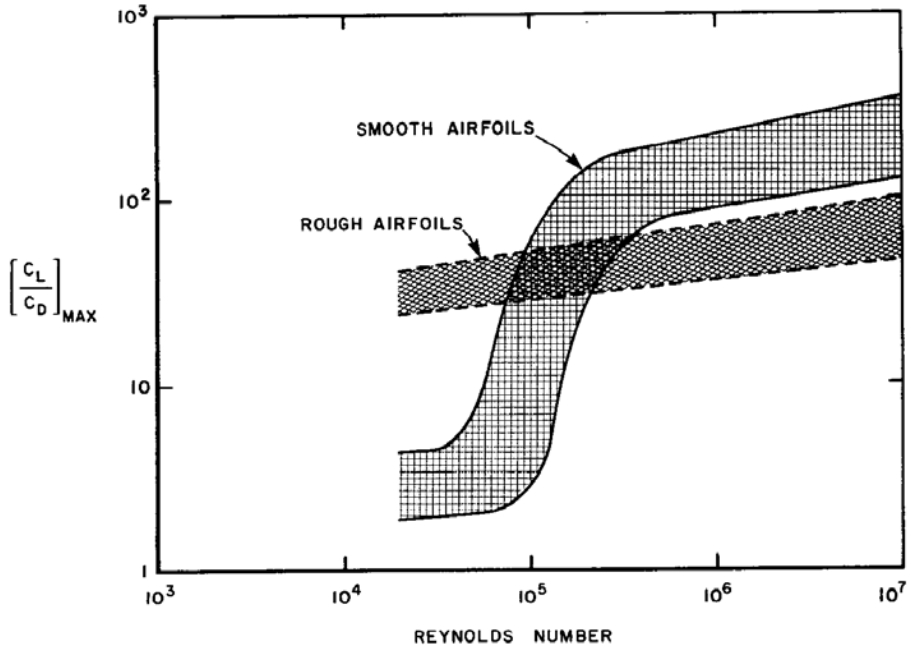

Figure 2.6: L/D versus Re ratio [2].

In this analysis $X-Foil$ was used as an analysis tool. X-Foil's analysis module consists of a 2^{nd} order panel method. Implemented within X-Foil is a method which takes the boundary layer surrounding the airfoil into account while solving for the flow field. The interaction between the boundary layer and external flow is modeled reasonably. The code can also handle small to medium sized separated regions. When the separation becomes larger or extends into the wake, the results are poor. The transition prediction, which is of utmost importance for low Reynolds number airfoils, is based on an e^n method, which is used as a simplified envelope method. In some cases, the errors introduced by this method can be large.

The analysis examined the effect of the transition point on the L/D ratio, more specifically the C_l/C_d ratio. To accomplish this the location of the transition was specified at 5, 10, 20, 30, 40, and 100 % relative to the chord length. In each case, the transition from laminar to turbulent could occur before the specified value but was required to transition from the specified point over the remainder of the airfoil. The Re was varied from 10, 50, 100, 200, 400, 600, 800, and $1000{\cdot}10^3$. Fig. 2.7, details the progress as the Re is varied from $10{\cdot}10^3$ to $200{\cdot}10^3$. Within these figures, the colored lines represent the specified transition point. The red line corresponds to a specified transition point of $5_c\%$ and the navy blue

corresponds to $100_c\%$.

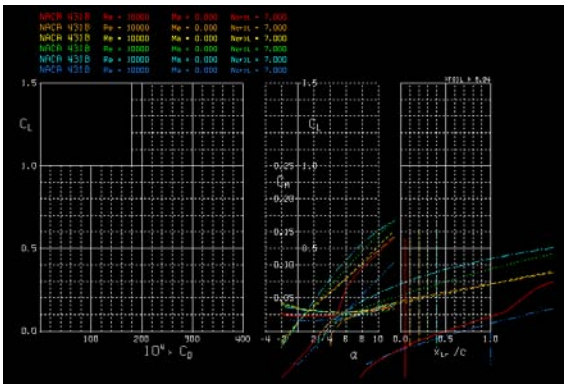

(a) $Re = 10{\cdot}10^3$.

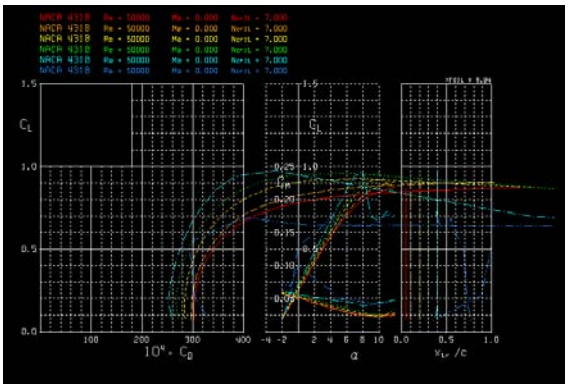

(b) $Re = 50{\cdot}10^3$.

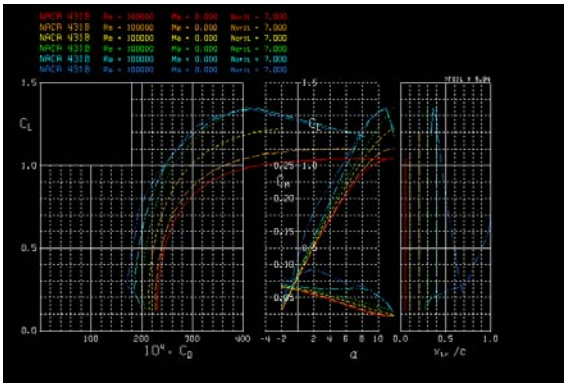

(c) $Re = 100{\cdot}10^3$.

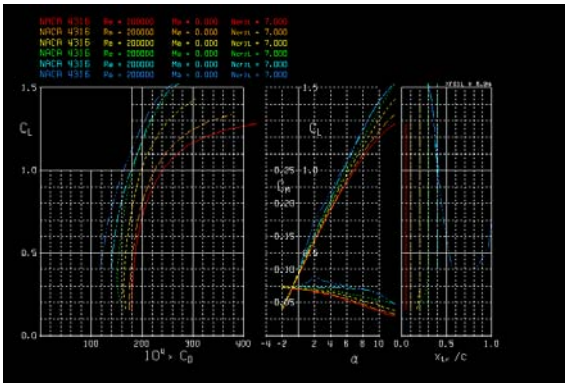

(d) $Re = 200{\cdot}10^3$.

Figure 2.7: C_l vs. C_d, C_l vs. α, C_m vs. α, and trip location vs. chord length for varying Re.

The results are shown in Fig. 2.8. The greatest benefit in forcing the trip to occur is at low Re numbers. At values below $100{\cdot}10^3$, the flow does not transition to turbulent and thus by forcing the flow to become turbulent we see a benefit in the L/D ratio. The benefit is discernible when the transition is forced to occur between 10 and $40\%_c$ as seen in Fig. 2.9.

At low Re, the inflatable profiles are an acceptable, perhaps even advantageous, wing choice. The reduction of separation by forced boundary layer transition makes an improvement. Performance begins to decrease in the range of $Re = 100,000 - 150,000$.[47] However, the performance is still acceptable beyond this level. At high Re near a critical value of $Re = 500,000$, the performance suffers. At this speed, skinning may be a requirement to achieve acceptable aerodynamic performance.

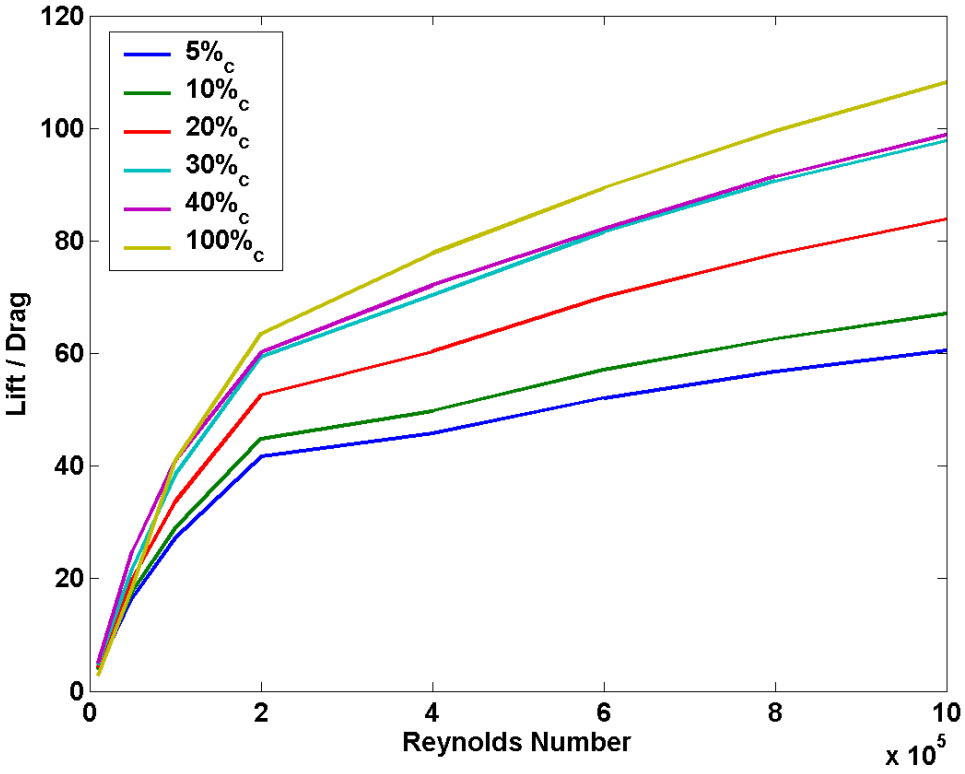

Figure 2.8: L/D versus Re ratio for different transition locations.

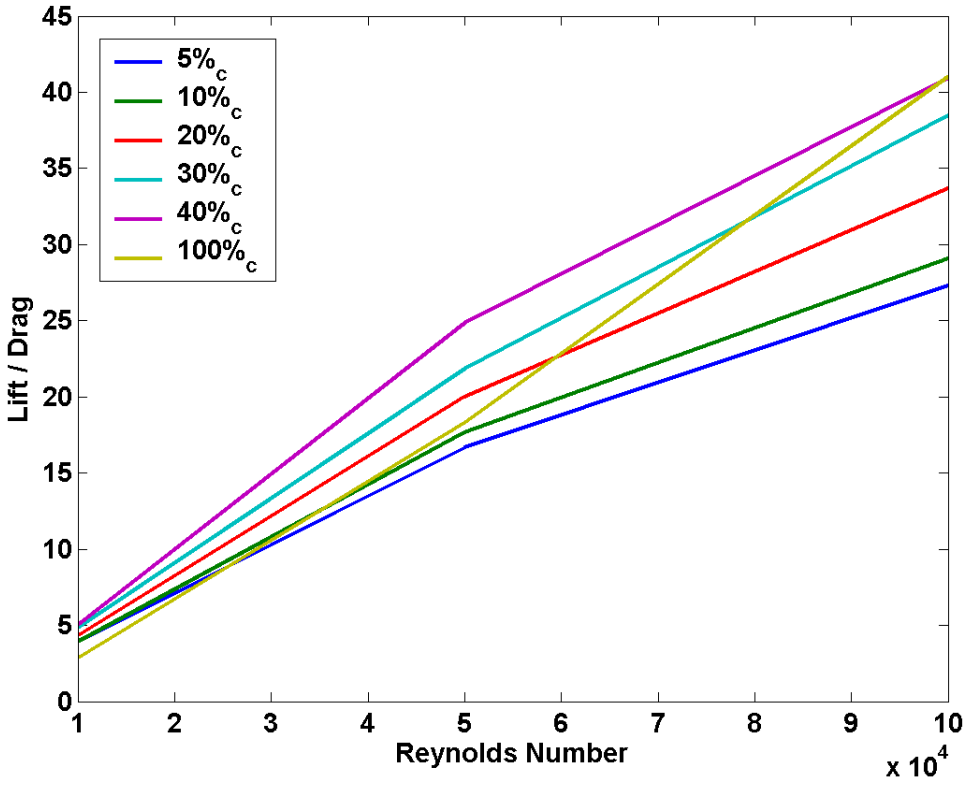

Figure 2.9: Low L/D versus Re ratio for different transition locations.

2.3.2 Aerodynamic Lift

Aerodynamic principles can be used to predict the flight characteristics of general aviation through characterizing and predicting fluid flow behavior around airfoils. Aerodynamic models exist that describe the flow around a wing, and these can be used to calculate forces acting on the wing. Because the flow surrounding wings is complex, researchers have made simplifying assumptions to aid in the analysis of the flow. The assumptions are that the flow is steady, inviscid, irrotational and incompressible.

- Steady: The parameters used to describe the flow (pressure, density, magnitude, and direction) can vary in space but do not vary with time,
- Inviscid: The flow is assumed to have negligible viscosity. Viscosity can be calculated using Eqn. 2.2,

$$\tau = \mu \frac{\mathrm{dU}}{\mathrm{ds}} \tag{2.2}$$

- Irrotational Flow: Flow that has zero vorticity. This is given in Eqn. 2.3,

$$\omega = \nabla \times \vec{U} = (\frac{dw}{dy} - \frac{dv}{dz})\hat{i} + (\frac{du}{dz} - \frac{dw}{dx})\hat{j} + (\frac{dv}{dx} - \frac{du}{dy})\hat{k} = 0 \tag{2.3}$$

- Incompressible Flow: The fluid cannot be compressed.

Here, τ is the shear stress, μ is the coefficient of viscosity, dU is the relative speed of two fluid layers and ds is the distance between the layers of fluid. Three different approaches to calculating aerodynamic lift are described next.

Calculating Aerodynamic Lift – Lifting Line Theory

Ludwig Prandtl developed the Lifting Line Model where an entire wing was replaced by one single line called the Lifting Line. Lift forces were assumed to act on this line instead of on the whole wing. Prandtl conducted experiments and developed theoretical descriptions of the aerodynamics of wings in Germany at the start of the 20^{th} century. The model developed from this research related wing shape to the lift and induced drag in low-speed flight. This model is called the Prandlt Lifting-line model or just the Lifting-line model (LLM).

Lifting-line theory is used for rapid estimation of span-wise load distributions and the basic aerodynamics of straight wings. Lifting-line equations can be used for determining the lift distribution for a given wing shape with given geometric and aerodynamic twist.

Utilizing this method gives a better understanding of how wing shape and twist contribute to the lift (or circulation) distribution[48].

Lifting-line theory involves a single integral equation that relates the span-wise circulation distribution with the span-wise shape of the wing and the geometric and aerodynamic twist of the wing. The goal is to specify the span-wise wing shape and the twist and to calculate the circulation distribution.

Fig. 2.10, shows a finite "flying" wing. Above the wing is the lift distribution which begins at one wingtip and ends at the other. Trailing behind each wingtip are tip-vortices while over the middle of the wing an inboard vortex sheet is displayed. This method aims to model the tip-vortices and the inboard vortex sheet with a series of "lifting lines".

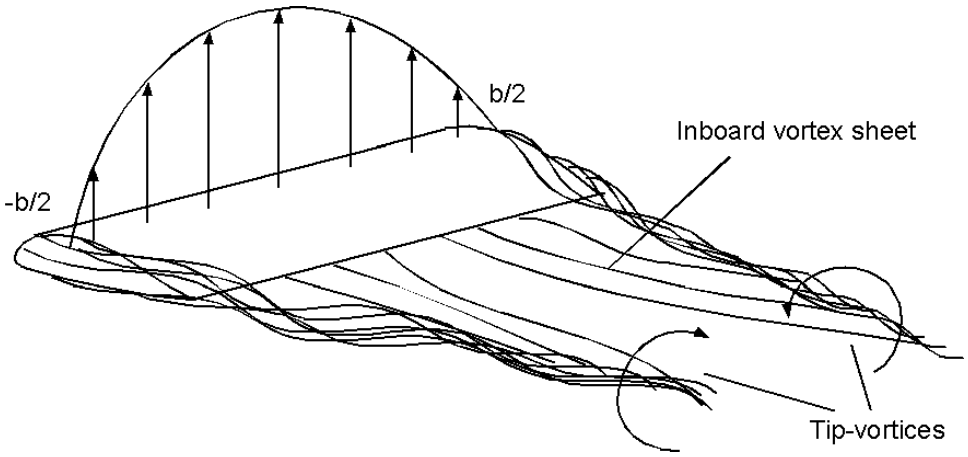

Figure 2.10: Wing with tip-vortices and inboard vortex sheet[6].

Prandlts model is derived here through Anderson's book *"Fundamentals of Aerodynamics"* [6] The model consisted of a vortex of strength Γ bound to a fixed location in the flow, in this case the quarter-chord line for a wing. The wing will experience a force ($L = \rho_\infty U_\infty \Gamma$) from the Kutta-Joukowski theorem. The bound vortex moves with the same fluid elements throughout the flow. A finite wing of span b is replaced with this bound vortex. The vortex begins at one wingtip ($y = \frac{-b}{2}$), extends over the span b, and ends at the other wingtip ($y = \frac{b}{2}$), as seen in Fig. 2.11.

However, due to Helmholtz's theorem, which states that a vortex cannot end in a fluid, it is assumed that the vortex filament continues as two free vortices trailing downstream from the wingtips to infinity. Together the bound and free vortices are called a "horseshoe vortex".

The downwash, w, induced by the bound vortex and the two trailing vortices are in

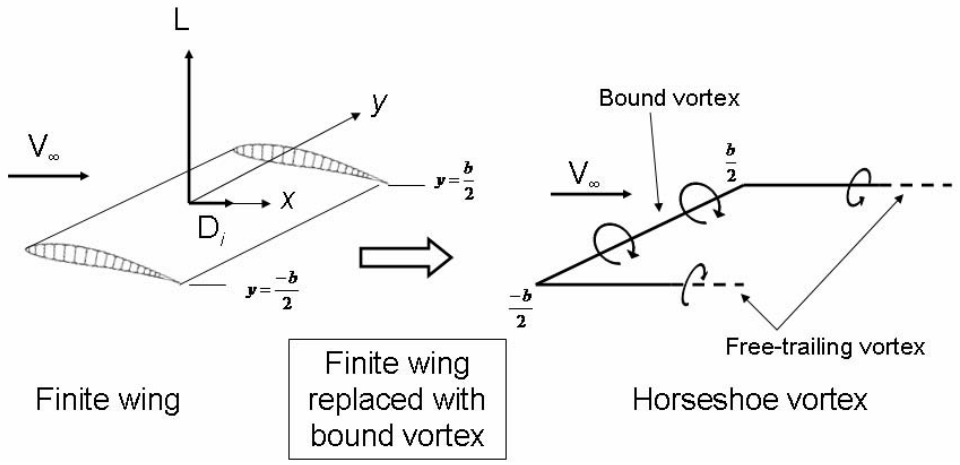

Figure 2.11: Finite wing replaced with bound vortex (adapted from [6]).

the downward direction of the xyz coordinate system in Fig 2.11. This downward velocity is negative. If the origin is taken from the center of the bound vortex, the velocity of any point y along the bound vortex induced by the trailing semi-infinite vortices is given by Eqn. 2.4

$$w(y) = -\frac{\Gamma}{4\pi(\frac{b}{2}+y)} - \frac{\Gamma}{4\pi(\frac{b}{2}-y)} \tag{2.4}$$

this reduces to Eqn. 2.5

$$w(y) = -\frac{\Gamma}{4\pi}\frac{b}{(\frac{b}{2})^2 - y^2} \tag{2.5}$$

A large number of horseshoe vortices are now superimposed with differing length bound vortices, but all have two trailing vortices. The bound vortices are all coincident along the same single line at the quarter-chord. This can be seen in Fig. 2.12. Eqn. 2.5 can now be modified from a single horseshoe vortex to multiple vortices. This results in an expression for the total velocity w induced at a y location by the trailing vortex sheet as a summation over all the vortex filaments from $-b/2$ to $b/2$. That is Eqn. 2.6

$$w(y_0) = -\frac{1}{4\pi}\int_{-b/2}^{b/2} \frac{(d\Gamma/dy)}{y_0 - y} dy \tag{2.6}$$

the induced angle of attack α_i is given by Eqn. 2.7. Here, w is much smaller than V_∞ and hence the angle is small. Thus we can approximate Eqn. 2.7 by Eqn. 2.8. Eqn. 2.6 can then be substituted into Eqn. 2.8 to obtain Eqn. 2.9, which is an expression for the induced angle of attack in terms of the circulation distribution $\Gamma(y)$ along the wing.

$$\alpha_i(y_0) = Tan^{-1}(\frac{-w(y_0)}{U_\infty}) \tag{2.7}$$

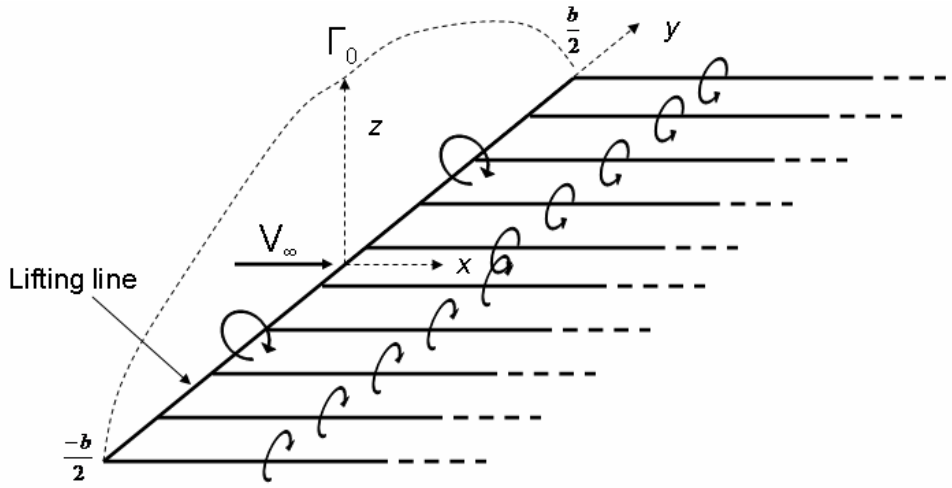

Figure 2.12: Coincident horseshoe vortices along the lifting line[6].

$$\alpha_i(y_0) = -\frac{w(y_0)}{U_\infty} \tag{2.8}$$

$$\alpha_i(y_0) = -\frac{1}{4\pi U_\infty}\int_{-b/2}^{b/2}\frac{(d\Gamma/dy)}{y_0 - y}dy \tag{2.9}$$

the effective angle of attack α_{eff}, is the angle of attack actually seen by the local airfoil section. This value varies across the span, and thus the lift generated from one section to the next also varies. Eqn. 2.10 describes the variation in the lift coefficient at the local airfoil section.

$$c_l = a_0(\alpha_{eff}(y_0) - \alpha_{L=0}) = 2\pi(\alpha_{eff}(y_0) - \alpha_{L=0}) \tag{2.10}$$

In Eqn. 2.10, the local section lift slope a_0 has been replaced by a thin airfoil theoretical value of 2π. For a wing with aerodynamic twist, the angle of zero lift $\alpha_{L=0}$ varies with y_0. If there is no aerodynamic twist, $\alpha_{L=0}$ is constant across the span. The value, $\alpha_{L=0}$ is known for the local airfoil sections. From the Kutta-Joukowski theorem and the definition of lift coefficient we have Eqn. 2.11.

$$\acute{L} = \frac{1}{2}\rho_\infty U_\infty^2 c(y_0) c_l = \rho_\infty U_\infty \Gamma(y_0) \tag{2.11}$$

from Eqn. 2.11, we obtain Eqn. 2.12

$$c_l = \frac{2\Gamma(y_0)}{U_\infty c(y_0)} \tag{2.12}$$

substituting Eqn. 2.12 and Eqn. 2.10 into Eqn. 2.11 and solving for α_{eff} we get Eqn. 2.13

$$\alpha_{eff} = \frac{\Gamma(y_0)}{\pi U_\infty c(y_0)} + \alpha_{L=0} \tag{2.13}$$

The effective angle of attack is defined as $\alpha_{eff} = \alpha - \alpha_i$. Thus substituting the above equations into this definition we obtain the fundamental equation of Prandtl's lifting-line theory (Eqn. 2.14).

$$\alpha(y_0) = \frac{\Gamma(y_0)}{\pi U_\infty c(y_0)} + \alpha_{L=0}(y_0) + \frac{1}{4\pi U_\infty} \int_{-b/2}^{b/2} \frac{(d\Gamma/dy)}{y_0 - y} dy \tag{2.14}$$

This equation states that the geometric angle of attack is equal to the sum of the effective angle plus the induced angle of attack. The only unknown in this equation is Γ. All other quantities, that is, α, c, V_∞, and $\alpha_{L=0}$, are known for a finite wing of given design at a given geometric angle of attack in a given free-stream velocity. The solution yields $\Gamma = \Gamma(y_0)$ and gives three main aerodynamic properties.

1. The lift distribution obtained form Kutta-Joukowski theorem, Eqn. 2.15:

$$\acute{L}(y_0) = \rho_\infty U_\infty \Gamma(y_0) \tag{2.15}$$

2. The total lift obtained by integrating Eqn. 2.15 over the span giving Eqn. 2.16:

$$L = \rho_\infty U_\infty \int_{-b/2}^{b/2} \Gamma(y) dy \tag{2.16}$$

   which is followed from Eqn. 2.16 by the lift coefficient given in Eqn. 2.17

$$C_L = \frac{L}{q_\infty S} = \frac{2}{U_\infty S} \int_{-b/2}^{b/2} \Gamma(y) dy \tag{2.17}$$

3. The induced drag obtained by inspection given as Eqn. 2.18:

$$D_i = \rho_\infty U_\infty \int_{-b/2}^{b/2} \Gamma(y) \alpha_i(y) dy \tag{2.18}$$

   which in turn gives the induced drag coefficient as Eqn. 2.19

$$C_{D,i} = \frac{D_i}{q_\infty S} = \frac{2}{U_\infty S} \int_{-b/2}^{b/2} \Gamma(y) \alpha_i(y) dy \tag{2.19}$$

Calculating Aerodynamic Lift – Vortex Lattice Method

The principle of a Vortex Lattice Method is to assimilate the perturbation generated by the wing to that of a sum of vortices distributed over the wing's planform. The strength of each vortex is calculated to meet the appropriate boundary conditions, i.e. non penetration conditions on the surface of the panels.

The main differences between the Vortex Lattice Method and Lifting Line Theory are:

1. The calculation of the lift distribution, the induced angles and the induced drag is inviscid and linear i.e. it is independent of the wing's speed and of the air's viscous characteristics.

2. The method is applicable to any usual wing geometry, including those with sweep, low aspect ratio or high dihedral, and winglets.

The force acting over each panel is the vectorial cross product, as seen in Eqn. 2.20

$$\mathrm{F} = \rho \mathrm{U} \times \Gamma \tag{2.20}$$

here, Γ is the vortex strength, ρ is the fluid density, and U is the freestream speed. The force is normal to each panel, and hence, the lift coefficient is defined as Eqn. 2.21.

$$\mathrm{C_L} = \frac{1}{\rho \mathrm{SU}^2} \sum_{\mathrm{Panels}} \mathrm{F.n} \tag{2.21}$$

where, n is the normal to each panel, and S is the planform's area

2.3.3 Efficiency and Performance Parameters

Principally, efficiency is maximized by increasing the lift L and decreasing the drag D or maximizing the lift-to drag ratio (L/D) for any configuration. A given airfoil profile has vastly differing lift and drag characteristics over the possible ranges of Re and Mach number (M) (recall: L/D=*f(Re)*). Thus, airfoils are typically designed for a narrow range of flight conditions. Alternatively, airfoils can be designed that perform adequately over a wide range of conditions, but do not perform well in any.

Morphing and warping airfoils have become a tantalizing solution to this problem. The concept is to alter the wings' shape in flight to better suit the operation conditions or to affect the control of the vehicle. Section 2.5, highlights current vehicles employing concepts that alter wing shape. Morphing and warping can take many forms, such as twisting, plan form change, span change, and body shape change. These techniques are discussed in detail later.

The lifting capability of an airfoil is defined by the lift coefficient (C_l)

$$\mathrm{C_l} = \frac{L}{q_\infty S} \tag{2.22}$$

where, L denotes lift, q_∞ denotes dynamic pressure, and S denotes wing area. Likewise, the drag coefficient (C_d) is given by

$$\mathrm{C_d} = \frac{D}{q_\infty S} \tag{2.23}$$

where, D denotes drag and the moment coefficient (C_m) is given by

$$\mathrm{C_m} = \frac{M}{q_\infty S} \tag{2.24}$$

above, q_∞ is the dynamic pressure, defined as

$$\mathrm{q_\infty} = \frac{1}{2}\rho U^2 \tag{2.25}$$

As highlighted by Bowman *et al.* [49], W/S is the main function dictating the speed at which a vehicle can fly. If the C_l remains constant, as the wing area is reduced, the result is an increase in flight speed. This is seen in equation 2.26 which is a modified version of equation 2.22. (where: $L \equiv W$.)

$$\mathrm{U} = \sqrt{\frac{2W}{\rho S C_l}} \tag{2.26}$$

A strong indicator of the agility, maneuverability and performance of an aircraft is its turning radius [49][50]. This is shown in Eqn. 2.27. Many factors determine the turning radius of an aircraft, and from this (Eqn. 2.27) we can see that the turn radius can be altered in a number of ways. The coefficient of lift or C_l can be altered by changing the camber of the wings[50]. This can be accomplished through leading edge flaps/slats, trailing edge flaps, and airfoil shape change[49]. The wing loading, or W/S, can be altered through fowler flaps or telescoping wings where the span of the wing is increased or decreased. And finally, the thrust to weight ratio, or T/W, can be altered through thrust vectoring [49]. Since lift can be increased for a given speed or maintained with decreasing airspeed with a change in angle of attack, the purpose of morphing is to modify lift to achieve a given lift force at a particular angle of attack[49].

$$\mathrm{R} = \frac{U_{true}^2}{g\left(q\frac{C_l}{W/S} + \frac{T}{W}sin\epsilon\right)} \tag{2.27}$$

in level and steady flight, the generated thrust T must balance the drag D and the generated lift L must balance the vehicle weight W, or

$$\mathrm{T} = D \tag{2.28}$$

$$\mathrm{L} = W \tag{2.29}$$

This simply shows that increasing L (or C_l) results in the ability to lift a vehicle of greater weight. The resulting power requirements can then be derived from the relation

$$\mathrm{P} \approx TU = DU = (D_o + D_i)U \tag{2.30}$$

substituting for D, we can write equation 2.31, which shows that minimal power exists for a specific U. The cubic term represents the power required to overcome increasing air resistance at increasing velocity while the hyperbolic term represents the power required to generate enough lift at low speeds to keep $L = W$. This is the velocity of maximum economy. By adding inflatable wings to the tips of traditional airfoils, one can modify the vehicle power requirements. This allows one to design around multiple optimal points; Fig.2.13 shows the required power curves for varying aspect ratio conditions. A change in aspect ratio of only 20% can reduce the minimum power speed by up to 50% while doubling the aspect ratio results in a gain only slightly more. Thus, small changes in aspect ratio can be leveraged for use in low-speed flight by use of deployable extentions.

$$\mathrm{P} \approx \frac{1}{2} C_d \rho U^3 S + \frac{2W^2}{\pi \rho b^2 U^2} \tag{2.31}$$

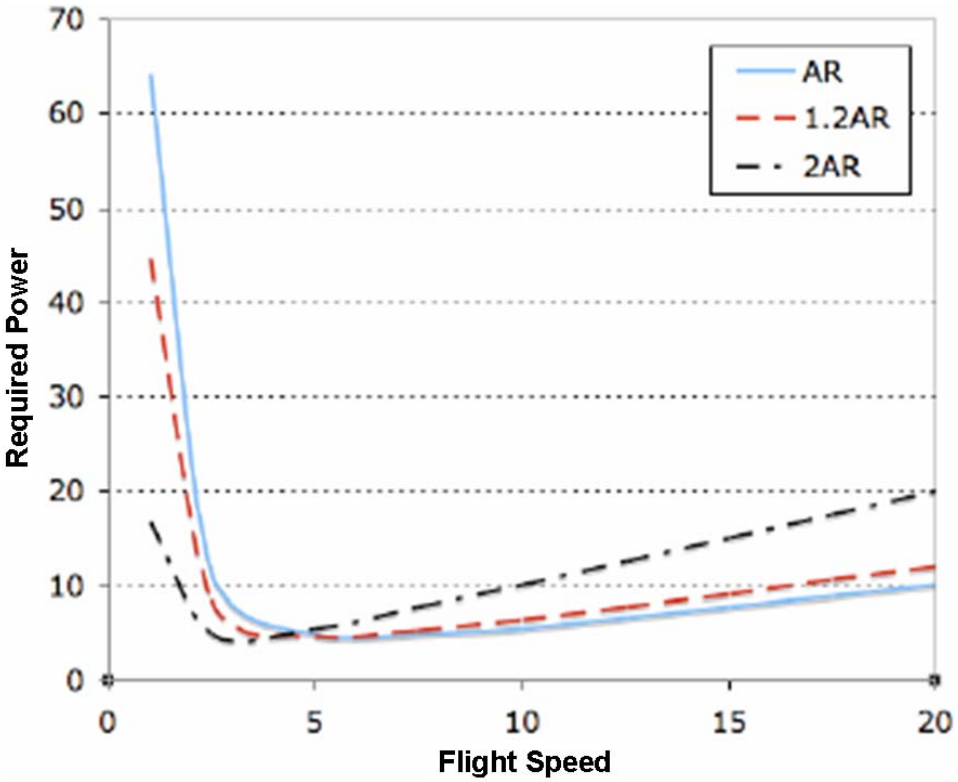

Figure 2.13: Power requirements for varying aspect ratio.

The point of minimum total drag can be determined from the point at which the D_i

and D_o are equal. From equation 2.30, this can be shown as

$$\mathrm{D_{min}} \approx 2W\sqrt{\frac{C_d}{2\pi AR}} \tag{2.32}$$

where, AR denotes the aspect ratio of the wing ($AR = \frac{b^2}{S}$) as graphed in Fig. 2.14 relative to the baseline AR used in the designs herein. Since $L = W$, this corresponds to L/D_{max} conditions and is the region of maximum aerodynamic efficiency. The drag increases hyperbolically at low velocities; therefore, it is typically more economic to fly at greater than minimum drag speed than it is to fly below it. A typical aircraft spends most of its time in a high velocity cruise mode, and the wing profiles are selected with this in mind.

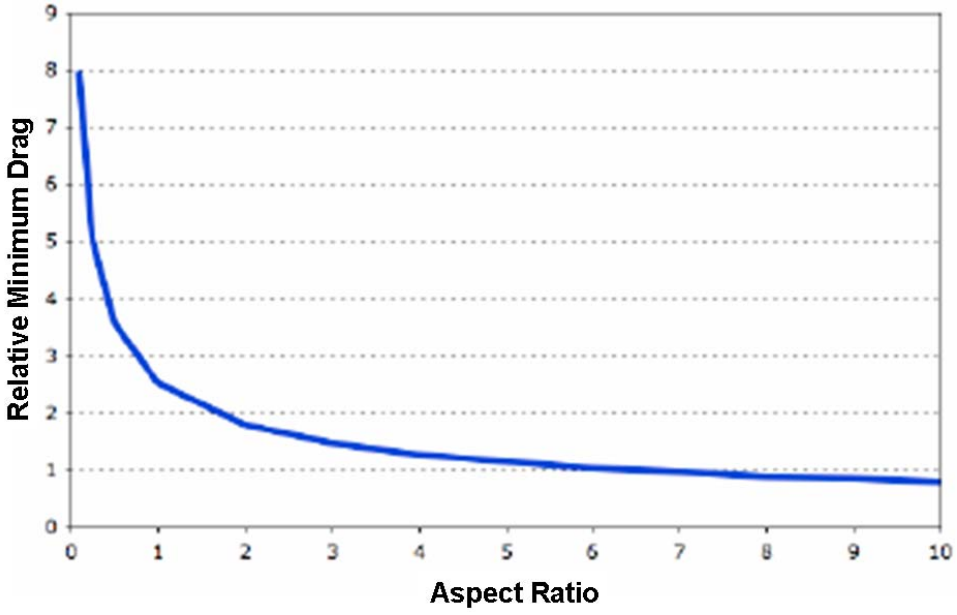

Figure 2.14: Minimum drag versus aspect ratio.

Separation Bubble

The post separation behavior of the laminar layer accounts for the deterioration in airfoil performance at low Re. This deterioration is apparent due to the increase in drag D and the decrease in lift L. The choice of airfoil is very important in this low Re – M range, as a small increase in thickness can have significant effects on laminar separation. The flow over the airfoil at these low Re is laminar, and slight changes in flow speed can have significant effects in the lift-to-drag ratio [50]. The laminar boundary layer is less capable of

handling adverse pressure gradient without separation compared to the turbulent boundary layer, which in general, has more momentum.

The generation of laminar separation bubbles at low Re values is shown in Fig. 2.15. Flow will separate as a result of the strong adverse pressure gradient. At these low Re the flow does not reattach. The separated flow creates a reverse flow region close to the surface, which has been described in detail by Lissaman[51]. Flow separation decreases the lift generation capabilities L and increases drag D. In this region, different types of flow phenomena occur, such as flow separation, transition and reattachment. Flow separation is the main contributor to the low L/D ratio. In order to increase the performance of the airfoil, it is necessary to eliminate or reduce flow separation. For $Re > 10^6$ flow separation is usually not a concern because the boundary layer has already transitioned to turbulent. Turbulent boundary layers have more momentum to overcome adverse pressure gradient and thus are less prone to separation.

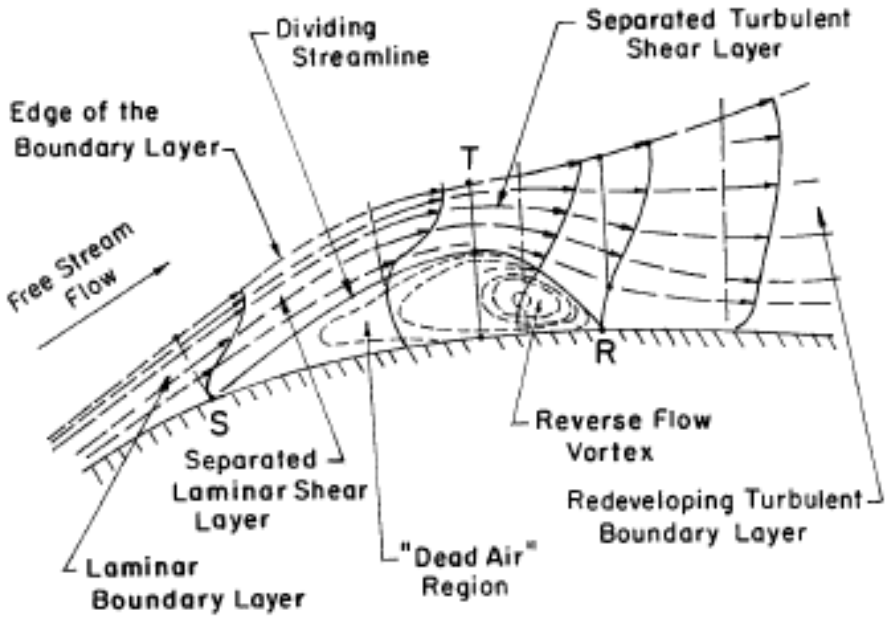

Figure 2.15: Close-up of laminar separation bubble [7].

2.3.4 XFoil

Analysis within this research was done using a version of XFoil[52]. Numerical simulation of low Re number flow is very difficult due to the strong interaction of the boundary

layer effects. XFoil addresses the problems associated with these viscous boundary layer interactions. The software is able to predict laminar and turbulent separated flows. An accurate transition prediction method has been implemented into XFoil to achieve reliable reattachment location, bubble size, and associated losses. XFoil uses a global Newton-Raphson method to couple viscous–inviscid flows.

XFoil has two major modes of operation, analysis and mixed inverse design. Mixed inverse design mode takes a user prescribed pressure distribution and builds an airfoil geometry that will most closely match it. This feature not use in the current research project and is not described in detail. The analysis mode employs user defined airfoil coordinates and solves for various boundary layer and airfoil characteristics. The analysis mode is the primary mode of operation for this research.

Boundary Conditions

XFOIL requires boundary conditions to ensure good results. In analysis mode, the airfoil surface defines the location of the initial streamline. As the simulation progresses the surface streamline is adjusted according to the local boundary layer displacement thickness [52]. The stagnation point is allowed to assume any position on the airfoils surface, such that the pressure is equal on either side of the airfoil. In the case of separated flow the stagnation streamlines aft of the airfoil are separated by the thickness of the wake displacement. The far-field boundary conditions are defined by a freestream pressure, vortex, source, and doublet. The vortex strength is derived from the Kutta-condition, the source strength from any viscous wakes, and the doublet strength from the requirement to minimize the discrete streamlines deviation from the analytic velocity potential [52].

Transition Prediction

XFOIL uses spatial-amplification theory, derived from the Orr-Sommerfeld equation to predict laminar to turbulent transition. The method utilizes the Orr-Sommerfeld equation solved for the group of Falkner-Skan boundary layer profiles at various shape parameters and unstable frequencies [52]. The solutions are then linearized for different constant shape parameter values in order to relate them to the amplification factor. Transition is assumed to occur when the most unstable frequency in the boundary layer has exceeded the value e^n, where n is a predetermined value, usually taken to be 9 to model the flow in a clean wing tunnel. Use of the en method is only appropriate in modeling flow where 2D Tollmien-Schlichting waves are the dominate cause of transition, which is the case in modeling low

Re number airfoils [52].

Limitations

There are known limitations of XFoil. XFoil restricts the minimum airfoil thickness to $1\%_c$, poorly predicts post stall airfoil performance, and distorts lift and drag results. The panel method that XFoil employs directly limits the minimum thickness of airfoils that can be tested. In the hypothetical case of zero thickness, the boundary layer matrix can not be solved. The reliability of converged solutions beyond stall, associated with the occurrence of C_{lmax}, is poor. In most cases Xfoil will converge on a solution, but large boundary layer thickness and fully separated flow are not well modeled which results in poor lift and drag values. In general only airfoil performance just after stall is relevant and additional data is not reliable. XFoil tends to over predict lift and under predicts drag.

2.4 Aeroelasticity

Aeroelasticity is the study of the static and dynamic behaviors of structural elements in a flowing fluid. Aeroelasticity is chiefly concerned with the interaction between the deformation of an elastic structure in an air stream and the resulting aerodynamic force. It is important in the design of airplanes, helicopters, missiles, suspension bridges, power lines, and tall chimneys. An example is the Tacoma Narrows bridge disaster. Here the elastic characteristics of the bridge were excited by the wind. The structure began to vibrate at resonance due to the energy extracted from the wind. At resonance the bridge oscillated wildly, causing its destruction [53, 54].

Aeroelastic phenomena have played a major role throughout the history of powered flight. The Wright brothers utilized controlled warping of the wings on the 1903 Wright Flyer to achieve lateral control. This was essential to achieving powered flight as the aircraft was laterally unstable due to anhedral of the wings. The 1903 Wright Flyer design used a rigid skeleton frame covered in a cloth skin, to resemble the wings of birds and bats. Thus, the wing was flexible and aeroelastic phenomena were prevalent.

The primary concerns of aeroelasticity include stability and control, flutter, and structural loads arising from maneuvers and atmospheric turbulence. Methods of aeroelastic analysis differ according to the time dependence of the inertial and aerodynamic forces. For the analysis of flying qualities and maneuvering loads wherein the aerodynamic loads vary relatively slowly, quasi-static methods are applicable. The remaining problems are dynamic, and methods of analysis differ according to whether the time dependence is arbitrary or

oscillatory.

The redistribution of air loads caused by structural deformation affects the performance of the aerodynamic surfaces from that of a rigid aerodynamic surface. The simultaneous analysis of the aerodynamic loads, the structural loads, and the total flow disturbance, including the disturbance resulting from structural deformation, leads to a determination of the equilibrium aeroelastic state. If the aerodynamic loads increase the total flow disturbance, the lift effectiveness increases If the air loads decrease the total flow disturbance, the effectiveness decreases.

The aerodynamic loads induced by control-surface deflection also induce aeroelastic loading. The effectiveness will differ from that of a rigid system and may increase or decrease depending on the relationship between the net external loading and the deformation.

2.4.1 Flutter

One of the major research areas in the field of aeroelasticity is "flutter". Flutter is a dynamic instability of a body subjected to external forces. The phenomenon occurs as a result of the interaction between aerodynamics, stiffness, and inertial forces on the structure. Flutter, primarily of the wings, has the potential to increase without bounds given the right conditions. In an aircraft, as the dynamic pressure increases, there may be a point at which the structural damping is insufficient to damp the motions which are increasing due to aerodynamic energy being added to the structure. This can be a catastrophic phenomena and its prevention forms a critical role in aircraft design [55]. However, most materials have some non-linearities associated with their behaviors, such as hardening or internal damping. Additionally, the fluid dynamics can be non-linear due to separation of flow, or due to the presence of a shock (usually not applicable with low Re flow, except when low densities and pressures are coupled with high speeds). These conditions of non-linearity, both structural and aerodynamic are usually beneficial with regard to the control of flutter.

A self-excited vibration is possible if a disturbance to an aeroelastic system gives rise to unsteady aerodynamic loads such that the ensuing motion can be sustained. At the flutter speed a critical phasing between the motion and the loading permits extraction of an amount of energy from the air stream equal to that dissipated by internal damping during each cycle, and thereby sustains a neutrally stable periodic motion. At lower speeds any disturbance will be damped, while at higher speeds, or at least in a range of higher speeds, disturbances will be amplified. Other natural sources of disturbance are wind shears, vertical drafts, mountain waves, and clear air. Storm turbulence imposes significant dynamic loads on

aircraft. Additionally, buffeting during flight at high angles of attack or at transonic speeds can cause disturbance.

2.4.2 Types of Flutter

Behavior characterized as types of flutter occurring on aircraft are: panel flutter, wake vortex flutter, stall flutter, limit cycle oscillations (LCO), engine whirl flutter, and flutter due to objects mounted on the wing.

Panel flutter refers to the aircraft skin. Here the skin of the aircraft in not adequately supported and skin vibrates under certain loading conditions. Wake vortex flutter (or Galloping flutter) is caused by the formation of wake vortices downstream of the object. The wake vortices are shed alternately from one side of the object and then the other, the phenomena is know as Von Karman Vortex shedding. The vortices cause oscillatory motion and forces, producing back-and-forth motions in the structure. This was the cause of failure of the Tacoma Narrows Bridge.

Stall flutter occurs at high wing loading conditions near the stall speed of the wing. The flutter mechanism is a torsional mode caused by airflow separating over the surface of the airfoil. Limit cycle oscillation (or LCO) behavior is a constant amplitude and periodic structural response. The frequency of the LCO are those of the aeroelastically-loaded structure. LCO is typically limited to a narrow region in Mach number or angle-of-attack and can signal the onset of flow separation. Engine whirl flutter involves a complex interaction of engine mount stiffness, gyroscopic torques of the engine and propeller combination, and the natural flutter frequency of the wing structure.

2.4.3 Wake vortex flutter – Motion

Wake vortex flutter is a combination of bending and torsional motion. If we consider an aircraft wing, the motion is initiated by a torsional rotation (nose-up) of the airfoil. The wing experiences increased aerodynamic loads, which cause the wing to rise. As the wing lifts or bends the torsional stiffness of the wing structure increases and restores the initial rotation of the wing. The bending stiffness of the wing returns the airfoil to the neutral position but causes the airfoil to rotate in a nose-down position. The increased aerodynamic forces cause the wing to plunge. The torsional stiffness returns the airfoil to its initial rotation. The bending stiffness of the wing returns the structure to the neutral position and also induces a nose-up rotation in the wing, completing the cycle. Fig. 2.16, shows the torsional and bending motion for an airfoil exhibiting flutter. Maximum positive

rotation ($t = 0$) gives rise to the maximum rise and zero rotation ($t = T/4$). The downward plunge of the airfoil gives rise to a nose-down twist ($t = T/2$) as the airfoil passes through the neutral position. The process is reversed for the bottom half of the plunge ($t = T/2$ to $t = T/T$)[55, 56, 57, 58, 59]

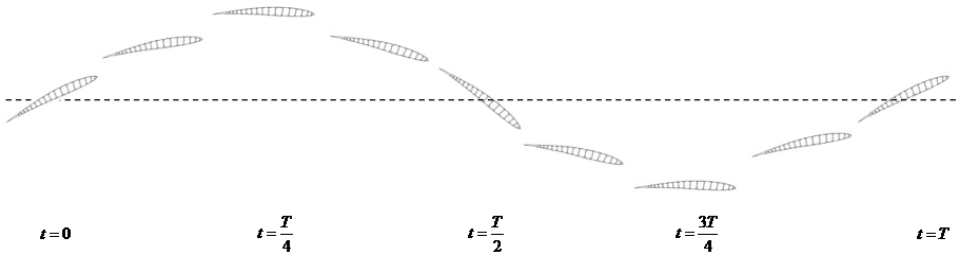

Figure 2.16: Flutter - torsional and bending motion.

Flutter results from the combination of the two structural modes: torsion and bending. The torsional mode is a span-wise rotation of the wing, and the bending mode is a vertical up and down motion at the wingtip. As the airfoil flies at increasing speed, the frequencies of the bending and torsional modes come together.

Flutter Modeling

Research into the causes and the prediction of flutter has been conducted and studied over the course of the last century. Theories have been proposed for the cause of flutter, and mathematical analysis tools have been developed to analyze the behavior. Disciplines involved in analyzing flutter include aerodynamics, structural finite element modeling, control theory (specifically aeroservoelasticity), and structural dynamics. These disciplines have given rise to theories such as aerodynamic strip theory, beam structural models, unsteady lifting surface methods (e.g. double-lattice) and finite element models.

One model used to analyze flutter is a simple two degree-of-freedom model. This model is shown in Fig. 2.17. Aerodynamic forces excite the structural spring and mass system. The plunge spring represents the bending stiffness of the structure and the rotation spring represents the torsional stiffness. The shape of the airfoil determines the aerodynamic center. The center of gravity is determined by the mass distribution of the cross-section. The model represents two "modes": bending and torsion.[55, 56, 57, 58, 59]

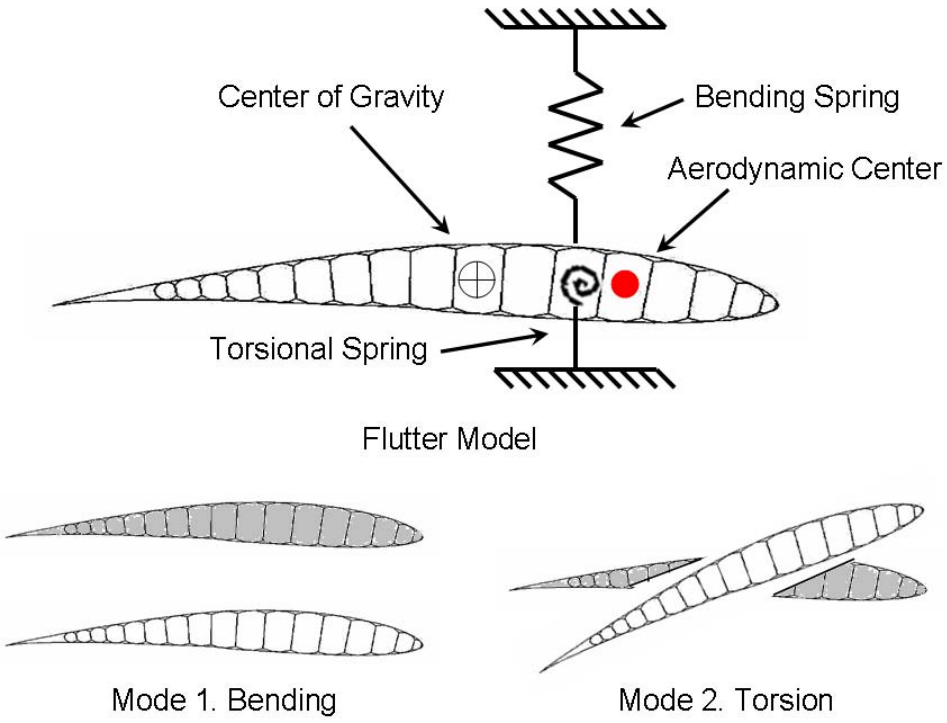

Figure 2.17: Airfoil flutter model and modes.

Flutter Equations of Motion

If modes of structural vibration are used in a dynamic analysis, the Eqn. 2.33 can be used to determine a model of flutter characteristics. This equation is the result of assuming simple harmonic motion $\{u(t)\}=\{u_h\}e^{i\omega t}$ and placing this into the corresponding second order ordinary differential equations that describe the linear dynamic behavior of a structure that is subjected to forces and moments due to fluid flow.[55, 56, 57, 58, 59] This is a representative example of the equations of motion for flutter.

$$\left[\mathrm{M_{hh}p^2} + \left(\mathrm{B_{hh}} - \frac{\rho \mathrm{cVQ^I_{hh}}}{4\mathrm{k}}\right) + \left(\mathrm{K_{hh}} - \frac{\rho \mathrm{V^2 Q^R_{hh}}}{2}\right)\right]\{\mathrm{u_h}\} = 0 \tag{2.33}$$

here, M_{hh} is the modal mass matrix, B_{hh} is the modal damping matrix, K_{hh} is the modal stiffness matrix, Q^I_{hh} is the generalized aerodynamic damping matrix, Q^R_{hh} is the generalized aerodynamic stiffness matrix, ρ is the air density, c is the mean aerodynamic chord length, V is the airspeed, $\mathrm{k} = \omega$ c/ 2V is the reduced frequency, ω is the circular frequency, p is the iω - (i=$\sqrt{-1}$), and u_h is the modal displacements.

2.5 Morphing and Warping Wings

As the name implies, "morphing" and "warping" wings change shape. The term "morphing wing" generally describes an aircraft wing or structure that can change size and shape during flight to enable the aircraft to drastically change its performance or flight characteristics. A "warping wing" describes a wing that can change either shape or size; however, the change is not as drastic as a morphing wing. Many vehicles in the past could potentially claim to be the first morphed wing aircraft. These include, the tilt-rotor V-22 Osprey, the swing-wing F-111 Aardvark, the F-14 Tomcat, and the 1903 Wright Flyer. However, true morphing is more than simply moving one solid wing element to a different angle or location with respect to other wing components on a fixed-wing aircraft. The "Defense Advanced Research Projects Agency" (or DARPA) describes morphing vehicles as being capable of "radical shape changes". The goal is to change wing areas, spans, chord and other dimensions by approximately 50%. According to DARPA, a morphing aircraft is a multi-role platform that:

1. Changes its state substantially to adapt to changing mission environments,
2. Provides superior system capability not possible without reconfiguration, and
3. Uses a design that integrates innovative combinations of advanced materials, actuators, flow controllers, and mechanisms to achieve the change.

The goal of morphing and warping is to change the shape of the wing in order to affect the aerodynamics of the wing. By altering the shape of the wing during operation, the L/D, and hence the performance of the vehicle can be changed. Wings whose shape can be altered in flight have the promise of revolutionizing aeronautics [50]. For example, a change in the geometry of the wing might be used to suppress flutter, reduce buffeting effects, maximize fuel economy, or improve flight control.

Aircraft are currently designed for single missions such as reconnaissance or attack. Wing shape is currently dictated by the primary mission of the aircraft. The vehicle is thus operating with a non-optimal wing shape during irregular missions and roles. The ability to change wing shape and vehicle geometry while in flight would allow a single vehicle to perform multiple missions. Most current aircraft have a fixed-geometry. They represent a design compromise between conflicting performance requirements in mission segments such as high-speed cruise, low-speed loiter, and low turn radius maneuvers.

Adapting the shape of wings in flight would allow an air vehicle to perform multiple, radically different tasks by dynamically varying its flight envelope. The wing can be adapted to different mission segments, such as cruise, loitering, and high-speed maneuvering by sweeping, twisting, and changing its span, area, and airfoil shape. Morphing wing technology is considered to be a key component of next-generation UAVs for military and civil application.

2.5.1 Biological Inspiration

"Look deep into nature, and then you will understand everything better." – Albert Einstein.

"When thou seest an eagle, thou seest a portion of genius; lift up thy head!" – William Blake.

These quotes seem especially apt when discussing flight and morphing structures. Understanding how birds change their wing shape or morph their wings during flight benefits our understanding of aircraft design, as reported by Bowman *et al.* [49]. Early aircraft design of the 20th century was largely inspired by natural flight systems such as those of birds, insects, and seeds. This inspiration is evident in aircraft designs, which were similar in appearance to birds. Early aircraft designs were constructed using a rigid skeleton frame covered in a cloth skin, to resemble the wings of birds and bats. With the eventual success of the Wright Brothers and the modernization of the airplane, designs became more abstract and less bird-like than their predecessors. Contemporary aircraft now have little apparent

similarity to birds

Birds easily outperform current aircraft in terms of maneuverability[49]. Birds alter their wing shapes dramatically in order to glide, make steep descents, and coordinate aggressive maneuvering. Birds have the ability to hover, fly backwards, fly sideways, and dive. Transitions between the maneuvers are extremely rapid owing to the precise shape changes in the wing. In addition, birds continually modify the shapes of their wings to accommodate changes in their environment. Flight capabilities in nature provide a demonstration of feasibility and proof-of-concept for man-made morphing.

Current aircraft may only be capable of one flight ability such as hovering, soaring for a long period or being extremely maneuverable. Conventional aircraft are also generally of fixed configuration, meaning that they are optimized for a very specific flight regime. Outside of this regime, the aircraft usually suffers from poor efficiency and poor aerodynamic performance. By changing the vehicle shape in flight, an aircraft can re-optimize itself for a variety of tasks, as birds do constantly.

Birds are capable of in-flight variations in wing geometry, such as wing twist[49]. Fig. 2.18*a*, shows initial twist in a pigeons wing. The twist changes from 0° at the root to 13° at the tip. Additionally, pigeons are able to twist their wings in flight, modify the camber, alter the aspect ratio, and change the sweep. Fig. 2.18*b* shows progressive decrease in wingspan with increase in speed. Mean chord increase from 10.2 cm at low speeds (8.6 m/s) to 20.5 cm at 22 m/s. At the lowest speed and full wing (630 cm^2) and tail spread (100 cm^2), a maximum lift coefficient was calculated to be 1.3. At the highest speed of 22 m/s, wings were swept back and the lift coefficient was 0.25. Fig. 2.19, shows a comparison between a pigeon's wing and a Falcon's wing during flight.

2.5.2 History of Wing-Warping

In 1903 the Wright Brothers used a wing-warping control system on the 1903 Wright Flyer as seen in Fig. 2.20. The wing warping concept was the first effective element of lateral control, and it essentially changed the camber of the aircraft wing to increase or decrease the lift [60]. The entire wing structure twisted slightly in a helical motion in the desired direction.

In 1909 Bleriot flew across the English Channel from France at a speed of about 60-mph. The Bleriot XI was an externally braced monoplane with wing warping control. Like the Wright Flyer, the effectiveness of the Bleriot wing warping control concept required keeping the wing torsional stiffness relatively low so the wing could be twisted by the pilot.

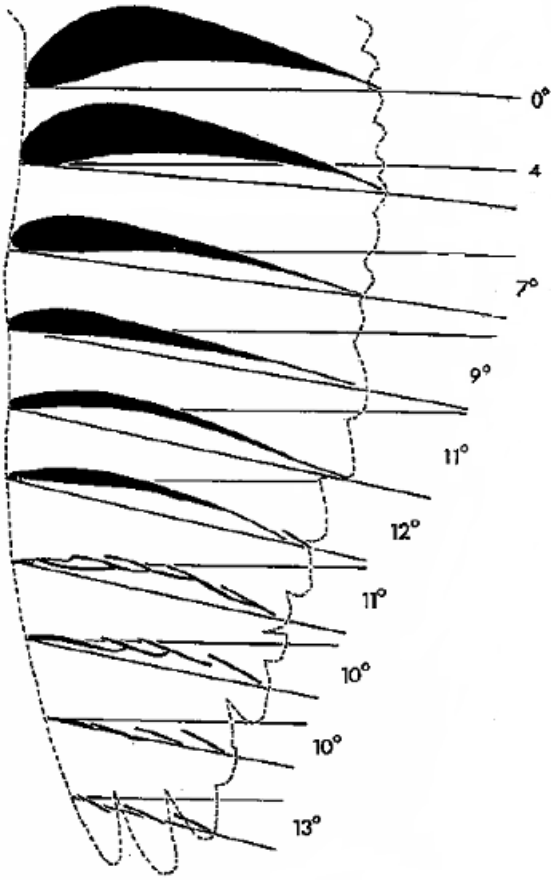

(a) Variation in camber and twist in a pigeons wing.

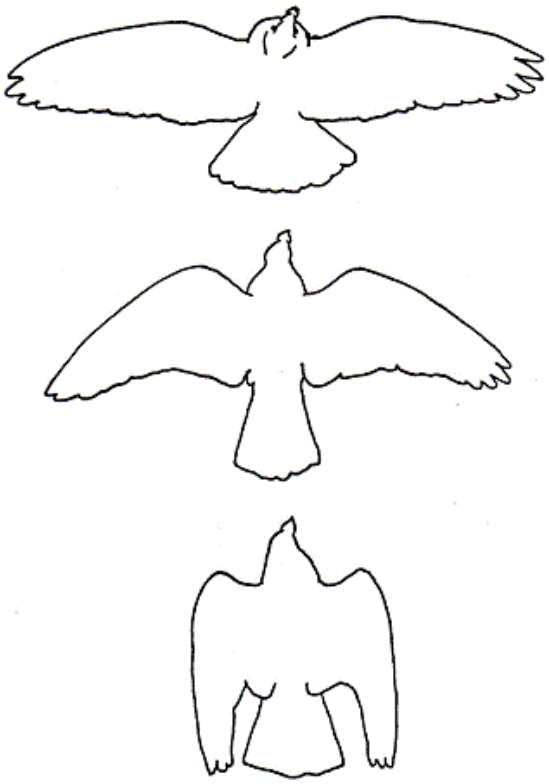

(b) Decrease in wingspan with increase in flight speed.

Figure 2.18: A pigeon's wing [8, 9].

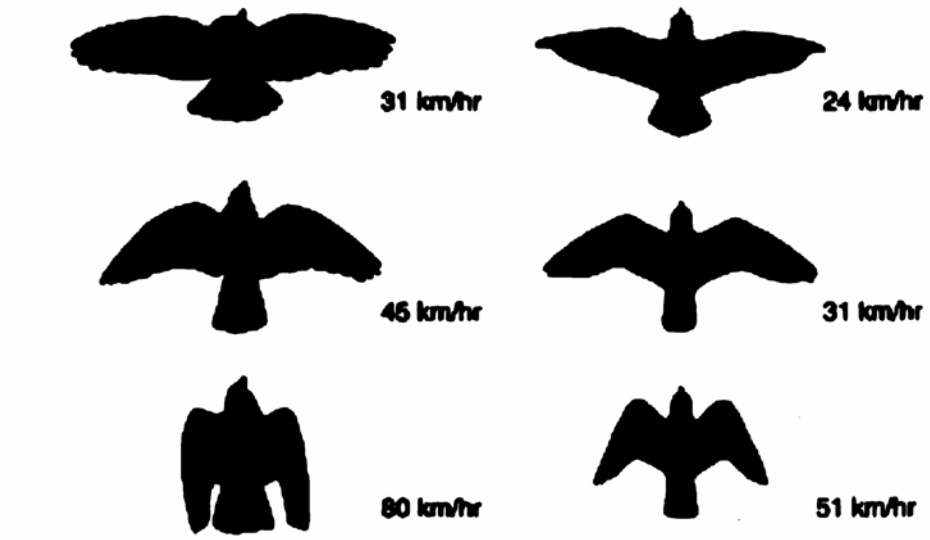

Figure 2.19: Comparison between pigeon and falcon at varying flight speeds [9].

Figure 2.20: Front view of the Wright Flyer with wing warped/twisted [10].

As engine power and airspeed increased this low stiffness created aeroelastic problems that led to wing failures since the wings were easier to twist at high speeds than at low speeds.

Due to its complexity, aeroelastic problems, and strict patent enforcement by the Wrights on their technology, the aileron was developed. Regardless of the patent enforcement, an alternative control mechanism would have been developed [21]. This was due to rapid advancement of aircraft and the need to fly faster, higher, and with more payload. Stronger wings were developed to accommodate these performance changes. Once it was discovered, during the First World War, that thicker airfoil profiles were better at creating lift, engineers began designing wings with greater stiffness and strength. Thus, a decade after the first powered flight, the idea of warping wings was essentially dead [50].

Modern engineers have returned to morphing wings through incremental steps, including the development of the variable pitch propeller (1924) and variable sweep wings (1952) [50]. Both of these concepts were developed to increase the efficiency of the airfoil in a given flight regime. Currently, there are modern airplanes that take advantage of "morphing wing" technology. However, these aircraft would not be categorized as true "morphing" aircraft through the definition above.

Concept – Twisting and Variable Camber Wings

Twisting the wing of an aircraft is not new [61, 62]; Otto Lilienthal in 1891, the Wright brothers, NASA, and many other groups have either proposed or utilized this technique. Wilbur Wright concluded that birds "...regain their lateral balance when partly overturned by a gust of wind, by a torsion of the tips of the wings". This was one of the most important discoveries in aviation history.

Among the properties associated with the camber of the airfoil are the chord wise load distribution, the angle of zero-lift, and the pitching coefficient. The ability to alter the camber of wings thus became an important concept and is now a widely used technique – flaps. A series of devices called flaps and slats were developed to alter the camber of the wing as seen in Fig. 2.21. These devices alter the camber of the wing and thus have a major effect on the lift generated by the wing. The camber is changed by mechanisms that slide back and forth from the structure of the wing. The wing remains rigid while the mechanisms move. However, the structure of the wing does not twist or change.

These devices are primarily used during take-off and landing. Wing flaps can be extended to increase the wing camber and the angle of attack of the wing. This allows the generation of high amounts of lift without increasing airspeed. Flaps increase wing lift but

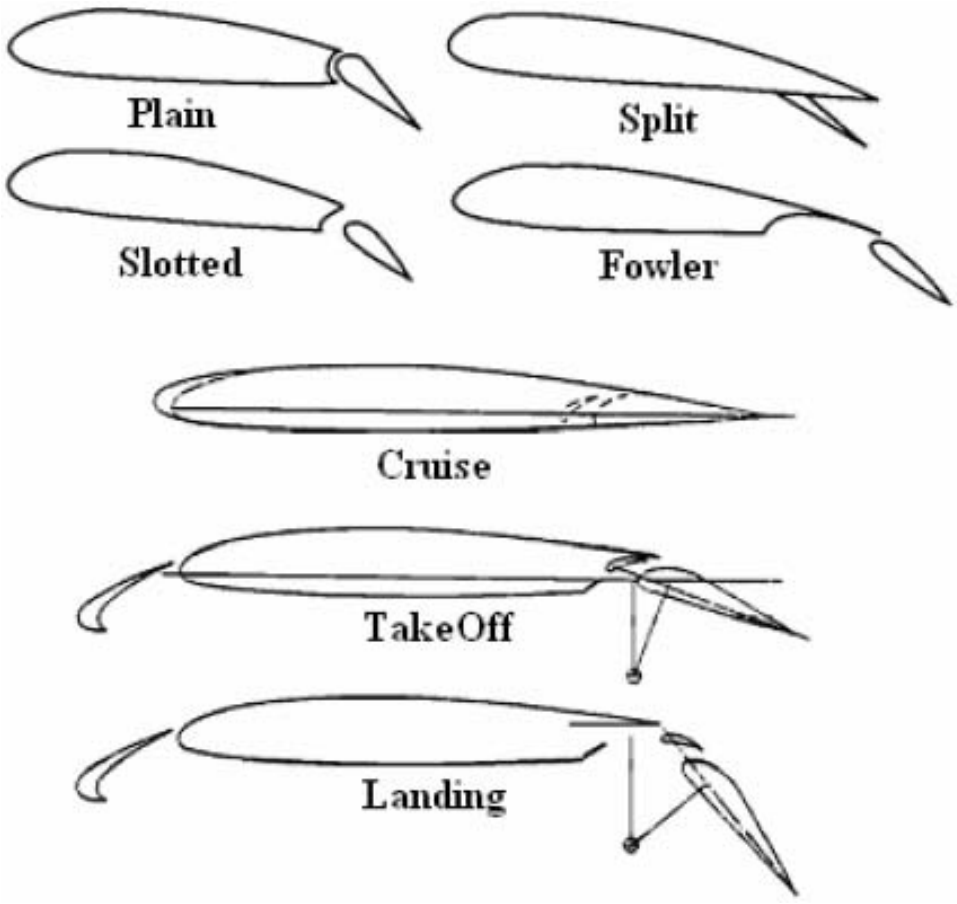

Figure 2.21: Types of flaps and slats [11].

also increase drag. Slats can also be seen in Fig. 2.21. These are devices which extend from the leading edge of the wings and are also used to increase lift.

Other devices used to alter the shape of wings are spoilers or air brakes. These are used to slow down the aircraft and to reduce or cut the lift. They are mounted on either the top or bottom of the center portion of the wings and protrude from the wing surface into the airflow to break the flow over a portion of the wing.

Pure wing twisting[63] can also be used to increase the lift generated by a wing. The concept is to twist the wing from the wing root to tip, as seen in Fig. 2.22*a*. The wing is fixed at the wing root and twisted in the span-wise direction toward the wing root. This is done in order to gain higher lift coefficients and more efficient aerodynamics. Twisting can also be used for roll control. Asymmetric shape changes through twisting generate differential lift between the two semi-spans, while deforming the semi-spans symmetrically provide an altered lift distribution that could be optimized for maximum L/D. Potentially, the differential loading scenario can be used to generate roll moments.

Concept – Variable Aspect Ratio Wings

Telescopic wings have been proposed by researches as a means of changing the aspect ratio of the aircraft[64]. Telescopic wings would have overlapping sections with a high speed central section and a retractable high lift outer section. The wings increase the aspect ratio by moving in the span-wise direction, as opposed to the chordwise direction of conventional flaps. Telescoping changes the lift generated by the wings in the same manner as chordwise flaps, except that the span increases, increasing the span and area instead of only the camber. Thus, the lift generated also increases. During takeoff and landing the high lift outer wing sections are extended. When transitioning to a high speed cruise, they are retracted. This leaves the high-speed low drag wing for cruise.

Bell's X-5

On 10 June 1951, the X-5 by Bell Aircraft became the worlds first aircraft to sweep back its wings during flight. In 1949, Bell began the X-5's program which was intended to be a new experimental platform for swing wing technology. The aircraft flew with a sweeping mechanism such that the wing was moved forward as it was swept aft. The X-5 was built to demonstrate the ability to sweep in flight angles of 20,45, and 60 degrees at subsonic and transonic speeds. The X-5s ability to successfully demonstrate this capability made way for the first military use of swept wings with Grumman Aircrafts F-10-F. It used a similar

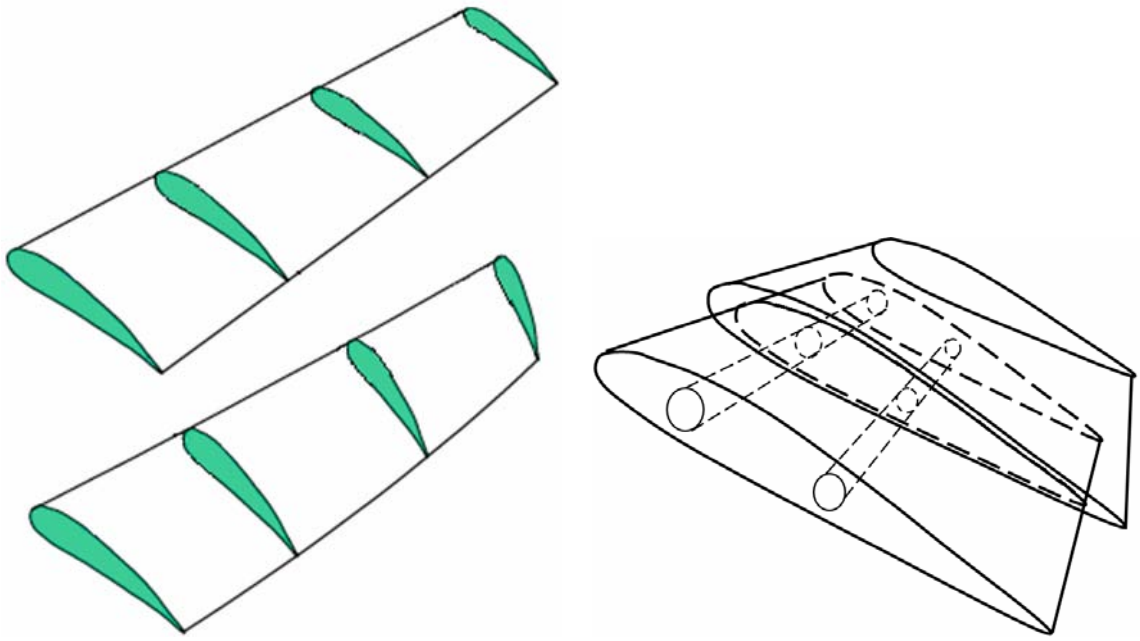

(a) Twisting Wing.

(b) Variable Aspect Ratio Wings.

Figure 2.22: Twist and aspect ratio concepts.

sweeping mechanism as the X-5. Several other swing-wing aircraft have followed, including the Soviet Sukhoi Su-17 (1966), MiG-23 (1967), Tupolev Tu-160 bomber (1981), the US F-14 Tomcat naval fighter (1970), bomber (1974), and the European Panavia Tornado (1974).

The F-14 Tomcat

The United States Navy today takes advantage of the ability to change the sweep angle with the F-14 Tomcat. The F-14s normal sweep range is from 20 to 68 degrees and can "over-sweep" to 75 degrees. The slightly swept wing position is ideal for short take offs and landings from carriers, as well as low speed and fuel-efficient flight. The fully swept back position is ideal for supersonic speeds, maneuverability, and aircraft storage on the carrier. The ability to morph gives the F-14 the ability to fly at speeds up to Mach 1.88 and up to a range of 500 nautical miles.

The B-1B Lancer

The B-1B Lancer wings are designed with a variable sweep, specifically using the "swing-wing" technology. It has a blended wing-body configuration and can change its wingspan from a mere 78 ft to almost 140 ft by changing the sweep of its wing. The wings

are swept back for supersonic flight, allowing better efficiency and control when traveling at high speeds. In the swept position the B-1B can achieve speeds above the speed of sound. However, during slow flight the wing is swung out perpendicular to the fuselage. This increases the wing span of the vehicles and is suited to low-speed flight. In the unswept position, the B-1B can take off in shorter distances and increase its range.

The AFTI/F-111 Mission Adaptive Wing (MAW)

In a joint effort between the United States Air Force (USAF) and National Aeronautics and Space Administration (NASA),the AFTI/F-111(Figure 2.23*a*) variable camber wing aircraft was developed. The goal was to improve an aircrafts performance by adapting its airfoil shape to suit each mission phase. The result was the mission adaptive wing (MAW) that allows the leading edge of the wing to travel from +2° to -21° and the trailing edge of the wing to travel from +4° to -22°.

The MAW consists of variable camber leading and trailing edges, controlled by surface actuation linkages, and hydraulic servo systems driven by digital computers. For the camber variation each wing has three trailing edge and one leading edge segment. On the variable camber edges a flexible fiberglass skin is used to cover the wing. While the upper edge is smooth and continuous, the lower edge of the wing has overlapping tapered edges and sliding panels that can accommodate for the chord changes with camber variation. The pilot can choose either manual or automatic modes for the flight control of the wing. In both modes the outboard and midspan MAW trailing edge surfaces respond to roll stick inputs from the pilot to provide flap assistance for roll control.

The F/A-18A Hornet with Active Aeroelastic Wing (AAW)

In the past engineers have eliminated twisting of wings by making them as stiff as possible. This made wing structures heavy but rigid. Designers are now working to use the natural warping of the wing to control the aircraft, and in turn, make it much lighter.

Understanding the ability to twist the wing allows for greater maneuverability. The Air Force Research Laboratory, Boeings Phantom Works, and NASA Dryden have collaborated to create a program called the Active Aeroelastic Wing (AAW) program. The collaborated research lead to the development of an F/A-18A that had the ability for the outer wing panels to twist up to four degrees(Fig. 2.23*b*). These designs allow the aircraft “to maneuver more quickly, achieve better lift to drag ratios, and to have greater ranges in flight”.

The F/A-18A was chosen for this project due to early problems in the aircraft’s design.

(a) The AFTI/F-111 - Mission Adaptive Wing (MAW).

(b) The F/A-18A Hornet - Active Aeroelastic Wing (AAW).

Figure 2.23: Current operational variable sweep aircraft.

Initial wings designed for the aircraft were too flexible at high speeds. These wings were discarded and replaced with stiffer wings. At the inception of this project these wings were taken out of storage and used due to the same trait for which they were originally discarded. Researchers believe that AAW concepts will eventually evolve to control wing twist at high speeds and improve roll maneuvering, to the point that the use of a vertical tail may not be needed. The degree of wing twist utilized at high speeds is small ($\pm 4^{\circ}$); however, this is sufficient to control the vehicle. Besides the major reduction in weight, the wing can reduce drag, increase range, and reduce fuel consumption.

Near Future Designs

Other variable aspect ratio concepts involve shape changes of the wing and aircraft body. An example of this can be seem in figures 2.24*a* and 2.24*b*, depicting Lockheed Martin's concept, which involves folding wing technology. The wings fold up to the fuselage during high speed "dash" and are deployed to their full span for take-off, loitering, and landings.

NexGen Aeronautics Inc.'s concept uses a sliding skin technology seen in Fig. 2.25*a* and 2.25*b*. The use of sliding skin allows for sweep, chord, and span change. Using the sliding skin technology, the air loads are distributed over a greater area, decreasing the necessary strength of joints and therefore, decreasing the weight of those joints. The NexGen concept is capable of optimizing performance for high speed flight, take off and landing, maneuvering, and loitering. The published data states that the wing area changes by 40%, the span

(a) Wings folded.

(b) Wings extended.

Figure 2.24: Lockheed Martin Aeronautics company's morphing UAV.

changes by 30% and the wing seep varies from 15° to 35°.

2.6 Inflatable Structures

Inflatable structures are engineered in the same way as traditional rigid structures, and have been successfully utilized in a number of life-critical applications. Some examples include automotive airbags and tires, aircraft escape slides, ship life rafts and life-preservers, surface watercraft (inflated boats, pontoons and hovercraft), space suits, airships (blimps and balloons), and many more. Knowledge of the performance capabilities of flexible composite materials and structures can often expand system architectural possibilities in a dramatic fashion.

Recently, new inflatable applications are being explored, including inflatable land structures. These structures are completely self-supported and require no solid structural members. These structures are used within the military as tents, hangars, roofs, and small buildings. The benefit of these structures is the convenience of inflatable structures to save assembly time, travel weight, and stowed volume.

The aerospace industry has developed inflatable "gossamer structures" for space appli-

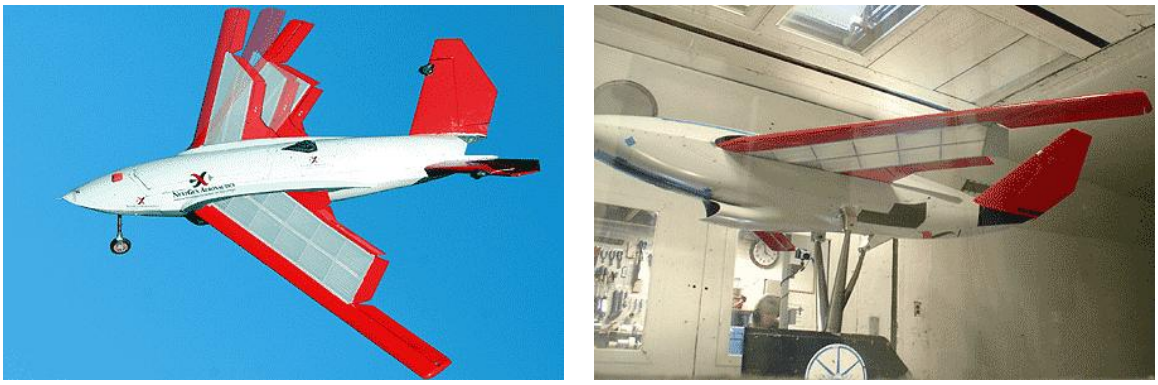

(a) Concept. (b) Wind tunnel tests.

Figure 2.25: NextGen Aeronautics Inc's. morphing UAV.

cations. A gossamer structure is a generic class of spacecraft, or space structure characterized by a low mass per unit area. These gossamer structures are used in applications such as sun shields, antennas, solar sails, habitats, and structural booms. Space applications take advantage of several features of inflatable structures, the key benefits being reduction in stowed volume, weight and cost compared to solid structures.

Inflatable technologies, including inflatable wing designs, have been restricted by volume constraints, or the requirement for low stowed volume at the same time they maintain functionality once deployed. Applications for inflatable wing technology are primarily threefold: aspect ratio morphing, munitions (sprout wings in flight), and small survivable UAVs. Reliability is the greatest concern with regard to this new technology.

2.6.1 Inflatable Wings

Inflatable aircraft have a long and rich history, including the development of LTAs, manned inflatable heavier-than-air vehicles and UAVs. While lighter-than-air vehicles also include inflatable structures, our focus herein is on inflatable structures used solely for lift generation. Various aspects of inflatable structures are discussed elsewhere [65] while a review of inflatable wing and related technologies is included in Cadogan *et al.* [18, 29, 66, 32].

Inflatable wings are a promising solution for many situations where wings need to be stowed when not in use [18]. Inflatable wings are conceptually possible in almost any size and have been developed with spans as small as 15 cm (6 in) for missiles and as large as 9.14 m (30 ft) or more for LTA vehicles. The most promising scale has been that of the medium or meso-scale UAV that can be carried by an infantryman or man-portable UAV.

Meso-scale UAVs are often requested with requirements for stowed wings, it is in this size where weight and volume make the inflatable wing a practical solution when compared to folding wing designs [67]. The ability to stow wings and control surfaces into small volumes has many incentives. Inflatable wings have the benefit of an extremely low packed volume. The packed volume can be more than ten times smaller than the deployed volume[18]. Inflatable wings that can be stored in fuselage and inflated to full span when needed.

One major drawback to inflatable wing use is the lack of roll control actuators (ailerons). This deficiency may be dealt with in several ways. One option is the use of the century old technique of wing warping originally developed by the Wright Brothers[50], as inflatable wings are deformable by their nature.

From a fluid dynamist's point of view, the performance of an aircraft is essentially controlled by the development of the boundary layer on its surface and its interaction with the mean flow. This interaction determines the pressure distribution on the airfoil surface and subsequently, the aero- dynamic loads on the wing. In order to obtain the highest levels of performance efficiencies for mission varying aircraft, it is necessary to either: ((a) alter the boundary layer behavior over the airfoil surface (flow control methods of interest here), and/or (b) change the geometry of the airfoil real time for changing freestream conditions (adaptive wing technology) [68]. The starting point toward achieving deterministic design of low-speed airfoils lies essentially in understanding the physics of the "fluid dynamic problem". Here, deformable inflatable wings are of interest.

Early Inflatable Wing Concepts

Inflatable aircraft and components have been proposed and developed since the 1930s.[12] Patents were filed on some of these early concepts, which included an inflatable spar vehicle by McDaniel (1933)[13], shown in Fig. 2.26a, and an inflatable reentry vehicle by Aerospace Corporation (1962) shown in Fig. 2.26b, and numerous variations of inflatable spar wings shown in Fig. 2.27$a-c$ [14, 15, 16]. These concepts focused around inflatable beams that are simple to construct but perform poorly in their resistance to bending loads. While patents for these vehicles and wings were filed, prototypes were apparently not developed beyond the patent stage.

Goodyear Inflatoplane

While the concept of inflatable structures for flight originated centuries ago, inflatable wings were only conceived and developed within the last few decades. Manned aircraft

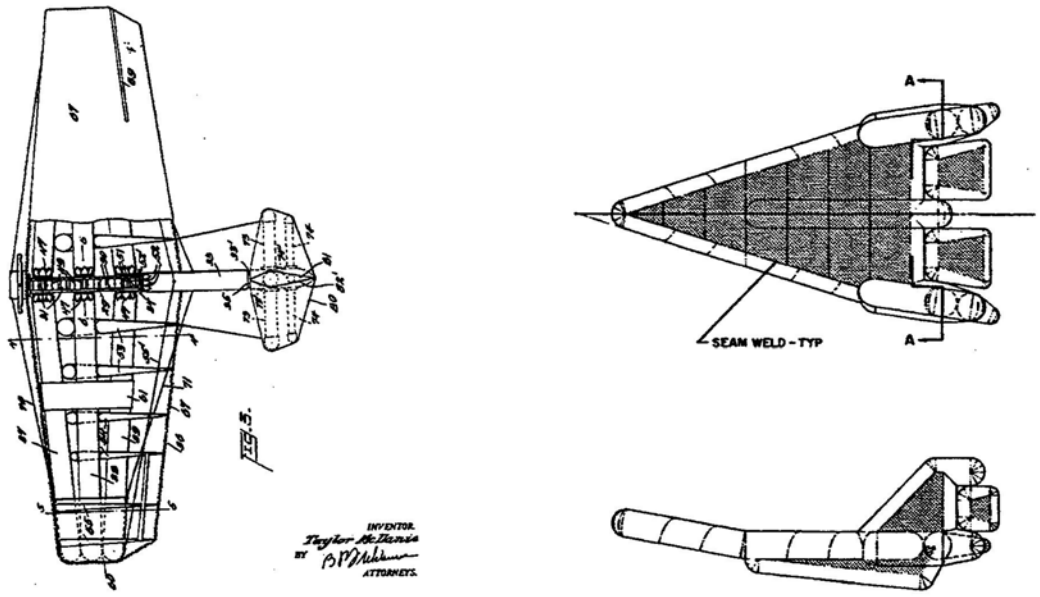

(a) Inflatable aircraft concept by McDaniel, 1933.

(b) Inflatable reentry vehicle by Aerospace Corporation, 1962.

Figure 2.26: Inflatable vehicle concepts [12, 13].

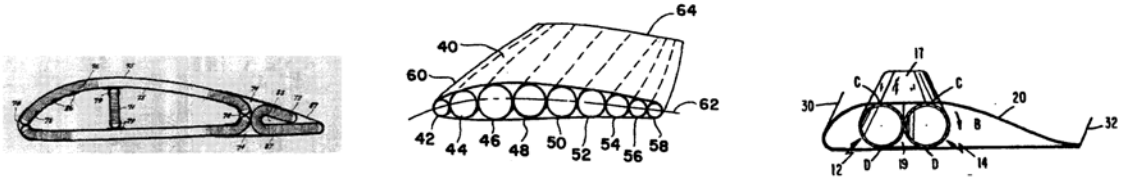

(a) Bain, 1963.

(b) Sebrell, 1976.

(c) Priddy, 1988.

Figure 2.27: Tubular spar wing concepts [14, 15, 16].

include some of the earliest and most recent uses of inflatable wings. The first successfully demonstrated inflatable winged flight was in the 1950s, with Goodyear's Inflatoplane (Model GA-468 is shown in Fig. 2.28 and is also on display in the Patuxent River Naval Air Museum). The 6.7 m (22 ft) wingspan aircraft was developed as a military rescue plane. The inflatable airplane could be deflated 2.29*a*, contained in a small lightweight package, and parachuted to a downed man for self-rescue. The aircraft was of a size and weight that the downed pilot could handle alone 2.29*b*. Technology developments, including delivery of dozens of aircraft, continued until the early 1970s.

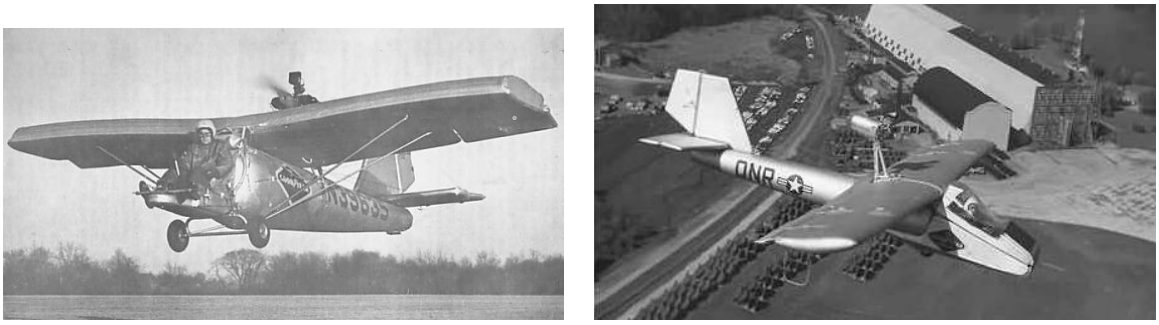

(a) (b)

Figure 2.28: Goodyear model GA-468 Inflatoplane [17].

The Inflatoplane was tested in the NASA Langley wind tunnel as seen in Fig. 2.30. The airplane was longitudinally stable, and had adequate roll and pitch control. However, aeroelastic effects were of concern. At low speeds and hence low load factors between 1 and 1.5 the vehicles performance was good. However, as the speed was increased, aeroelastic effects associated with wing twist produced an increase in the lift-curve slope and the loss of stability near the stall [17]. Wing deflections were moderate below a load factor of 2, but column-type buckling of the wing occurred at load factors just over 2. This caused the inboard wing section to fold up and invariably contact the engine above the wing. The wing buckled at a speed of 71 mph and at an angle of attack of 5°, at a load factor of slightly in excess of two. The buckling occurred suddenly after about 30 sec at this loading condition.

The British answer to the Inflatoplane was a tailless design by ML Aviation, also developed in the 1950s seen in Fig. 2.31. Both the Inflatoplane and the ML Aviation Mkl pressurized the wing skin while controlling shape with tension elements between top and bottom surfaces. McDaniel used pressurized fabric tubes inside the wing skin envelope as the primary structure.

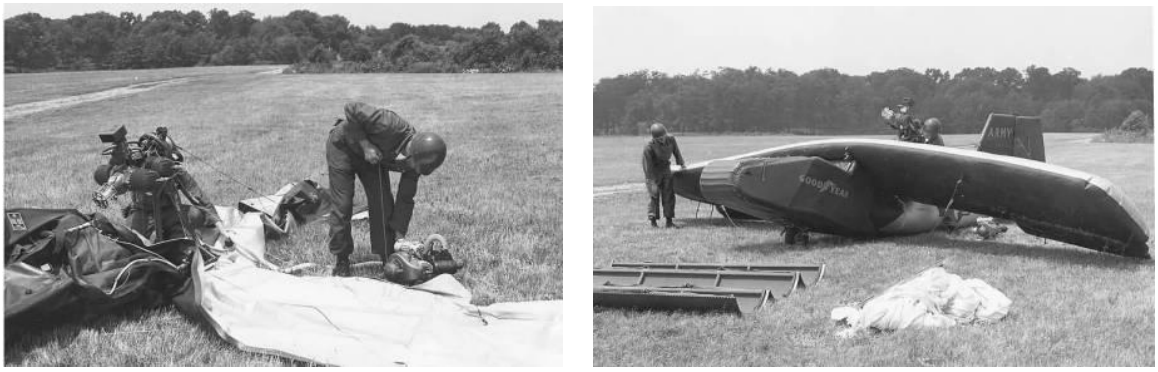

(a) Deflated Inflatoplane.

(b) Inflation and flight preparation of Inflatoplane

Figure 2.29: Gound preparation and inflation of Goodyear model GA-468 Inflatoplane [17].

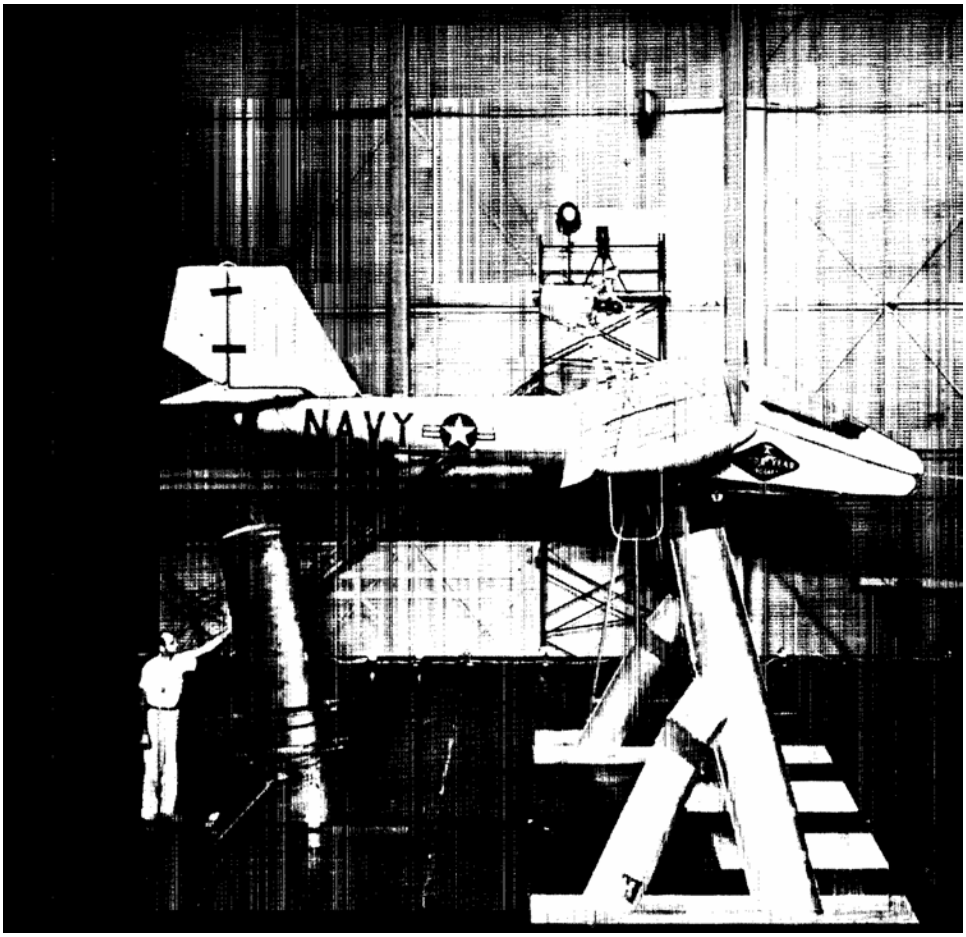

Figure 2.30: Goodyear Inflatoplane in the Langley full-scale tunnel [17].

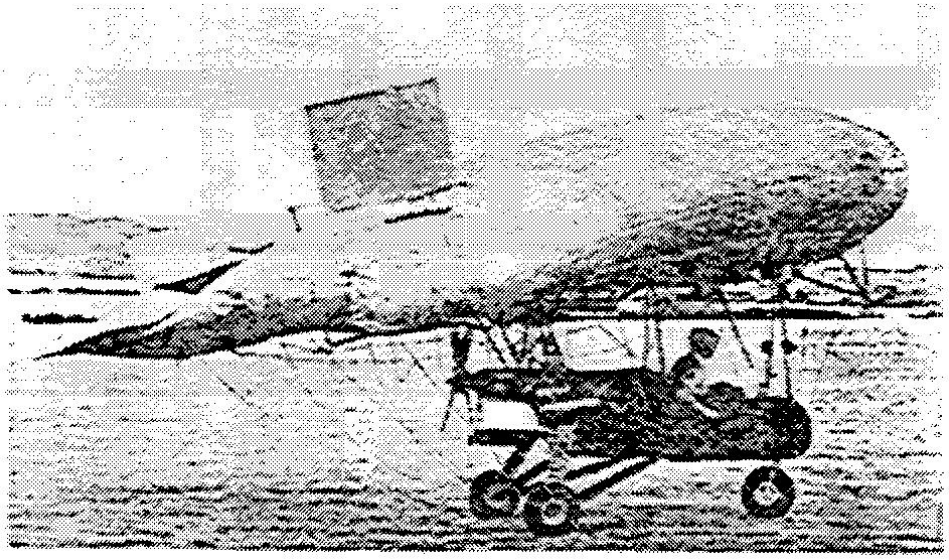

Figure 2.31: ML Aviation Mkl [12].

Apteron

Inflatable winged UAVs were developed in the 1970s by ILC Dover, LP. The Apteron UAV (Fig. 2.32) had a 1.55 m (5.1 ft) wingspan, a 373 W (0.5 hp) engine, a 3.18 kg (7 lb) gross weight and was remotely-controlled via elevons mounted on the trailing edge. The Apteron was successfully flight tested, but was never put into production. ILC Dovers has since developed three inflatable wing designs, an inflatable-rigidizable wing and two inflatable wings. These are discussed in detail in later chapters.

NASA Dryden I2000

A small-scale, instrumented research aircraft was flown by NASA Dryden Flight Research Center to investigate the flight characteristics of an inflatable winged aircraft. Three successful flight tests of the I2000 UAV using inflatable wings were conducted in 2001 by researchers at NASA Dryden.[19] The UAV was launched from beneath R/C carrier airplane at a low-altitude (800-1,000 ft). As the I2000 separated from the carrier aircraft, its inflatable wings "popped-out," deploying rapidly from pressure provided by an onboard nitrogen bottle. The wings were developed by Vertigo, Inc. for the Navy as a gun-launched observation vehicle. The skeleton of the wing was made of inflatable tubes, surrounded with crushable foam to provide the airfoil cross-section. After the aircraft was released, the five-foot span inflatable wing was successfully deployed in about one-third of a second. To

Figure 2.32: ILC Dovers Apteron UAV [18].

maintain suitable wing strength and stiffness, nitrogen gas pressurization of 1380-1725 kPa (200-250 psi) was required. The deployment is shown in Fig. 2.33.

Highlighted below are some of the conclusions and results from the study [19]:

- Mechanics of materials analytical methods were effective in modeling the multiple-spar wing configuration for a range of inflation pressures.
- Integration of the inflatable wing test article into a research aircraft configuration is possible at small scale. Powered flight, using only the control surfaces on the tail of the aircraft, was demonstrated.
- For the angle-of-attack range spanned in the flight program, the flight data demonstrated the rigid-wing configuration to be an effective simulator of the inflatable-wing configurations.
- The asymmetric twist distribution of the inflatable wing required significant differential elevon deflection to achieve trimmed flight. A small trim tab on one wing was sufficient to achieve trimmed flight.
- The feasibility of ballistic airdrop and in flight inflation of the wing, with transition to controlled lifting flight, was demonstrated in three flight operations. Wing inflation and transition to lifting flight was rapid, and vehicle dynamic response was benign and limited primarily to roll and heave motions. No indications of instability or divergence were evident.

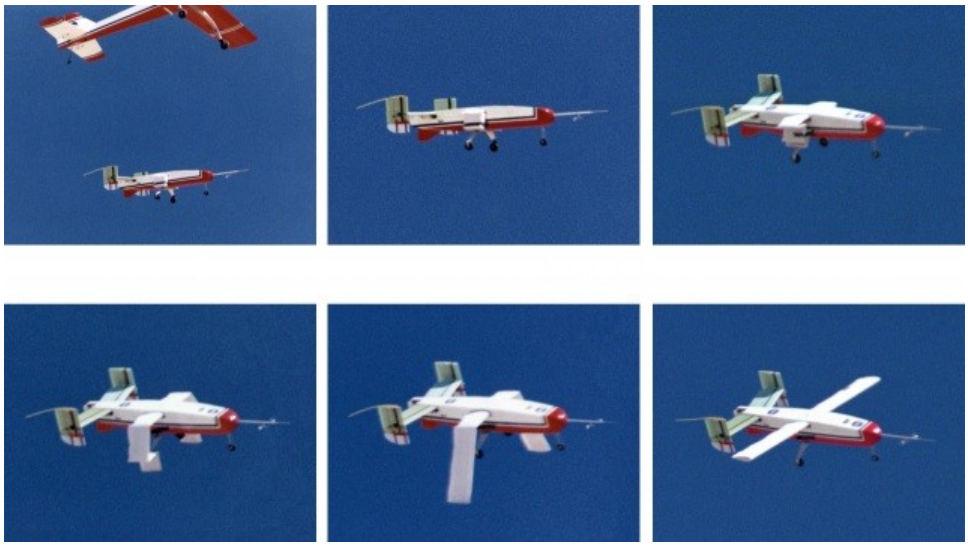

Figure 2.33: In flight deployment of NASA Dryden I2000 inflatable wing [19].

Fig. 2.34 shows the wing layout of the I2000 inflatable wing. The wings consisted of five cylindrical inflatable spars that ran span-wise through the wing from tip to tip.[19] The spars consisted of a urethane bladder covered with spirally braided vectran threads. A open-cell foam filled the gaps between the cylinders. Finally, a rip-stop nylon covering was used as the outer skin of the airfoil. The wing span was 1.63 m (64 in), and chord length was 0.18 m (7.25 in). A NACA 0012 symmetric airfoil profile was used. A center manifold provided a rigid mounting connection and inflation point. The wings did not contain control surfaces, and the roll, pitch and yaw control for the vehicle was provided by the empennage.

Stingray and PNEUWING

More recently, the "Stingray" (Figure 2.35) single seat ultralight has been flight tested. Using chord-wise spars, the vehicle has a 13 m (42.6 ft) wingspan and 70 m^3 (2,500 ft^3) of internal volume. The developer, "Prospective Concepts", proposes to use helium as the inflation gas to provide an additional lifting component [20].

In addition to the Stingray, Prospective Concepts has developed the "PNEUWING". High-strength materials and air pressure 70 kPa (10.2 psi) gives the wing strength, as the wing contains no rigid structural components as seen in Fig. 2.36. The vehicle is controlled through traditional ailerons controlled by means of wires. The landing flaps are able to change shape (curvature) by varying the air pressure. The vehicle has a 8.2 m (26.9 ft) wingspan and 16.5 m^2 (177.6 ft^2) of wing area. Prospective Concepts is no longer pursuing

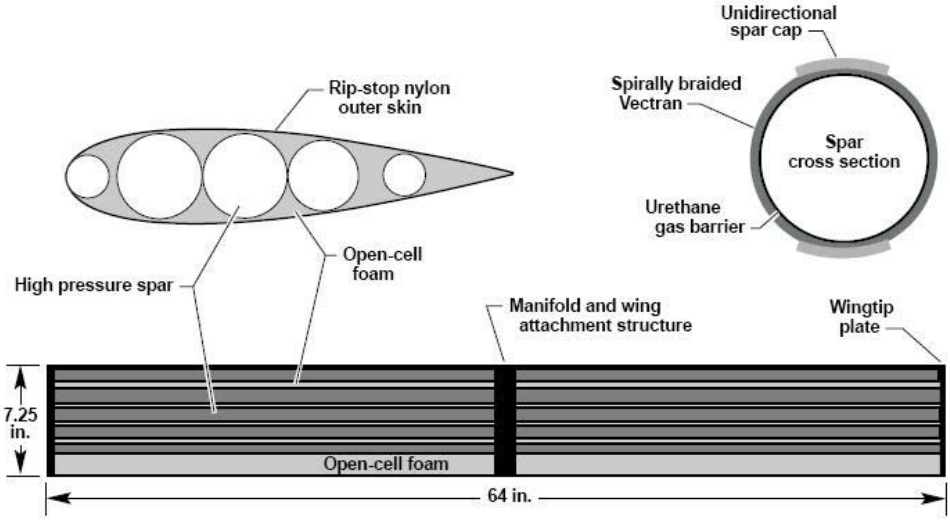

Figure 2.34: NASA Dryden I2000 inflatable wing structure [19].

Figure 2.35: Prospective Concepts' "Stingray", a single seat inflatable wing aircraft [20].

work on either the Stingray or the PNEUWING.

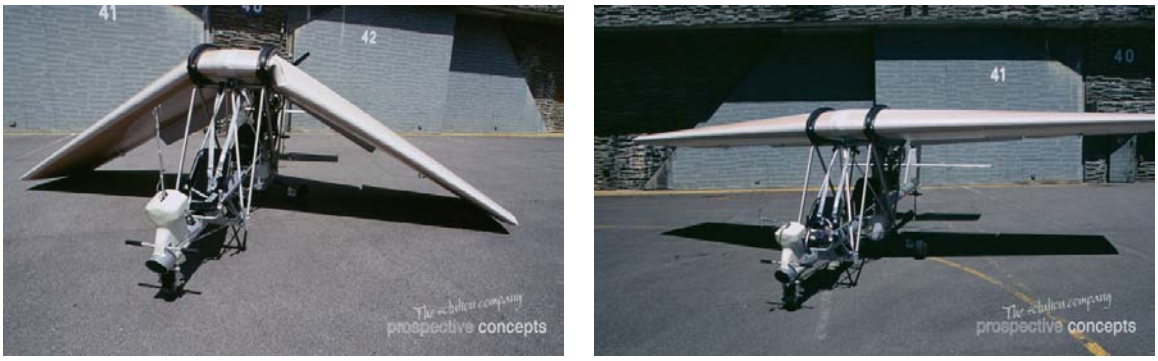

(a) Deflated PNEUWING.

(b) Flight-ready PNEUWING

Figure 2.36: Prospective Concepts - "PNEUWING", a double seat inflatable wing aircraft [20].

At least four companies have developed inflatable aircraft and inflatable wings. Currently, ILC Dover is the only company continuing development of inflatable wings.

2.7 Modeling of Inflatable Wings

Inflatable structures are part of a structural group called tensile structures. These are membrane-like structures that require pre-stress in order to bear externally applied loads [69]. Structural analysis of inflatable structures is not as developed as analysis of solid structures. Inflatable wings are made up of a series of inflatable beams placed parallel. The most complete discussion of the analysis of inflatable beams placed parallel to each other is the Ph.D. work of S.L. Veldman [69]. Here, a design example of three inflatable beams is analyzed theoretically and using finite element analysis. This research determined that the thickness of the beams had little affect on the predicted deflection. Varying the taper ratio was also examined. While it was determined that this would reduce the load deflection behavior, the optimum taper ratio differed for different torque and shear load combinations.

2.7.1 Aerodynamic and Aeroelastic modeling of Inflatable wings

Randall *et al.* [30] gives a synopsis of current analytical aeroelastic models. A review of this work is detailed here. The authors note that inflatable wings exhibit unusual behavior in bending and shear. Unlike conventional wings, inflatable wing skin wrinkles. This has a softening nonlinearity effect in bending, and when combined with high structural damping

of the inflatable wing, can produce limit cycle oscillations [30]. Randall *et al.* developed static aeroelastic model and a dynamic aeroelastic model summarized here.

Static Aeroelastic Model

The model is based on the work of Crimi [70] and other work by Main *et al.* [71]. Crimi, [70] developed a method for finding the torsional collapse speed for an inflatable wing that consists of several distinct cylindrical spars. Crimi, [70] deduced that the torsional stiffness of the wing arises from the shear forces in each of the spars and the torque in the wing is proportional to the third derivative of the twist. The torsional stiffness due to bending of a wing with N tubular spars was determined and is repeated here [70]. The pure torque τ was applied span-wise down the wing. the shear V_i in the spars provided the reaction such that we get Eqn. 2.34

$$\tau(\mathrm{x}) = \sum_{i=1}^{N} z_i V_i \tag{2.34}$$

Because no net force is exerted, it followed that

$$\sum_{\mathrm{i}=1}^{\mathrm{N}} \mathrm{V_i} = 0 \tag{2.35}$$

δ_i is the deflection of spar i,

$$\mathrm{V_i} = EI_i \frac{d^3\delta_i}{dx^3}_i \eta_i \tag{2.36}$$

where EI_i is the equivalent spar bending stiffness. Because the fabric skin prevents chord-wise deformation, and θ is the section angle in the plane, θ can be determined and differentiated. This derivation is shown in Crimi, [70]. Using the derivations above for V_i and η_i, and N linear equations for unknown shears. τ, was determined in Eqn. 2.37

$$\tau(\mathrm{x}) = k_b \frac{d^3\theta}{dx^3} \tag{2.37}$$

Crimi [70], also deduced a divergence formulation for inflatable wings. If q is dynamic pressure , c is chord, ec is the distance aft of the center of pressure of the elasitic axis, and a is the section lift coefficient derivative with respect to angle of attack, the aerodynamic torque per unit span is given by Eqn. 2.38

$$\frac{\mathrm{d}\tau}{\mathrm{dx}} = qec^2 a\theta \tag{2.38}$$

If the wing has constant chord and in not swept, the torque at span-wise coordinate x is given by

$$\tau(\mathrm{x}) = k_b \frac{d^3\theta}{dx^3} = qec^2 a \int_x^s \theta(x^{'})dx^{'} + \tau_\nu \tag{2.39}$$

where s is semispanand τ_ν is the shear torque exerted by the end cap. By differentiation of Eqn. 2.39,

$$\mathrm{k_b}\frac{\mathrm{d}^4\theta}{\mathrm{dx}^4}\mathrm{qec}^2\mathrm{a}\theta = 0 \tag{2.40}$$

the end conditions are defined [70].

To specify τ_ν, the equilibrium of the end cap must be considered. The end cap is subjected not only to the reaction shear torque - τ_ν but also to the torsional reaction of the individual spars. If GJ is the sum of the spar torsional stiffness, it follows that

$$\tau_\nu = -(GJ/s)\theta(s) \tag{2.41}$$

because all of the spars are twisted an equal amount $\theta(s)$ at the wing tip.

Crimi [70], lets $\xi = x/s$, and defined β according to

$$\beta^4 = \frac{qec^2s^4a}{4k_b} \tag{2.42}$$

so that Eqn. 2.40, can be written in dimensionless form as

$$\frac{\mathrm{d}^4\theta}{\mathrm{d}\xi^4} + 4\beta^4\theta = 0 \tag{2.43}$$

the general solution of this equation is,

$$\theta = sin\beta\xi(C_1 sinh\beta\xi + C_2 cosh\beta\xi) + (cos\beta\xi(C_3 sinh\beta\xi + C_4 cosh\beta\xi) \tag{2.44}$$

The work by Crimi [70] was combined with Main *et al.* [71], which related the softening effect of inflatable spars with skin wrinkling. The combination of the two methods was used to determine the maximum deflection (and maximum stored energy, E_{max}) based on the collapse load of the beam detailed by Randall *et al.* [30]. An energy criterion for failure at a deflection $x_{collapse}$ may then be defined (Eqn. 2.45), assuming a constant lift force L acts while the wing deflects to the point of collapse after an initial perturbation in translational velocity v_0, Eqn. 2.45. This yields the airspeed for static collapse given in Eqn. 2.46.

$$\frac{1}{2}\mathrm{Mv}_0^2 + \mathrm{C_{Lmax}}\frac{1}{2}\rho\mathrm{V}^2_{\mathrm{collapse}}\mathrm{Sx_{collapse}} = \int_0^{x_{collapse}} Fds = E_{max} \tag{2.45}$$

here, M is the Mass of the 2D wing model (Kg), and $x_{collapse}$ is Deflection at collapse [m]

$$\mathrm{V_{collapse}} = \sqrt{\frac{E_{max} - \frac{1}{2}Mv_0^2}{C_{Lmax}\frac{1}{2}\rho S x_{collapse}}} \tag{2.46}$$

In order to increase the collapse speed ($\mathrm{V}_{collapse}$)[30], E_{max} should be made as large as possible according to Eqn. 2.46. E_{max} is increased by increasing the stiffness of the inflatable wing, which is accomplished through increasing the internal inflation pressure.

2.7.2 Bending and Analysis of Inflatable Beams

Wing Stiffness Calculation

Inflatable wings can be treated as linearly elastic cantilever beams. With a tip load, the flexural rigidity of the wing can be calculated from Eqn. 2.47 [72].

$$\mathrm{EI} = \frac{FL^3}{3\Delta} \tag{2.47}$$

where EI is the flexural rigidity, F is the applied tip load, L is the beam length, and Δ is the beam deflection at tip.

Brown *et al.* [12], argued that the effective bending strength of an inflatable beam was dictated by the "wrinkle" moment and was analogous to the yield strength of metallic structures. The wrinkle moment was the load condition under which fibers within the beam section first reached zero tension. This did not imply that the inflatable beam had visible wrinkles but marked the boundary between small elastic deflections and large deflections leading to buckling. Pre-wrinkle behavior was governed by the same equations as would apply to a rigid composite structure with the same fiber type, distribution, weight and orientation.[12] The generic behavior of these inflatable structures is presented in Fig. 2.37. As the load increases, the inflatable beams deflect in a linear manner. Once the wrinkling threshold is reach, the relation becomes non-linear. Soon after, the beam buckles. This will scale depending upon the type of structure involved.While buckling is the failure mode, the onset of wrinkling indicates the maximum design load and will be used for the design limit. It should be noted that unlike metal or composite rigid structures will either plasticly deform or crack, respectively, once the yield stress is reach, the inflatable beam will return undamaged to its original state one the load is removed. Inflatable sections can either be made out of plastic or fabric material with fabric tubes either woven or braided, the latter typically referred to as "airbeams". A tube of fabric rolled up to form a tube of diameter d, and pressurized to differential pressure P, will wrinkle with an applied bending moment given by the equation 2.48:[12]

$$\mathrm{M}_{\mathrm{Wrinkle-Weave}} = \frac{\pi}{16} P d^3 \tag{2.48}$$

Brown *et al.* [12], also determined that for a given bending moment, the minimum inflation pressure required would be given by equation 2.49

$$\mathrm{P} = \frac{8M}{\pi d^3 \left(1 - \frac{2}{tan^2\beta}\right)} \tag{2.49}$$

It was noted that the weight of the gas required to provide the inflation pressure in the wing spar is sometimes greater than the weight of the spar itself.

Brown *et al.* [12], also expressed the bending stiffness of a beam as a parameter of EI, the product of the modulus of the material, and the section moment of inertia. Deflection was determined by the applied bending moment, the stiffness parameter EI, and a constant that depends on the geometry of the loading. For engineering estimates, the equation below assumed a linear load-strain curve and allowed the spar cap webbing to be sized according to its breaking strength, F_{brk}.

$$\mathrm{EI} = \frac{d^2 F_{brk}}{2\epsilon_{brk}} \tag{2.50}$$

Brown *et al.* [12],determined that a reasonable approximation for ϵ_{brk} was 1.5 times the breaking elongation of the yam used to make the spar cap webbing. This equation applied to pre-wrinkle stiffness and does not contain Pressure (P). Pre-wrinkle bending stiffness was independent of pressure.

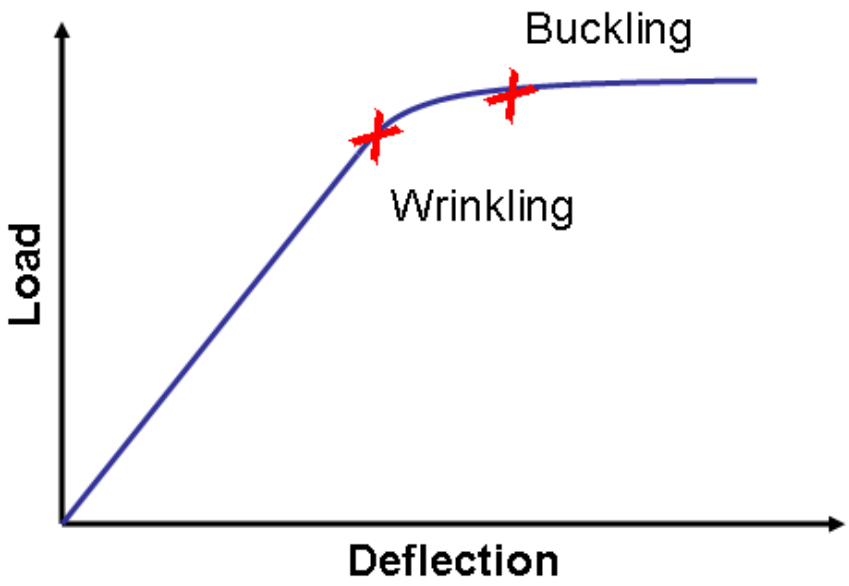

Figure 2.37: Load versus deflection for generic inflatable structure.

Wing Torsional Stiffness Calculations

Similar to the bending, we can treat the wing as a linearly elastic cantilever beam with a torque load at the tip. The flexural rigidity of the wing can be calculated from 2.51 [72].

$$\mathrm{GI_p} = \frac{TL}{\phi} \tag{2.51}$$

where GI_p is the torsional rigidity, T is the applied torque load, L is the beam length, and ϕ is the angle of twist.

Chapter 3

INFLATABLE WING DESIGN AND DEVELOPMENT

Numerous advanced material configurations have been explored for inflatable wings: unsupported films such as 10 mil Polyethylene (Fig. 3.1*a*); bladder and restraint material such as vectran or S/E – Glass and a 10 mm polyurethane (Fig. 3.1*b* and *c*); and coated fabrics such as polyurethane coated nylon (Fig. 3.1*d* and *e*). Note that the research relating to the unsupported films (Fig. 3.1*a*) was not part of this research.

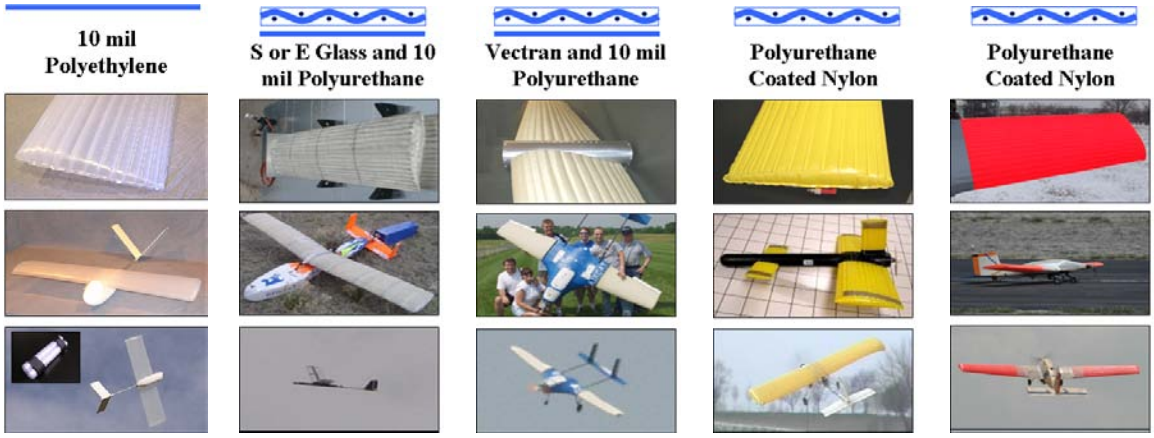

(a) Un-supported film. (b) Bladder and restraint. (c) Bladder and restraint. (d) Coated fabric. (e) Coated fabric.

Figure 3.1: Wing material configurations.

The wings use a baffled wall design, described later in detail. The baffled wall design of the inflatable wing lowers the required inflation pressure to keep the wing rigid. The design inflation pressure ranges from 34.5 – 276 kPa (5 – 40 psi). The design is constrained by the airfoil thickness, which is required to be large due to the manufacturing process. Thinner airfoils are desirable for good aerodynamics however they increase the required number of baffle walls and thus can be problematic to manufacture. Increasing the number of baffles increases losses in the length of the trailing edge. Thus, thicker wings are optimal from a manufacturing standpoint.

Fig. 3.2, shows the difference between a thin airfoil (S7012) and a thick airfoil (E398) when manufactured into an inflatable wing using the baffled wall design. The S7012 is a low

Re airfoil designed by Selig. The S7012 airfoil (Fig. 3.2) would have 19 baffle walls if used as an inflatable wing and would lose approximately 0.2c of the trailing edge. The E398 is an Eppler airfoil designed for human powered aircraft. The thicker E398 (Fig. 3.2) would have 16 baffle walls and lose 0.13c of the trailing edge. Thus, thicker airfoils are better suited for inflatable wings as the shape is less compromised.

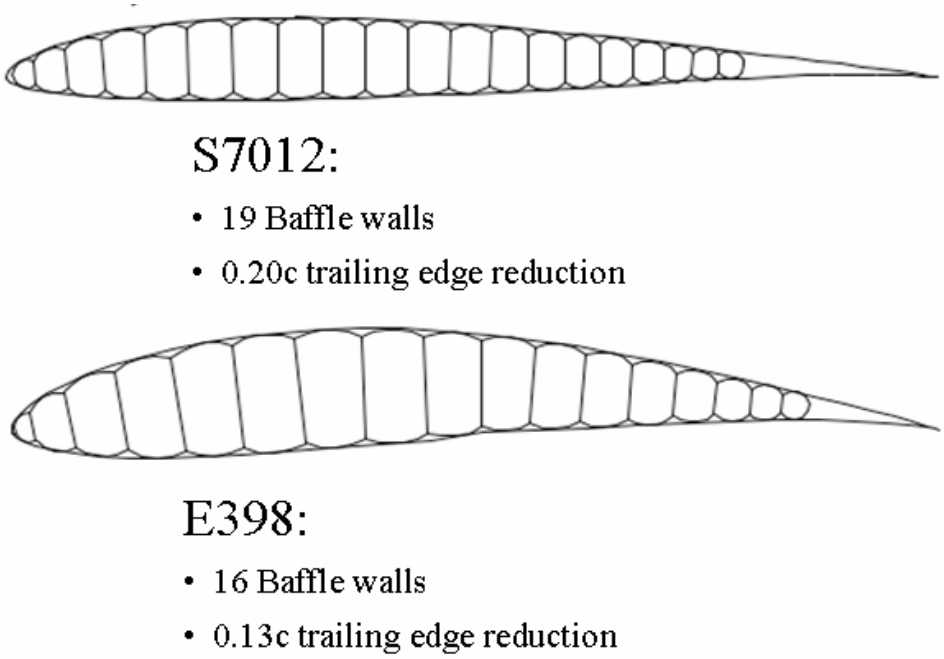

Figure 3.2: Loss in trailing edge due to manufacturing.

The first inflatable wing design examined within this project was the "inflatable-rigidizable wing". This wing was comprised of an internal containment bladder inserted into a fabric outer restraint which was impregnated with a UV curable resin. This design was based on the E398 profile. The design underwent two iterations in which the outer restraint was optimized for weight. The second design was the "Vectran" inflatable wing design which used a NACA 4318 profile. This design included an inflatable bladder surrounded by a fabric outer restraint. The fabric restraint was not impregnated with a UV curable resin, and thus constant inflation pressure was required during operation. The third design was the "Nylon" inflatable wing design. This wing design was comprised of a single containment layer and no outer restraint. The nylon wing design also went through two design iterations, in which the shape was optimized. Further details follow.

3.1 Inflatable-rigidizable Wings at the University of Kentucky

The inflatable-rigidizable wings were developed in conjunction with ILC. UV-curable resins under development for spacecraft applications were considered for the inflatable-rigidizable wings [18, 73, 29, 66, 74]. Motivation for the research was the NASA Langley and Ames Mars exploration UAVs, and the NASA Dryden "I2000" inflatable wing concept. Here a vehicle was conceived that would be capable of flight in low-density environments and would operate with inflatable wings.

Applications for vehicles utilizing inflatable-rigidizable wing technology were initially aimed at planetary exploration. Here the focus of the research was on extremely low density environments such as Mars. Using UAVs to explore other planets is one of NASA's focus concepts for further exploration of the Solar System. Design concepts have been examined in the past decade to explore both Mars [75, 76, 77, 78] and Venus [79]. Vehicle operation in these conditions presented extreme constraints to the airfoil design process. These constraints are;

1. operating conditions (cruise velocity, altitude, density), and
2. stored or stowed space constraints.

Potential mission profiles incorporated different flight regimes in terms of speed, altitude and maneuvering requirements. Past concepts have opted for "folding wing" designs. Folding wing designs are used on conventional aircraft, such as aircraft carriers, in order to occupy less space. Utilizing a folding wing and empennage design on UAVs increases the ruggedness of the vehicle, as it allows for convenient storage and protects the UAV when not in operation, or during transportation. Folding wing designs have been developed by many groups, including NASA Langley and Ames, for potential Mars exploration vehicles. These designs use conventional wings that are hinged to allow for compact stowage.

An alternate approach to high altitude Mars vehicles was desired. This took the form of inflatable winged Marscraft. Here the wing is capable of being stowed in any shape and then inflated when required. The aircraft was to be evaluated at high earth altitude as a prototype Marscraft. In the development of any Marscraft, one of the principle requirements is a minimal packed-volume-to-weight ratio. Marscraft efforts to date include flights of high-altitude rigid-wing gliders with folding wings and of low-altitude inflatable wing aircraft. A NASA Ames [80] project conducted a successful flight test of a prototype Mars airplane utilizing a folding wing design. The eight-foot span folding-wing glider was balloon-launched to 101,000 ft and released.

The University of Kentucky BIG BLUE project ("Baseline Inflatable Glider Balloon Launch Unmanned Experiment") is in essence a combination of the Ames-Marscraft and Dryden-Inflatable wing (detailed in Chap. 2.6.1) flight-test programs. ILC developed the inflatable-rigidizable wing [18] that was used. The objective of the BIG BLUE project was to deploy inflatable-rigidizable wings on a glider while it ascended to an altitude greater than 80,000 feet via a weather balloon. The wings were constructed of UV-curable composite material that became rigid on exposure to UV light. With this approach, the wings are compactly stowed, pressurized and deployed, and then rigidize with exposure to UV radiation from the sun. Once rigid, the wings no longer require pressurization to maintain shape.[22] Fig. 3.3 shows the inflatable-rigidizable wing before inflation (above) and shows the wing after inflation and curing during laboratory testing (below). The final phase of the mission was to release the glider from the balloon and establish controlled flight to ground using the empennage control.

3.1.1 BIG BLUE Flight Experiments 1 and 2

Initially, research focused on the development and testing of the inflatable-rigidizable wing designs during Big Blue 1 and 2. Feasibility of the inflatable wing concept culminated in a series of high-altitude experiments. The flight experiments consisted of the following three stages:

1. balloon-launched ascent to deployment altitude,

2. deployment of inflatable-rigidizable wings and continued ascent and hover near 100,000 ft, and

3. release from the balloon and return under a parachute.

Note that sea-level Mars atmospheric density and temperature is approximated on Earth at 100,000 ft. Balloon-launched high-altitude experiments to date include the first-ever demonstration of inflatable-rigidizable wing technology: "Big Blue 1" on 3 May 2003, with successful deployment of inflatable wings at 55,000 ft, curing on continuing ascent to 89,603 ft, and descent to recovery.[81]

The designers of "Big Blue 2", considered tailoring the composite layering of materials in the inflatable-rigidizable wings for weight reduction[81]. A second demonstration experiment, on 1 May 2004 resulted in deployment and curing of the second-generation inflatable-rigidizable wings. Fig. 3.4 shows the test article. Required flight characteristics,

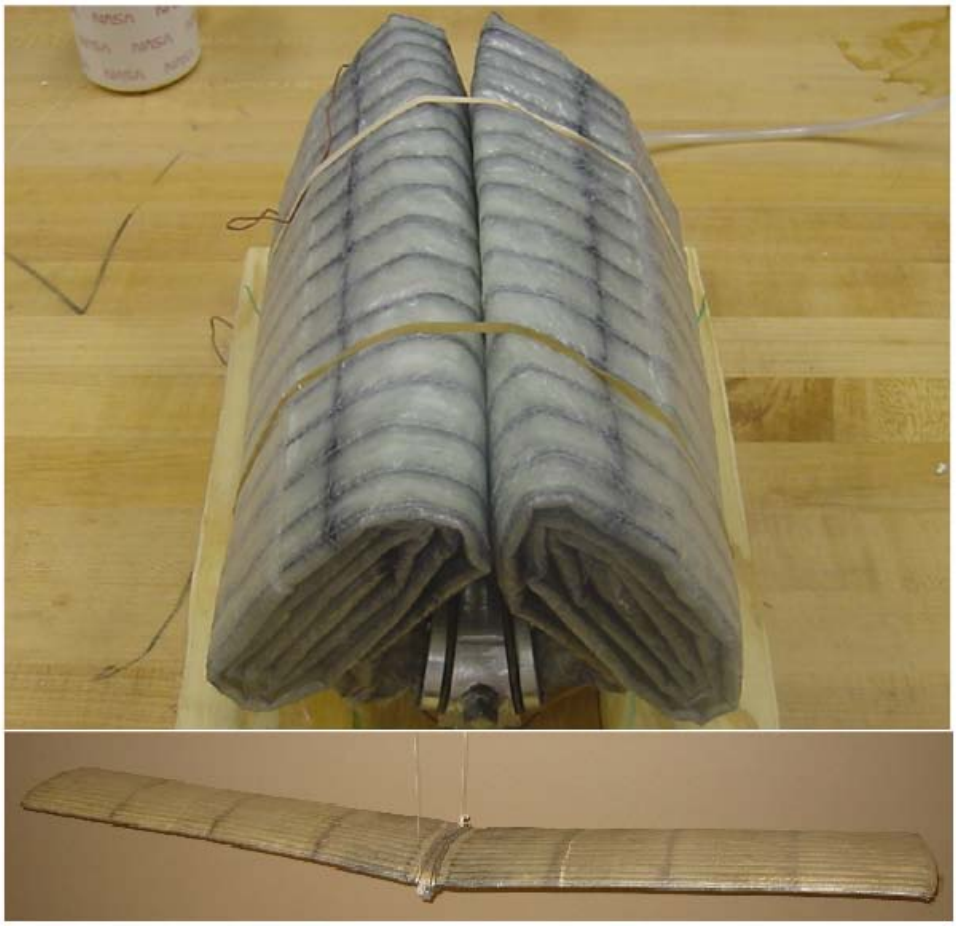

Figure 3.3: BIG BLUE inflatable-rigidizable wings.

aerodynamic performance, aerodynamic analysis and wind-tunnel testing for the inflatable-rigidizable wings are detailed elsewhere [21, 23, 24]. Extensive flight testing of the inflatable-rigidizable wings was performed prior to this experiment, the details of which can be found in Simpson *et al.* [23, 24].

Figure 3.4: Recovery of second-generation inflatable-rigidizable high-altitude test article.

3.1.2 Inflatable-rigidizable Wing Design, Construction, Analysis and Testing

The inflatable wing is designed such that an internal wing pressure is required to attain the wing shape. Once the wing has attained the desired shape the UV curable resin hardens the wing, and the internal inflation is no longer required. High stiffness is achieved with low inflation pressure by maximizing the inflated sectional moment of inertia.

Since the wing is constructed of a flexible fabric material, it can be stowed by folding or rolling. The multi-spar design does not use foam spacer material, as seen in other designs[19], and so packs compactly, and spacer material is not a concern. A detailed description of the design, analysis, and testing of these wings can be found in the Master's thesis work of M. Usui. [21]

The wing profile was selected from several low Re candidates. The candidates were

selected after analysis of aerodynamic performance in XFoil 6.9 over a range of Re (60,000 $\sim$ 500,000).[52] Five candidate airfoils were selected – E387, S7012, DAE31, E398, and DAE11 – with adequate aerodynamic characteristics. Due to the internal baffling of the inflatable wing required for manufacture, the thickest profile, E398, was selected as seen in Fig. 3.5.

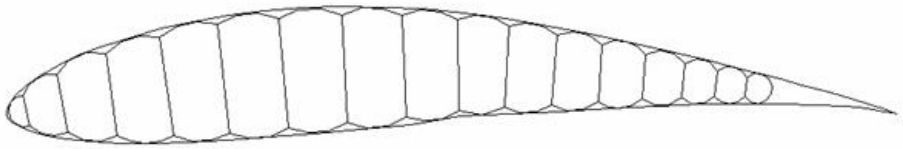

Figure 3.5: Profile of the inflatable-rigidizable wing – with ideal profile superimposed.

The wings were assembled by sewing woven material to create the airfoil and internal baffling. For the inflatable-rigidizable wings, a layered material was used. It consisted of an external contain- ment film, layers of resin-impregnated woven fabric selected for handling characteristics, and an internal containment layer. The woven fabric baffle walls were initially stitched onto the bottom surface of the wing from the trailing to the leading edge. The process was then reversed over the top surface from the leading to the trailing edge. An inflatable urethane bladder was inserted, with long finger-like sections filling each baffle of the sewn wing. This can be seen in Fig. 3.6. The outer wing fabric (in this case, fiberglass) was impregnated with a resin. The resin cured under an external catalyst (UV light). The wing was initially pressurized to a nominal design inflation pressure of 48.3 kPa (7 psi), but once the resin cured, pressurization was no longer required to maintain airfoil shape and the internal inflation bladder was vented to atmosphere. Typical cure times were on the order of minutes, though this was dependent upon ambient UV radiation and resin formulation. The wing is shown in both stowed and deployed states in Fig. 3.3. It was worth noting that the final wing profile has a blunt trailing edge, due to the manufacturing process, as seen in Fig. 3.5.

The wings were constructed in two semi-spans and were joined by an aluminum plenum used for inflation and mounting. The plenum at the center of the wing held the wing spars in position and provided a rigid connection between the inflation tubes and the wing semi-spans. Inflation gas passed into each semi-span through an inflation port mounted on the plenum. Each semi-span was bolted to the plenum to provide a contiguous wing structure.

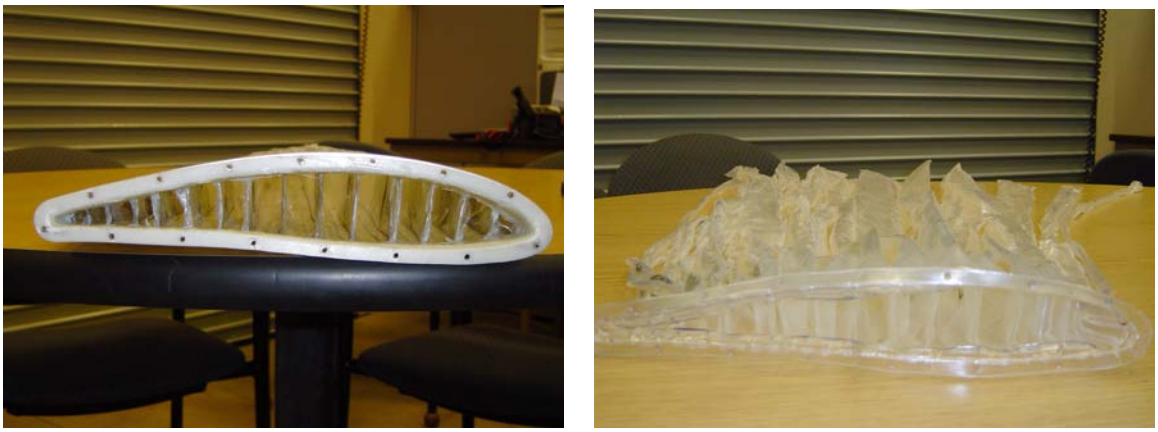

(a) End-veiw of wing baffles.

(b) Internal "finger–like" bladder.

Figure 3.6: Inflatable-rigidizable wing.

Inflatable Wing Modeling

Since the inflatable-rigidizable design relies on solid composite layers and not on internal inflation pressures to maintain stiffness, a finite element analysis of the inflatable-rigidizable wing was conducted using ANSYS. The purpose of this analysis was to determine the maximum stress expected for the wing and to determine the number of composite layers required in the wing fabric (restraint). The model was constructed using the cross section geometry and composite material properties provided for the wing design. Since the material is a woven composite, it was assumed to be an isotropic material. The center of each inflation chamber and radius were obtained from the CAD drawing of the design and the geometry replicated in ANSYS. Fig. 3.7 is the cross-sectional view of the wing model. External loads were determined by using an elliptical pressure loading distribution for several load factors.

The initial ANSYS analysis included three different cases: one layer, two layers, and three layers using the ANSYS linear Layered Structural Shell Element, SHELL99. An example of the stress concentrations is shown in Fig. 3.8 for a single layer. As the number of layers was increased to two and three, the value of the maximum stress decreased, as expected. The maximum stress also changed locations, however. Since the stress on the wing was so small, the wing manufacturer decided on a wing using two plies for the initial wing design. In further ANSYS analysis, other layering cases were examined. These cases involved the stepped reduction in composite layers from wing root to wingtip. This was performed in an attempt to simultaneously reduce the overall wing weight and provide better rigidity in high stress locations. This was used to design a version of the wing that

was lighter in weight than the original design. More details are provided in Usui [21].

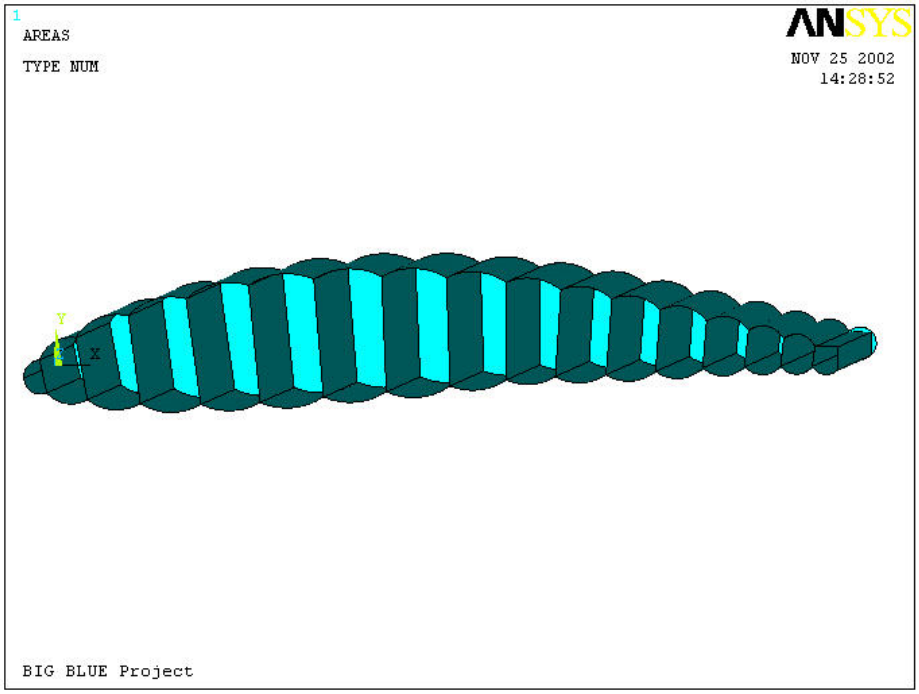

Figure 3.7: Interior of wing [21].

Aerodynamic Performance of inflatable-rigidizable Wing

Since *Re* is related to density, Marscraft must be designed for low-Re flight. At low Re, flow over wings tends to separate and form laminar separation bubbles due to adverse pressure gradients. This leads to poor aerodynamic performance. To address this problem, designers typically increase wing span. However, for Marscraft, larger wing spans lead to increased launch costs due to the associated increases in weight and volume. To be viable wings for planetary exploration, inflatable wings need to perform well at low *Re*, reduce weight, and maximize the deployed to packed volume ratio.

Due to the peculiar wing profile, an investigation of the aerodynamic performance of an inflatable design was conducted by comparing the actual "bummpy" profile of the inflatable-rigidizable design with that of the ideal "smooth" profile. The initial consideration was to improve aerodynamic performance by placing a "skin" over the wing to reduce the perturbation of the baffles and to provide a sharper trailing edge.

Since this particular design was being considered for a Mars mission scenario where

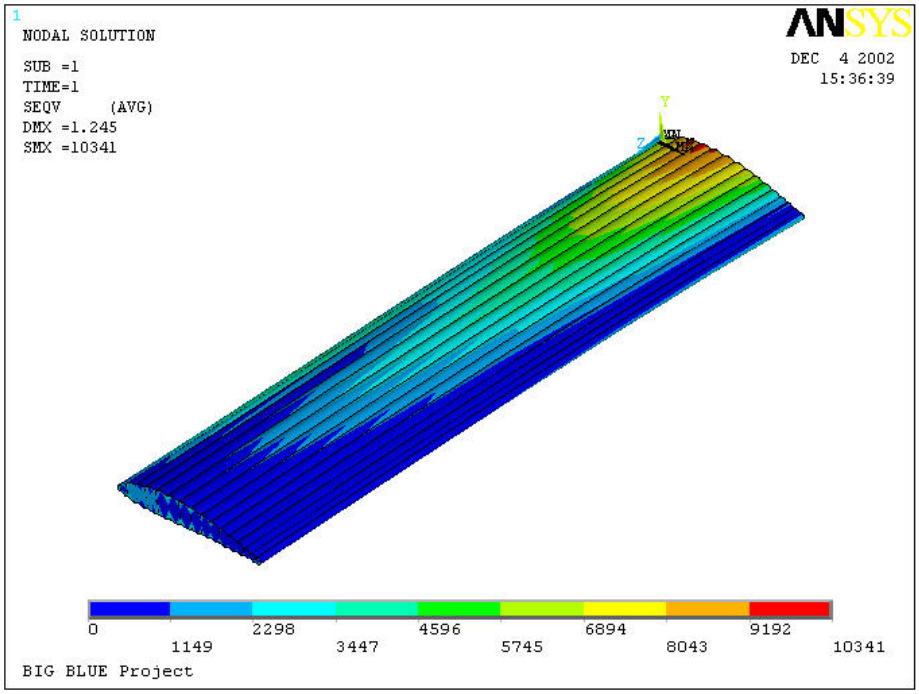

Figure 3.8: Stress contour plot of one layer [21].

very low densities, hence Re would be encountered, experiments were conducted over a wide range of Re from 25,000 to 500,000. In the lower Re range, smoke-wire flow visualization observations were made. This test was conducted as described in Batill and Mueller [82]. A stainless steel and tungsten wire (diameter of 0.006 in) was doped with a model train smoke mixture which contained mineral oil, oil of anise and blue dye. The wire was stretched and mounted on a stand placed in front of the wing. A power supply was connected to this wire inducing a current. Due to Joule heating, the oil evaporated, making smoke trails around the wing. A Sony XC-55BB camera was placed next to the test section, and then a Matrox Pulsar frame grabber package was used to capture images. This test was limited to low Re , so the range of Re examined was 25,000 to 100,000, over a range of α.

The results of some of the tests are shown in Fig. 3.9. At the lowest Re case the surface perturbations improved the flow over the wing. Here, the ideal E398 performed poorly compared with the inflatable-rigidizable profile. At $Re = 25 \cdot 10^3$ and $\alpha = 0°$-α, separation starts very close to the leading edge for the ideal E398 profile, and there is no reattachment, as shown in Fig. 3.9a. Also, the flow streamlines adjacent to the surface in the separation region are well demarcated, suggesting the flow is laminar prior to experiencing separation. For the same (Re, α) and chord-wise position, the bumpy profile 3.9b shows attached flow, and the streamlines adjacent to the surface are not distinctly clear. This is due to the bumps tripping the flow to promote transition to turbulence earlier than in the previous case. It can be observed that the position of the separation point is shifted further downstream of the laminar separation point (Fig. 3.9b), due to the addition of the bumps. The disturbance level posed by the bumps was not enough to fully promote transition ahead of the maximum thickness point in the bumpy profile, and the unstable laminar-turbulent boundary layer separated from the surface at the point of maximum thickness.

Fig. 3.10 is the result at $Re = 50 \cdot 10^3$ with $\alpha = 0°$. This shows the separation region for both the ideal and inflatable wings. The separation region of the inflatable wing is significantly smaller than that of the ideal wing. This result can be seen at various angles of attack. Better separation results are seen for the bumpy inflatable profile due to the indentations from the baffles.

As expected, at $Re = 50 \cdot 10^3$ and $\alpha = 4°$ (Fig. 3.11a), the flow separates earlier upstream for the ideal profile, compared to the $Re = 25 \cdot 10^3$ case (Fig. 3.9a). The bumpy profile shows marked control in the separation extent as seen in Fig. 3.11b; more than the equivalent lower (Re, α) case discussed earlier. The higher flow momentum and angle of attack, coupled with the bumps - produce a higher disturbance level in the flow (as compared with the lower (Re, α) case), and flow is tripped closer to the leading edge.

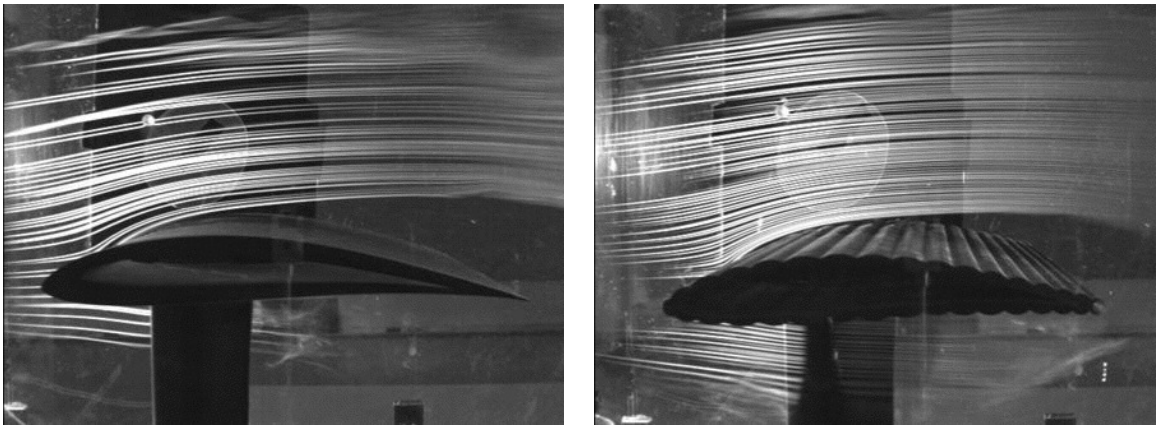

(a) **E398 ideal wing** (b) **Inflatable wing**

Figure 3.9: $Re = 25,000$; $\alpha = 0°$ [21].

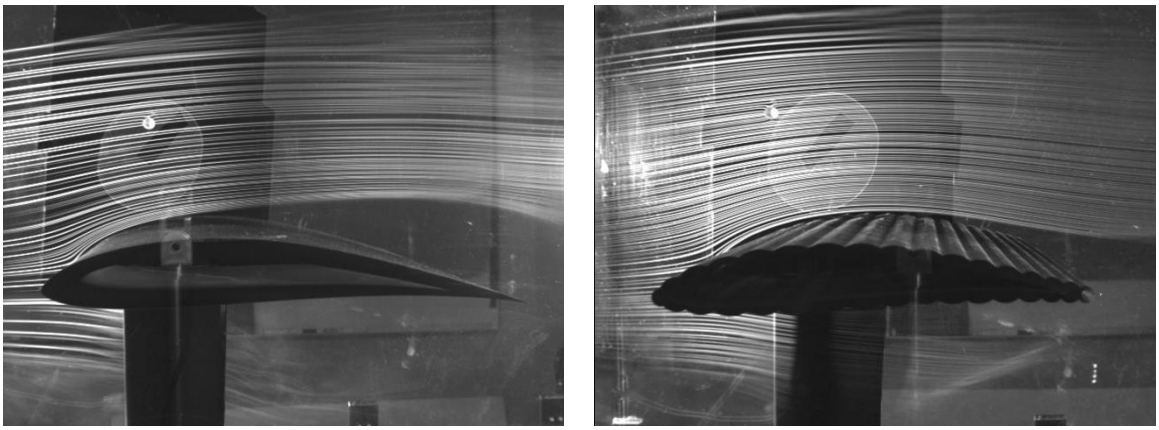

(a) **E398 ideal wing** (b) **Inflatable wing**

Figure 3.10: $Re = 50,000$; $\alpha = 0°$ [21].

This gives the flow greater momentum which allows it to stay attached longer. The greater turbulence level can be seen as the streamlines adjacent to the wing surface that are not distinctly clear, indicating a mixing of adjacent layers.

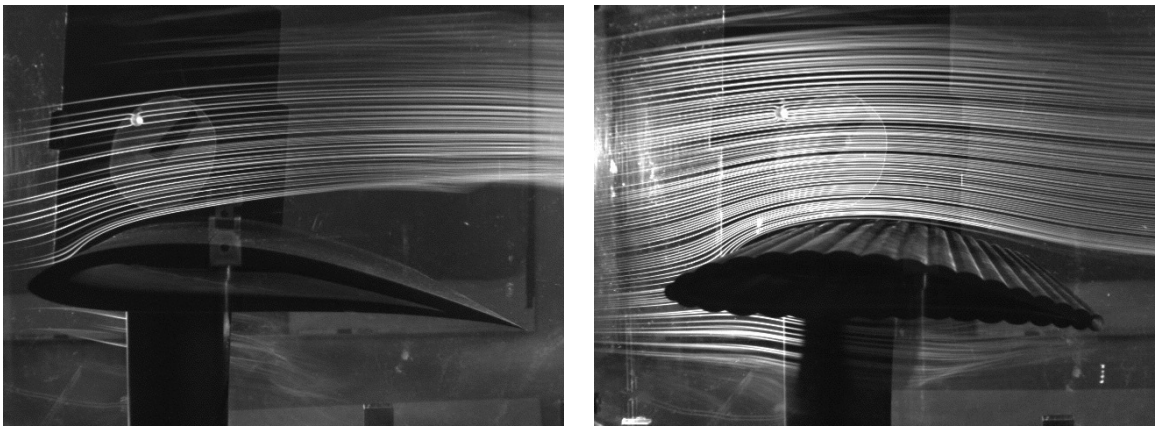

(a) E398 ideal wing

(b) Inflatable wing

Figure 3.11: $Re = 50,000$; $\alpha = 4^\circ$ [21].

Fig. 3.12 is the result with the same Re , but $\alpha = 12^\circ$. For higher α values the separation region decreases. A larger α value trips the boundary on the leading edge of the wing which helps to minimize separation. Note that flow stream lines above the trailing edge are not distinct in Fig. 3.9(a) and Fig. 3.10(a) due to the transition region that disrupts the stream lines. At $Re = 100,000$ (figure 3.13a and 3.13b), the inflatable-rigidizable profile is still improved, though only marginally, over that of the E398.

For all Re and α values cases observed, the separated shear layer did not reattach. This did not occur for either the ideal or bumpy profiles. A laminar separation bubble was not expected at these low Re_c values, in line with the observations of Lissaman [2] ($(Re_c)_{min} = 50 \cdot 10^3$ for "closed" bubble formation). Among the perturbed wing cases, the extent of separation is lesser for a higher Reynolds number and higher angle of attack. At smaller α values, the separation region difference is also noticeable for $Re = 25 \cdot 10^3$ and $Re = 100 \cdot 10^3$ (not shown). For the very low range of Re considered here, the critical roughness height expressed by Re_c needs to be on the order of 1000, which is fairly large compared to the chord length [47]. The flow visualization was limited to values of Re_c lesser than 100,000.

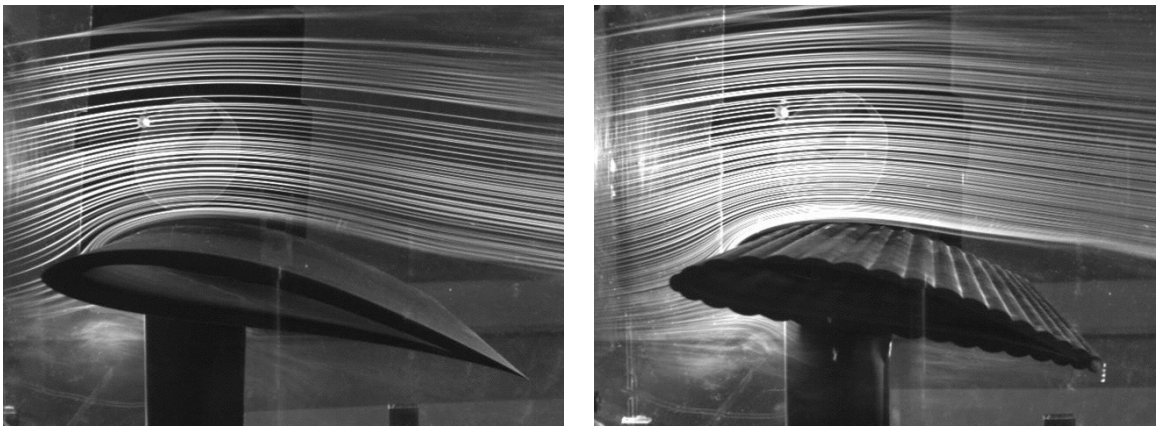

(a) **E398 ideal wing** (b) **Inflatable wing**

Figure 3.12: $Re = 50,000$; $\alpha = 12°$ [21].

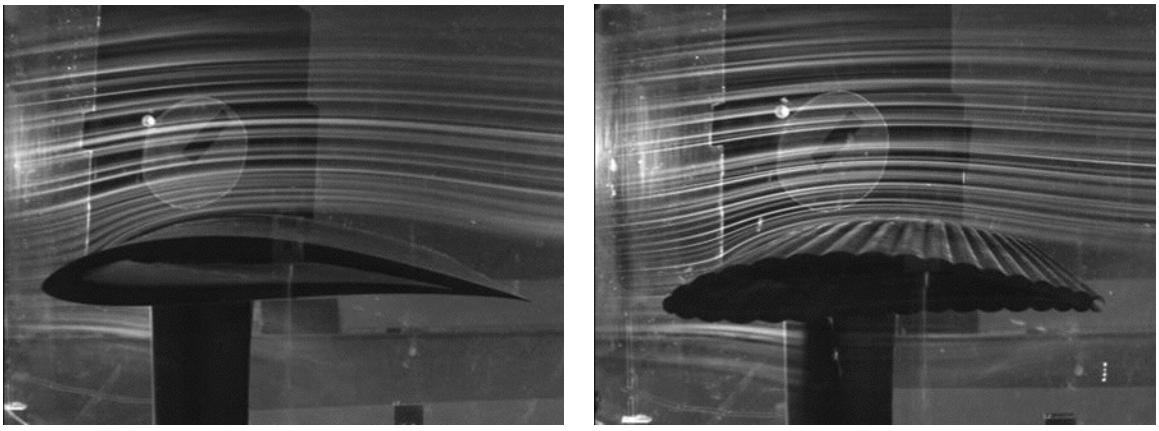

(a) **E398 ideal wing.** (b) **Inflatable wing.**

Figure 3.13: $Re = 100,000$; $\alpha = 0°$ [21].

3.1.3 BIG BLUE High Altitude Flight Experiments 1 and 2

In May of 2003 and 2004, University of Kentucky BIG BLUE teams conducted wing deployment tests of the inflatable-rigidizable wings at high altitude. With the aid of EOSS (Edge Of Space Science), the BIG BLUE glider was launched from Fort Collins, Colorado. The wings were inflated at an altitude of approximately 50,000 feet in 2003 and 60,000 feet in 2004. This altitude was pre-determined by the cure time of the composite wings. Approximately an hour after the launch, the gliders were released from the balloons and descended under parachute. The maximum altitude attained was 89,603 feet (27,311 m) in 2003 and 60,000 feet (18,288 m) in 2004 (due to premature bursting of the balloon). Both landed later following a parachute deployment. Fig. 3.14 details the wing deployment sequence of the 2003 flight via an on-board video camera. Fig. 3.15 is a series of images from an on board still camera showing the wing during ascent and decent of the 2003 flight. Fig. 3.16 shows images of the 2004 flight. Here a camera with a fish-eye lens was situated on the nose of the vehicle. Fig. 3.16*a*, shows the balloon bursting and Fig. 3.16*b* shows the vehicle descending under parachute.

The high-altitude inflatable-rigidizable wing deployment tests verified several important aspects of this technology including inflation and unfolding deployment at low temperatures (wing temperature approximately 10 °C and external temperature approximately -20 °C. These experiments mark the first time an inflatable wing was successfully rigidized with exposure to UV radiation in a flight experiment. Post-flight evaluation of the flight wings (including material characterization, in-flight data analysis and wind-tunnel testing) has been presented elsewhere.[22, 23, 24]

3.2 Inflatable Wing Research at the University of Kentucky

The research shifted focus to potential benefits of an inflatable wing without rigidization. While rigidization provides the security of a rigid structure once cured, it has a few drawbacks. Foremost, the wing can only be deployed in a single mission. Once the UV curable resin is activated the wing hardens. This does not allow the wing to be reused in future missions requiring the initial stowed configuration. The wings also require storage in a UV free environment. Leaking UV light to the stowed wings can cause the wings to harden in the stowed configuration. Difficulty can also arise if the hardening process begins while the wing is not in the correct shape. This would result in a functionally useless wing, cured in an undesirable shape. Finally, the wing can not accommodate control surfaces from within the wings surface. The researchers proposed the idea of constructing a wing without

(a) Stowed wing prior to deployment; 55,000 feet.

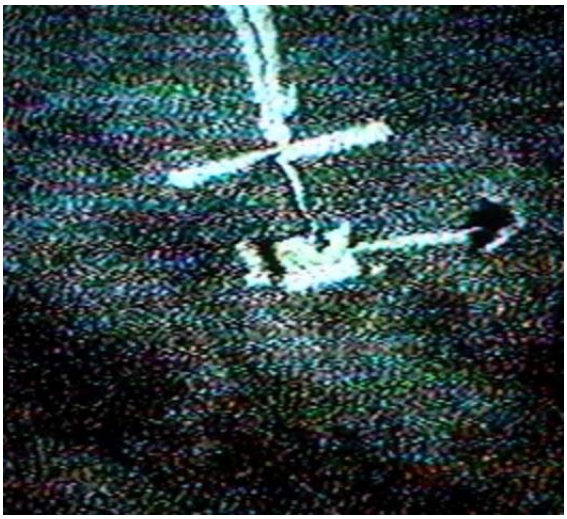

(b) Wing deployment; port wing deploying.

(c) Wing deployment; starboard wing deploying.

(d) Inflated wings during ascent just prior to release; 89,000 feet.

Figure 3.14: Big Blue 1 – Wing deployment sequence, 2003 [22].

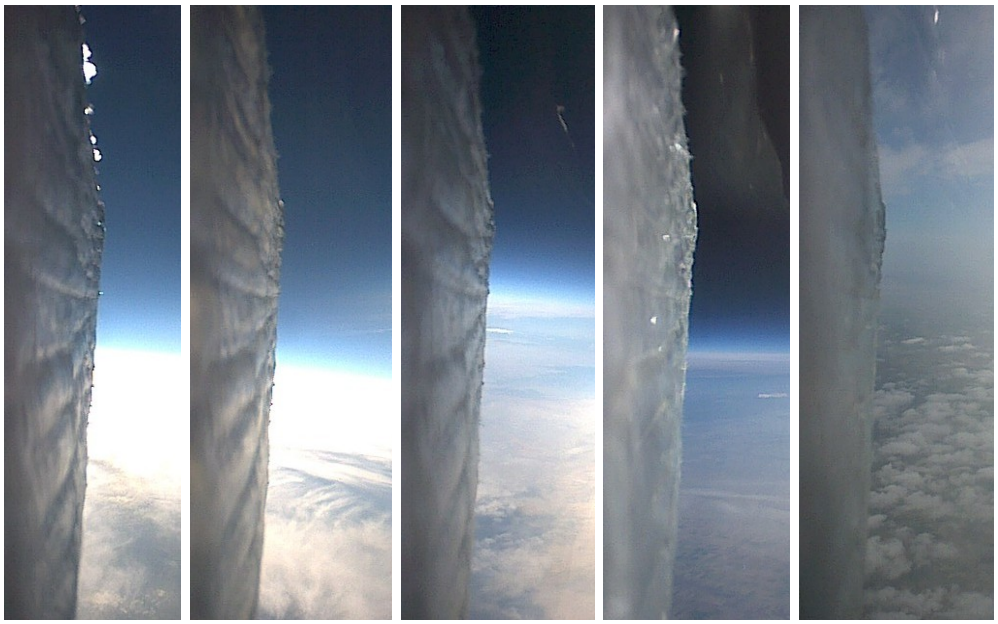

Figure 3.15: Images from high altitude deployment testing of the first-ever inflatable-rigidizable wing; from left to right, 58,000 ft, 63,000 ft, 86,000 ft, 89,603 ft, 17,000 ft [22].

(a) **Balloon burst.** (b) **Vehicle descent.**

Figure 3.16: Big Blue 2 – Flight experiment 2004 [23, 24].

impregnating the material with UV curable resin. This change would provide potential benefits;

- wings would not contain the UV curable resin hence be potentially lighter,
- wings can be deflated and redeployed in subsequent missions,
- wing could be repacked into original stowed areas without harm and would not required stringent storage conditions,
- wings could accommodate control mechanisms,
- wing warping could be used for flight control.

The most intriguing possibility is in wing warping. As the wing contains no solid structure, inflation pressure is required for stiffness during the entire flight. However, this fact allows the wings shape to be modified during the flight to either improve efficiency or alter the performance of the vehicle.

3.2.1 BIG BLUE Flight Experiments 3 and 4

Following the same mission profile, the University of Kentucky undertook BIG BLUE 3 and 4. The projects made use of the "Forward Air Support Munition" (FASM) or "Vectran" inflatable wing variant, shown in Fig. 3.17. The Vectran wing was developed by ILC. The design is similar to the rigidizable version with an internal inflation bladder and external restraint, but does not include the impregnated resin and the external or internal containment film. The inflatable wing is designed such that constant internal wing pressure is required to maintain wing shape. The cross-sectional shape differs from the inflatable-rigidizable wing as the Vectran wing uses a NACA 4318 profile and not the E398 profile. Vectran has a design inflation pressure of 186 kPa (27 psi).

The Vectran wings have been flown in a number of configurations. Fig. 3.18, shows flight test vehicles with the Vectran inflatable wings.

3.2.2 BIG BLUE High Altitude Flight Experiments 3 and 4

In May 2005, the University of Kentucky BIG BLUE III team conducted a wing deployment test of the inflatable Vectran wings at high altitude. A 54,600 ft^3 Raven plastic balloon was used to carry the 23.7 lb combined UK and EOSS (Edge of Space Sciences) payload to a maximum altitude of 97,873 ft. The wings were successfully deployed at approximately

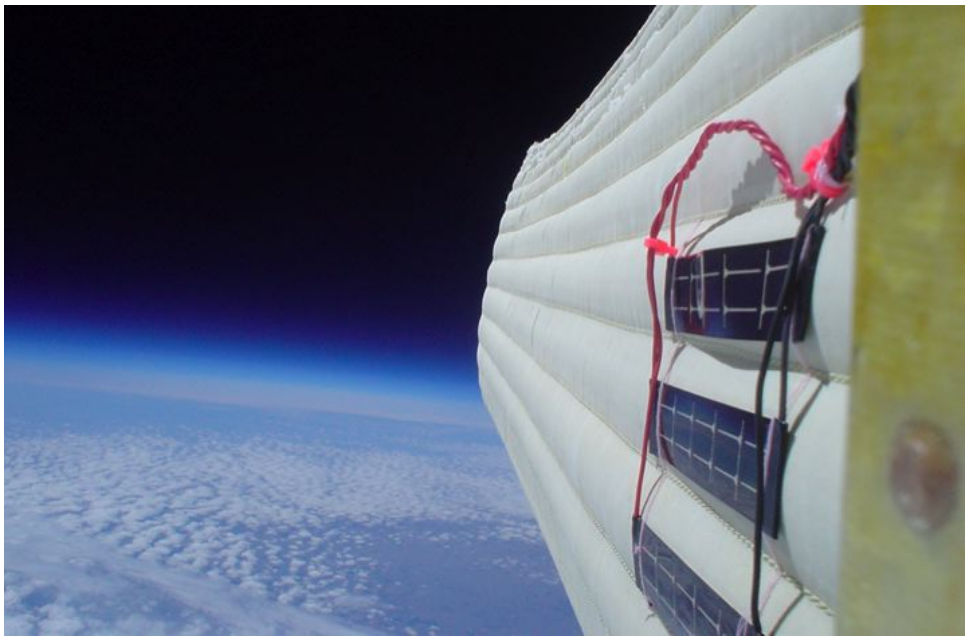

Figure 3.17: Vectran inflatable wing, high-altitude test at 98,000'.

(a) Primary research vehicle.

(b) NASA Ames 729 fuselage with inflatable wing.

(c) BIG BLUE **3** and **4** "AIRCAT".

Figure 3.18: Vectran wings on numerous flight test vehicles.

96,000 ft. The wings continued ascent with the balloon to the maximum altitude and then descended under a parachute for recovery. The wing pressurization maintained a wing shape suitable for flight throughout demonstrating the feasibility of inflatable wing technology for Mars exploration. The inflation system was designed to vent upon ascent and included make-up gas to maintain 185 kPa (27 psi) until landing.

An onboard still camera captured the wing deployment as can be seen in Fig. 3.19. Flexible solar cells attached to the surface of the wing are seen in the images and generated power after deployment. Other images from the edge of space include the moon and stars, while images from closer to ground level show the snowy countryside and recovery team moving into position for the touchdown.

3.2.3 BIG BLUE High Altitude Flight Experiment 5

The technical goal of BIG BLUE 5 is to demonstrate the feasibility of inflatable wings for flight in a low-density atmosphere. In order to accomplish this, the mission concept was similar to previous BIG BLUE experiments and is shown in Fig. 3.20. The nylon wings were used during this high altitude flight. The objectives of the BBV Colorado Mission was:

1. to verify long-range (near 100,000 ft altitude) communication with the commercial Piccolo autopilot

2. to verify use of the autopilot for mission operations such as to initiate inflation, take pictures, monitor sensors, cut away and deploy the emergency parachute and

3. to test at high altitude a new lightweight aircraft (designed targeting a total weight less than 15 lb compared to the almost 40 lb weight of the AIRCAT with inflatable wings)

Prior to the high altitude flight test, low altitude flight testing was conducted which included many successful parachute deployment flights and autopilot tests, in preparation for a low-altitude cut-away. The launch and lower ascent proceeded as planned, with clear ATV transmissions from EOSS and UK cameras. As the balloon reached about 70,000 ft, aircraft control was successfully transferred from the launch-site ground station to the down-range ground station. The communication link to the autopilot was stronger over longer distances than expected. The command was issued to inflate the wings. The on-board video cameras showed the wings inflated, but the wings did not completely unfold. This was due to a wing restraint that had not released. After a delay, the restraint suddenly gave way

(a) Ascent; starboard wing.

(b) Stowed wing prior to deployment.

(c) Wing deployment; 96, 000 ft.

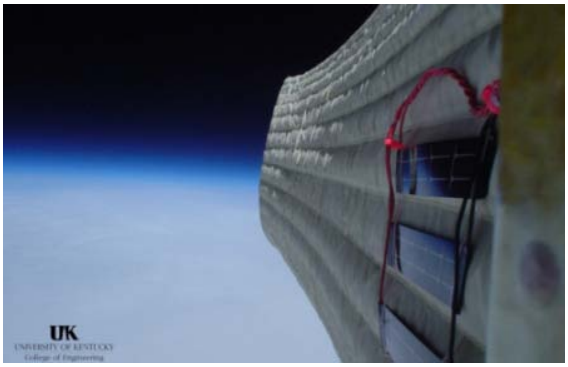

(d) Wing inflation.

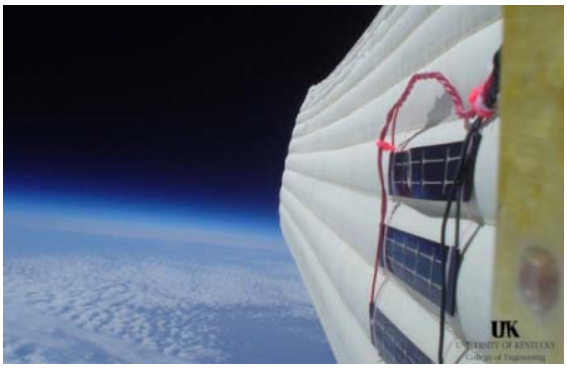

(e) Maximum altitude; 97, 873 ft.

(f) Decent under parachute.

Figure 3.19: High Altitude Flight Experiments [25].

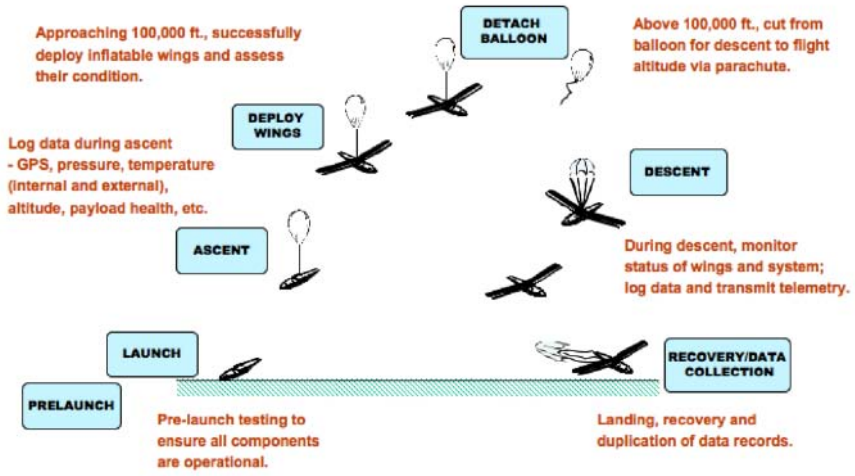

Figure 3.20: BIG BLUE 5 flight profile.

and the nylon wings snapped open. The snap opening of the wings was unexpected, and the wing mounts failed at the fuselage due to the high dynamic load. As a result the right wing detached from the fuselage and fell away. From analysis of the video evidence, the nylon wing was undamaged, with the wing mount failing causing the wing to detach from the fuselage.

Although the vehicle had only one wing attached during the decent, the decision was made to continue with the planned cut-away from the parachute. The remote autopilot ground station transmitted the cut-away signal. The result was a successful cut-away from the EOSS parachute and successful deployment of the aircraft emergency chute. The aircraft was recovered, but the lost right wing is still missing.

3.2.4 Inflatable Wing Design and Construction

The Vectran wing design uses internal span-wise baffles or inflation cavities to help maintain structural stiffness at lower internal pressures (Fig. 3.21). The outer wing (restraint) and internal baffles are constructed from high strength fibers. The current incarnation as tested herein uses an outer restraint and internal baffle walls made of Vectran, a manufactured fiber spun from Celanese Vectra liquid crystal polymer. The fibers have high-temperature resistance, high strength, high modulus, high resistance to moisture, and resistance to chemicals. The material is also able to retain these properties in hostile envi-

ronments.

Since Vectran is porous, a polyurethane elastomer bladder is used to keep the internal volume pressurized. The Vectran wings have a mass of approximately 3 kg (6.6 lbs), including an aluminum plenum used for inflation and mounting. The plenum at the center of the wing holds the wing spars in position and provides a rigid connection between the inflation tubes and the wing semi-spans. High pressure gas passes into each semi-span through an inflation port that is mounted on the plenum. Each semi-span is bolted to the plenum to provide a contiguous wing structure.

Design pressure is 186 kPa (27 psi), though the wing has been successfully flight tested at values down to 52 kPa (7.5 psi) with sufficient wing stiffness for low-speed applications. The wing is constructed in semi-span sections and mounted to a plenum that can the be attached to an aircraft fuselage as seen in Fig. 3.21. The wing profile is based around a NACA 4318 with a 4° incidence angle. The wings have a span of approximately 1.8 m (6 ft), a taper ratio of 0.65, and an aspect ratio of 5.4. Table 3.1, details the Vectran wing specifications. Note that the ribbed profile and blunt trailing edge are similar to the inflatable/rigidazable wing discussed above. Generally, low *Re* airfoils are designed to have thin profiles. [24] Here, manufacturability dictated a thicker profile which is typically a poor performer at low *Re* . However, the airfoil actually has improved performance in the speed regime of interest due to the roughness of the inflated profile, which has been noted in the case of bird wings, for example. [51, 83] This is discussed in more detail in Chapter 1, above, and elsewhere [84].

Table 3.1: Vectran wing specifications.

Nominal NACA shape	4318
Dihedral	4°
Incidence Angle	4°
Full span planform area	1037 in^2
Aspect Ratio	5.4
Taper Ratio	0.65
Internal Volume	2118 in^3
Full span weight (Wings only)	3.4 lb
Inflation Pressure	27 psi

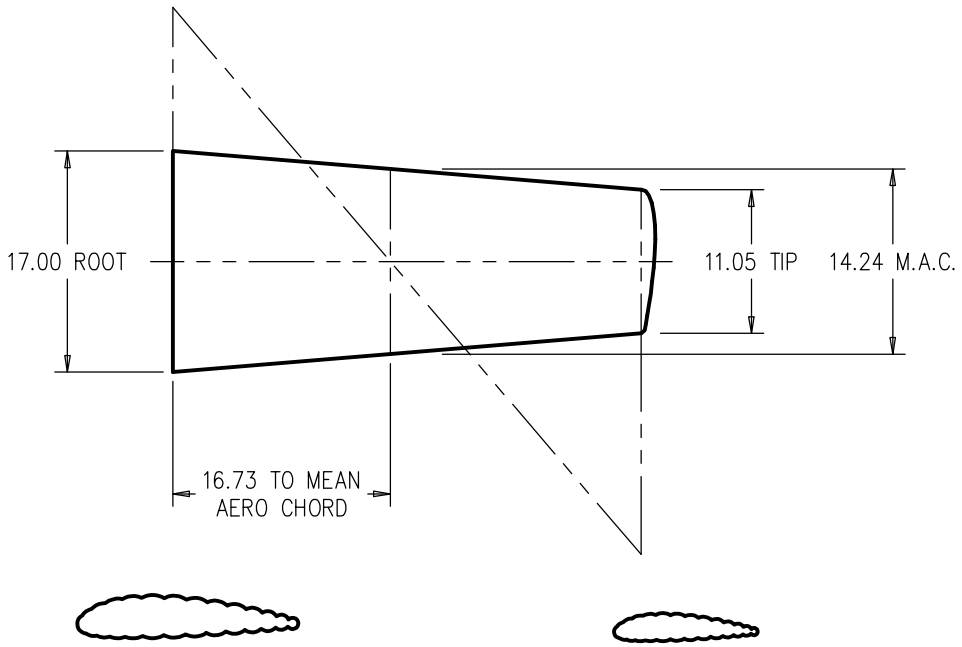

Figure 3.21: Vectran inflatable wing.

3.2.5 Finite Element Modeling of Inflatable Wings

Work has been done on analytical models and experimental studies of bending and deployment of inflatable cylinders and spacecraft structures, called gossamer structures [71, 85, 86, 87]. Analytical models based on the response of inflated cylinders have been developed for static and dynamic response of inflating beams and for aeroelastic response of inflatable wings for UAVs [88, 30].

The University of Kentucky has also been pursuing the development of finite element (FE) models [81, 89, 90]. The desire is to evaluate wing warping strategies through the use of these wing warping models to reduce lengthy trial and error design cycle times. Ultimately, the interest in the development of a finite element model of inflatable wings lies in the desire for the ability to predict responses of the wings to combined-loading situations including applied aerodynamic loads from wind tunnel or actual flight testing and forces applied to change the shape of the wings.[90]

FE models of Vectran Inflatable Wings

The wing was initially modeled in ProEngineer^{TM} and then imported into ANSYS, where, Shell 181 elements were used. The elements were suitable for thin to moderately-thick shell structures and had four-nodes with six degrees of freedom per node. Orthotropic material properties were defined representing the different warp and fill properties of the plain weave, 53 x 53 thread count per inch, silicon-coated Vectran woven fabric material. The model had a flat end at the wingtip and not a rounded seamed tip of the true wing. This allowed pressure forces to stiffen the fibers along the span-wise direction within the model. The actual wing had a nominal semi-span of 0.914 m (36 in) with leading and trailing edge lengths of 0.889 m (35 in) For the FE model, due to the simplification of modeling a flat wingtip, semi-span length for the wing, including leading and trailing edges, is 36 in. To date the model has been run for four different cases were considered: 69 kPa (10 psi), 103 kPa (15 psi), 138 kPa (20 psi) and 172 kPa (25 psi).

The model was initially set-up to mimic the internal pressure of the wing. Initially, the model was validated by placing upward vertical forces on the wing, corresponding to the location of the applied experimental forces. Vertical deflection results were obtained at nodes corresponding to measurement locations from the experimental bending test [90]. Results of this bending test can be seen in Fig. 3.22. These results are compared for deflections of the experiments and the deflections generated from the model at 10 psi internal pressure. Fig. 3.23, shows the experimental results compared to the model results for 15 psi. The current model does not perform well at higher internal pressures. Thus, the bending stiffness of the wing model does not increase with pressure as the actual wing does. Current work is tackling this problem.

A comparison between angle of twist from experimental results and FE analysis is shown in Fig. 3.24. The results show that the inflatable wing FE model is too stiff in torsion[90]. For 10 psi internal pressure, computed angle of twist at the wingtip was on average only 16% of experimentally determined angle of twist. For 15 psi, computed results on average were 29% of experimental. The University of Kentucky's Dynamic Structures and Controls Laboratory (DSC), is actively pursuing this problem with the aim of developing models of the inflatable wings. For a detailed examination of the modeling of inflatable wings please refer to the Masters Thesis of Johnathan Rowe [26].

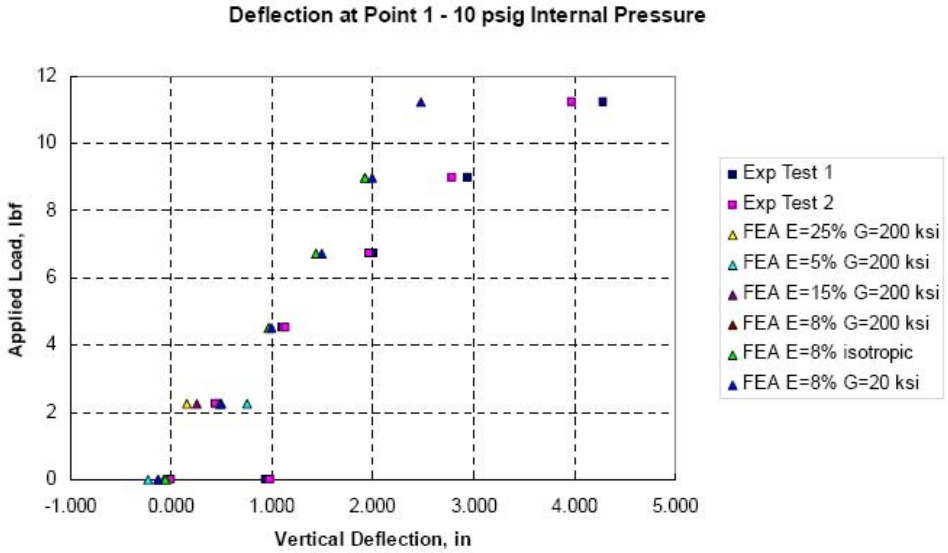

Figure 3.22: Comparison of experimental and FE wing deflection results (10 psi) [26].

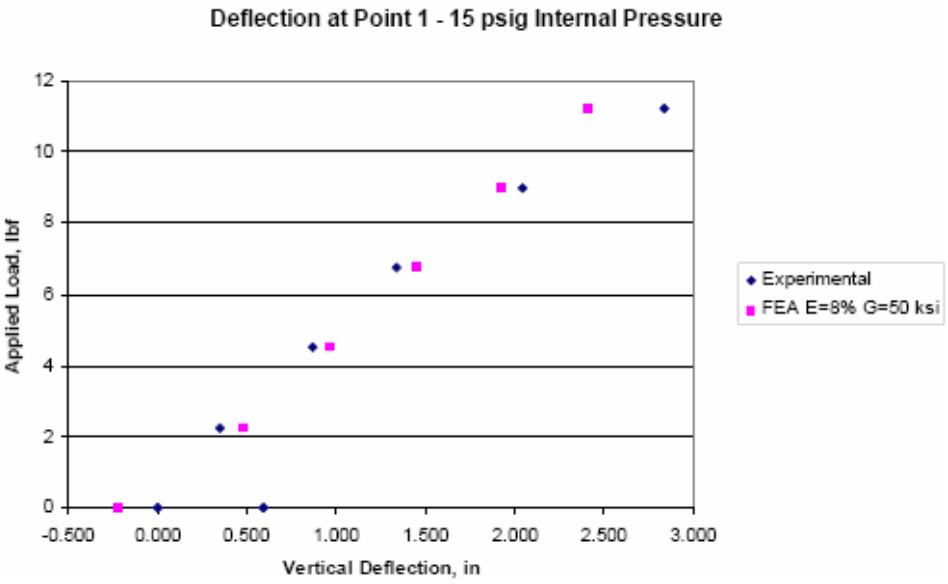

Figure 3.23: Comparison of experimental and FE wing deflection results (15 psi) [26].

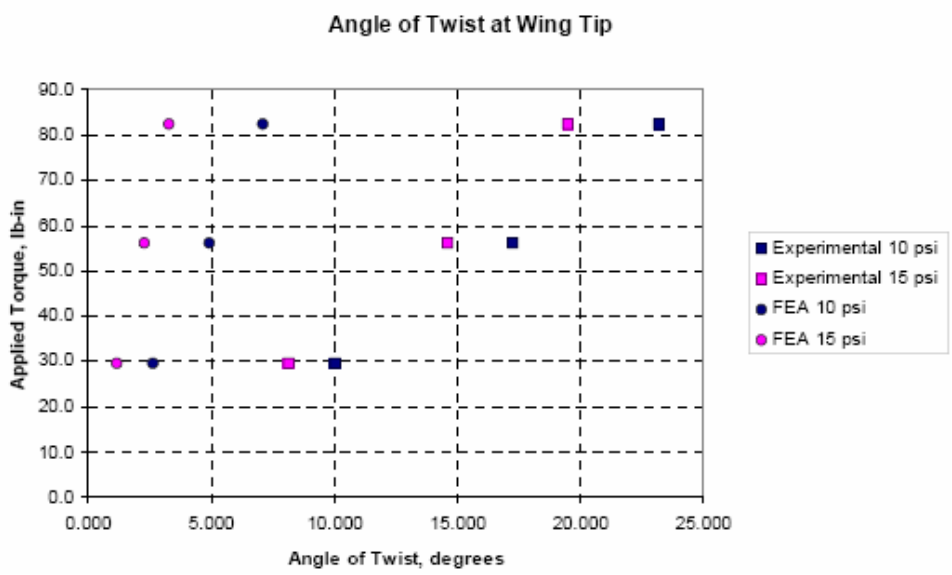

Figure 3.24: Comparison of angle of twist at wingtip, negative twist applied [26].

3.3 Inflation Requirements

The primary consideration for failure in an inflatable structure is the maximum sustainable bending moment [27]. For an inflatable wing to be practical the inflation pressures required to sustain the root bending and other associated forces on the wing (such as twist) must be small enough that the wing design does not impose severe inflation and material requirements [27]. Higher pressures will increase mission risk by reducing the reliability of inflatable components through increased chances of leaks. While leakage effects can be countered with make-up gas and onboard compressors, these must be factored in as increased weight during the trade study portion of the vehicle design[27]. To determine the load carrying capability of an inflatable wing design, we begin with the well known Euler-Bernoulli beam equation that relates the beam deflection with applied moment and material properties on a cantilever beam; This is derived in detail in [27].

In terms of required inflation pressure for a given bending moment, the equation can be written as

$$\mathrm{P} = \frac{2M_0}{\pi r^3} \tag{3.1}$$

While P is linear with M_0, doubling the tube radius reduces P by a factor of 8. Thus, thicker tubes are extremely beneficial when used on wings. The required pressure can be reduced by 1/2 by using a braided beam that groups the active axial fibers to double the

moment of inertia in the bending direction as noted in Section 2.7.2.

$$\mathrm{P} = \frac{M_0}{\pi r^3 \left(1 - 2tan^2\beta\right)} \tag{3.2}$$

where β is the angle of the bias braid. Further increases in the allowable bending load can be made by applying the principle of tensairity where tension and compression elements are designed integrally with the airbeam[91]. While not extensively tested, it has the potential to increase the allowable load by an order of magnitude. Other methods to increase allowable bending moment include increasing the materials elastic modulus and the wings cross-sectional moment of inertia[27]. Multiple spars or baffles accomplish the latter.

Jacob *et al.* [27] determined the required inflation pressure for a wing given an entirely inflatable solution (b/2 = 0) or an inflatable outboard portion with a rigid center section ($0 \leq$ b/2 ≤ 1). In this small scale case, a baffled design was used with polyurethane coated nylon and a resulting design inflation pressure of 14 psi as seen in Fig. 3.25.

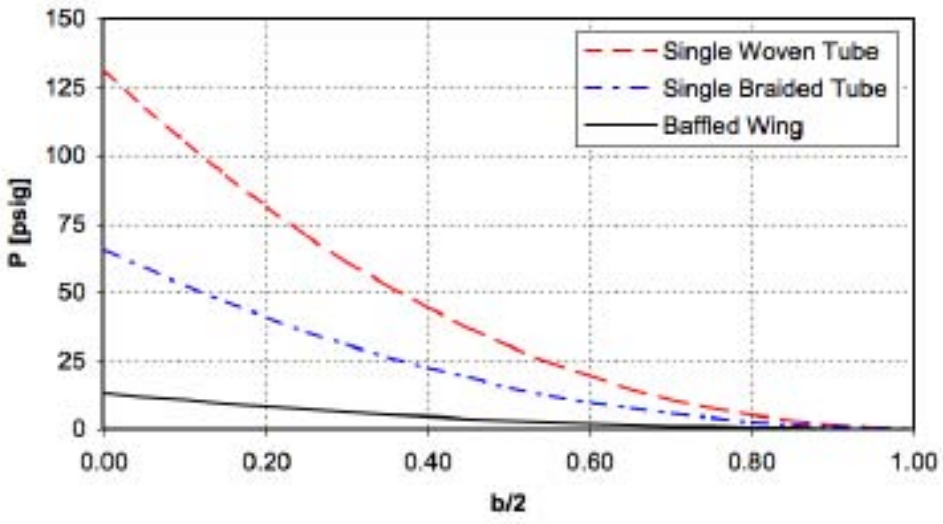

Figure 3.25: Pressure requirements for vehicles for 3 different inflatable wing configurations [27].

For the baffled wing design, higher pressures are required than previously tested for this design using an inflatable wing for the entire span, but even using only a 20% semi-span rigid center section reduces the required inflation pressure to the previously proven designs. Collapse of the wing can be predicted using static aeroelastic models, such that the never exceed speed can be determined [30, 70].

$$U = \sqrt{\frac{2E_\ell}{C_{L_{max}}\rho S\delta}} \tag{3.3}$$

These values can be adjusted based upon the modulus of elasticity of the material as well as the design details, so they should be considered as a first estimate only [27].

Jacob *et al.* [27], shows that for a vehicle with fixed wing loading W/S (fixed weight and wing area), the bending moment will increase as the aspect ratio (AR) increases. The impact of this is shown in Fig. 3.26 for an aircraft with an AR = 16. Since the root bending moment is a nonlinear function of the span, then the inflation pressure will also be a nonlinear function of the AR. One can quickly see that as bending moment increases to realistic levels that the required inflation pressure becomes unsustainably high, thus necessitating other inflatable design options.

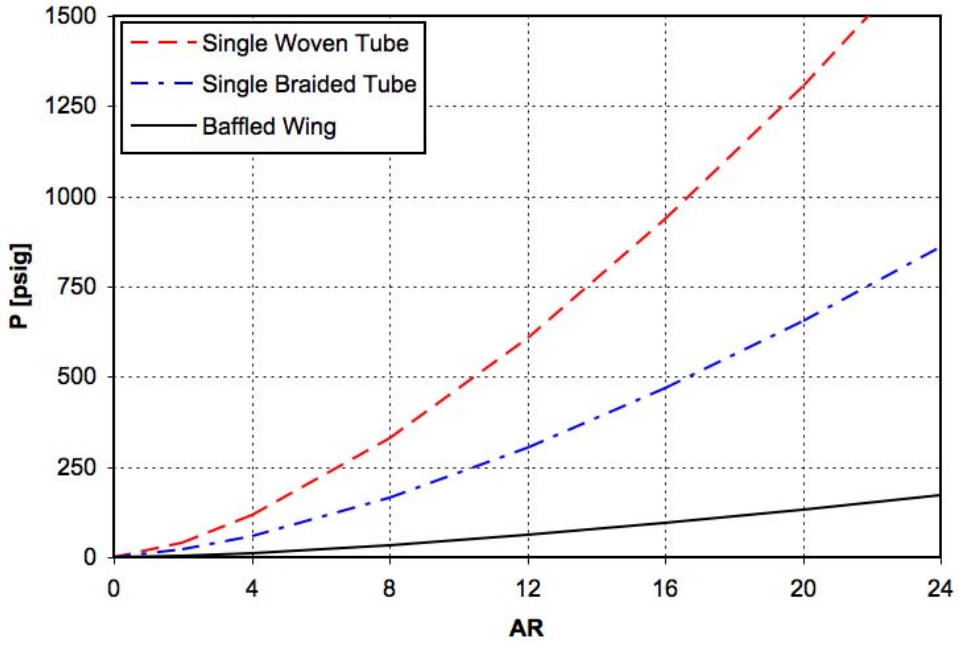

Figure 3.26: Required inflation pressure for aircraft with an AR= 16 [27].

3.3.1 Current Inflatable Wing Research

The latest non-rigidizable wing design is Nylon or MIAV, short for "Multi-Functional Inflatable Aerial Vehicle" as seen in Fig. 3.27*a*. [32] The nylon wing design is similar to the Vectran wing. The outer wing and internal baffles are both constructed from polyurethane coated rip-stop nylon, which is used to keep the internal volume pressurized. Unlike the

Vectran wing the wing does not have an outer fabric restraint. The wing is constructed in two variations, the first utilizes a single span which is attached to the UAV fuselage. The second is constructed in semi-span sections and attached to a UAV fuselage through the use of wing mounts. The tested wing profile is based around a NACA 4318 with a taper ratio of 1, an aspect ratio of 3.7 and a span of approximately 1.22 m (4 ft). Spans greater than 1.22 m are possible. The second nylon wings have a span of approximately 1.8 m (6 ft), a taper ratio is 0.65, and an aspect ratio of 5.4. The construction method is similar to those outlined above however, the urethane material is heat-sealed and not stitched as in the Vectran wings. Nylon wings have a design inflation pressure of 42.4 kPa (6 psi). Fig. 3.27*b*, shows the nylon wings on a flight test vehicle. The data outlined in this dissertation is obtained from the Vectran and nylon airfoils.

(a) Nylon Inflatable Wing.

(b) ILC Dovers multi-spar nylon inflated wing on flight test vehicle.

Figure 3.27: Nylon inflatable wing.

Chapter 4

RESEARCH EQUIPMENT AND TECHNIQUES

The following chapter introduces the experimental arrangements, research equipment and techniques used in this dissertation. Primarily, the research was conducted in the wind tunnel at the University of Kentucky, Mechanical Engineering department. The equipment and techniques discussed here are common techniques used in the Fluid Mechanics Laboratory and Dynamic Structures and Controls Laboratory.

4.1 Photogrammetry and Videogrammetry

Photogrammetry is defined by the American Society of Photogrammetry as "...the art, science, and technology of obtaining reliable information about physical objects and the environment through processes of recording, measuring, and interpreting photographic images and patterns of recorded radiant electromagnetic energy and phenomena"[92]

Photogrammetry and videogrammetry are techniques of measuring objects (2D or 3D) from photographic or videographic images. The most important feature is that the objects are measured without being touched. Photogrammetry can be divided into groups, dependent on lens settings. In far range photogrammetry the camera distance settings are set to infifity. In close range, aerial, and terrestrial photogrammetry the camera distance settings are set to finite values. Aerial and terrestrial photogrammetry are also called "remote sensing". However, this term is confined to working with aerial photographs and satellite images.

Measurements can be made using photogrammetry. Photogrammetry unobtrusively measures spatial parameters from photographs. Capturing numerous digital images from a variety of positions, and referencing the images to each other, produces accurate three-dimensional representation of the image subject. Common points are identified on each image. A line is then constructed from the camera location to the point on the object. The intersection of these lines (triangulation) determines the three-dimensional location of the point.

Videogrammetry is a measurement technology in which the three-dimensional coordinates of points on an object are determined by measurements made in two or more video images taken from different angles. Videogrammetry differs from photogrammetry due to

the fact that video images are used. Individual frames are extracted from the video sequence. The frames are then processed in the same manner as photogrammetry. The processed data can then be compiled to give the motion of the subject.

4.1.1 The Photogrammetric Process

The photogrammetric process can be separated into four steps: camera calibration, high contrast imaging, target marking and matching, and bundle adjustment. [93, 94, 95, 96, 28]

First the cameras are precisely calibrated in order to calculate the focal length, location of the principal point, radial lens distortion, and decentering lens distortion of each camera. This process allows the software package to compensate for any distortions in the image caused by imperfections of the camera. The calibration of the cameras removes the distortions, enabling accurate measurements.

The second step of the process is to obtain the high-contrast images of the desired subject matter. High contrast markers or targets are placed on the surface of the object. The targets are either brighter or darker than the object, allowing the targets to be clearly visible. The high contrast between the targets and the remainder of the image permits automatic and accurate detection of the target locations.

The third step is to load the images into the photogrammetry software (PhotoModeler Pro) along with the associated camera calibration files. The targets within the images are marked to sub-pixel accuracy using a centroiding process based on a least squares matching (LSM) algorithm with an elliptical template to account for off-normal viewing angles [95, 97]. The resulting points, correspond to the exact centers of the targets are matched across the photographs, as shown in Fig. 4.1.

Step four is a "bundle adjustment". This simultaneously iterates the camera locations and orientations from which the photographs were taken. The process also calculates the 3D point locations and corresponding precision values, a process called intersection. To obtain these point locations in three-dimensional space, a line is projected from each camera to the point, also shown in Fig. 4.1. Projected light rays are infinitesimally wide, so in general the rays from multiple cameras never intersect. However, they do establish the bounds of an intersection region. The intersection region in space is assumed to contain the true point location. This method of calculating point locations requires each target to appear and be marked in at least two images. Note that using more photographs in the photogrammetry process increases the redundancy, and hence, the accuracy. The closer the camera locations are to right angles with each other the more accurate the out-of-plane measurement will be.

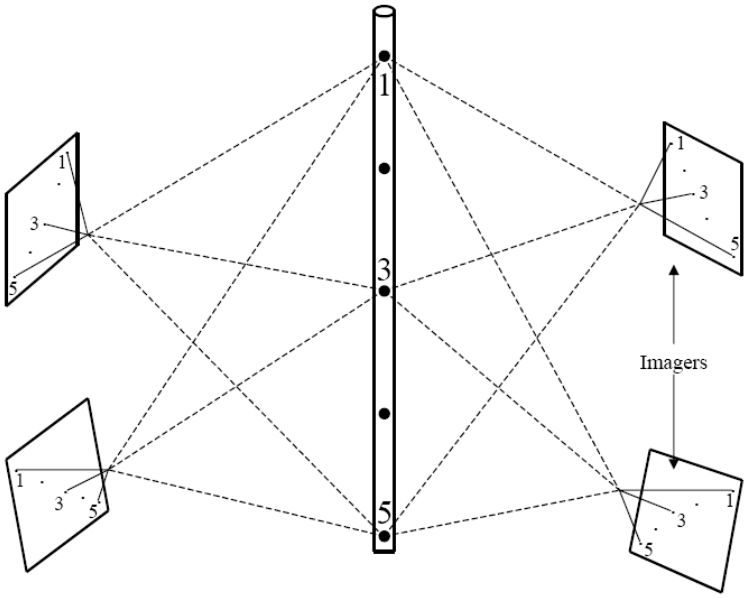

Figure 4.1: Photogrammetry process [28].

The final result of the photogrammetric process is a set of 3D points called a point cloud that, with an axis and scale defined, can be exported and measured [28].

4.1.2 Photogrammetry on the inflatable wings

In order to obtain photogrammetry results, high contrast markers were placed on the surface of the wing as seen in Fig.4.2*a*. Higher concentrations of markers were placed toward the wing tip than at the root, as greater movement was expected in these areas. The wing could then be deformed into a new shape, and the process repeated. Changes from the original shape to the new configuration were tracked, as well as hysteresis effects when the process was reversed. Wing surface maps were then generated and the deflection correlated with the applied force and the internal inflation pressure. Fig. 4.3, shows the photogrammetry of the inflatable wings in the wind tunnel. The markers were placed in lines from wing root to tip and from leading edge to trailing edge on the top surface of the wing. Spacing between markers was approximately 2.5 cm (1 in) and each marker was 0.6 cm (0.25 in) in diameter. In addition to the markers placed on the wing surface, reference markers were also placed in fixed positions. The reference markers were placed in two orthogonal directions at known distances.

The field of view of each captured image encompasses the reference markers. Two

options are available, either one camera used to capture numerous images of a stationary object, or multiple cameras triggered simultaneously for a moving object as seen in Fig. 4.2. Additional lighting was used when capturing the images, which ensured maximum contrast. Each image was captured in such a way as to encompass all markers and occupy the entire field of view of the camera. Camera calibration was conducted before the image capturing process to correct lens distortions. The calibration results were then used to adjust the captured images for these distortions. Two or more images were imported into PhotoModeler. The markers seen on the wing surface in the images were then marked using a sub-pixel marking function in PhotoModeler. Once all the markers were selected, a few were referenced between images. PhotoModeler automatically references all common points identified in each image. PhotoModeler processes the referenced data and creates 3D point data as seen in Fig.4.3$b-d$. This is done by constructing a line from the camera location to the point on the object. Triangulation of these lines determines the three-dimensional location of the points [28]. Four Olympus E-20N 5-Megapixel SLR digital cameras were used to capture the images for measurement. The error in using this technique is approximately 0.3 of a pixel, which corresponds to 0.07 mm (1 pix = 0.24 mm).

4.1.3 Videogrammetry

A stereo videogrammetry system was used to measure the instantaneous deflection of the wing. The videogrammetry system was comprised of two synchronized Pulnix (M-6710CL) one mega-pixel progressive line scan cameras. The cameras can capture images at 120 frames per second. The cameras were placed at a distance away from the wing and at an approximate 40° angle of separation between the respective optical axes of the cameras. For measurements made in the wind tunnel, the cameras were moved further away, and the wing and the angle of separation was increased to approximately 45°. The cameras have approximately 1000 × 1000 pixel resolution and can provided spatial resolution of 1:1000, or 1/1000 the size of the object being imaged. The cameras capture 400 images at 75Hz. The images are then fed into Photomodeler Pro for static and dynamic measurements.

4.2 Laser Displacement Sensors

A “Keyence” laser displacement sensor (LDS) capable of resolving displacements greater than 10 μm was used to accurately measure displacements. The sensor was either static, measuring the movement of an object in motion, or placed on a moving rack to measure a stationary object. Accompanying the sensor was a data acquisition system. The laser

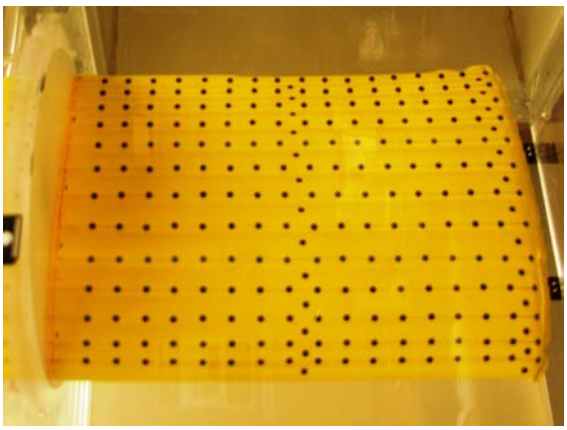

(a) Wing surface populated with markers.

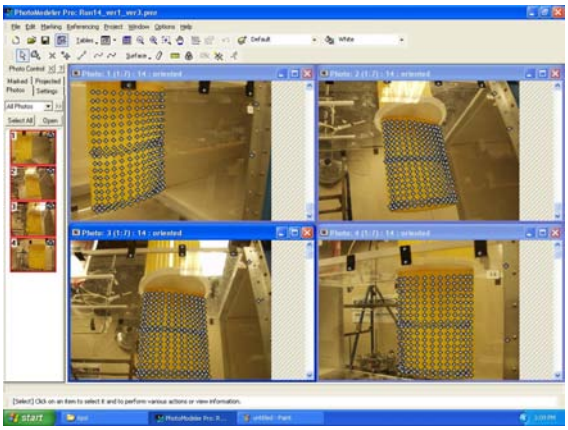

(b) Marked points in PhotoModeler.

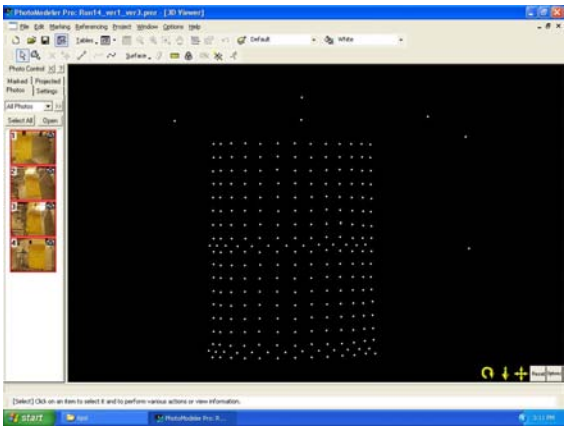

(c) 3D point data including reference markers.

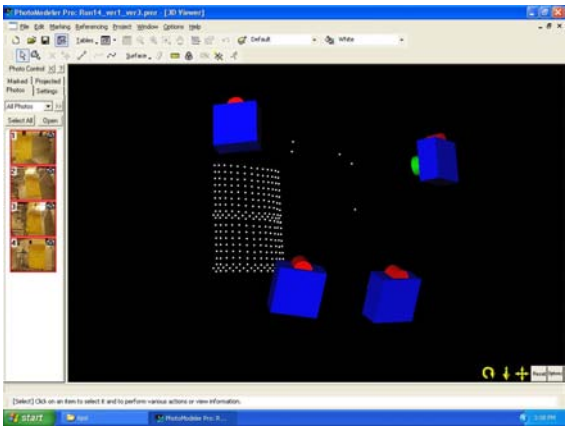

(d) Reconstructed image of the wing with camera locations.

Figure 4.2: Photogrammetry setup.

(a) Cameras set up on the outside of the wind tunnel.

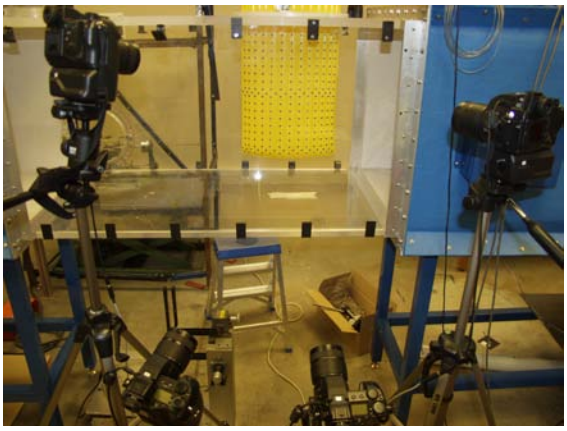

(b) Camera arrangement with nylon wing.

Figure 4.3: Photogrammetry.

displacement sensor consisted of a point laser emitter and a CCD camera that images the laser spot on the test article and triangulates its displacement.

4.3 Smoke-Wire Flow Visualization

The flow visualization technique carried out herein is described by Batill and Mueller [98]. A thin stainless steel wire (0.15 mm diameter) is placed upstream of the airfoil at the midspan. The wire is held taut to prevent the wire from coiling or moving in the flow. The wire is then coated with blue gage oil that has a specific gravity of 1.910. The oil beads due to the surface tension within the fluid. A voltage of 22 V is passed through the wire. The blue gage oil then burns into thin streak-lines which are visualized in the flow field. The test section is illuminated by a lamp to better visualize the streak-lines. The images are captured using a Sony XC-55BB camera and then stored as binary files. These binary files are then converted into viewable video format. Figures in Chapter 3.1.2 show the results of the smoke-wire visualization technique.

4.4 PIV – Particle Image Velocimetry

Particle Image Velocimetry (PIV) is an advanced, non-intrusive measurement technique used to obtain instantaneous velocity vector data from a given 2-D cross-section of a flow field. To acquire PIV measurement data, velocity vectors are derived from the flow. This is done by capturing two images of the flow field within a small period of time. The flow

field must be populated with small tracer particles that are carried by the flow, and these particles are tracked from one image to the other. The time between the images is known, and PIV algorithms compute the particle velocities.

4.4.1 PIV Procedure

Initially the tunnel flow is seeded with smoke particles on the order of 1 μ m in diameter, generated with a SAFEX F2010 Fog Generator. A 2-D light sheet is projected perpendicular to the flow in the tunnel. This is accomplished using a dual-head 50 mJ Nd:YAG laser from New Wave Research (Solo PIV III). The light sheet is aligned and adjusted using a series of 3 lenses. First, the beam emitted from the laser is focused using a converging lens. The second lens is a diverging lens, placed at the focal length of the first lens, and serves to create a thinner and more concentrated beam. The third lens is cylindrical, and it spreads the beam into a 2-D sheet with a thickness of approximately 2 mm. The laser is pulsed in sync with a Kodak Megaplus ES 1.0 CCD camera, which has 1008×1018 pixels. A timing control unit from Taitech allows time between a pair of pulses to be varied from 1 μs to 1 ms. The camera is placed downstream of the airfoil in the flow. A schematic illustrating the PIV layout is shown in Fig. 4.4.

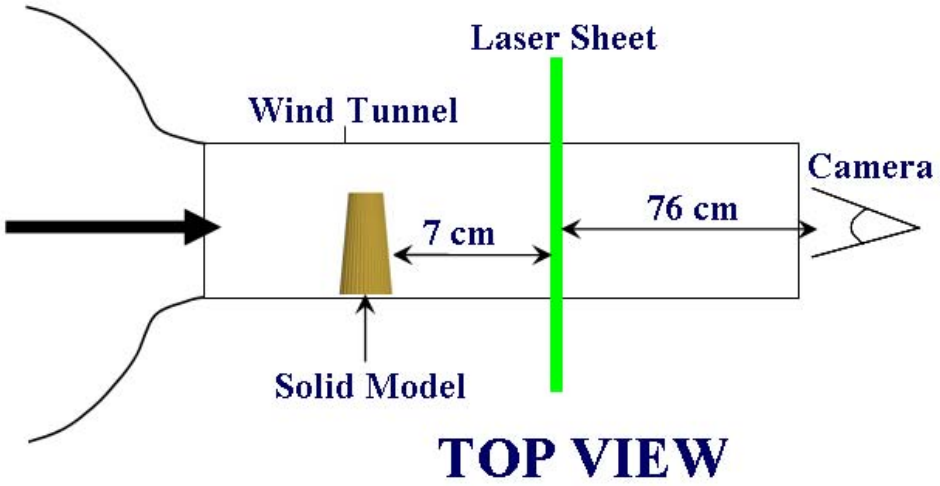

Figure 4.4: Schematic of PIV layout.

The Epix frame grabbing hardware and software is used to acquire binary image pairs for processing. For each run, 124 images are captured with the computer software XCAP. Within XCAP, camera timing is correlated with the laser pulsing, and imaging issues such as

image clarity and focus, particle seeding, and laser intensity can be addressed and corrected.

To ensure good results, particle density is correlated with laser intensity. This is because the smoke particles in the flow will reflect light based on the smoke density in the flow. Limitations also exist when dealing with different flow speeds. Here the timing between the laser pulses and image captures must be adjusted. The pulse and capture times must coincide so as not to capture any residual light from a previous laser pulse. In higher speed flows, the particles will travel a greater distance in a given amount of time. This means that the particles will travel a greater distance between the image pairs. In general, it is accepted that the particle should only travel one-third of the window size for the best results from the PIV algorithm. Therefore, the pulse timing must also be adjusted according to the particle travel speed.

4.5 Wind Tunnels

4.5.1 Large Wind Tunnel

The large wind tunnel is an Eiffel type wind tunnel in the Fluid Mechanics Lab at the University of Kentucky. This open-circuit wind tunnel is driven by an axial fan with a 30 kW (40 hp) motor located at the tunnel exit (Figure 4.5). The upstream section of the tunnel has an inlet with an aluminum honeycomb and high porosity screens to reduce the free-stream turbulence level to less than 0.25%.

The speed range of this tunnel is approximately 3.0 m/s (10 ft/s) to 60 m/s (180 ft/s) with velocity variations less than $\pm 1\%$ from the free-stream velocity. During operation, air goes into the inlet, through the screens, and accelerates in the nozzle. Air flow then reaches the test section, as seen in Fig. 4.6. The test section consists of a 0.6 m (24 in) by 0.6 m (24 in) cross section with a length of 1.2 m (48 in). The diffuser behind the test section slows down the flow as it approaches the axial fan and the acoustic diffuser before exiting.

4.5.2 Small Wind Tunnel

The small tunnel is a Low-Speed Wind Tunnel in the Fluid Mechanics Lab at the University of Kentucky. The tunnel is a low-turbulence, open-circuit, blow-down wind tunnel with a 7.5 hp motor driving a radial fan at the inlet. Upstream of the nozzle, a vibration damper, flow straightener and turbulence damping screens condition the flow. The inlet has a cross-sectional area of 0.08 m^2, while the outlet has a cross-sectional area of 0.064 m^2, producing an inlet area to outlet area ratio of 1.25. The nozzle has a contraction ratio of 6.7, and the test section has a cross-section of 0.2 m $\times$ 0.4 m. The test section is

(a) Front view.

(b) Rear view.

Figure 4.5: Low-turbulence wind tunnel at the University of Kentucky.

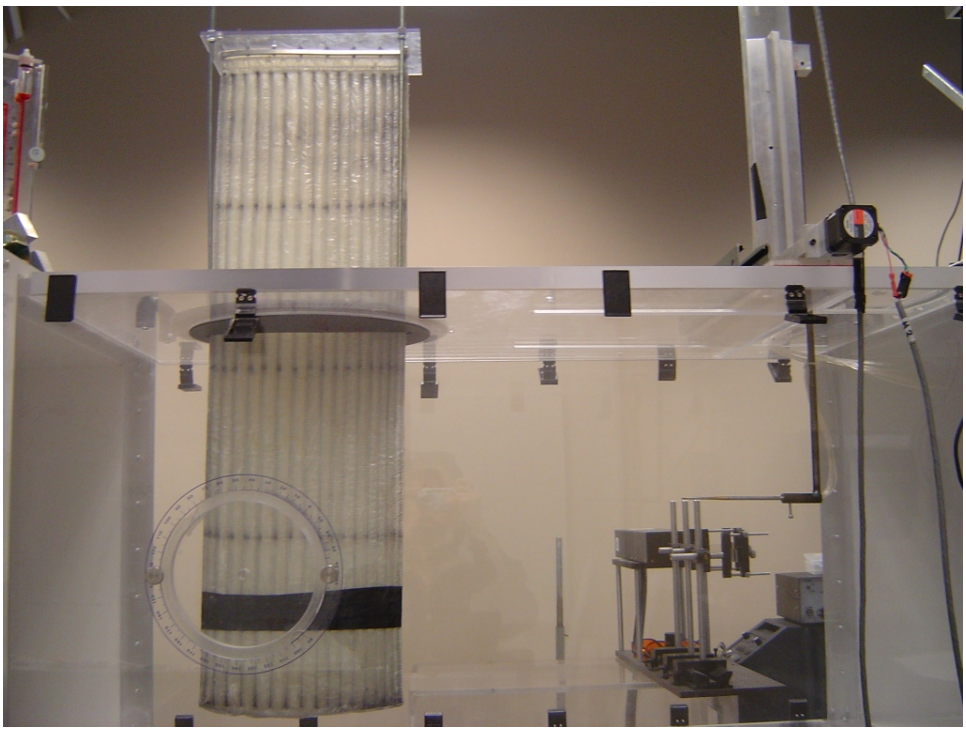

Figure 4.6: Tunnel test section.

constructed from 1/4 in thick clear polycarbonate, with movable exit walls that allow for variations in the exit angle from 80° to 100°. The maximum velocity in the test section is 35 m/s. The nominal free-stream turbulence intensity is measured with a hot-wire anemometer to be $\approx 0.6\%$.

4.6 Seven-Hole Pressure Probe

A seven hole probe manufactured by Aeroprobe Inc. was used to quantify the time-averaged pressures in the wake of the airfoil. The data acquisition system consists of a seven-hole probe, an ESP 8 port multi-channel pressure scanner, a two-axis traverse with stepper motors, a multi-axis stepping motor controller, a CIO-DAS08 Analog/Digital data acquisition board, and a ESPIO signal conditioner. The data acquisition board was connected to the motor controller to regulate the speed and distance of the pressure probe.

The seven-hole probe system is capable of automatically measuring all three-components (u, v, w) of velocity and the static and stagnation pressures on a pre-defined user grid. The measurement plane was normal to the free-stream direction and located at midspan (Figure 4.7). The probe was positioned at a distance of 33%c from the trailing edge of the airfoil. The computer controlled traverse was used to move the probe in the vertical direction and acquire data for a total of 100 grid points, distributed evenly across a total distance which included 100mm above and 150mm below the upper surface of the airfoil respectively. The tests were conducted for Re_c values from 150,000 to 500,000, and for an α range from -4° to 12° with 2° increments.

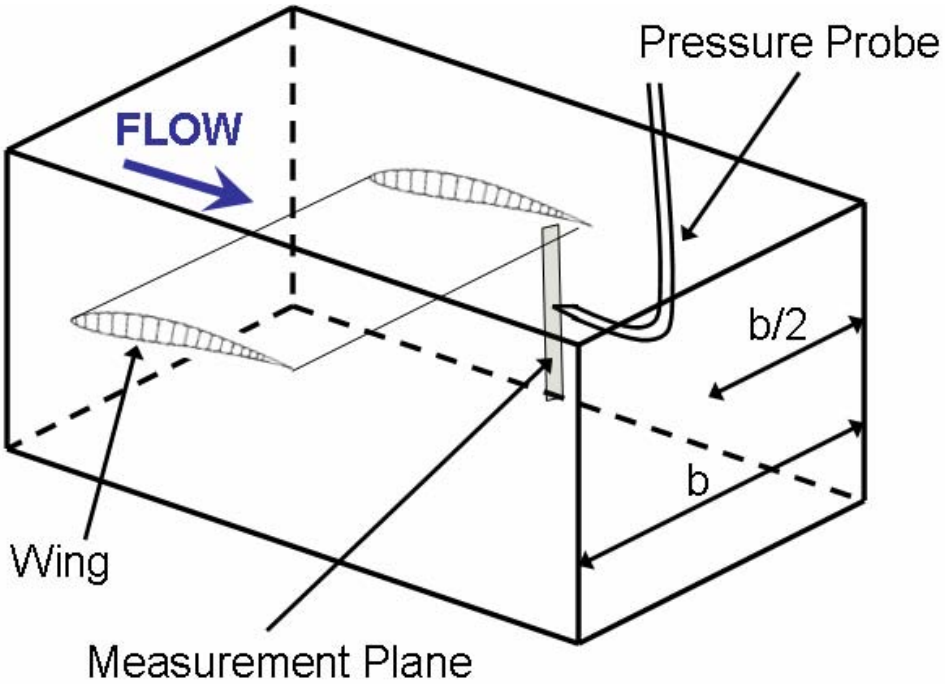

Figure 4.7: Schematic of wake survey set-up.

Chapter 5

AEROELASTIC EFFECTS AND WING WARPING

Inflatable wing research shifted from inflatable-rigidizable wing development to inflatable wing development. This shift occurred due to the potential of inflatable wings for inflation and deflation, and the potential for manipulation in flight to affect the performance of the vehicle. The wings examined henceforth are inflatable, thus they do not contain solid structural members and rely solely on inflation pressure for rigidity. Research focused on aeroelastic concerns and the possibility of warping the wings. Inflatable wings do not contain ailerons; vehicles employing inflatable wings must generate roll moments either through the empennage or by manipulating the shape of the inflatable wings. Aircraft using inflatable wings in the past relied exclusively on the empannage for control. However, it was possible because the shape of inflatable wings can be manipulated by applying external forces to the wing surface. This method was examined by lifting-line analysis that reveled the potential benefits of wing warping. The lifting-line analysis is detailed in Chapter 6.2.1. Initial research efforts focused on warping inflatable non-rigidizable wings to provide roll control. Research initially focused on determining the forces required to manipulate the wings through a series of simple experiments. This data could then be used to determine methods for warping the inflatable wings. Three different wing warping techniques are ultimately examined: a tensile force on the surface of the wing from the wing root to the wingtip; a chord-wise tensile force between the leading and trailing edges; and a mechanical force applied to the trailing edge.

5.1 Wing Deformation

Due to the design of the inflatable wings, wing stiffness varies as a function of inflation pressure. To examine wing deformation, static and dynamic load tests were conducted. The static deflection was tested in three groups; point loading at the wingtip, distributed wing loading in different patterns, and torsional loading. In addition the wings were deformed dynamically using “nitinol” (a shape memory alloy) and mechanical devices.

5.1.1 Point Loading

Fig. 5.1 shows the deflection of the Vectran inflatable wing with a point load at the wingtip. The point load was applied at the thickest portion of the wing (approximately the 1/4 chord), where the wing has the greatest resistance to bending. Force transducers were used to measure the applied force and the LDS system was used to measure the deflection. Five point loads were applied (10, 20, 30, 40, and 50 N), at seven different inflation pressures ranging from approximately 34 – 138 kPa (5, 7.5, 10, 12.5, 15, 17.5, and 20 psi). The wingtip deflection was measured by the LDS at the 1/4 chord. At the most extreme loading case (50 N) and the lowest inflation pressure (5 psi), the maximum tip deflection was less than 3% of the span.

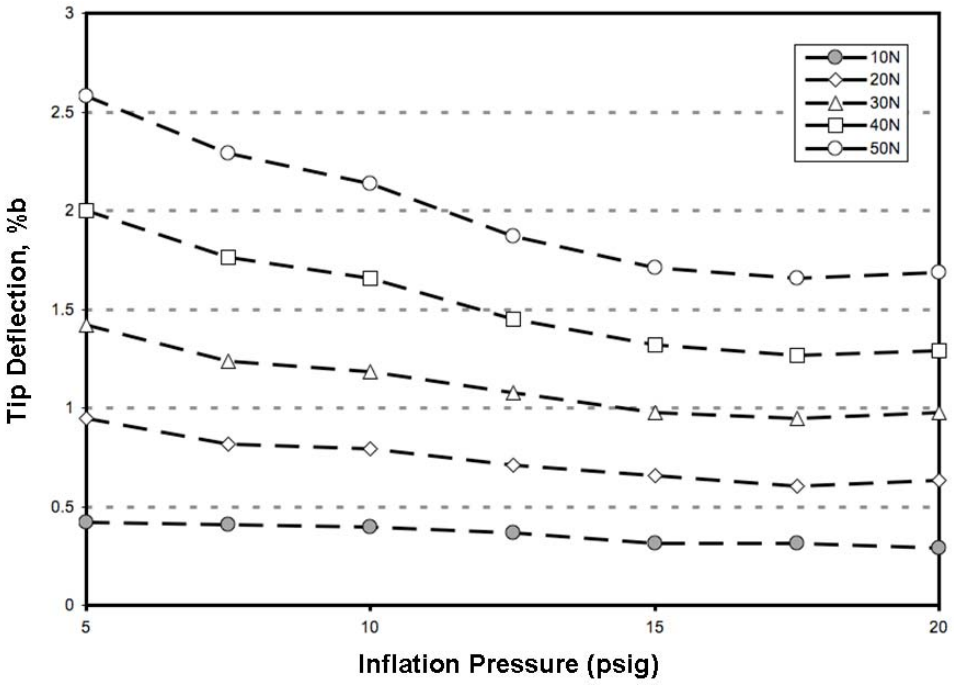

Figure 5.1: Tip deflections from point loading at various inflation pressures on the Vectran wing.

5.1.2 Distributed Loading

For the distributed loading tip deflection measurements, the Vectran wing was set-up in a test stand upside down. Weight was applied on the surface in three different loading patterns and at four different internal pressures ranging from 69 – 172 kPa (10, 15, 20, and

25 psi). The first loading pattern (Case 1) held 4.5 kg (10 lbs) of weight situated 0.23 m (9.15 in) from the wing root and 2.3 kg (5 lbs) situated 0.45 m (17.88 in) from the wing root. The second loading case (Case 2) held 4.5 kg (10 lbs) at 0.23 m (9.15 in) from the wing root and 2.3 kg (5 lbs) at 0.7 m (27.4 in) from the wing root. The final loading case (Case 3) held 2.3 kg (5 lbs) at 0.23 m (9.15 in) and 1 kg (2.2 lbs) of loading at 0.7 m (27.4 in). The loading configurations simulated flight loads under approximately 1, 2, and 2.5 G conditions. While the magnitude of the deflections change depending upon the loading conditions, the qualitative behavior is the same as can be seen in Fig. 5.2. Response appears to be monotonically decreasing with increasing inflation pressure. Even in the most extreme case at the highest loading and the lowest inflation pressure, the maximum tip deflection was less than 2% of the span. These results can be seen in Simpson *et al.* [67].

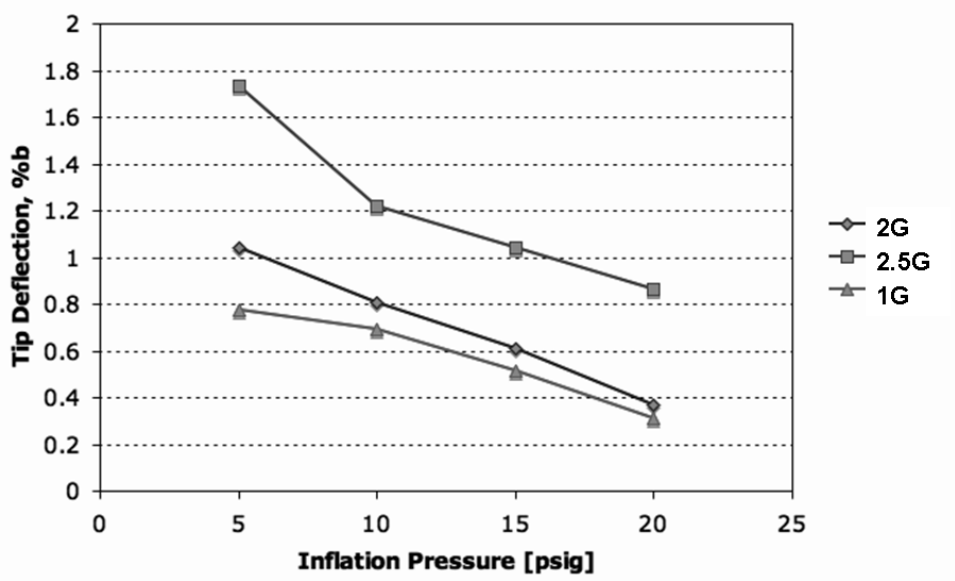

Figure 5.2: Tip deflections for distributed loading on the Vectran wing.

5.1.3 Torsional Loading

The wing was set up in a test stand and was mechanically manipulated by applying a tensile force to the surface of the Vectran wing. Vectran fabric (the same material as the wing) was bonded to the surface of the wing on the top leading edge and the bottom trailing edge of the wing. Both pieces were modified to be attachment points for the tensile members. A thin wire was then attached and drawn taut to the opposite side of the wing at the wing base. The attachment point for the top surface wingtip was 8 in above and

Table 5.1: Wing tip twist of the Vectran wings.

Inflation Pressure	Loading	Wing Tip Twist
kPa [psi]	N	°
69 [10]	50	17°
103 [15]	50	10°
138 [20]	50	5°
172 [25]	50	2.5°

1 in behind the trailing edge of the wing. This made an angle of approximately 15° from horizontal. The attachment point for the bottom surface wingtip was 8.5 in below and 3 in ahead of the leading edge of the wing base. This made an angle of approximately -20° from horizontal. The goal was to induce torsion in the wing from tip to root. Force transducers were connected linearly along the length of wire between these points. The transducers were connected to a DAQ that enabled real-time force measurement. The force transducers were connected to an adjustable tensioning mechanism, which could be used to adjust the force exerted.

Four inflation pressures were examined: 69, 103, 138, 172 kPa (10, 15, 20, 25 psi). At each inflation pressure, five different forces (10, 20, 30, 40, and 50 N) were applied to the wing on both the top and bottom surfaces of the wing in conjunction with each other. The deformations were then measured via photogrammetry. Individual applied forces or combinations of applied forces were not examined. From measurements of typical twist deformations, seen in Fig.5.3*a*, span-wise load distributions for baseline, maximum and minimum cases were generated and then placed into a lifting line code, discussed in detail later. Fig. 5.3*b* shows the effect of torsional loading on the span of the Vectran wing. Here both the undeformed wing and the torsionally loaded wing are shown. Three dimensional (3D) models were made of the deformed wing. These models were produced on a 3-D printer from photogrammetry data of the deformed wing. These models were used in tunnel PIV performance analysis of the deformed wing shape. This analysis can be seen in Chapter 6.1.2. Table 5.1 details the maximum amount of twist generated at each inflation pressure at the wingtip.

5.1.4 Dynamic Deformation – Nitinol

Dynamic deformation testing has taken two primary forms, smart materials and mechanical actuation. Piezoelectric materials (PZTs) have been used to alter camber and

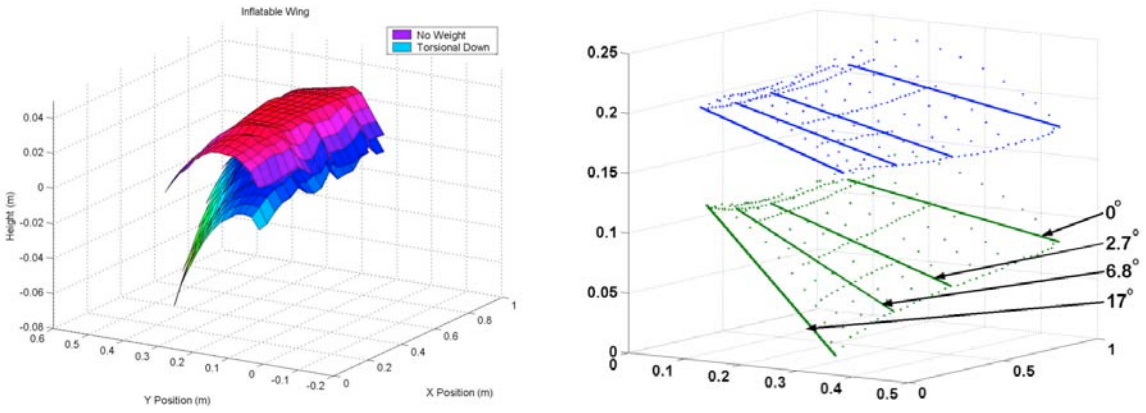

(a) Surface plot.

(b) span-wise angle of attack variation.

Figure 5.3: Vectran Wing torsional loading – undeformed (upper) and deformed wing (lower).

deform leading and trailing edges. Rapid and controlled actuation of the material makes these materials desirable. However, the substantial equipment requirements for operation of these materials hampers flight testing. The smart material used in this project was "Nitinol".

Nitinol is an acronym for "*Ni*ckel *Ti*tanium *N*aval *O*rdnance *L*aboratory", where the alloys properties were discovered. Nitinol is an alloy containing nearly equal numbers of nickel and titanium atoms, leading to its common compositional representation as $NiTi$. The relative amounts of Ni and Ti can be varied by a few percent in order to control the temperature of the phase change responsible for its "smart" behavior. A more accurate representation of its composition is $\mathrm{Ni}_x\mathrm{Ti}_{1-x}$ where x represents the percentage of Ni in the alloy. The property that makes this material unique is the fact that the material changes shape when heated. Nitinol used in this project is in the form of wire. The wire contracts, shortening in length when heated. The degree to which the material shortens depends on the diameter of the wire used and the temperature to which the material is subjected. Nitinol offered a wide range of shapes and actuation mechanisms.

The Vectran wing was warped in laboratory tests using nitinol actuators. Here, the wing was placed in the test stand and the nitinol attached to the wingtip trailing edge and fuselage near the root. As shown in Fig.5.4 the wing experienced substantial deformation under actuation. Note that under this configuration, the trailing edge is deflected downward while the leading edge remains in the same location. When measured from leading to trailing edge at the wingtip, the twist comprises an effective increase in α of 3°. If the deflection is

measured from the first deformation point (approximately 0.75c), the effective flap deflection is approximately 16°.

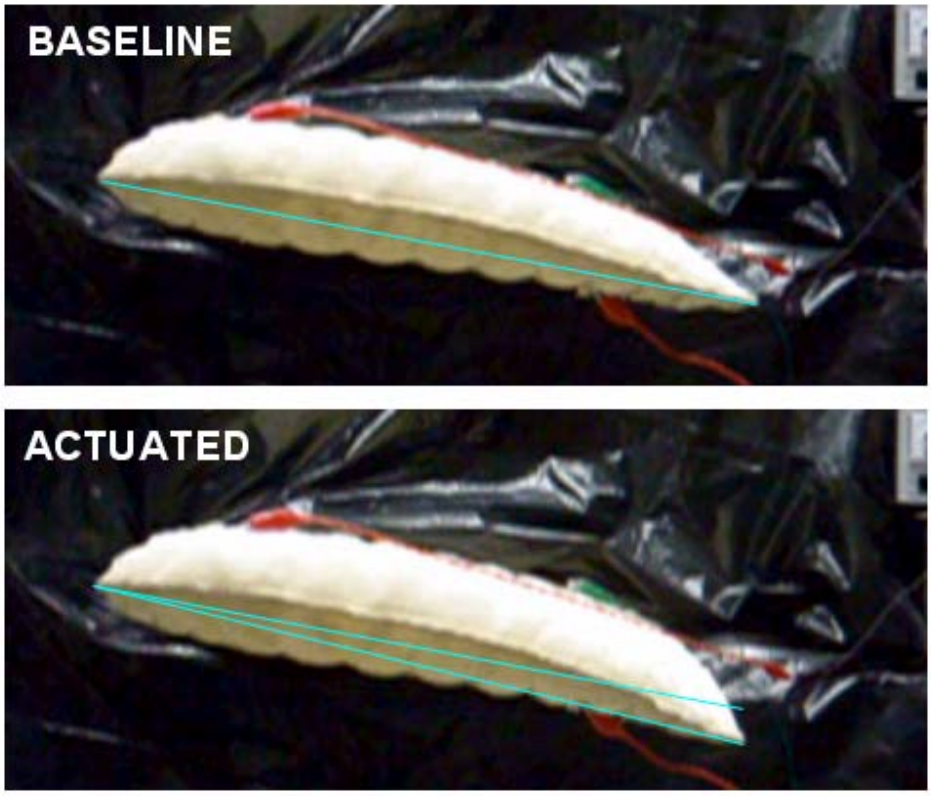

Figure 5.4: Wing warping using nitinol actuator.

5.1.5 Dynamic Deformation – Mechanical devices

Mechanical actuators were applied to the Vectran wings during laboratory testing. High torque servos (Hitec HSC-5998TG) mounted beneath the wing root were connected to the wing at the wingtip as outlined for the nitinol tests. The servos delivered 14.4 kg.cm (200 oz.in) of torque at 4.8 V and were actuated using a typical R/C controller. As the actuation was dynamic, photogrammetry could not be employed to monitor the shape change of the wings. Rather, videogrammetry was used to capture the dynamic shape changes to the surface of the wing.

The twist in the wings was not linear; higher α deflections were measured toward the wingtip. Note that one semi-span produces nominal lift while the other semi-span produces increased lift, and only one semi-span was warped at a time in the positive (increasing α)

direction. Substantial roll control is available with inflation pressures at or lower than 138 kPa (20 psi). Above this value, roll control droped significantly. While still non-negligible, adequate roll control may not be available for gust response and rapid maneuvering. Section 5.3.1 deals with this mechanism in greater detail.

5.2 Inflatable Wing Warping

As shown in Section 5.1 the Vectran wings could be manipulated through forces on the wing surface. The Vectran and nylon wings were constructed in a similar manner and thus display similar behavior when warped. The Vectran wings had a higher inflation pressure than the nylon wings and thus were stiffer. Warping mechanisms used on the Vectran wings would thus be more effective on the nylon wings.

As the goal was to warp the wings in order to control the vehicle, the method of wing warping investigated was focused on manipulating the camber for flight control. Research focused on wing warping through embedded devices mounted on the wing's surface. The surface-mounted actuators altered the camber of the wing gradually over most of the chord length as opposed to attached trailing edge devices that deflected the trailing edge only. The method aimed to alter the lift distribution over the wings as seen in Fig. 5.5. Here the red line represents the lift distribution during straight and level flight. The aim was to create the lift distribution of the black line. The difference in the area below the lines on each side of the vehicle is what generates roll. As noted in Section 2.5.2 this was done using ailerons.

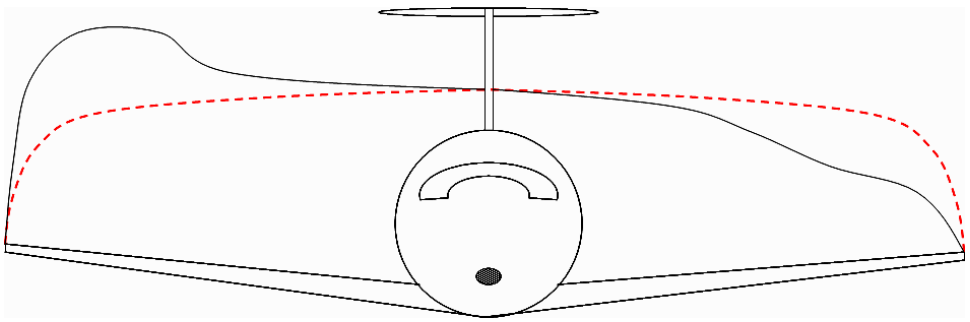

Figure 5.5: Lift distribution over the wings.

Due to the unique wing design, inflatable wings allow simple wing shape warping. Inflatable structures rely on inflation pressure for tension in the walls of the structure, maintenance of shape, and structural load carrying capability. The external application

of devices that unload tension in the fibers of the inflatable wings facilitate this motion, and through properly balancing loads, shape morphing is possible while maintaining wing integrity[32].

Several actuation methods were studied by Cadogan *et al.* [29]. Performance requirements included roll rate response, frequency response, ability to be folded and packed, low mass, low power consumption, and high cycle life. Actuator types originally considered included piezoelectric actuators, electro-active polymers, pneumatic chambers, and nastic cells. Three warping concepts detailed by Cadogan *et al.* [29] are reviewed below.

5.2.1 Initial Warping Strategies

Nastic Structures

Nastic structures are devices that form an active part of the structure of the design and are capable of generating large strains when activated. Conceptually, nastic structuring involves the design of a series of parallel tubes built into the surface of the wing profile. Fluids of varying pressure can be pumped within these tubes. As the fluids are pumped into the cells, the tubes transition from a flat to a circular cross section. This reduces the cells length and provides a tensile force on the surface of the wing. However, tensile force is limited by the angle of the cell wall. As the tube inflates the angle of the cell wall increases to perpendicular and the tube's shape approaches a circular cross section. This causes a reduction in the resultant force that can be transmitted [29]. This can be seen in Fig. 5.6.

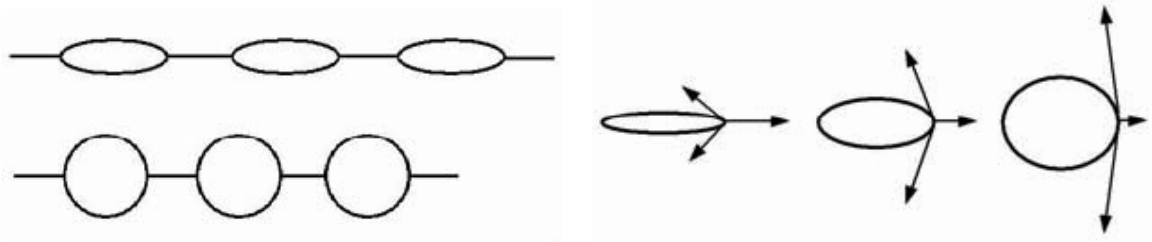

(a) Foreshortening.

(b) Force Limitation.

Figure 5.6: Nastic concepts [29].

A nastic structure can be applied to wing warping an inflatable wing. A series of cylindrical inflatable tubes can be oriented span-wise along the surface of the wing on both the upper and lower surfaces. The inflatable tubes can be isolated pneumatically from the inflation volume of the wing. By independently varying the pressure within the tubes in

the upper and lower surface, the airfoil trailing edge can be made to constrict and bend in the direction of the inflated cells, as seen in Fig.5.7.

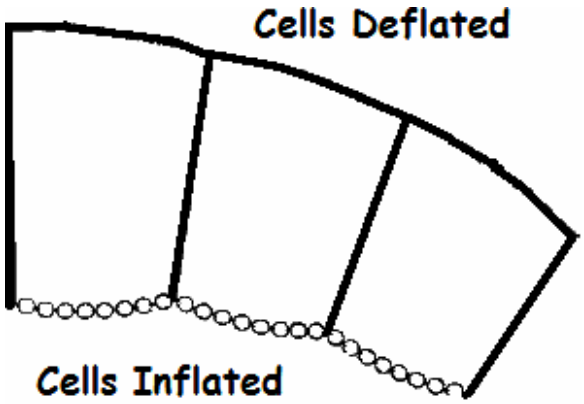

Figure 5.7: Nastic morphing concept [29].

The force requirements for this method of actuation are based on the skin stress that is linearly proportional to wing inflation pressure. Cadogan *et al.* [29] indicates that suitably sized nastic tubes palced on the wing surface would have difficulty generating the tensile force necessary to overcome skin stress caused by wing inflation pressure. Additionally, not enough displacement would be available due to the small number of tubes that could be placed on a wing. Further, calculations indicated slow reaction times, and the design would require substantial support hardware.

Bump Flattening

This technique uses actuators applied to the wing surface that flatten individual bumps on the inflatable wing. A piezoelectric actuator is attached to a rigid substrate, and then bonded to the wing restraint fabric surface. When the actuator is energized, a force is generated perpendicular to the plane of the actuator, resulting in a flattening of the individual bumps caused by the wing spar spacing. By flattening individual bumps, a net increase in length is generated, resulting in deflection of the trailing edge, as seen in Fig.5.8. Fig.5.9 shows the Vectran inflatable wing with the "bump flattening" mechanism. In this case the piezoelectric actuators are attached to the surface of the wings.

Unfortunately, it was found that the actuator could not develop the necessary force required to flatten the bump. Additionally, the mechanism was limited by actuator availability and packing volume.

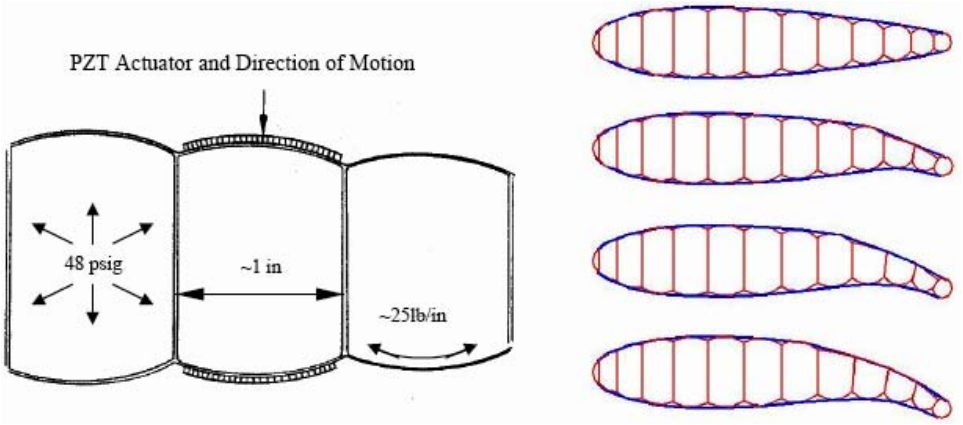

Figure 5.8: Bump flattening concept [29].

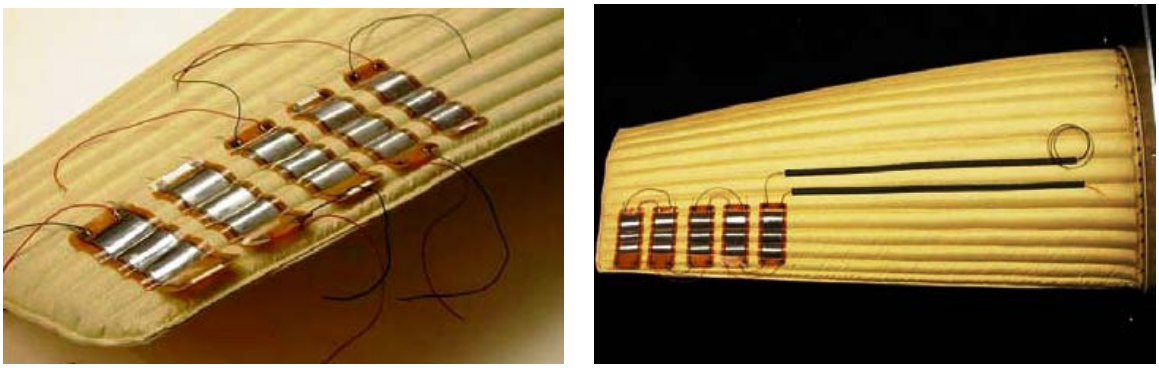

(a) Piezoelectric actuators on Vectran wing.

(b) Actuator placement.

Figure 5.9: Bump flattening prototype [29].

Trailing Edge Deflection

This approach adds an additional length to the wing section, which is manipulated. The technique modifies a baseline inflatable wing configuration with PZT actuators that flex the trailing edge of the wing. The actuators form a seamless connection to the inflatable wings and thus present an uninterrupted surface to the air stream. The actuators were considered in both unimorph and bimorph configurations. In the bimorph configuration, two MFC actuators from Smart Material were bonded to a metallic substrate. The actuators expanded or contracted in response to the application of a positive or negative voltage. By applying opposite polarity voltages to the upper and lower actuator, the substrate flexed as seen in Fig.5.10.

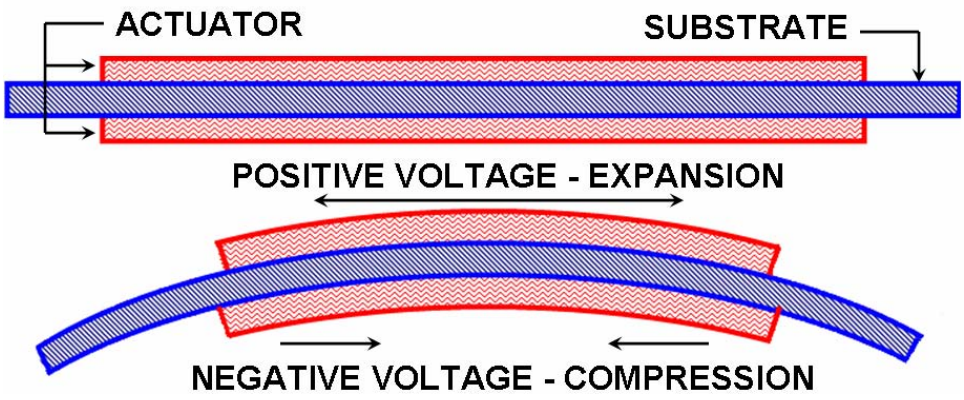

Figure 5.10: Trailing edge actuator concept of operations [29].

The PZT actuators were attached to the upper surface of the wing, extending rearward and terminating at the nominal trailing edge location as seen in Fig.5.11. The actuators were arranged with span-wise gaps to facilitate folding and packing of the wing. Upon application of a voltage, the actuators curve upward or downward, depending on the polarity of voltage applied. When the voltage was removed, the actuator returned to its nominal un-deflected position. An elastic fabric could be stretched from the trailing edge of the upper wing surface to the trailing edge of the lower wing surface to enclose the actuators. This would have provided a sharp trailing edge to the wing.

The trailing edge plates that deform assist in creating a sharp trailing edge and enable a variety of actuator options, but may be more susceptible to deployment damage. Additionally, power supply and control hardware are cumbersome to implement on a UAV.

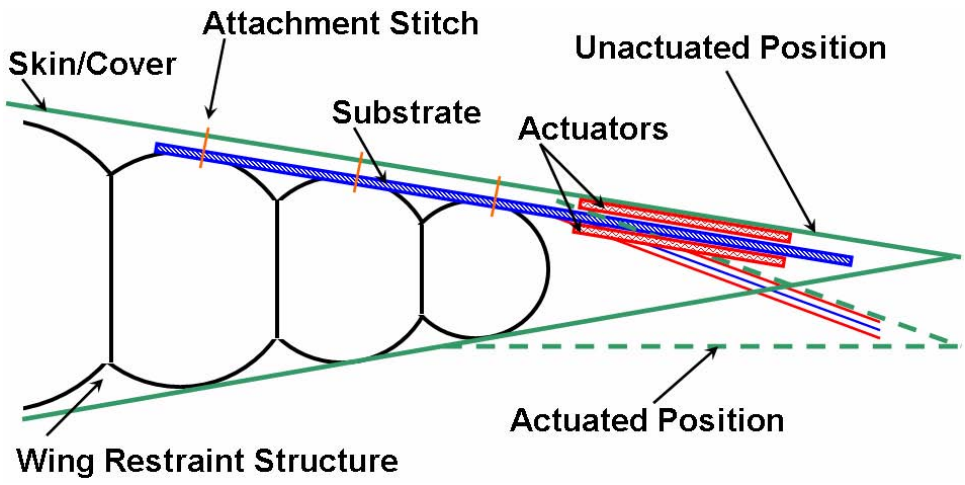

Figure 5.11: Trailing edge actuator concept of operations [29].

5.3 Current Inflatable Warping Strategies

Experimental efforts have been focused on actively deforming the nylon inflatable wings to provide roll control through wing warping. As the wings are entirely inflatable, they do not include traditional ailerons. Thus, vehicles employing inflatable wings must generate a roll moment by other means. However, as the wings are non-rigid, it is possible to actively manipulate the shape of the wings to provide this roll moment.

Inflatable wing warping has taken two primary forms: smart materials and mechanical actuation. Smart materials such as piezoelectric's (PZT) and shape memory alloys offer a range of potential benefits e.g., see Kudva *et al.* [99, 100] Piezoelectric materials have been used to alter camber and deform leading and trailing edges. Shape memory alloys offer many alternatives as a wide range of shapes and actuation mechanisms exist. Both the Vectran and nylon wings have been warped in the laboratory using nitinol actuators. The goal has been to alter camber and deform leading and trailing edges. However, the operational equipment required for operation of these strategies has hampered flight testing. Mechanical actuators such as servo motors and other devices offer reliability and simple operation, though hindered compact stowage.

This warping technique focuses on manipulation of the camberline as seen in Fig. 5.12 and is accomplished through two different techniques. The first technique involves manipulation of the camber by mechanical actuators (servos) adhered to the surface of the airfoil. The second uses nitinol (a common shape memory alloy) to achieve the camberline change.

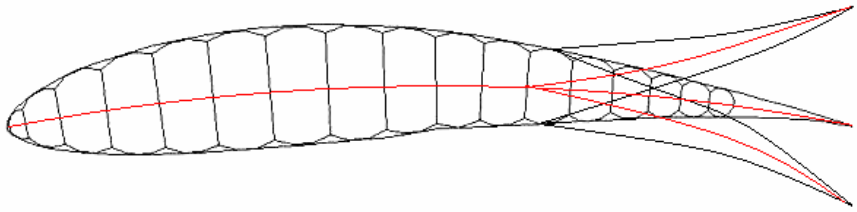

Figure 5.12: Warping inflatable wing through camber variation.

By manipulating the camber of the wing, the wing shape can be altered between each semi- span. Asymmetric shape changes generate differential lift between the two semi-spans while de- forming the semi-spans symmetrically. This provided an altered lift distribution that could be optimized for maximum L/D. The differential loading scenario could potentially be used to generate the required roll moments for the aircraft.

5.3.1 Mechanical Mechanisms

Mechanical actuators have been applied to the Vectran and nylon inflatable wings. Two mechanical warping systems have been developed and flight-tested. Both mechanisms utilized typical high torque remote control (R/C) servos.

Pulley Mechanism

This approach used control lines attached to the wingtip trailing edge to warp the wing. The control line applied a tensile force to the wing causing the wing to bend. The tensile force pulled the wingtip down and toward the wing-root leading edge. The deformation was primarily to the wingtip and caused an increase in camber and angle of attack at the wingtip. The effect of this mechanism was limited to the wingtip and did not cause the wing to buckle. A typical R/C servo delivering 14.4 kg/cm (200 oz.in) of torque at 4.8 V warped the wings using a typical R/C controller. The mechanism was a pulley system attached to the fuselage of the vehicle, as seen in Fig.5.13.

The servo was mounted on the tail boom located under the trailing edge of the wing on the fuselage centerline. Nylon lines were run from the servo control horn, forward through the pulley, and then to the attachment points on the pressure surface of the wing at the

wingtip. As the servo arm rotated, the control line applied a tensile force to the wingtip causing it to warp. Note that one semi-span was warped down as the line tightened, while the other side slacked. Thus, in this configuration, only one semi-span was warped at a time, and the warped semi-span produced higher than normal lift compared to the the non-warped semi-span. The differential lift between the wing semi spans provided the roll control of the vehicle.

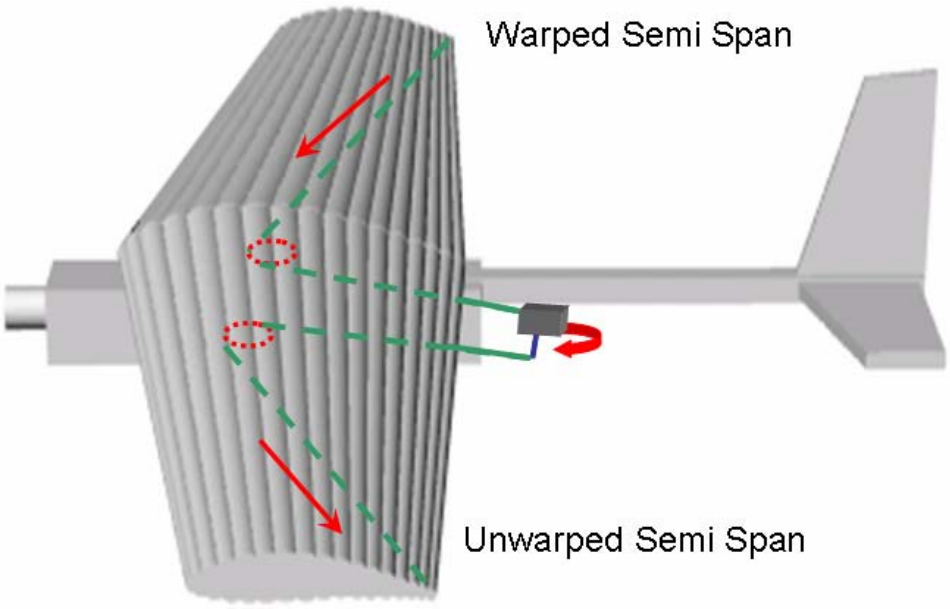

Figure 5.13: Pulley warping mechanism.

Note that the left hand semi-span produced nominal lift while the right hand semi-span pro- deuced increased lift as only one semi-span was warped at a time in the positive (increasing α) direction. Fig.5.14 shows the effect of the mechanism on the angle of attack of the wing. Stiffness is affected by inflational pressure, as can be seen in Fig.5.14. Substantial deformation is seen at the lowest inflation pressure of 69 kPa (10 psi The mechanism was capable of warping the wing at all the inflational pressures examined.

Servo Mechanism

Warping was accomplished through the use of servos delivering 14.4 kg.cm (200 oz.in) at 4.8 V or 14.4 kg.cm (250 oz.in) at 6V of torque. The servos and control horns were attached to plexiglass plates, which were then adhered to the pressure surface of the wing. Two servo arrangements were used. The first consisted of a single servo attached at the

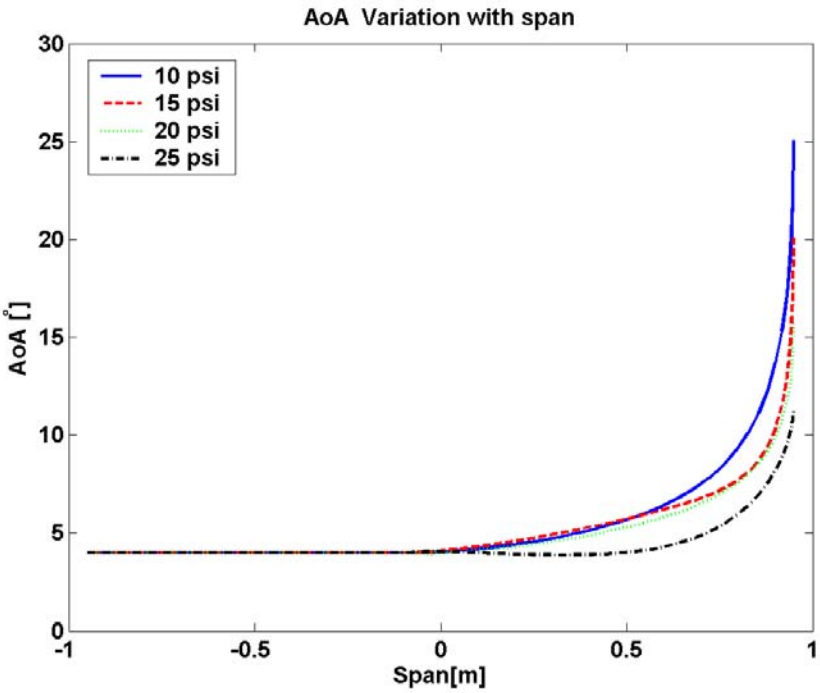

Figure 5.14: Angle of attack variation over the span.

wingtip, and the second introduced an additional servo to the midpoint of the semi-span. For each servo, two plexiglass plates were attached to the wing surface. The first was attached at the 1/4 chord, and the second to the trailing edge. The servo and control horn were then mounted to the plexiglass plates. Fig. 5.15 shows a schematic of the servo arrangement for tunnel testing of the nylon inflatable wing.

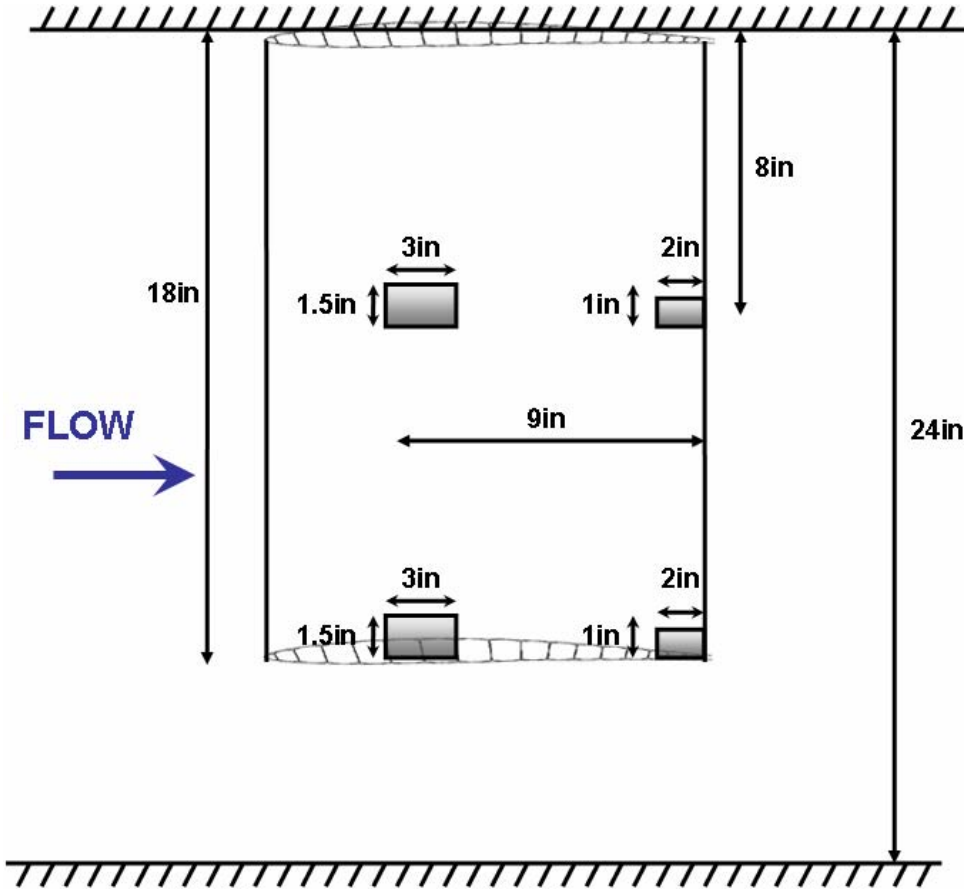

Figure 5.15: Servo arrangement on pressure surface of the nylon wing.

Fig. 5.16 shows the deformation of the upper surface wingtip of the nylon wing due to manipulation by the servos. The neutral or undeformed upper surface is shown along with the deformation of the trailing edge when the servo is actuated up and down. The sub-plot shows the error bars for this data. (It should be noted that these error bars apply to all the photogrammetry data in this research.) Substantial deformation is obtained at the trailing edge comparable to conventional (hard mounted) trailing edge flaps.

As the servo was actuated it caused the wing to bend chord-wise along one or more of the longitudinal baffles, as seen in Fig. 5.17$a-c$. This had the effect of changing the

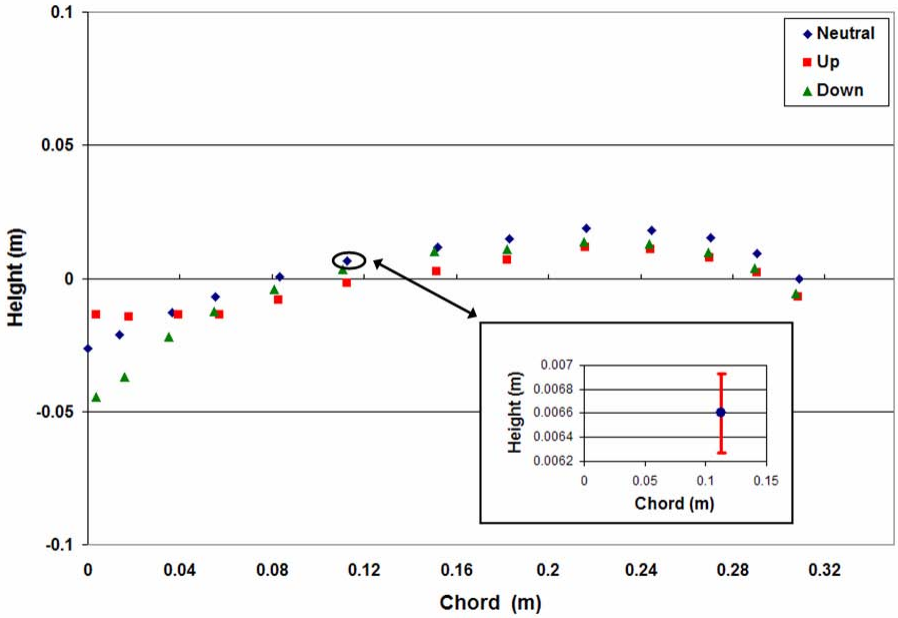

Figure 5.16: Nylon wing chord-wise deformation at wingtip; measurement error is shown in inset.

chamber of the wing. The region affected by the chord-wise bending was dictated by the position and size of the plexiglass plates. The degree to which the region was affected is governed by the torque produced by the servo.

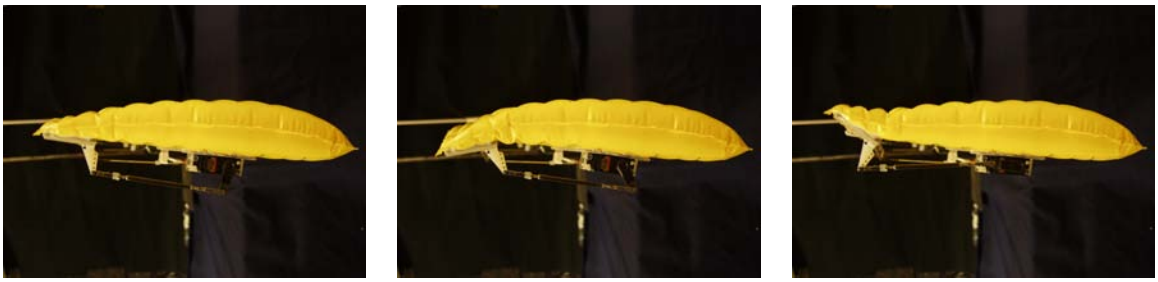

(a) Neutral Position. (b) Warp Down. (c) Warp Up.

Figure 5.17: Nylon wing warping using servo actuators.

Fig. 5.18 shows the degree to which the servo actuators are able to manipulate the trailing edge of the nylon inflatable wing. The servos deformed 23% of the wing chord due to the size and placement of the plexiglass plates. The trailing edge was deformed up by 17° and down by 12°, as seen in Fig. 5.18. The amount of deformation is dictated by the

torque of the servo and the arrangement of the mechanism joining the servo and the control horn. From these measurements, X-Foil was used to predict the effect this shape change would have on the sectional lift coefficient (C_l). Fig. 5.19 shows these results. There was a significant change in the lift generated from the deformed wings.

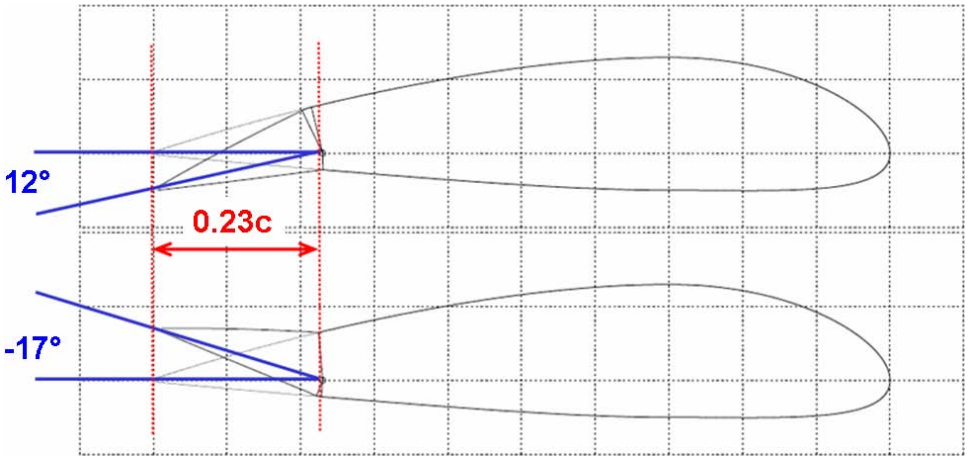

Figure 5.18: Nylon wing deformation.

Fig. 5.20 and 5.21 show a comparative effect of using one servo compared to using two servos. Both figures show the height of the trailing edge of the nylon across the semi-span. Fig. 5.20 shows the deformation of the trailing edge of the wing using one servo, while Fig. 5.21 shows the deformation using two servos. The black vertical lines show the approximate location of the servo for each case. Note that while the magnitude of the deformation does not change, it does affect a greater region of the span, thus capable of more control and authority on a vehicle.

Fig. 5.22*a* and 5.22*b* show contour plots of the deformation of the wing using a single servo. The dark shapes indicate the position of the plexiglass plates adhered to the bottom surface of the airfoil. In both figures the wing is viewed from above. The wingtip is on the left hand side of each figure and the trailing edge is at the bottom of each figure. Contour lines display lines of constant height; thus, Fig. 5.22*a* shows the upward deformation of the wing. Note the orientation and color of the contour lines on the trailing edge at the wingtip, indicating the deformation of the wing. Fig. 5.21*b* shows the downward deformation of the wing. The red contour lines indicate downward deformation across approximately half the semi-span. Fig. 5.23*a* and 5.23*b* show contour plots of the deformation using a dual servo arrangement. As the dual servo arrangement deforms the wing down, as seen in Fig. 5.23*a*, we can see a substantial portion of the trailing edge of the wing deformed up. The contour

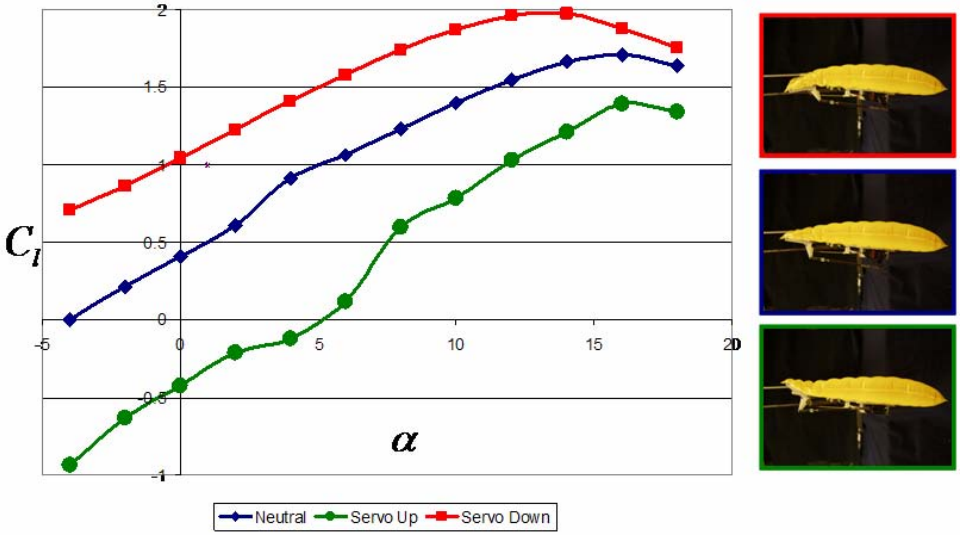

Figure 5.19: X-Foil prediction of sectional C_l vs. α.

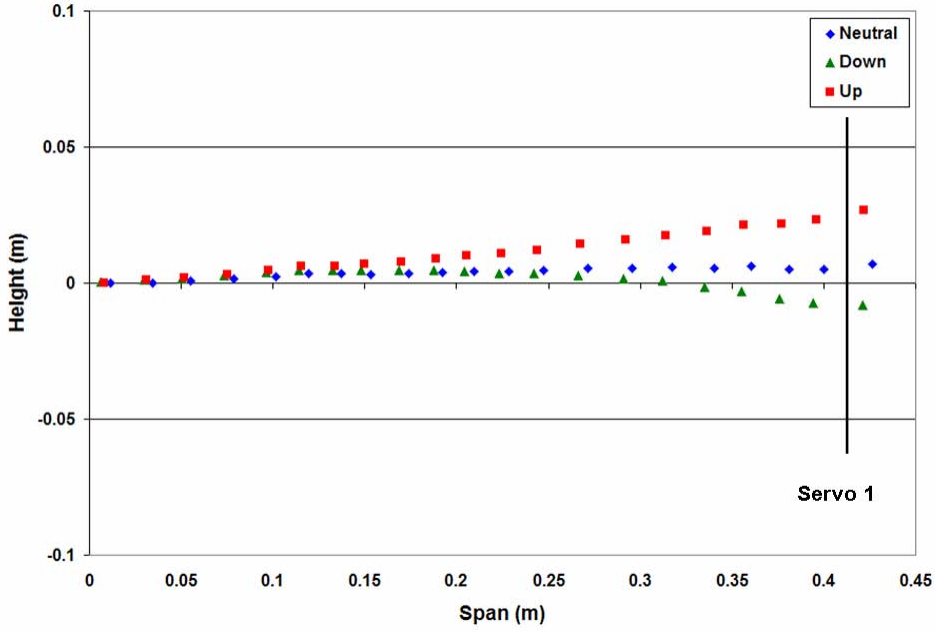

Figure 5.20: Spanwise trailing edge deformation using single servo.

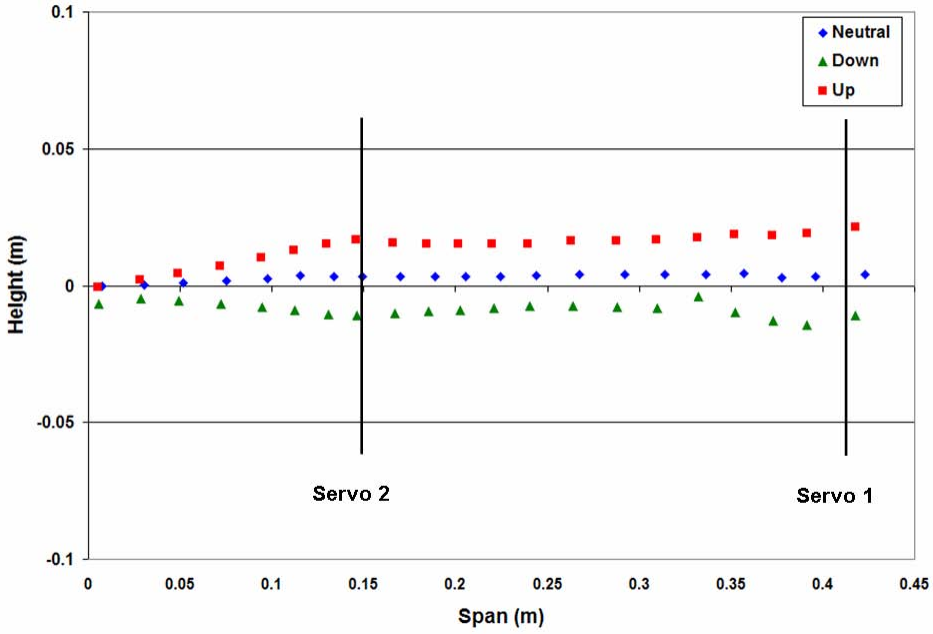

Figure 5.21: Spanwise trailing edge deformation using double servo.

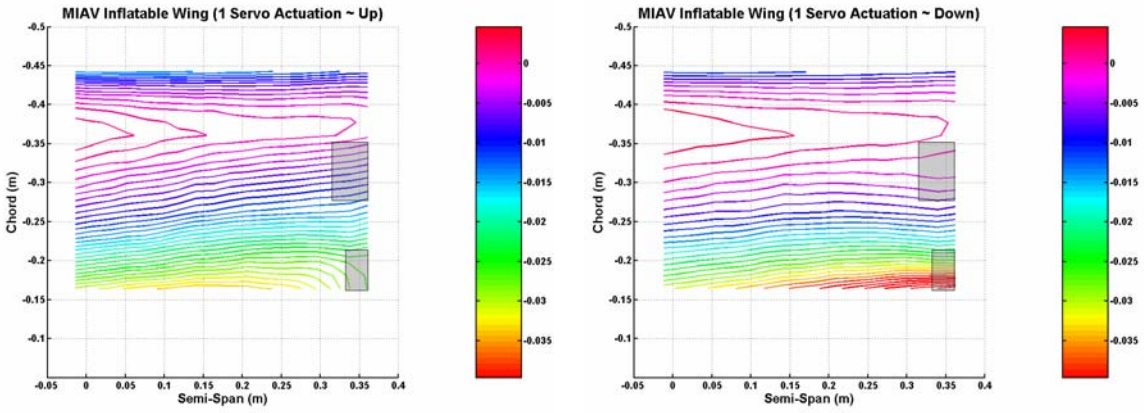

(a) Trailing edge deformed up.

(b) Trailing edge deformed down.

Figure 5.22: Contour plots of deformation using single servo.

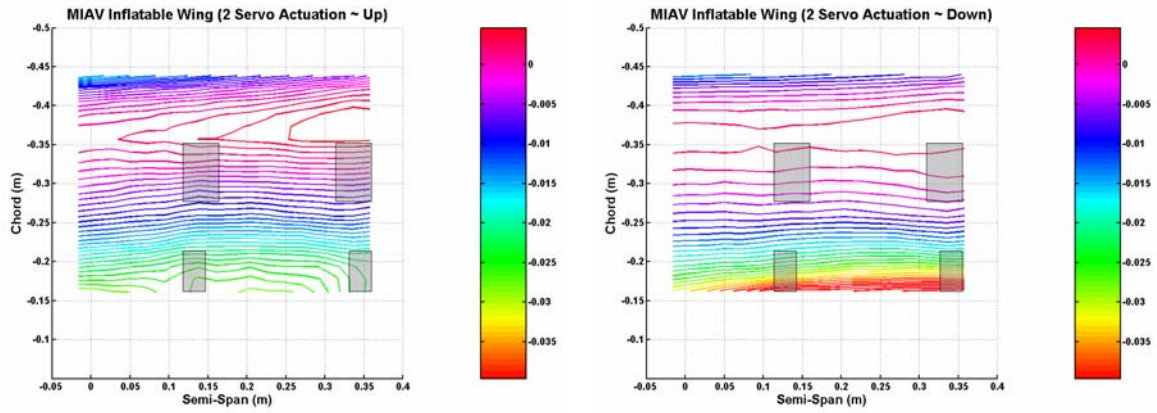

(a) Trailing edge deformed up.

(b) Trailing edge deformed down.

Figure 5.23: Contour plots of deformation using dual servos.

lines indicate two main areas where the trailing edge is deformed. This coincides with the positions of the servos. Fig. 5.23*b* shows the dual servo arrangement deforming the wing down. Note that using the dual servo system increases the wing area that is deformed up or down.

This servo mechanism, adhered to the wings, makes good use of conventional off-the-shelf hardware. Significant deflection of the trailing edge is possible with rapid response rates. The shape of the deflected wing is closer to that of a wing flap arrangement at the trailing edge, but blended into a gradual camber change along the span toward the root. Configurations that minimize hardware size and, if necessary, provide better control of the airfoil shape, are possible. With minor changes to components and added protection of the equipment, this can be a very low cost design for production.

5.3.2 Nitinol Warping System

Both the Vectran and nylon wings have been warped in the laboratory using nitinol actuators. The warping strategy utilized the nitinol in a "boot-lace" configuration, as seen in Fig. 5.24. This configuration anchored the nitinol to the wingtip at the trailing edge and ran back and forth from trailing to leading edge. The configuration was placed on both the pressure and suction surfaces toward the wingtip. The contraction varied as a function of total length; thus, the change in length or actuation distance was increased using this boot-lace configuration. When actuated, the constriction in the nitinol caused a localized change in the chamber of the wing. To counteract nitinol's slow response time returning to its neutral position, it was placed on both the upper and lower surfaces .

Figure 5.24: SMA wires integrated to an inflatable wing.

Fig. 5.25 shows warping of the nylon wing in the laboratory. In the top image, the Nitinol on the lower surface is actuated causing an increase in chamber. The lower image shows the nylon wing undeformed.

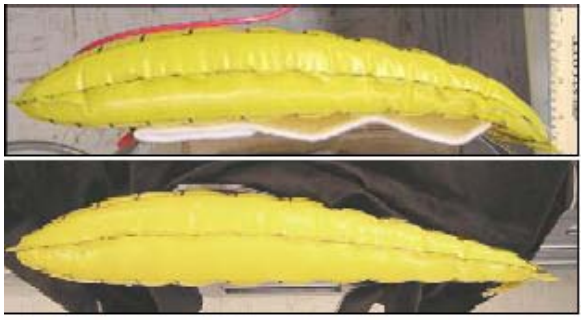

Figure 5.25: Inflatable wing with SMA chord morphing (deflected down and undeflected).

The nitinol was alternately actuated between the suction and pressure surfaces. The experiment was conducted in quiescent flow as the goal was to determine the deformation of the wing without aero-elastic influences. Photogrammetry was used to quantify the deflections generated by the current arrangement. Fig. 5.26 shows the deformation of the nylon wing using the nitinol actuators on the top and bottom surfaces. Fig. 5.26 shows the deformation of the nylon wing using the nitinol actuators on the top and bottom surfaces.

In Fig. 5.26 the wing is shown deformed up, down, and in the neutral position. The trailing edge is deformed up and down by approximately 0.02 m. This is much smaller than the deformations induced by the mechanical system discussed above. To date this system has not been successfully flight tested.

Warping of the nylon inflatable wings is possible through either servo or nitinol actuators. The warping deforms the camberline of the nylon wing. Servo actuators adhered to the wing surface warp the wing to provide adequate roll control to the vehicle. This has been demonstrated through flight testing of the nylon wing with the servo warping mechanism. The nitinol SMA actuators warp the wing, but insufficiently for flight control. The nitinol also has a severe actuation lag and thus, has not been flight tested. The current servo warping system is effective but is bulky and hinders compact stowage. Additionally, the servos disturb the airflow over the airfoil while the nitinol warping system is compact and allows stowage of the wing. Current work is focused on finding the middle ground.

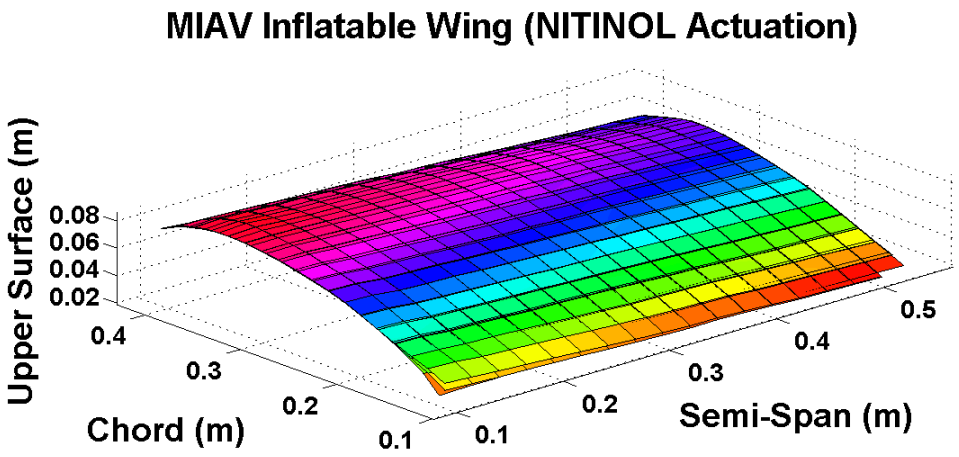

Figure 5.26: Wing warping using nitinol.

5.4 Nylon Inflatable Wing – Aeroelastic Deformation

Aeroelasticity is a primary concern of inflatable wings. It is defined as the interaction between aerodynamic and elastic forces, as well as the influence of these forces on airplane design.[59] Aeroelastic phenomena arise when structural deformations induce additional aerodynamic forces; these forces produce additional structural deformations which induce even greater aerodynamic forces.

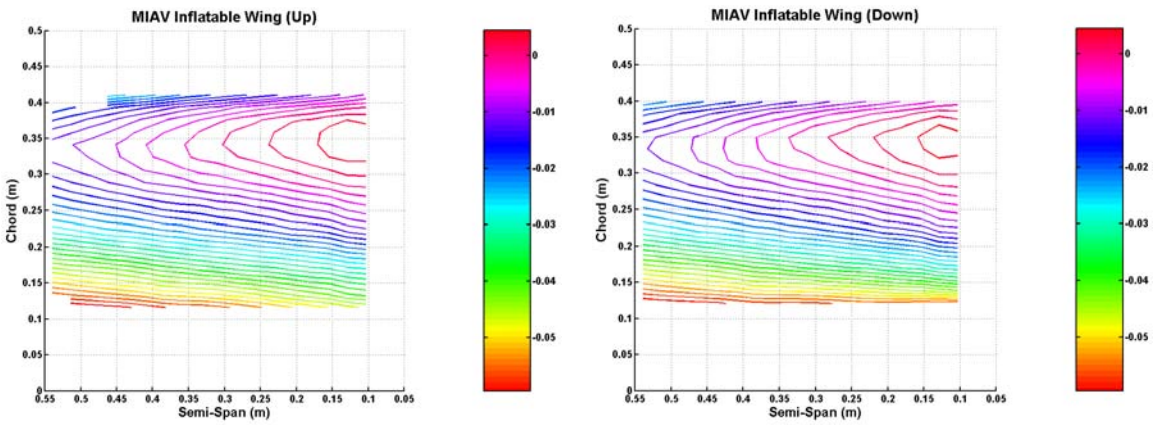

(a) Trailing edge deformed up.

(b) Trailing edge deformed down.

Figure 5.27: Contour plots of deformation using nitinol.

The interaction between the structure and the aerodynamic forces has the potential to cause instabilities. These instabilities, such as flutter, can result in catastrophic failures. Flutter is initiated from stiffness and frequency changes due to aerodynamic deformation. Stiffness and frequency are dependent on the forces and moments applied on the wing. These forces change during aerodynamic deformation.

The onset of flutter is seen when modal coupling occurs between the natural torsional and bending modes. This can be seen in Fig. 5.28*a* where the bending and torsional frequencies couple with one another as the dynamic pressure increases. Large elastic deformations result, which profoundly influence the vehicle's performance, handling qualities, flight stability, structural load distribution and control effectiveness/reversal phenomena.

Composite materials were shown by Lynch and Rodgers[101] to couple the bending and torsional deformations depending on the orientation of the laminate skin. The skin laminate can be oriented in certain directions in order to benefit or adversely effect the deformation. The technique is known as aeroelastic tailoring. In section A-A of Fig. 5.28*b*, the stiffness of the wing is orientated along the wing's axis. Aerodynamic loads mostly induce bending, which in turn creates a geometric nose-down twist. This is called "wash-out." Wash-out characteristics include maneuver drag reduction, maneuver load relief and divergence prevention. Laminates orientated as indicated in the B-B section of Fig. 5.28*b* introduce coupling between bending and torsion, so that the wing will bend upward and twist in the nose-up direction. This is a situation called "wash-in." Wash-in characteristics include control effectiveness and flutter prevention. Wash-out reduces the aerodynamic

loading when the wing bends. On the other hand, wash-in increases the loading. The effect of torsional flexibility on the non-swept lifting surface is to significantly change the span-wise aerodynamic load distribution. The resultant aerodynamic load distribution will increase as a result of the elastic torsional rotation increasing from the root (i.e. out along the span).

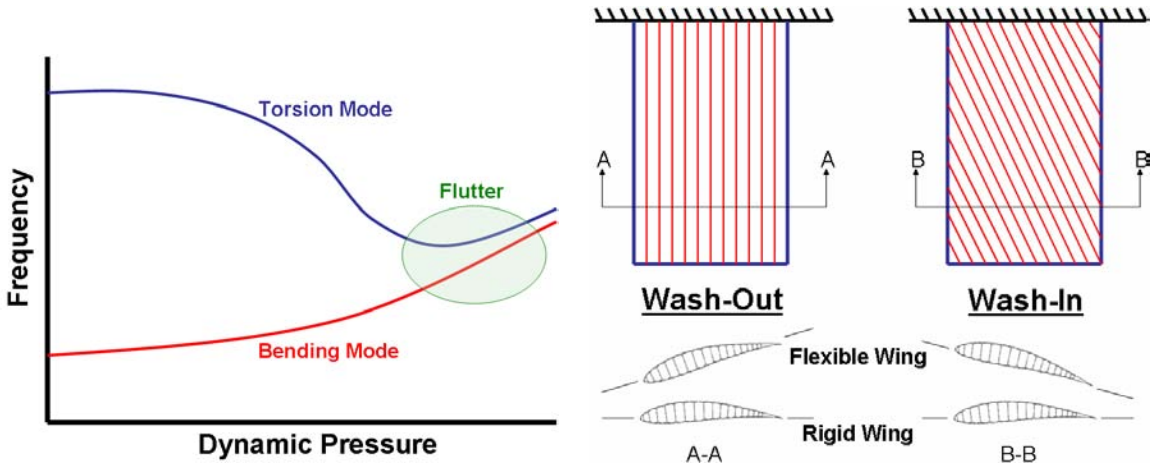

(a) Modal coupling.

(b) Aeroelastic deformation.

Figure 5.28: Aeroelasticity phenomena.

5.4.1 Experimental Set-Up

The present experiments with the nylon wings were conducted in an Eiffel type wind tunnel discussed in Chapter 4.5.1. The nylon wings used in these tests have a semi-span of 0.45 m and a chord length of 0.33 m. The wing was mounted vertically in the tunnel test section through a circular access cover as seen in Fig. 5.29*a*. As the tunnel test section was 0.6 m (24 in) by 0.6 m (24 in), the full semi-span could not be placed in the tunnel. The wing was partially inserted into the tunnel to a distance of 0.45 m (18 in). A fixed boundary condition was achieved by cutting a hole in an access cover to the tunnel which was a slightly smaller profile to that of the nylon wing. The wing was then inserted into the cut profile and inflated. A "press-fit" held the wing in place, which mimicked the attachment mechanism during flight testing. Three vertical rods extending above the tunnel ensured the wing section remained vertical, as seen in Fig. 5.29*a*. The circular access cover rotated, thus changing the angle of attack of the wing. Fig. 5.29*b* shows a schematic of the nylon wings in the tunnel.

The design inflation pressure for the nylon inflatable wings is 41.4 kPa (6 psi), however,

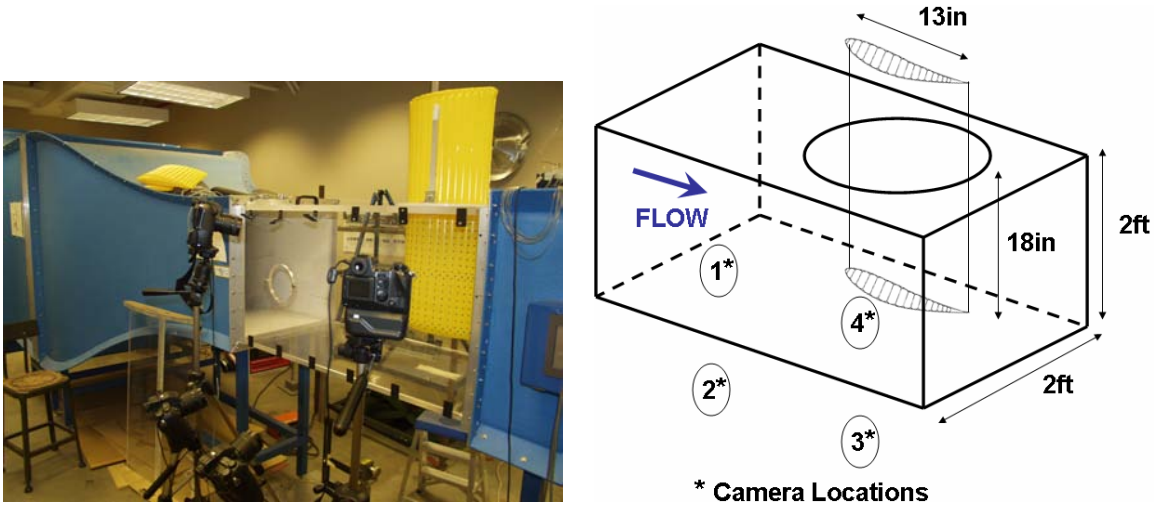

(a) Nylon wing in tunnel.

(b) Set-up Schematic.

Figure 5.29: Photogrammetry set-up for nylon inflatable wing.

the nylon wings were tested at internal inflation pressures of 13.8 kPa (2 psi), 27.5 kPa (4 psi) and 41.4 kPa (6 psi). The angle of attack was varied from -4° to 16°, in steps of 4°. Finally, five different dynamic pressures (q_∞), were examined: 0 N/m^2 (quiescent flow), 100 N/m^2, 178 N/m^2, 280 N/m^2, and 400 N/m^2. The non-zero dynamic pressures correspond to approximate chord based Re numbers of $3 \cdot 10^4$, $4 \cdot 10^4$, $5 \cdot 10^4$, and $6 \cdot 10^4$, respectively. The expected flight velocity of a vehicle utilizing the nylon wings is approximately 15 m/s (q_∞ between 100 - 178 N/m^2). An example of the m-files used to plot the data can be seen in Appendix A.1.

5.4.2 Results - Aeroelastic Deformation

41.4 kPa (6 psi) Inflation Pressure

Fig. 5.30*a* shows the nylon wing at an inflation pressure of 41.4 kPa (6 psi) and at an α of 4°. As the dynamic pressure increases, aerodynamic loads increase causing the wing to bend. Minimal aeroelastic bending is experienced over the range of dynamic pressures examined at this angle of attack. The largest deflection was experienced at the highest dynamic pressure and was 1.6 cm or 3.6% of the semi-span. However, at the expected vehicle flight speeds, the deflection was 0.2 cm, less than 0.5% of the semi-span.

The wing experienced greater aerodynamic loading as the angle of attack increased. The nylon wing at an inflation pressure of 41.4 kPa (6 psi) and an α value of 8° is in Fig. 5.30*b*. The maximum deformation, which is 1 cm, is at the largest dynamic pressure. As

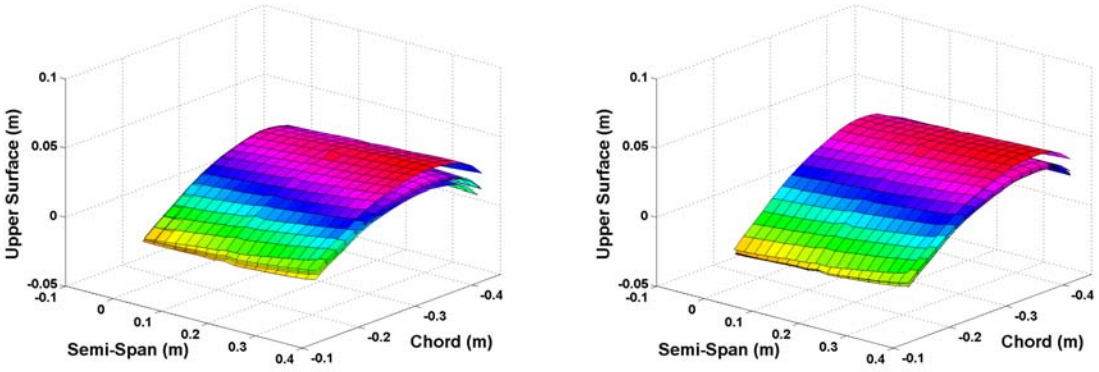

(a) $\alpha = 4°$.

(b) $\alpha = 8°$.

Figure 5.30: Upper wing surface deflection at 41.4 kPa (6 psi) with increasing dynamic pressure.

shown in Figures 5.30*a* and 5.30*b*, there is little difference in the magnitude of deformation between 4° and 8° angle of attack.

Fig. 5.31 shows the nylon wing at an inflation pressure of 41.4 kPa (6 psi) and an α of 16°. The maximum deformation is at the largest dynamic pressure of 400 N/m^2. At this angle of attack and dynamic pressure the deflection is 2.5 cm or 5.6% of the semi-span. At the expected flight dynamic pressures the deflection is 0.7 cm or 1.6% of the semi-span.

At the design inflation pressure of 41.4 kPa (6 psi), the aero-elasticity of the nylon wing is minimal. The expected flight velocity of a vehicle utilizing the nylon wings is approximately 15 m/s (between 100 - 178 N/m^2). At a dynamic pressure of 178 N/m^2 and an angle of attack of 4°, the maximum wing deflection is 0.2 cm. At a dynamic pressure of 400 N/m^2 and an angle of attack of 4°, the maximum wing deflection is 1.6 cm. Table 5.2 highlights the aero-elastic deformation over a range of α values and dynamic pressures. At design inflation pressures the nylon wings do not deform substantially under the expected dynamic pressures. In all cases "wash-in" torsion and bending of the wing was observed.

27.5 kPa (4 psi) and 13.8 kPa (2 psi) Inflation Pressures

Wing stiffness is dependent on inflation pressure. Therefore, the effect of operating the nylon wings at lower inflation pressures, or the effect of a loss in inflation pressure on aeroelasticity, was also examined. Inflation pressures of 27.5 kPa (4 psi) and 13.8 kPa (2 psi) were explored. For brevity, only deflection results for the 13.8 kPa (2 psi) cases are detailed below since this is the most extreme case. The results are useful in determining

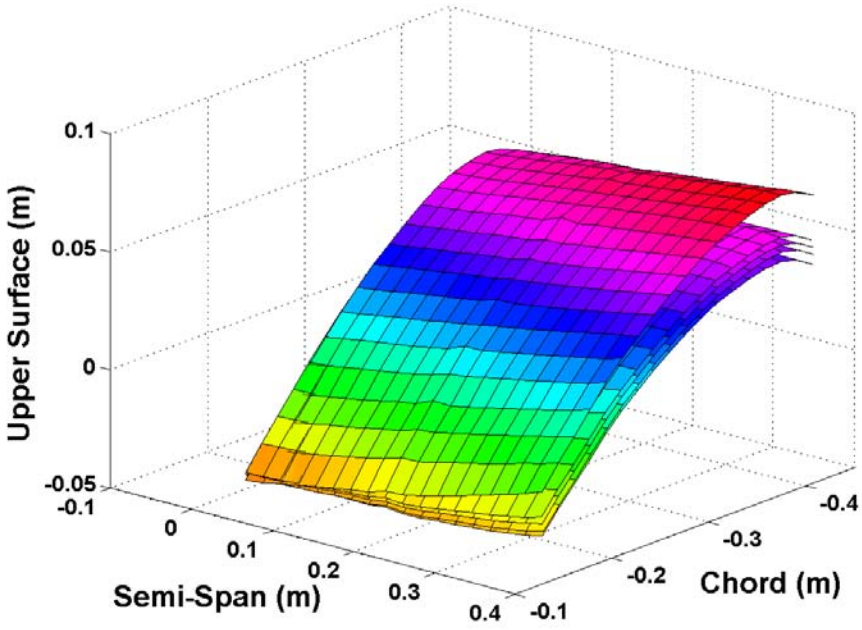

Figure 5.31: Upper wing surface deflection at 41.4 kPa (6 psi) with increasing dynamic pressure and $\alpha = 16°$.

the operational range of nylon wings, while it must be noted that these pressures are not recommended inflation pressures.

Fig. 5.32 shows the nylon inflatable wing at an inflation pressure of a 27.5 kPa (4 psi) and an α value of 8°. The figure demonstrates that as the dynamic pressure increases, the wing deforms. The deformation of the wing is approximately equal to that of the 41.4 kPa (6 psi) case for the same flow conditions and α.

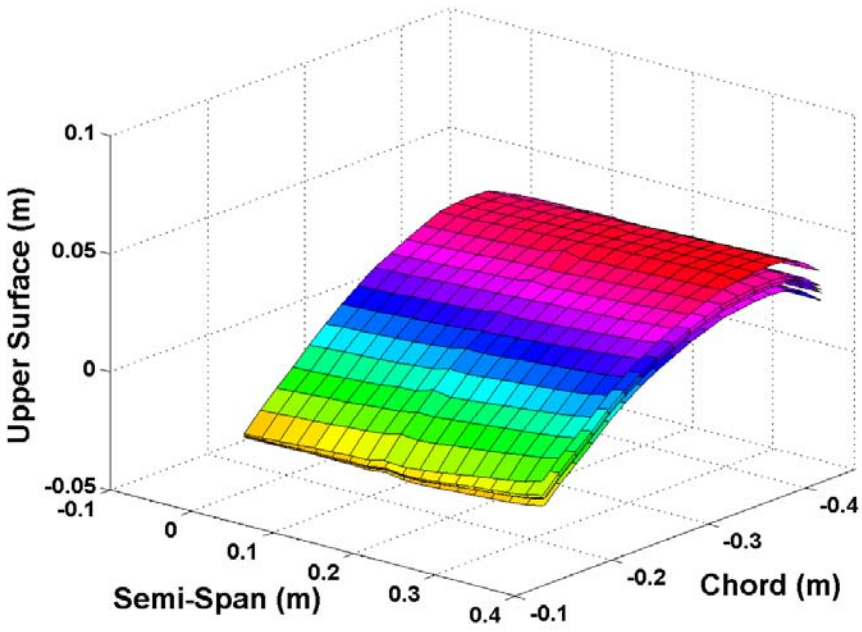

Figure 5.32: Upper wing surface deflection at 27.5 kPa (4 psi) with increasing dynamic pressure and $\alpha = 8°$.

Substantial deformation is experienced at inflation pressures of 13.8 kPa (2 psi), one-third of the recommended inflation pressure. Fig. 5.33 shows the nylon wing at an inflation pressure of 13.8 kPa (2 psi) and an α of 8°.

Predictably, the most interesting aeroelastic cases were obtained at low inflation pressures, high angles of attack and high dynamic pressures. At an inflation pressure of 13.8 kPa (2 psi) and an angle of attack of 16°, the nylon wing buckles at a dynamic pressure of 400 N/m^2. This is displayed in Fig. 5.34 where the dynamic pressure is increased over the range. As the angle of attack increases to 16°, there is a substantial increase in the deformation of the wing. Fig. 5.35 shows this large deformation progression as the angle

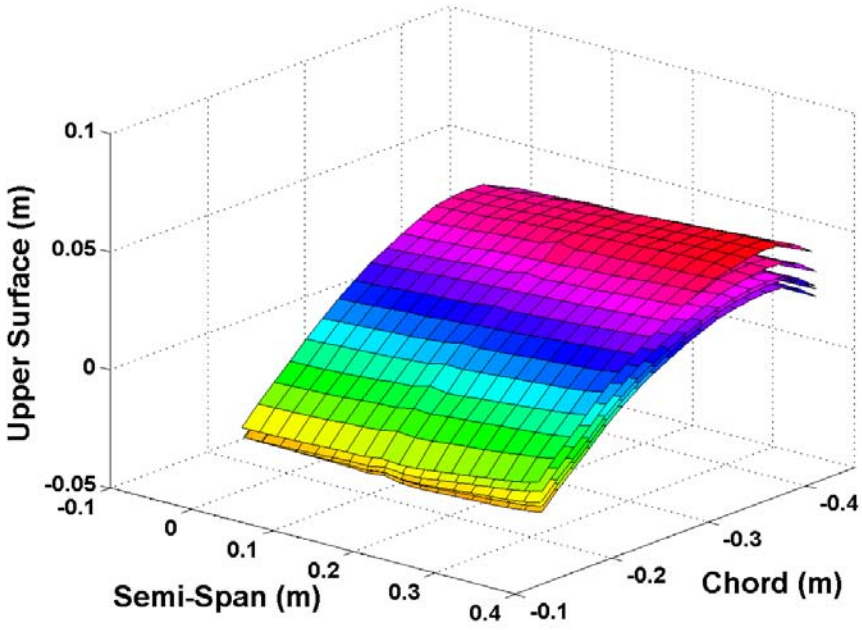

Figure 5.33: Upper wing surface deflection at 13.8 kPa (2 psi) with increasing dynamic pressure and $\alpha = 8°$.

of attack is increased from 9° to 13°. Inflation pressure and dynamic pressure are held constant at 13.8 kPa (2 psi) and 400 N/m^2, respectively.

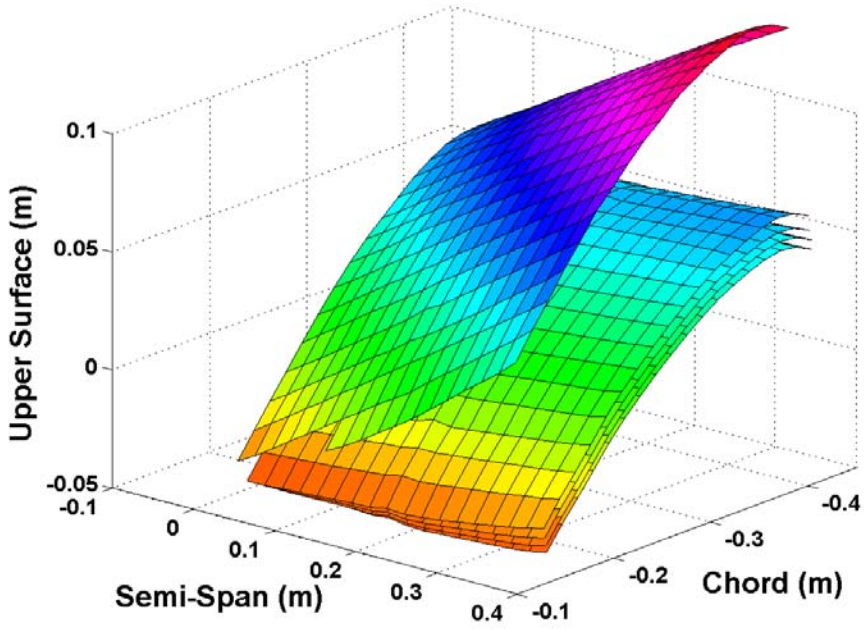

Figure 5.34: Upper wing surface deflection at 13.8 kPa (2 psi) with increasing dynamic pressure and $\alpha = 16°$.

The aeroelasticity of the nylon wings is evident at an inflation pressure of 13.8 kPa (2 psi). At a dynamic pressure of 178 N/m^2 and an angle of attack of 4°, the maximum wing deflection is 0.4 cm or 0.9% of the semi-span. At a dynamic pressure of 400 N/m^2 and an angle of attack of 4°, the maximum wing deflection is 1.5 cm or 3.3% of the semi-span (these deflections are comparable to the deflections at an inflation pressure of 41.4 kPa (6 psi)). At an α value of 8° the maximum deflection experienced was 1.6 cm at 400 N/m^2 and 1.5 cm at 178 N/m^2. Finally, at an α value of 16°, the maximum deflection experienced was 0.8 cm at 178 N/m^2 and the wing buckles with a dynamic pressure of 400 N/m^2.

Table 5.2 provides the deformations values over a range of α values and dynamic pressures. The nylon wings do not deform substantially under the expected dynamic pressures at the design inflation pressures. The deformation of the wing increases at high loading conditions; thus as the angle of attack increases, the deformation experience by the wing also increases. In all cases "wash-in" torsion and bending of the wing was observed.

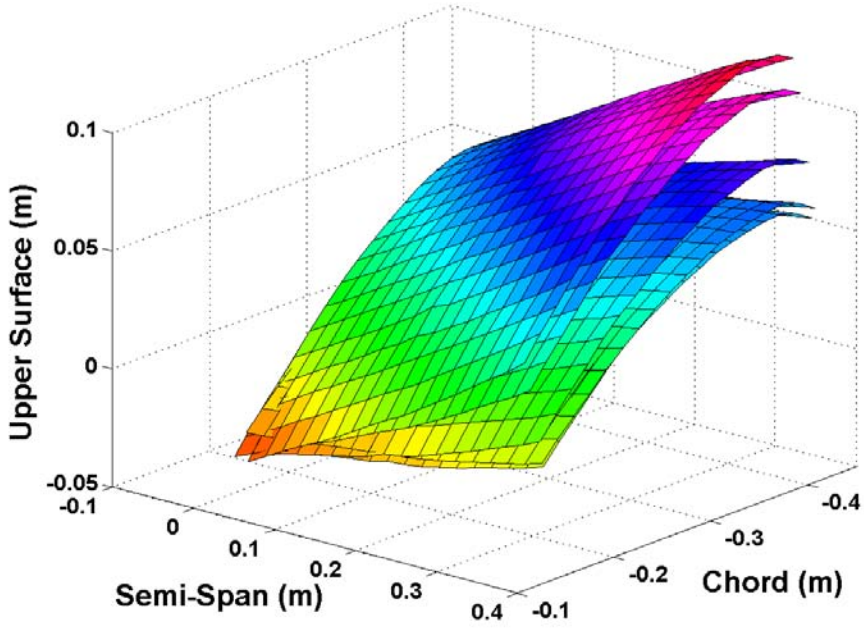

Figure 5.35: Upper wing surface deflection at 13.8 kPa (2 psi) and 400 N/m^2; α = 9 - 13°.

Table 5.2: Wing tip deflection of the nylon wing under various loading conditions.

Angle of Attack, α [°]	Dynamic Pressure [N/m^2]	Inflation Pressure [kPa (psi)]	Wingtip Deflection [cm]
4	178	41.4 (6)	0.1916
		13.8 (2)	0.3748
	400	41.4 (6)	1.5556
		13.8 (2)	1.4738
8	178	41.4 (6)	0.1655
		13.8 (2)	0.4792
	400	41.4 (6)	1.0900
		13.8 (2)	1.5607
16	178	41.4 (6)	0.7046
		13.8 (2)	0.7810
	400	41.4 (6)	2.5713
		13.8 (2)	Buckles

The aeroelastic deformation results are plotted in Fig. 5.36 and 5.37. Fig. 5.36 shows the change in α from the quiescent flow case for each non-zero dynamic pressure. This change in α is plotted relative to the span location. The angle of attack of the wing increases from wing root to tip. The increase in angle of attack along the semi-span is consistent with wash-in deformation. Fig. 5.37 shows the wingtip deflection relative to the dynamic pressure of both the leading and trailing edges of the wing. Here, the wash-in deformation of the wing is clearly evident as the gap between the leading and trailing edge heights is diverging, which indicates twist. Next, a lifting line code predicts the lift change from the semi-span for these α variations (this is detailed in Chapter 6.2.2).

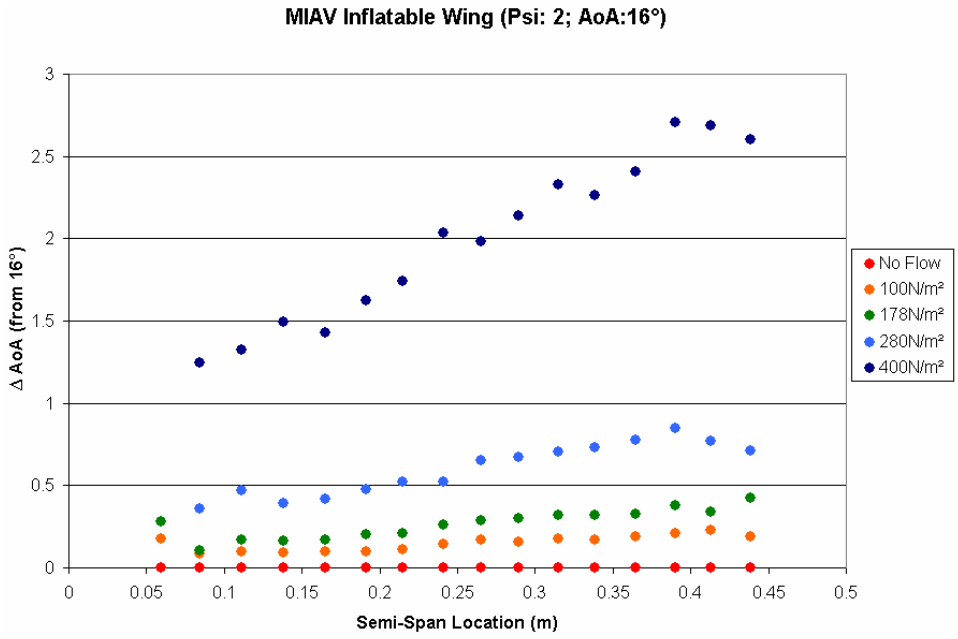

Figure 5.36: Change in angle of attack across semi-span with increase in dynamic pressure (Inflation pressure of 13.8 kPa (2 psi) and $\alpha = 16°$).

5.5 Buckling Prediction

As highlighted in Chapter 2.7 Crimi [70] developed a method for finding the torsional collapse speed for an inflatable wing that consists of several distinct cylindrical spars. The model related the softening effect of inflatable spars with skin wrinkling developed by Main *et al.* [71]. These two models were synthesized by Randall *et al.* . [30]. Fig. 5.38 indicates the nonlinearities that arises from wrinkling of the skin material in an inflatable beam [30].

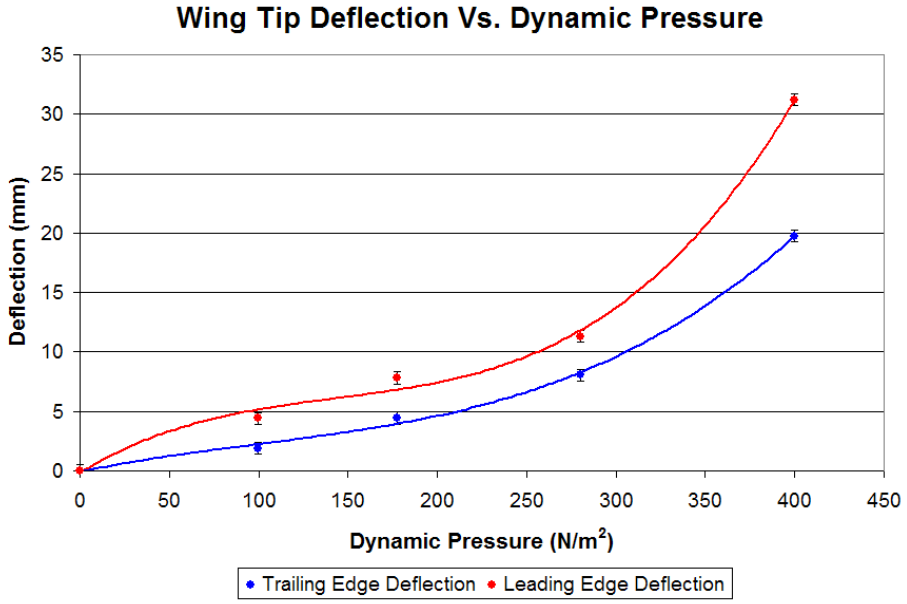

Figure 5.37: Nylon inflatable wingtip deflections due to increasing dynamic pressure.

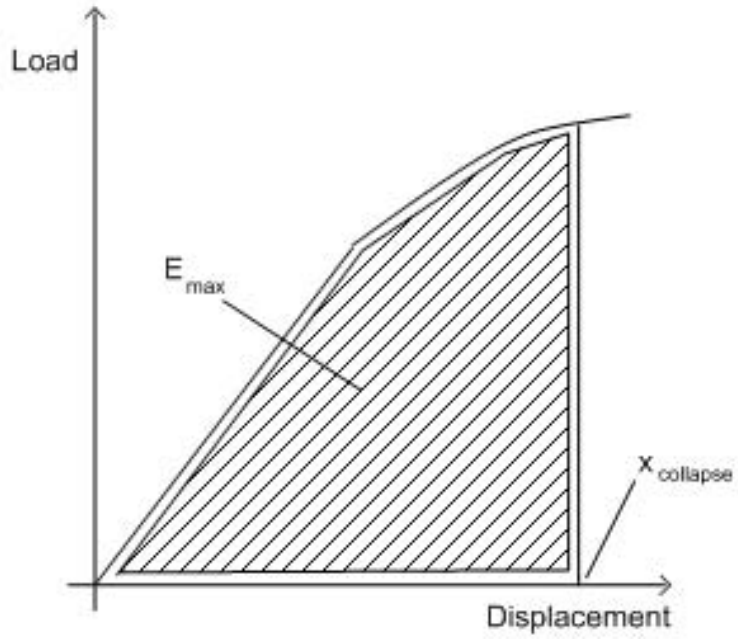

Figure 5.38: Typical load vs. deflection curve for an inflatable beam [30].

The combination of the two methods was used to determine the maximum deflection (and maximum stored energy, E_{max}) based on the collapse load of a beam. Eqn. 2.45 and Eqn. 2.46 can be used to determine the airspeed for collapse. These equations are repeated here.

$$E_{\max} = \frac{1}{2}Mu_0^2 + C_{Lmax}\frac{1}{2}\rho U_{collapse}^2 S x_{collapse} = \int_0^{x_{collapse}} F ds \tag{5.1}$$

$$U_{\text{collapse}} = \sqrt{\frac{E_{max} - \frac{1}{2}Mu_0^2}{C_{Lmax}\frac{1}{2}\rho S x_{collapse}}} \tag{5.2}$$

Initially the nylon inflatable wing was set-up in the tunnel as highlighted in Chapter 5.4.1. Here, the wing was set at a specified inflation pressure and α value. The tunnel's dynamic pressure was then steadily increased until the wing buckled. These results can be seen in Fig. 5.39. In this figure, wing loading (L/S) in N/m^2 is plotted relative to wing inflation pressure. Here the blue dots represent data where the wing did not buckle and the red dots represent buckled points. Generally, the red dots represent data points at high α and dynamic pressure values. As the wing's inflation pressure increases, stiffness increases. This effect in Fig. 5.39. At higher wing inflation pressures, greater wing loading can be carried by the wing before buckling. At the inflation pressure of 27.5 kPa two blue dots can be seen amongst the red dots. This is as a result of using two distinct nylon wings during this testing. One of the wings was able to carry a greater load before buckling. It is assumed that this is due to slight variations in the orientation of the wing skin material. Overall both wings followed the same trend; however, this variation should be noted.

Buckling of the wing is always possible given a large enough initial perturbation. Note: for this analysis, the initial perturbation was ignored by setting u_0 to zero; this yields the airspeed for static collapse. The C_l value was also based on 2D XFoil data corrected for a 3D low aspect ratio straight wing configuration. In order to increase the collapse speed, E_{max} should be large as seen in Egns. 5.2. This amounts to having a larger stiffness. For an inflatable beam or an inflatable wing, the stiffness in the linear section of the load deflection curve (Fig. 5.38) may be increased by raising the internal pressure.

Initially, E_{max} was calculated based on the collapse speeds from the tunnel data. The deflection at collapse ($x_{collapse}$) was set at 15% of the semi-span length, yeilding a wing deflection of 0.066 m (2.6 in) for the tunnel experiments. This was consistent with deflections highlighted in Chapter 5.4.2. The E_{max} values were plotted relative to α. A polynomial line was fitted to the data as a means of predicting E_{max}. Fig. 5.40 shows the buckling velocity relative to α. The blue and green dots are tunnel data shown in Fig. 5.39. The red and light

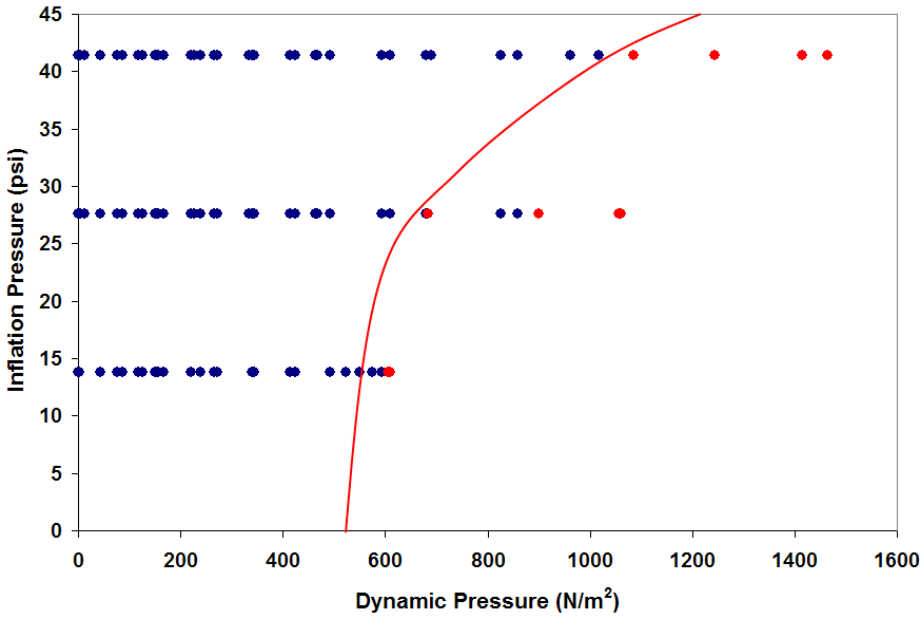

Figure 5.39: Inflation pressure vs. Dynamic Pressure.

blue lines represent the predicted buckling velocity verse α from Eqn. 5.2. There was good agreement between the actual buckling velocities and the predicted buckling velocities. The predicted buckling velocities are greater for the 41.4 kPa case than for the 27.5 kPa case. Both predict higher buckling velocities at lower α values. This was reasonable as at lower α values, C_l is lower and hence the velocity was greater for the wing to buckle. At higher α values, the buckling velocity decreases, which was also instinctual.

Eqn's. 5.2 were then used to predict the buckling velocities as the semi-span length was increased. The chord length was set at 0.3302 m, while the semi-span length was varied. The variable $x_{collapse}$ remained set at 15% of the semi-span length. The results can be seen in Fig. 5.41*a* with the nylon wing at 27.5 kPa and Fig. 5.41*b* with the nylon wing at 41.4 kPa. In both figures, the buckling velocity reduces as the semi-span increases. Fig. 5.42 shows a comparison between the 41.4 and 27.5 kPa cases at $\alpha = 4°$. The 41.4 kPa case buckles at a higher velocity than the 27.5 kPa case for a given semi-span. At a semi-span length of 1 m, the 27.5 kPa case is predicted to buckle at 19 m/s, while the 41.4 kPa case buckles at 23.3 m/s.

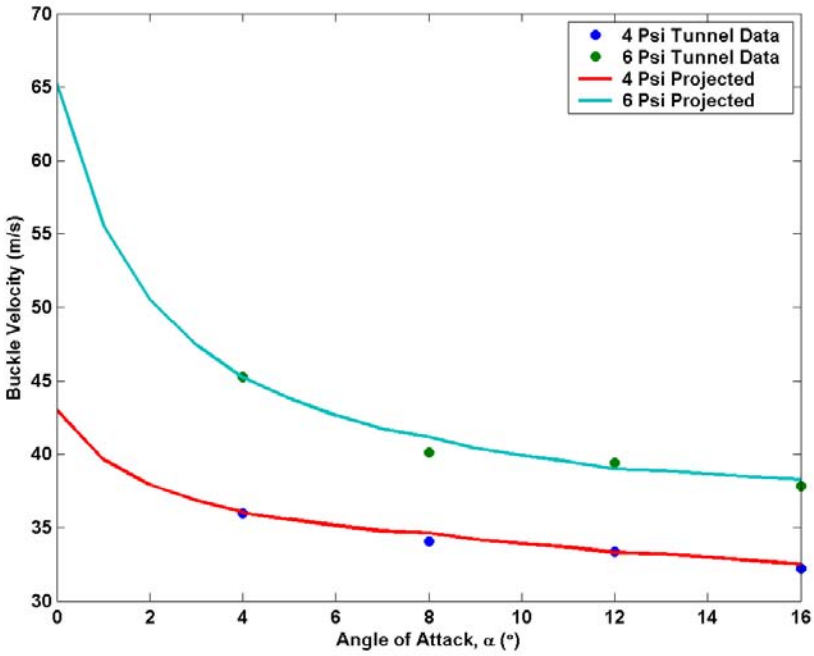

Figure 5.40: Buckling Velocity vs. α.

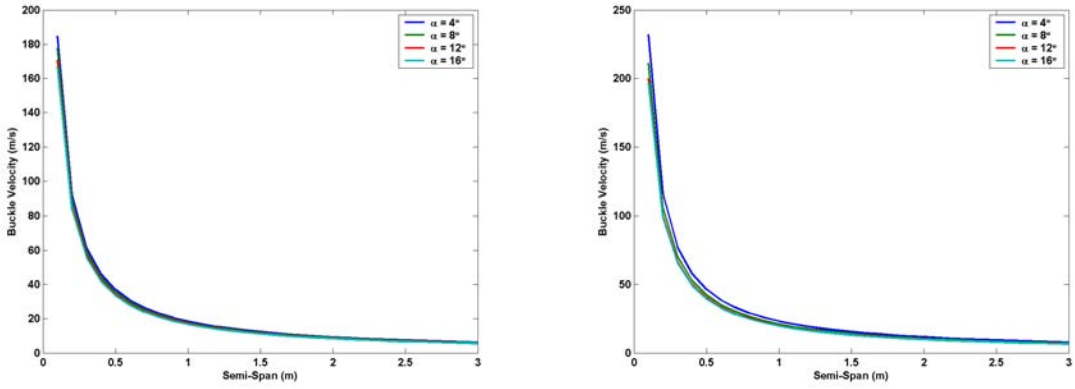

(a) 4 Psi.

(b) 6 Psi.

Figure 5.41: Buckling Velocity vs. Semi-Span length.

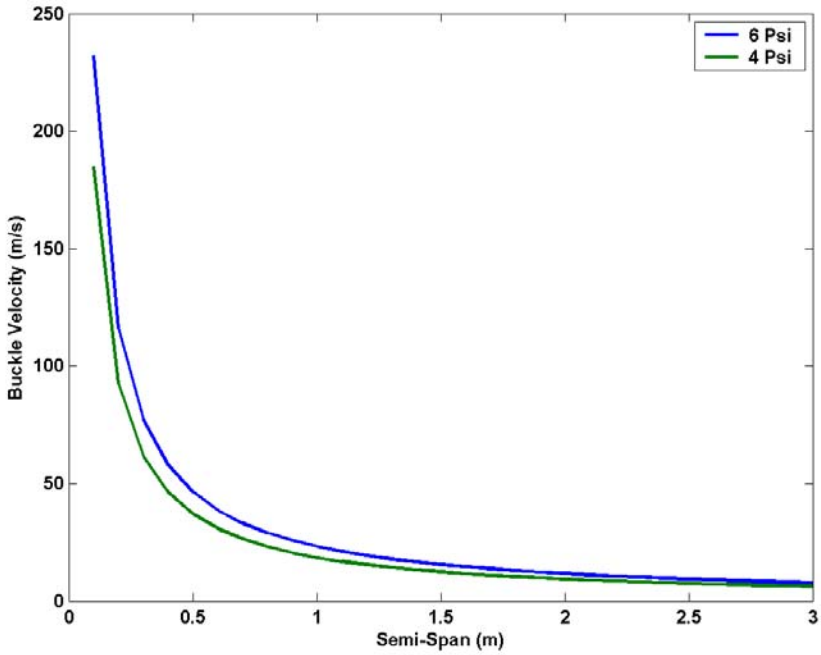

Figure 5.42: Buckling Velocity vs. Semi-Span length at $\alpha = 4°$.

5.6 Free and Forced Vibration of the nylon Inflatable Wing

The properties making the inflatable wings suitable for warping (i.e. non-rigid) introduces concerns regarding the behavior of the wings in flight. Modal response and vibration due to dynamic pressure were examined to investigate these concerns. The nylon inflatable wing displays aeroelastic instabilities at certain dynamic loading cases that have been demonstrated in the wind tunnel testing. These instabilities were experienced primarily at low inflation pressures and high dynamic pressures.

5.6.1 Modal Testing Arrangement and Procedures

A series of cantilevered modal tests were performed to determine the free vibrational characteristics of the inflated wing at various internal pressures. The semi-span was mounted to a test stand, as shown in Fig. 5.43*a*, where the cantilevered semi-span was 70.5 cm (27.75 in). Small, lightweight uni-axial accelerometers were secured to the coated nylon surface with silicone rubber adhesive. The accelerometers were attached at the location 2 and 11 shown in Fig. 5.43*b*: near the mid-chord and near the trailing edge. An impact hammer applied an impulse force to the wing at varying points. Inputs were applied at all locations on the wing as indicated in Fig. 5.43*b*, including the locations of the two accelerometers for driving-point measurements. The impulse was applied to the reverse side of the wing. The test was repeated at wing pressures of 13.7, 27.6, and 41.4 kPa (2, 4, and 6 psi). A schematic of the test set-up is included in Fig. 5.44.

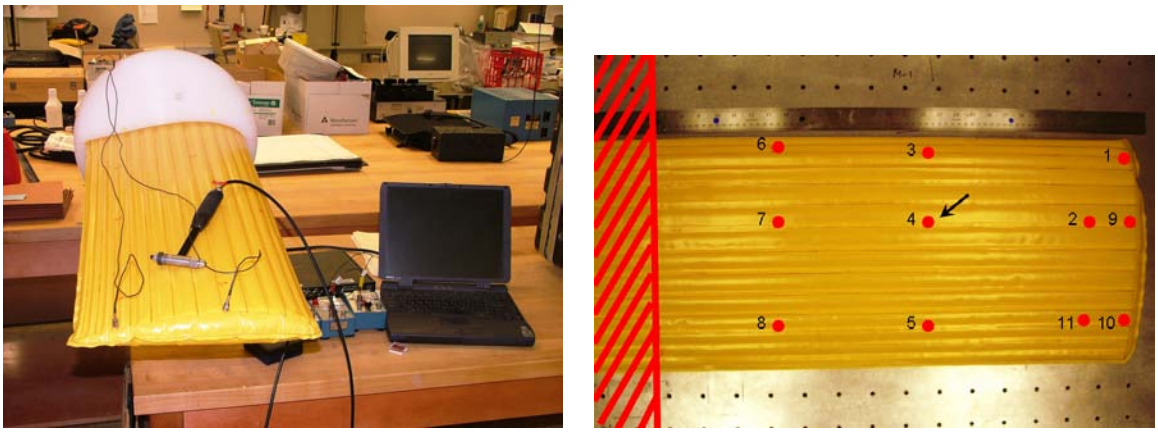

(a) Impact hammer test set-up.

(b) Hammer impulse locations (1-11) and measurement locations (9, 10).

Figure 5.43: Impact hammer testing.

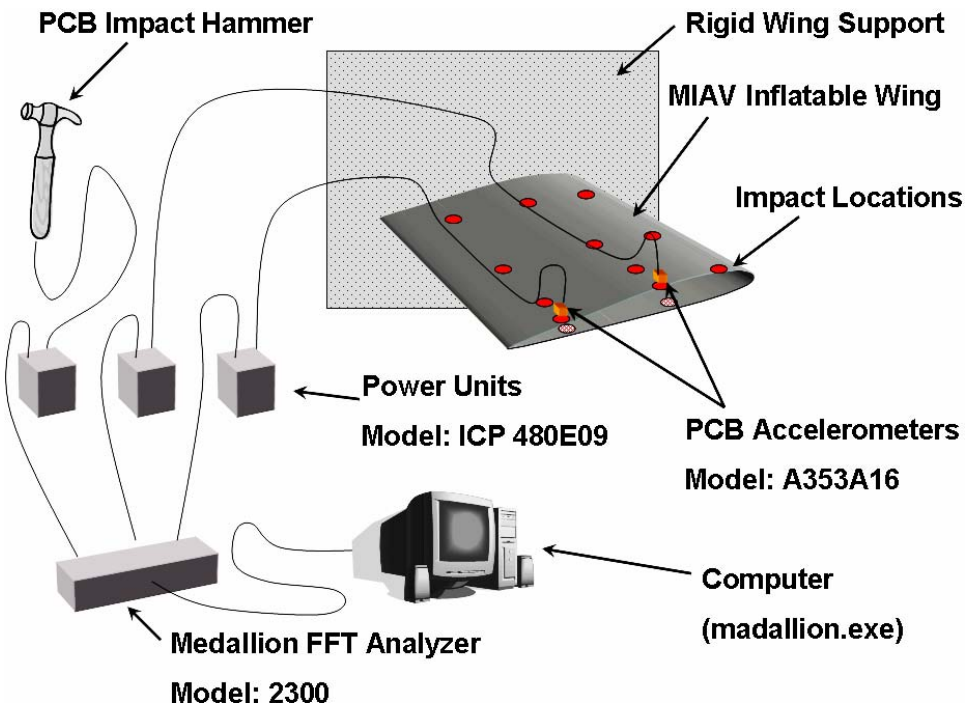

Figure 5.44: Schematic of impact test set-up.

Frequency Response Functions (FRFs), including magnitude, phase and the coherence of each input/output pair were calculated using a Zonic Medallion multichannel data acquisition system and signal analyzer software. A sampling frame size of 2048 with a bandwidth frequency of 500 Hz was used for data acquisition and signal processing. This resulted in a frame period of 1.6 s, with a frequency resolution of 0.625 Hz. Ten averages were used at each measurement point. The data indicated that for the frequency range of interest, (0 to ±100Hz), ten averages were suitable and sufficient to obtain an accurate FRF. An exponential window was also used for processing of the Fast Fourier Transforms (FFTs) used to compute the FRFs.

FRF processing is usually determined with ± 30 impact averages. However, for simplification, tests were conducted using 10 averages. A comparison between the two techniques was performed resulting in an immeasurable difference for the frequency range of interest, (0 to ±100Hz). From this, it was determined that 10 averages were sufficient to obtain an accurate FRF.

Fig. 5.45*a* and 5.45*b*, show example results from the impact test. The top and middle graphs demonstrate the magnitude and phase of the frequency response function; the bottom graph displays coherence. The red plots show data from the accelerometer near-

est the trailing edge of the wing, while the blue plots show data from the accelerometer nearest the chord midpoint. These data are for an internal wing pressure of 41.4 kPa (6 psi) and 27.6 kPa (4 psi), and an impulse input at the location designated by the arrow in Fig. 5.43*b*. This test proves useful for determining wing response modes below 150-200 Hz because there are multiple modes, possibly as many as six or seven, seen below 150 Hz in the frequency response plot.

Typical FRF and coherence results for two simultaneous response measurements are presented in Fig. 5.45. Here the impulse is input at point 4 and the acceleration response is measured at both locations. The two sensors are positioned to identify both the bending and torsional modes. Therefore, the FRFs are not expected to be identical. In the FRF and coherence plots, results above 150-200 Hz are seen to degrade, while results below 150-200 Hz are reasonable. Results will be presented for the range 0 to 100 Hz, rather than the full range of 0 to 500 Hz.

In conducting the test, dynamic response was recorded due to impact inputs applied at the locations of each accelerometer. With this data, it is possible to evaluate wing reciprocity to determine the linearity of the wing response. Fig. 5.46*a*, shows the FRF measurements recorded at each measurement point due to an input at the other measurement point, for the 27.6 kPa (4 psi) internal pressure case. Fig. 5.46*b*, shows the same for the case of 41.4 kPa (6 psi) internal pressure. In each figure, the blue data represents the accelerometer located at the midpoint and the red data represents the accelerometer located near the trailing edge. It is evident that the frequency and phase correlate reasonably well for the 27.6 kPa (4 psi) case at frequencies up to approximately 150 Hz. Fig. 5.45*b*, indicates that for the case of an internal wing pressure of 6 psi, the frequency ans phase also matche well, up to approximately 150Hz. Appendix A.2 shows an example of the m-files used to determine the reciprocity.

The process was repeated for an inflation pressure of 13.7 kPa (2 psi). However, localized wing surface deformation hindered the data collection process. The impact of the Modal hammer deformed the wing surface and did not trigger data collection. Thus, data for this inflation case could not be examined.

5.6.2 Modal Analysis

To identify frequencies, mode shapes and damping, modal analysis was conducted using the X-Modal software package. X-Modal does not acquire frequency response function (FRF) data, but utilizes FRF data acquired from any data acquisition system (as long as

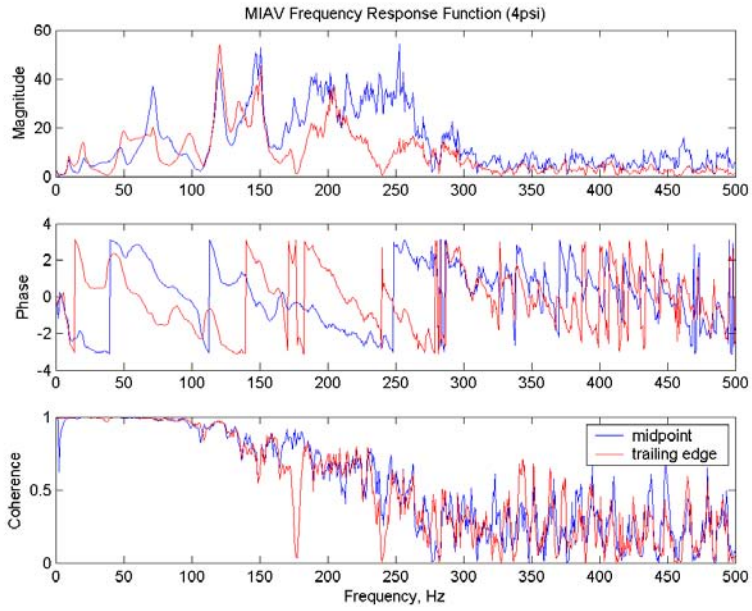

(a) Frequency Response Plot, 27.5kPa (4psi).

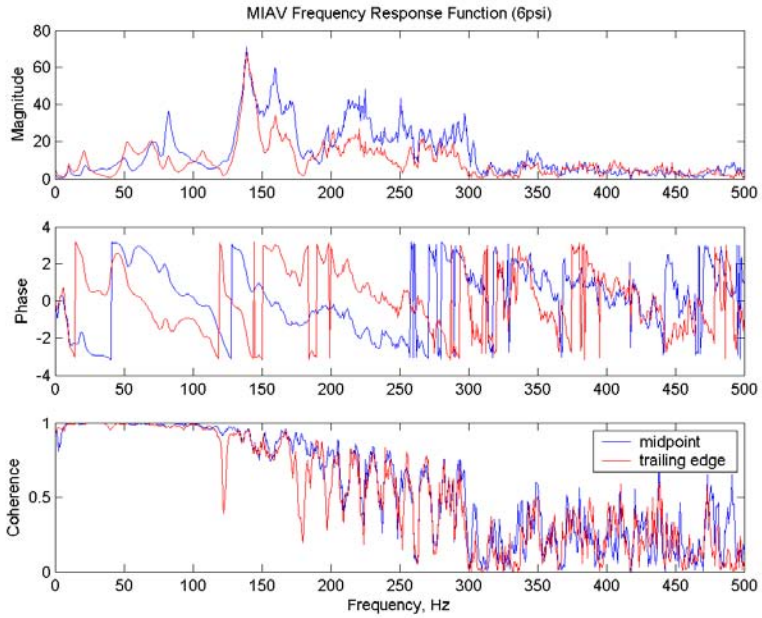

(b) Frequency Response Plot, 41.4kPa (6psi).

Figure 5.45: Hammer impact results for nylon wings.

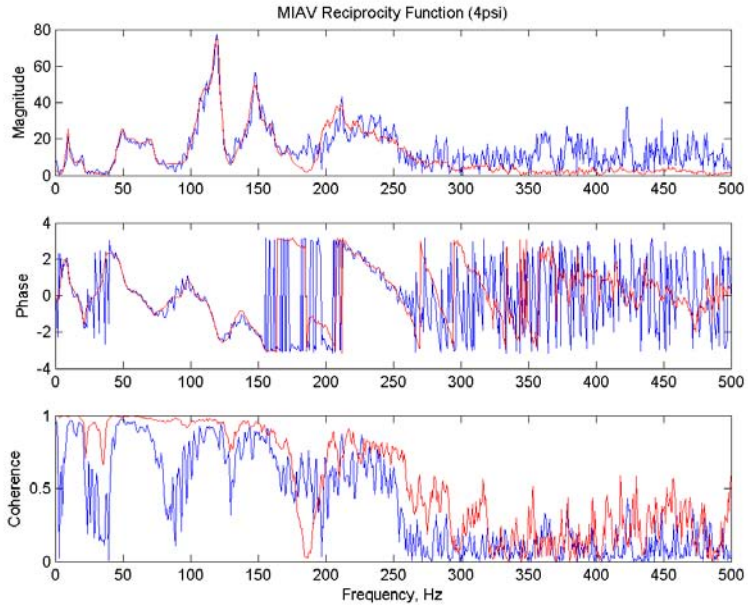

(a) Reciprocity plot, 27.5 kPa (4 psi).

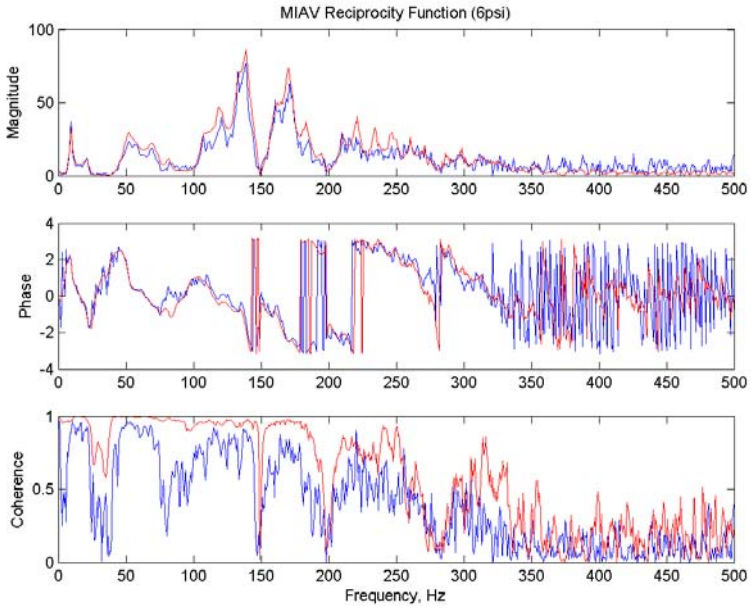

(b) Reciprocity plot, 41.4 kPa (6 psi).

Figure 5.46: Frequency response function plots demonstrating reciprocity.

the data can be provided in Universal File Format). X-Modal utilizes MATLAB to provide user programmability, as well as to implement all the major modal parameter estimation algorithms documented in the literature.

The universal file was prepared and imported into X-Modal. Initially the "pole set-up" function was used in order to define which parameters to examine. Fig. 5.47 is an example of this initial step. Here, the upper figure was used to define the frequency range of interest, in this case from 0.2 Hz to 140 Hz. The bottom figure was used to define the time range of interest. The time frame examined in Fig. 5.47 was 0.2 to 1 s. Algorithms and methods to determine modes were defined in the pole set-up. An ERA algorithm was used in this research to determine the modes of the inflatable wing. This process was repeated in order to explore the effect on varying these parameters of the model results. The frequency range was varied by holding the initial value at 0.2 Hz and varying the second parameter; this was varied between 80 Hz and 150 Hz. The time range was held constant during the repetition of the analysis. Once the frequency range, time range, and algorithm were selected, the data were processed.

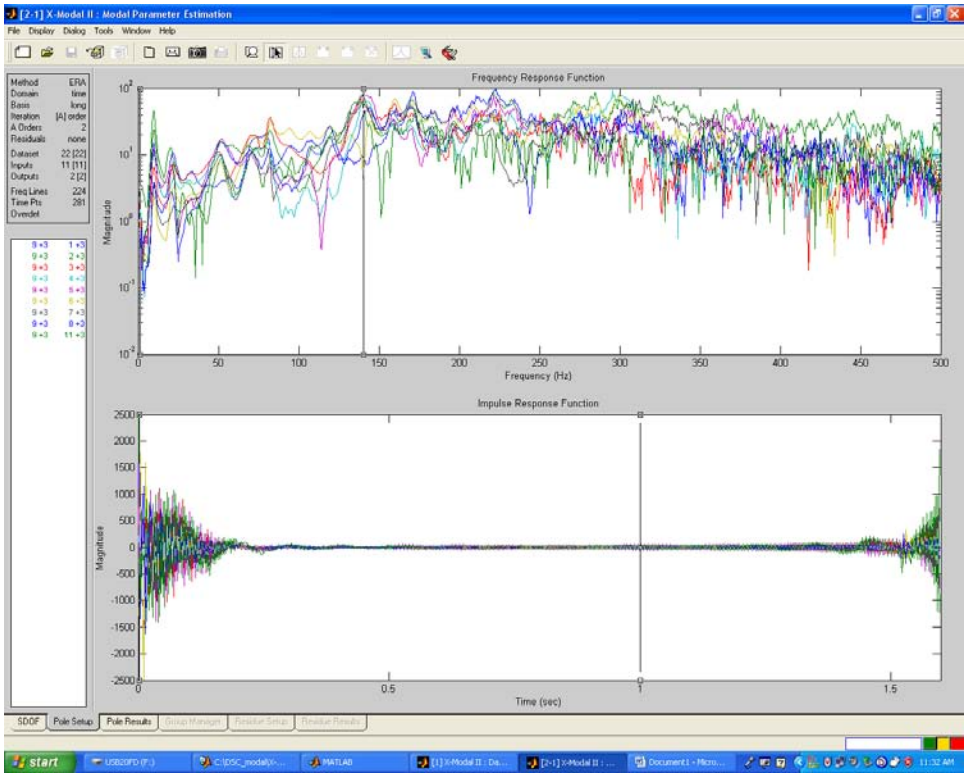

Figure 5.47: Pole set-up.

The processed data is visualized in a consistency diagram (Fig. 5.48). On the consistency diagram, the x-axis is the frequency (Hz) while the y-axis is the model iteration. The vertical lines of model iteration shapes indicate potential modes. The shapes represent the model certainty that a mode shape is present at the frequency of interest. Blue diamonds and green triangles represent fair certainty of a mode shape at the frequency in question. Potential mode shape frequencies are then selected for further processing. In this case they were found at 7.98, 23.04, 50.28, 71.76, 80.74, 95.01, 105.04, and 115.62 Hz.

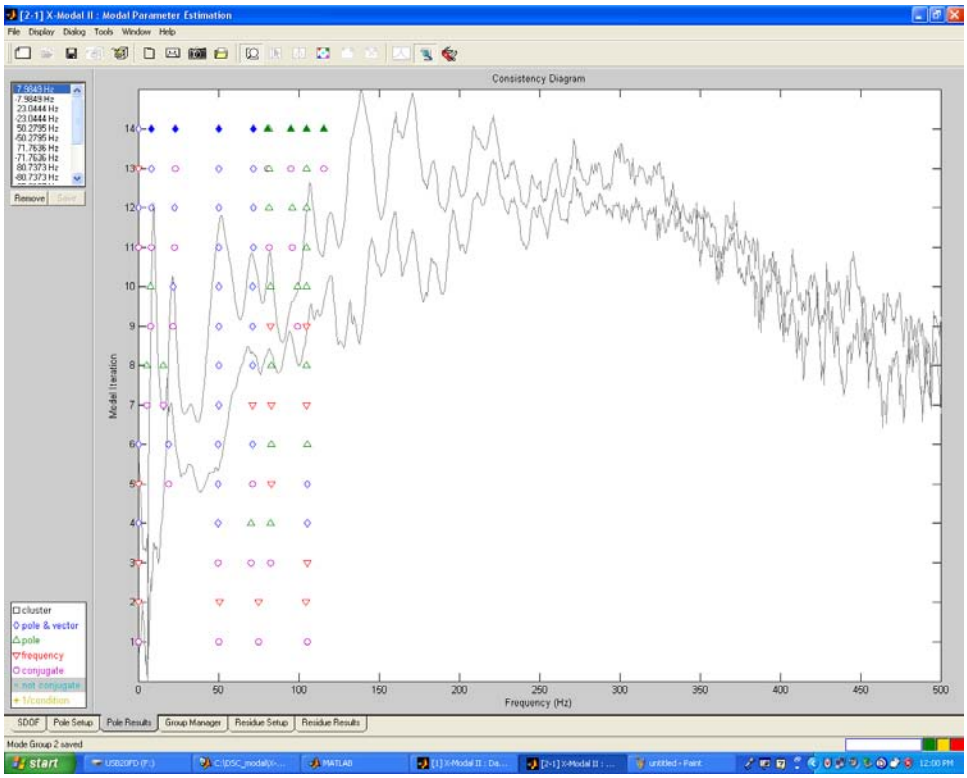

Figure 5.48: Consistency diagram.

Fig. 5.49 shows the residue set-up with frequency plotted against magnitude. The solid blue line represents the measured data from the impact test. The dashed line represents the model's prediction of the response to the impact. In this example, the model performs ineffectually below 50 Hz as it fails to predict the initial response of the wing due to impact. However, from 50 – 140 Hz the model predicts the response of the inflatable wing to the impact. The data are further processed to determine the mode shapes identified with the model prediction.

The mode shapes can be visualized after data processing. Fig. 5.50 shows the first

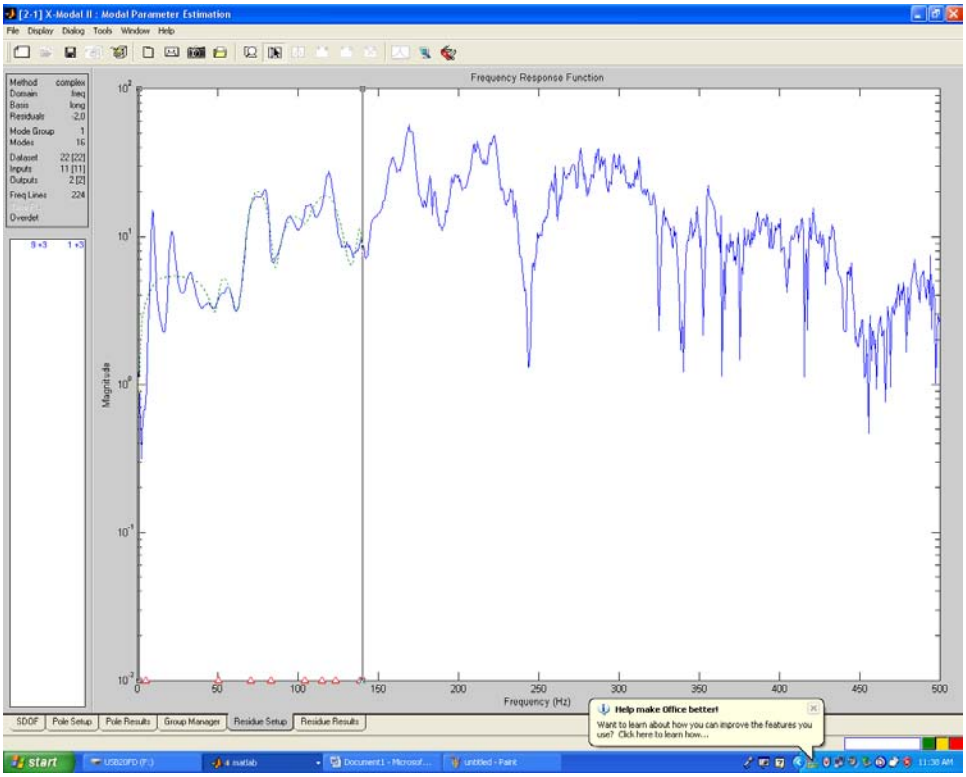

Figure 5.49: Residue set-up.

bending mode of the inflatable wing. The red lines connect the points where the static wing was impacted by the hammer. Thus, the red lines represent the non-displaced wing. The black lines represent the movement of the inflatable wing due to excitation of the first bending mode (note that the scale of the image is exaggerated in order to visualize the mode shape). The first torsional mode shape is seen in Fig. 5.51. The second bending and torsional mode shape can be seen in Fig. 5.52.

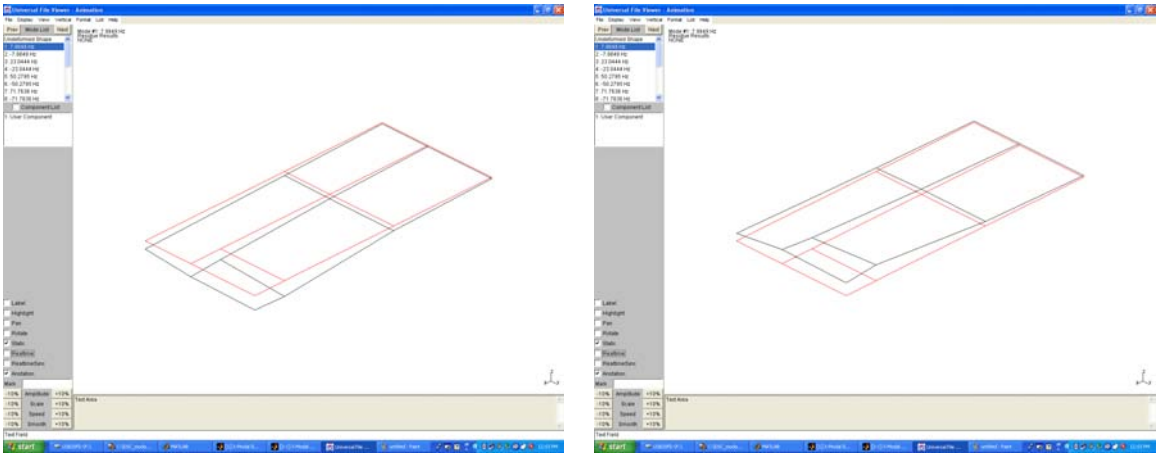

(a) 1^{st} Bending mode shape.

(b) 1^{st} Bending mode shape.

Figure 5.50: Deformed shape of the inflatable wing – 1^{st} bending mode shape (8.3 Hz).

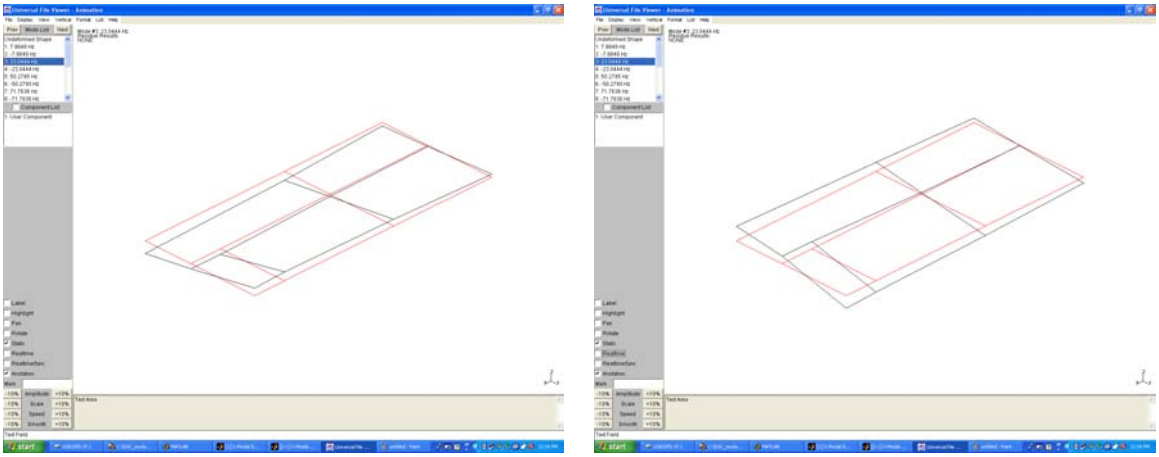

(a) 1^{st} Torsional mode shape.

(b) 1^{st} Torsional mode shape.

Figure 5.51: Deformed shape of the inflatable wing – 1^{st} torsional mode shape (23.0 Hz).

Table 5.3 shows the identified results of the first and second bending and torsional modes. Note that the damping values for the inflatable wings are high. A typical damping

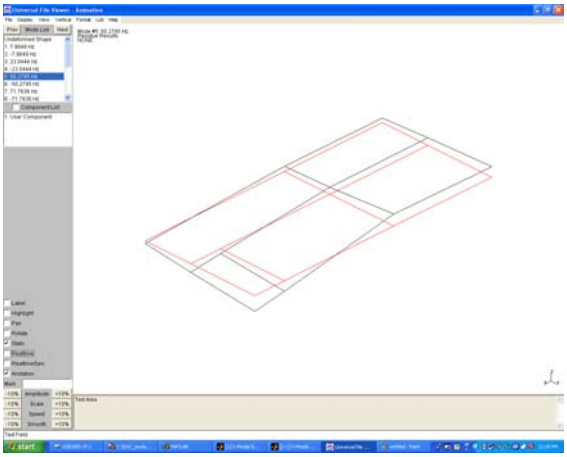

(a) 2^{nd} Bending mode shape.

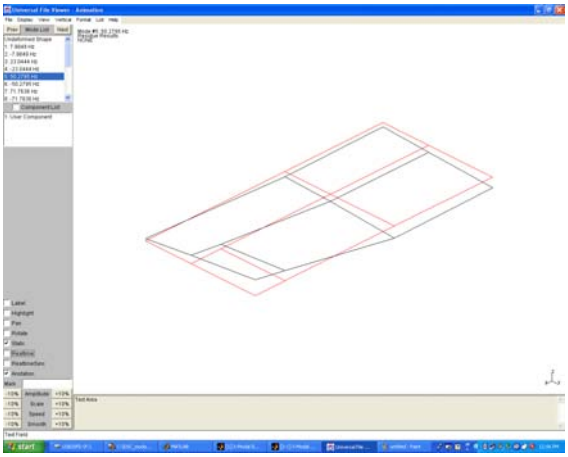

(b) 2^{nd} Bending mode shape.

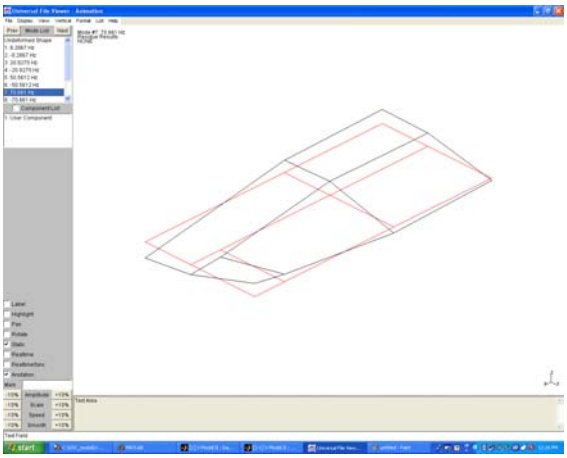

(c) 2^{nd} Torsional mode shape.

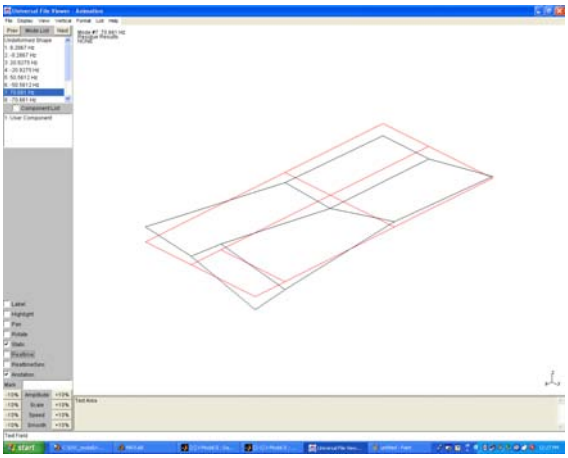

(d) 2^{nd} Torsional mode shape.

Figure 5.52: Deformed shape of the inflatable wing – 2^{nd} bending (50.7 Hz) and torsional (70.6 Hz) mode shapes.

Table 5.3: Ranges of 1^{st} and 2^{nd} bending and torsional modes.

Mode Shape	Range	Damping (%)
1^{st} Bending	8.3 Hz	≈10
2^{st} Bending	50.7 Hz	≈6
1^{st} Torsion	23.0 Hz	≈9
2^{st} Torsion	70.6 Hz	≈6

value for a metallic structure is 3 – 4%

5.6.3 Forced Vibration due to Dynamic Loading

Experiments were conducted in the Eiffel-type wind tunnel described previously. Fig. 5.53 and Fig. 5.54 respectively present demonstrate the laser set-up and a schematic of the set-up of the nylon wings in the tunnel.

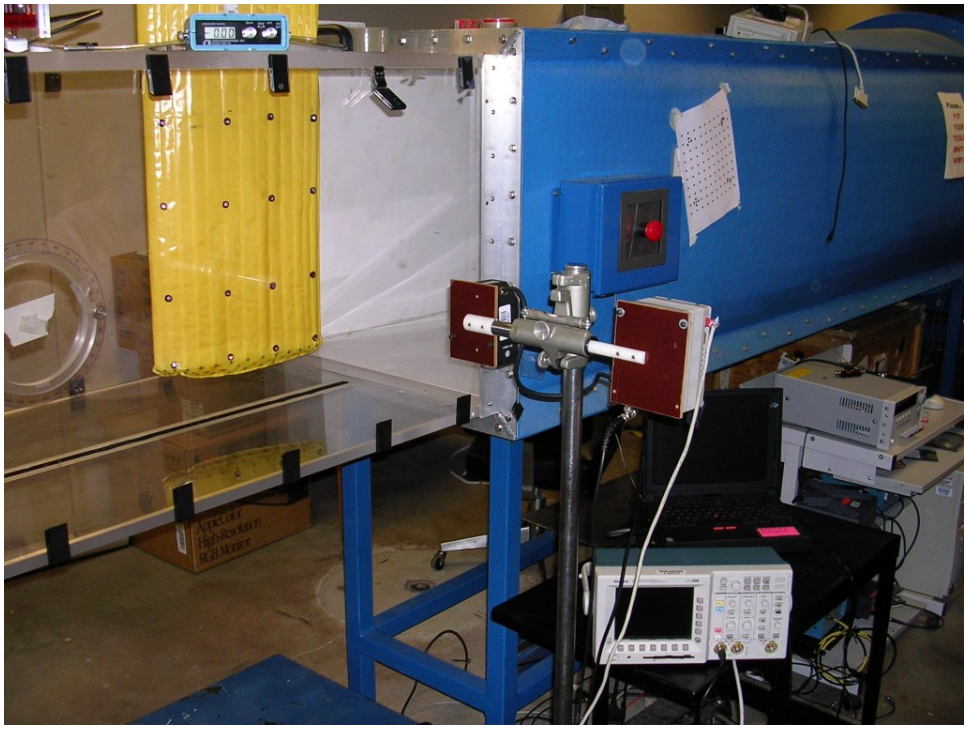

Figure 5.53: Laser set-up.

The design inflation pressure for the nylon inflatable wings was 41.4 kPa (6 psi). Vibrational data were collected for this inflation pressure only. The angle of attack was varied

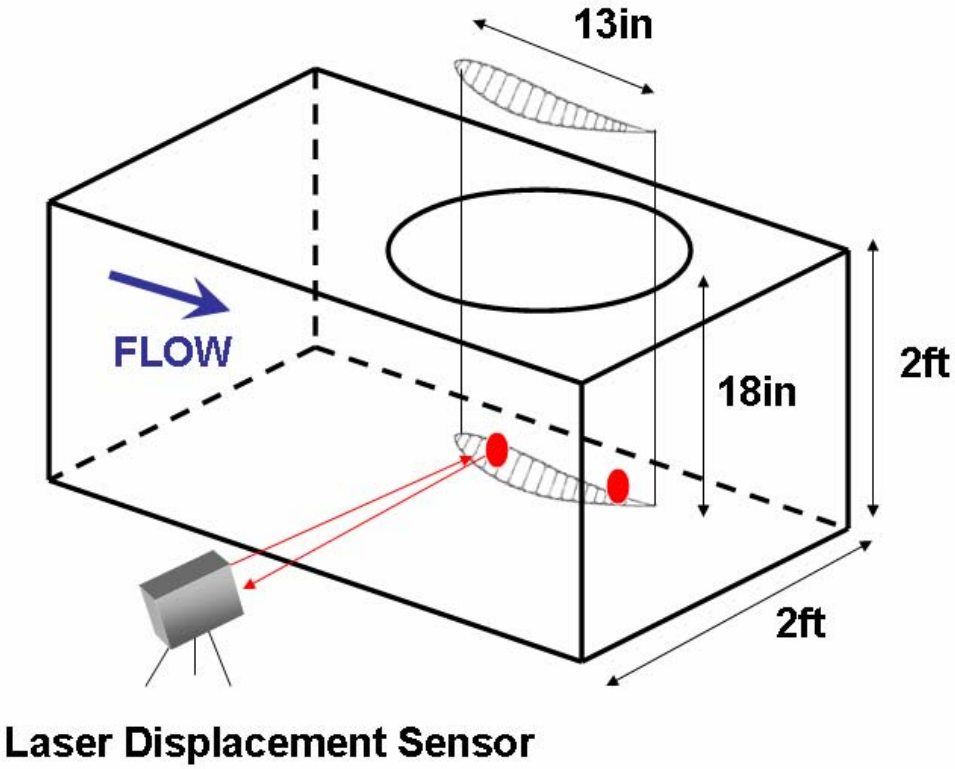

Figure 5.54: Schematic of laser set-up.

from -4° to 16°, in steps of 4°. Finally, seven different dynamic pressures, q_∞, were examined: 100 N/m^2, 178 N/m^2, 280 N/m^2, 400 N/m^2, 548 N/m^2, 807 N/m^2,and 1115 N/m^2. The dynamic pressures corresponded to approximate chord based Re numbers of $3 \cdot 10^5$, $4 \cdot 10^5$, $5 \cdot 10^5$, $6 \cdot 10^5$, $7 \cdot 10^5$, $8.5 \cdot 10^5$,and $1 \cdot 10^6$, respectively. The expected flight velocity of a vehicle utilizing the nylon wings was approximately 15 m/s (q_∞ between 100 - 178 N/m^2).

Arrangement and Experimental Procedure

Deformation measurements were made using a laser displacement sensor. The laser displacement sensor unobtrusively measured the displacement of the wing surface (Fig 5.54). The laser (Keyence LK-503) was connected to a laser controller (Keyence LK-2503) and then to a Zonic Medallion multichannel data acquisition system; these were set to high-precision mode. The laser was adjusted to ± 350 mm from the wing surface and gave an output of 10 mm/V. Thus, 1 mV corresponded to a wing displacement of 0.01 mm. The FFT analyzer was connected to a notebook PC via a PCMCIA card. Medallion fundamental acquisition software (ver. 4.00) was used to set a frame size of 8192, a bandwidth of 500 Hz, and a frame period of 6.4 s.

Two positions on the wing's surface were examined for each angle of attack and dynamic pressure case. The first position was near the 1/4 chord and the second was near the trailing edge of the wing. The locations were selected to identify different modes of response, including bending and torsional modes. After setting the appropriate dynamic pressure and angle of attack, the system was allowed to stabilize to steady state responce before data were recorded. Examples of the m-files used to examine this data can be seen in Appendix A.3.

Results

Spectral analysis of the data shows a typical response of the nylon inflatable wing at α = 4° and Re = $7 \cdot 10^5$ (Fig 5.55). The x-axis displays frequency while the y-axis is magnitude. Figs 5.56, 5.57 and 5.58 are cases corresponding to zero lift and stall. In these figures, the angle of attack (α) is held constant and the dynamic pressure is increased. Fig 5.56*a*, shows the frequency response at α = -4°. Fig 5.58*b*, shows the frequency response at α = 16°. This α value corresponds to the stall point to the wing and the flow surrounding the wing is unsteady. Hence in Fig 5.58*b*, more broadband response can be seen. Fig 5.59 shows the frequency response at $\alpha = 4°$ corresponding to a typical flight α value. Each Fig. has seven sub-plots. These sub-plots represent different Re values from 300,000 to 1,000,000. All the

sub-plots within the image represent data at the same angle of attack.

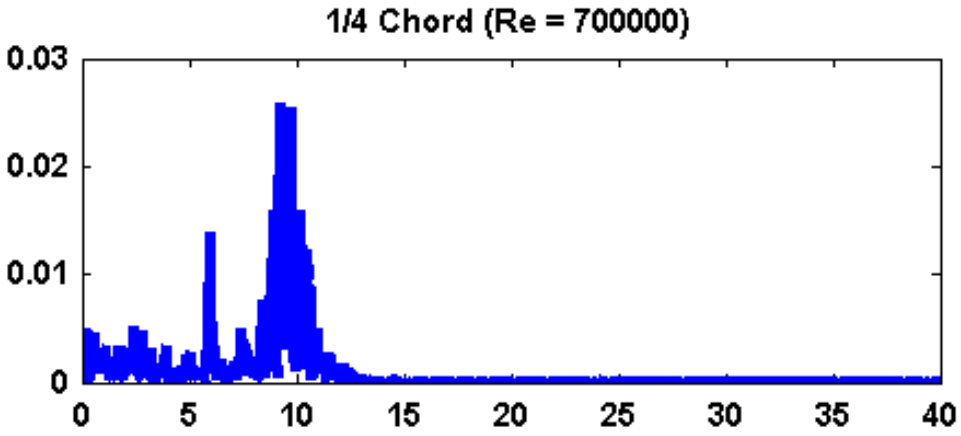

Figure 5.55: Frequency content at $\alpha = 4°$ ($q_\infty = 548$ N/m^2).

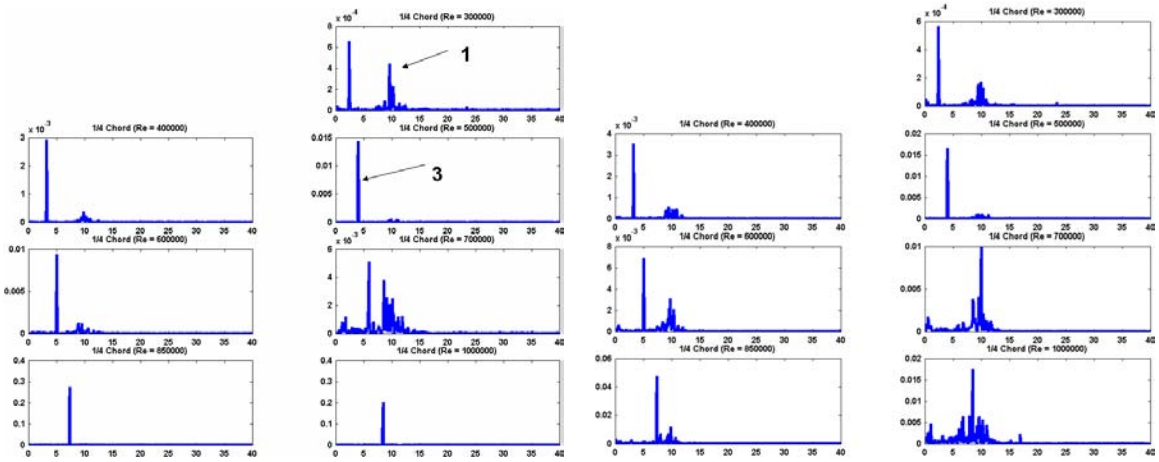

(a) Angle of attack (α) = -4°.

(b) Angle of attack (α) = 0°.

Figure 5.56: Frequency content results at α = -4° and $\alpha = 0°$.

Broadband frequency content is seen around 10 Hz. This can be seen as the arrow marked "1" in Fig's 5.56*a*, 5.58*b* and Fig 5.59. This broadband content is seen for all α values at low Reynolds (Re) numbers. The content does not change frequency over the range of α values and low Re values. As the Re values increase, the broadband frequency content in this range disappears. Thus in general as the Re number increases the broadband frequency content at 10 Hz diminishes. This can be seen in Fig's 5.56, 5.57, 5.58 and Fig 5.59.

A very low frequency response (with broadband character) is seen at 1.5 Hz. This low

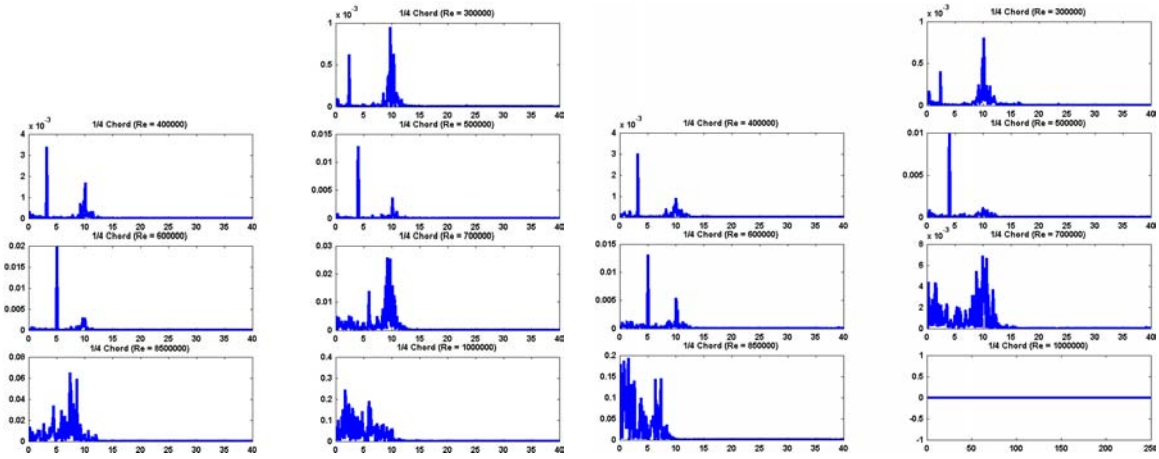

(a) Angle of attack (α) = 4°. (b) Angle of attack (α) = 8°.

Figure 5.57: Frequency content results at $\alpha = 4°$ and $\alpha = 8°$.

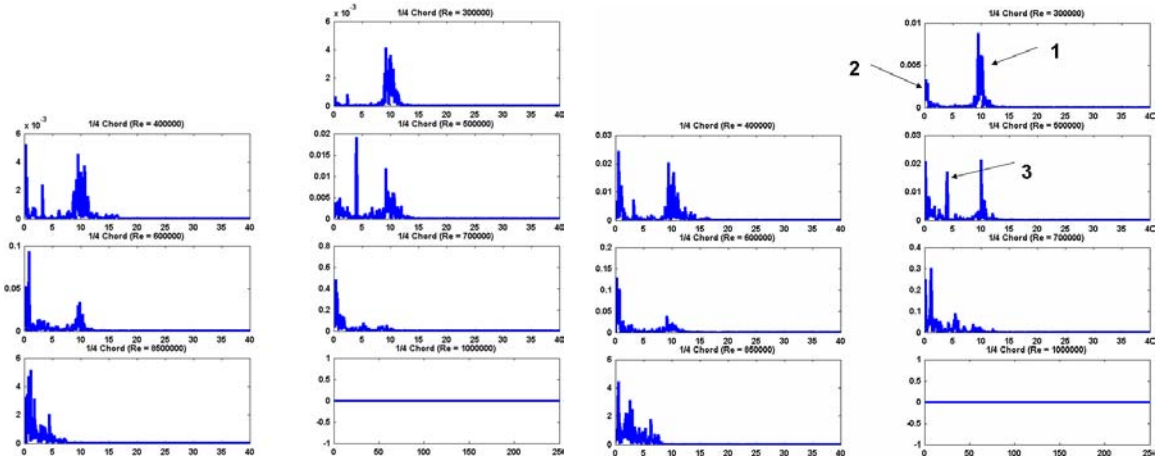

(a) Angle of attack (α) = 12°. (b) Angle of attack (α) = 16°.

Figure 5.58: Frequency content results at $\alpha = 12°$ and $\alpha = 16°$.

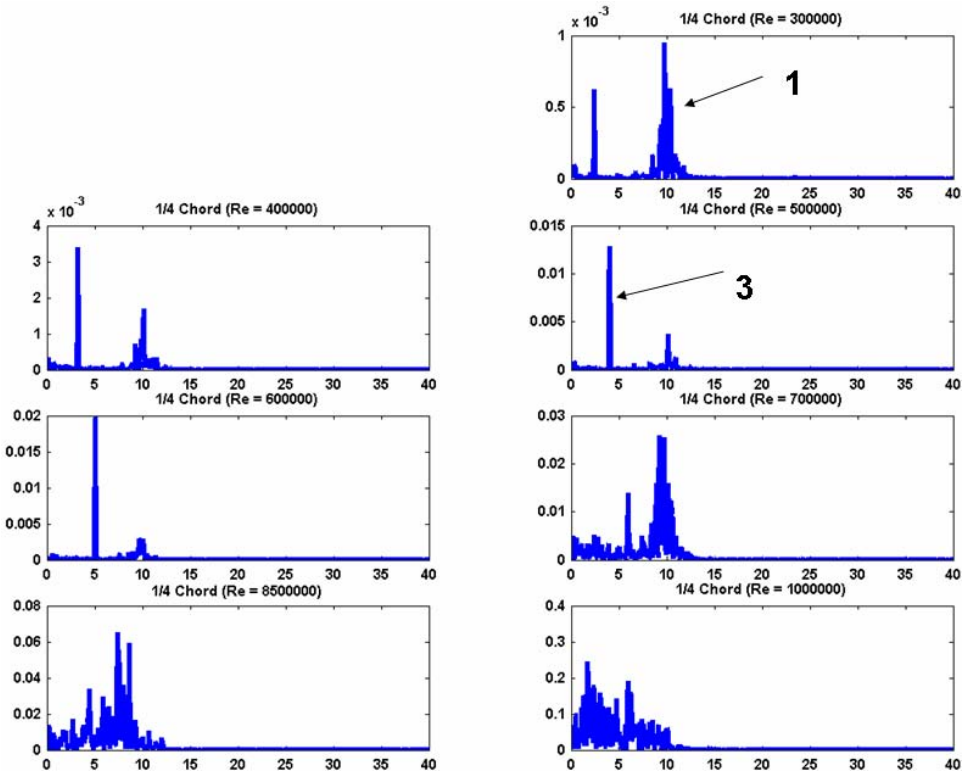

Figure 5.59: Frequency content results at $\alpha = 4°$.

frequency response is only seen at higher α values. The response is initially seen at $\alpha = 8^\circ$ and is prevalent throughout the higher α cases. This response can be seen in Fig 5.58*b*, highlighted by the arrow marked "2". The frequency response has a broadband character and is only seen at higher α values and was not affected by Re.

A narrow-peak harmonic response was seen at a frequency of 2.4 - 8 Hz (2.4 Hz $\leq$ f $\leq$ 8 Hz). This response can be seen in Fig 5.56*a* and Fig 5.59 highlighted by the arrow marked "3". The harmonic disappears as α increases above 8° and Re increases above $7 \cdot 10^5$. Generally the harmonic can be seen at low α values and tends to shift with Re. The harmonic has a combined effect between α and Re. At low α values the harmonic can be seen for a wide range of Re values. However, as α increases, the harmonic can only be seen at low Re. Thus, at high α and Re values, the response content is lost.

Chapter 6

AERODYNAMICS AND FLIGHT MECHANICS

The airfoil section and wing planform of the lifting surface are critically important to the performance of all flying vehicles [3]. Thus it is critical to understand the impact of the wing profile and the planform shape of the wing. In this Chapter a wake survey is used to understand the impact of the bumps on the wing surface, PIV is used to analyze the warped shape of the inflatable wing and various modeling techniques are used to calculate the impact of the warped shape of the wing.

6.1 Wind Tunnel Measurements

Inflatable wings contain internal baffles which are required to maintain the airfoil shape. These internal baffles cause surface perturbations or bumps on the profile surface. The bump radius is generally on the order of $2_c\%$. The effect of the bumps on the airfoil aerodynamics was analyzed through smoke-wire visulization detailed in Chapter 3.1.2. The initial investigation was qualitative, primarily at low dynamic pressures. Qualitative wake surveys were conducted to visualize the flowfield, which is important to better understand the aerodynamic performance. Quantitative three-dimentional wake surveys are a natural extention of wake imaging[102]. Thus, in addition, a quantitative investigation to examine the effect of the surface bumps on the airfoil's aerodynamic performance was performed. The dynamic pressure for this investigation was higher than for the wake imaging. The three-dimentional wake surveys compared the actual profile of the inflatable-rigidizable design with that of the ideal design.

6.1.1 Wake Survey

Traditionally, a wind tunnel using a strain-gauge type balance measures aerodynamic forces. This approach is recommended for measuring lift, but may not be the ideal methodology for measuring drag. This is because drag of a typical aircraft at reasonable incidence angles is often an order of magnitude less than the lift, making it more difficult to measure. Wake surveys allow for separate measurement of profile drag, induced drag and lift. The wake traverse method uses a seven-hole pressure probe to measure pressures and velocities

which are then converted into aerodynamic forces[102]. By applying the momentum integral theorem, through the use of a control volume, the following equation for drag can be obtained:

$$D = \int\int p_{t\infty} - p_t dS + \frac{\rho}{2}\int\int V^2 + W^2 dS + \frac{\rho}{2}\int\int ({U_\infty}^2 - U^2) dS \tag{6.1}$$

where p_t is the total pressure, ρ is density, and V, W are the cross-flow velocity components in the measuring plane perpendicular to the tunnel axis. U and ρ denote the velocity in the direction of the tunnel axis and the density, respectively. The subscript ∞ indicates the undisturbed free-stream values. The first term is an integral of the total pressure deficit, which is a measure of the profile drag. The second term, identified as the vortex drag, represents the kinetic energy of the cross flow. The third term contains contributions from both profile drag and induced drag. The second term is ignored because the drag measurements of interest are two-dimensional. The drag equation then becomes the following with the first and second terms ignored:

$$D = \frac{\rho L}{2}\int ({U_\infty}^2 - U^2) dx \tag{6.2}$$

the momentum integral theorem is then applied to obtain the lift equation:

$$L = \rho\int\int ({W_\infty}^2 - W^2) V dS = \rho L\int ({W_\infty}^2 - W^2) dx \tag{6.3}$$

where L is the width of the tested section. U_∞ and W_∞ are the free-stream velocity, which can theoretically be determined by the wind tunnel speed.

Wake Survey Investigation

The Re was varied from 150,000 to 500,000; the results are shown in Fig. 6.1. Note that the red curves correspond to ideal profile and the blue curves correspond to the bumpy profile. The graphs depict the momentum deficit in the wake. The x-axis represents the height of the pressure probe, while the y-axis depicts the momentum deficit. The relevant quantity is the momentum deficit in the wake, given by the difference between free-stream speed U_∞ and velocity at the region of interest u. As highlighted in Chapter 2.3.1, the ideal or smooth E398 profile would start to show better performance at Re values greater than 0.5 million. This is evidenced by the ideal profile showing slightly fewer momentum deficits than the bumpy profile at an Re value of 0.25 million shown in Fig. 6.1a. At an Re value of 0.5 million (closer to the design point of E398), the bumpy profile shows drastic momentum deficits as compared to the smooth profile (Fig. 6.1d). The latter case approaches the rough

airfoil borderline performance limit suggested by McMasters and Henderson. The m-file used for this data can be seen in Appendix B.1.

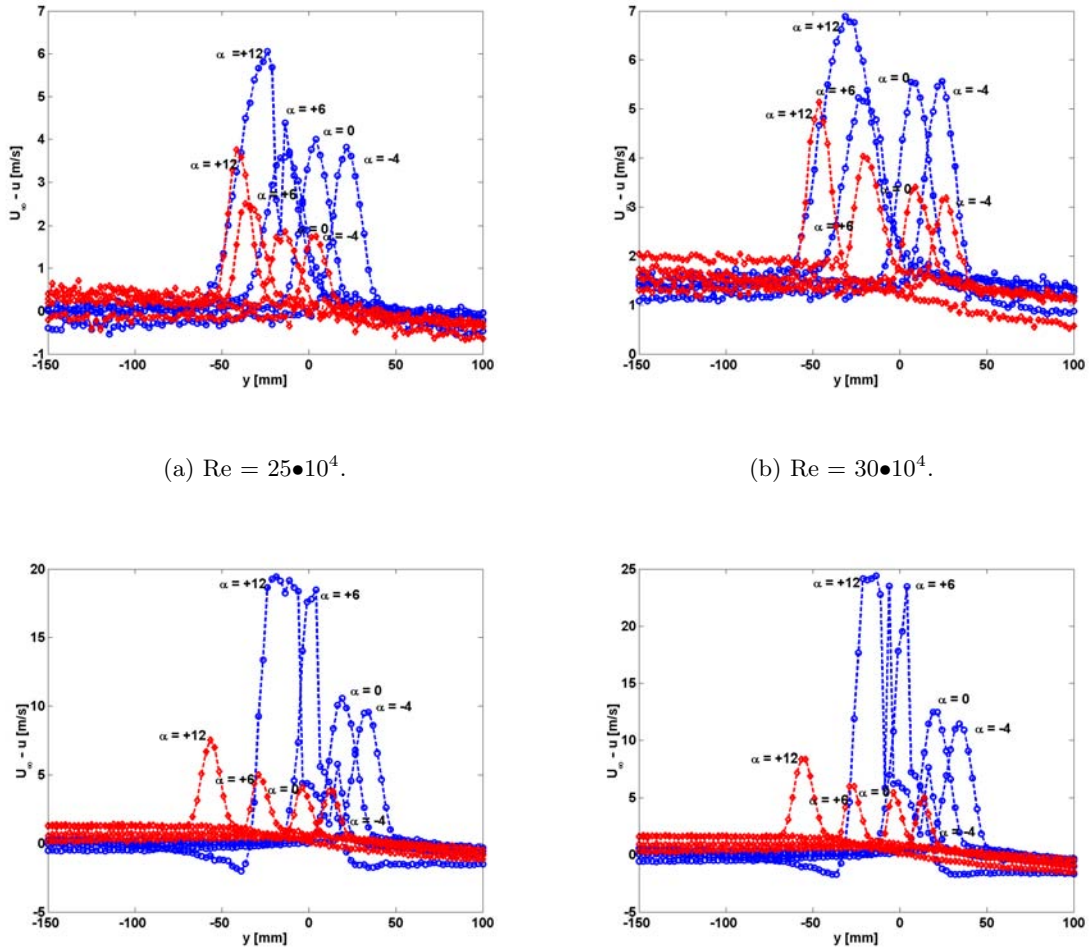

(a) Re = 25•10^4.

(b) Re = 30•10^4.

(c) Re = 40•10^4.

(d) Re = 50•10^4.

Figure 6.1: Wake Survey Results – Momentum deficit vs. Height (Red – Ideal profile, Blue – Bumpy profile).

6.1.2 PIV Circulation Analysis

A three-dimensional printer was used to construct solid wind tunnel models of the Vectran wings. Five models were made from the data generated from the photogrammetry analysis of the torsional warping of the Vectran wing (highlighted in Chapter 5.1.3). The models varied from the baseline model with no warp, to the most extreme case of 17° of warp at the wingtip. The models constructed had twists of 0°, 2.5°, 5°, 10°, 17° degrees of

twist at the wingtip. The degree and location of the twist matched the photogrammetry results generated above from the deformation forces applied to the Vectran wings. The models had a semi-span of 25.5 cm, a mean aerodynamic cord of 10.8 cm, and an aspect ratio of 5.39, a scaled (28%) copy of the Vectran wings.

Experiments were then conducted in a low-speed wind tunnel detailed in Section 4.5.2. The tunnel was used for PIV measurements using the technique detailed in section 4.4. Each of the models were tested at six different α values: -4°, 0°, 4°, 8°, 12° and 16°. Additionally, the models were tested at two different Re: 5×10^4 and 1×10^5. The equipment and methods used for the PIV measurements is described in Section 4.4.

Each PIV run recorded over 120 images for processing; this resulted in a minimum of 61 vector and vorticity fields from which to generate mean flow field and statistics. Fluid particles registered by individual CCD pixels were advected with individually estimated velocities and total accelerations. The velocity field needed to initialize the Lagrangian Parcel Tracking (LPT) [103] process was obtained from a standard DPIV algorithm which uses multiple passes, integer window shifting and adjustable windows. Both the LPT and DPIV algorithms employed a rigorous peak-detection scheme to determine velocity vectors and use the local-velocity gradient tensor to identify spurious velocity vectors. It was noted that the LPT algorithm worked well in the vortex flow field, which was characterized by high-deformation rates where DPIV algorithms were plagued by biasing and limited dynamic range. No smoothing algorithms or other post-processing techniques were employed on the data. Vorticity, being a component of the velocity-gradient tensor, was calculated spectrally at each grid point as an intrinsic part of the LPT algorithm. The raw images were processed as image pairs in 32x32 interrogation areas to give 61 tensors containing the flow information, i.e. the velocities and velocity gradients. Note that the sampling rate of the present PIV system was limited to a nominal value of 10 Hz. Appendix B.2, contains the m-file used for this research.

Circulation (Γ), was then calculated at a range of distances from the vortex center. Lift can be calculated as,

$$L = \rho_\infty U_\infty \Gamma b$$

and

$$\Gamma = \frac{2C_L U_\infty S}{b\pi}$$

which gives

$$C_L = \frac{2\Gamma b}{U_\infty S} = \frac{2\Gamma bc}{\nu ReS}$$

Fig. 6.2*a* shows the raw images captured by the PIV system. The images were then processed in MATLAB as seen in Fig. 6.2*b*.

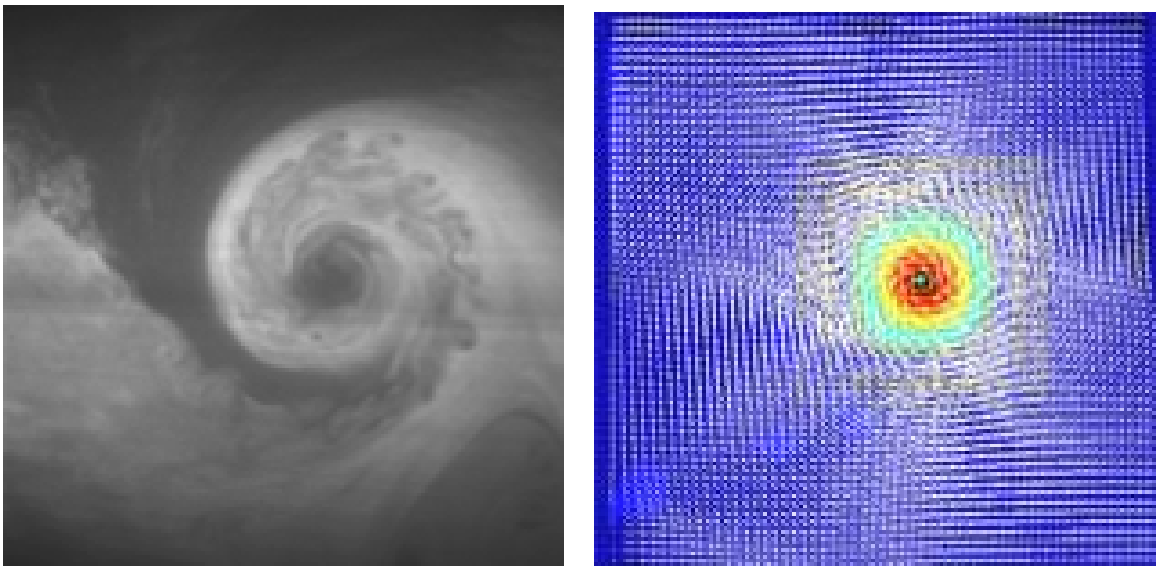

(a) Raw image.

(b) Flow field.

Figure 6.2: Raw image of tip vortex generated from solid models and resulting flow field.

Results can be seem in Fig's. 6.3*a* and *b*. Fig. 6.3*a*, show the circulation generated from the non-warped wing model. Additionally, Fig. 6.3*b* shows the circulation generated from the warped wing model. Note that the warped wing model generates approximately four-times the amount of lift of the non-warped case. These figures verify the lifting line code seen in Section 6.2.1. The deformed wing is shown to produce substantially more lift than the non-deformed wing. Thus, roll authority is possible through manipulating the wing in this manner. The warped wing at 17° twist, produced four times the lift as generated by the non-warped wing. Both figures in 6.3 calculate circulation in two different methods. The upper curve calculates circulation from velocity data obtained directly from the PIV data. The lower curve calculates circulation from vorticity; this calculation is typically under-predicted. Note that the y-axis on the plots in Fig. 6.3 are on different scales.

6.2 Aerodynamic Modeling of Inflatable Wings with Wing Warping

As seen in Chapter 5, elastic deformation of the inflatable wings due to flight loads can have a profound influence on the wing structure. This can influence performance, handling qualities, flight stability, and control effectiveness/reversal phenomena. Here, some of the

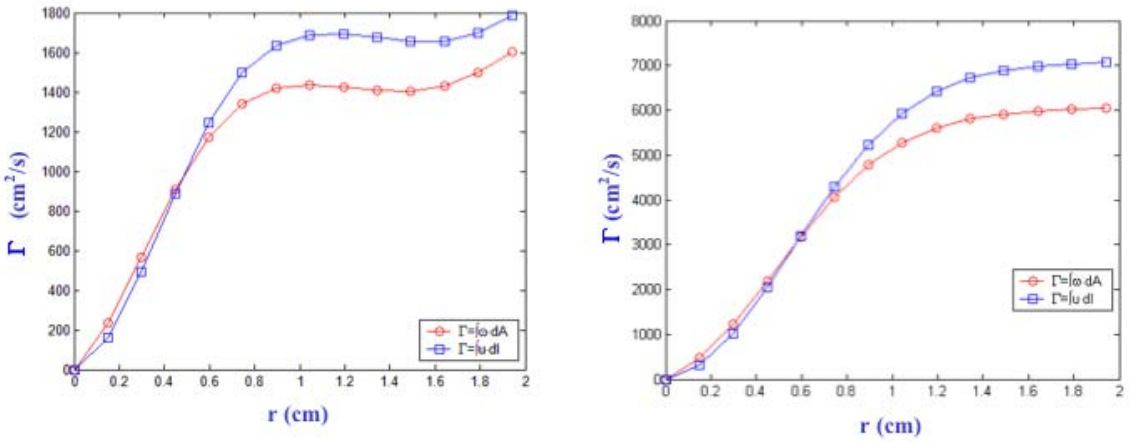

(a) Re=100K, AoA=4°, Warp=0°.

(b) Re=100K, AoA=4°, Warp=17°.

Figure 6.3: Sample circulation distribution from solid models.

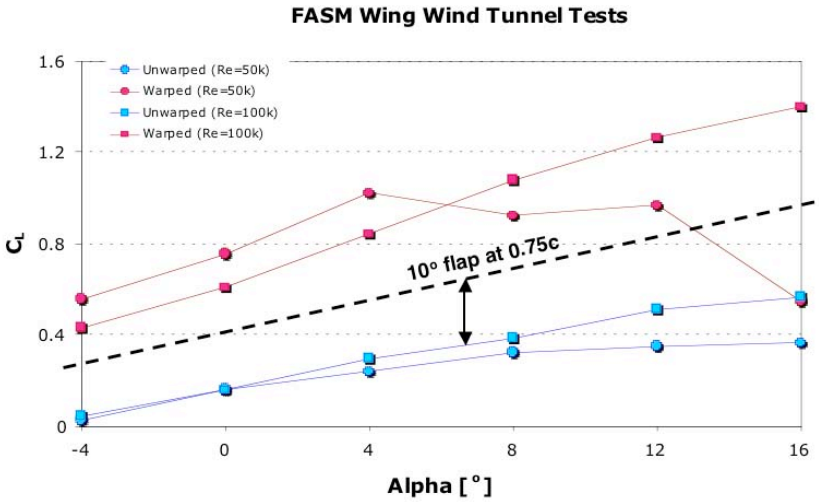

Figure 6.4: Lift coefficient vs. α of the Vectran wing.

performance characteristics of the inflatable wings are modeled.

6.2.1 Lifting line analysis – Vectran wings

A lifting line analysis was done on the Vectran inflatable wings. Analysis was performed to determine the effect of warping on wing performance. Data used in this analysis were obtained from Chapter 5.1.3. The amount of circulation produced by the wing due to the warping mechanisms was examined to determine aerodynamic performance. The warping was assumed to symmetric implying that the warping mechanism could increase or decrease the span-wise angle of attack. This model used $\alpha = 0°$, $a_o = 0.14$/radian, $\alpha_{C_l=0} = -4°$ and a tip twist of $\pm 16°$. Lift distribution results are shown in Fig. 6.5. In this figure, circulation is shown relative to the semi-span. The blue line depicts the non-warped semi-span while the warped wing is represented by the red lines. The top red line represents a positive wing twist, where the local α value increases from wing root to tip. The lower red line represents a negative wing twist, where the local α value decreases from wing root to tip. Substantial positive and negative modifications to the baseline distribution are possible through span-wise twisting of the airfoil. This illustrates that substantial rolling moments could be generated if the wing was warped across the entire semi-span. This process was repeated for the warped shapes of the Vectran wings highlighted in Chapters 5.1.3 and 6.1.2. Appendix B.3, shows an example of the m-files used for during this lifting line analysis.

As noted in the Chapter 6.1.2, physical properties of the inflatable wings were acquired using photogrammetry. The data were captured during laboratory warping of the Vectran wing detailed in Chapter 5.1.3. Analysis revealed span-wise variations of the profile between the warped and non-warped cases. Solid models (Fig. 6.8) of the Vectran wings were constructed based upon this surface data (Chapter 6.1.2). The data gave a detailed description of the warped wing surface, including no warp, to the most extreme case of 17° of warp down at the wingtip as seen in Fig. 6.6. Fig. 6.6 and Fig. 6.7 show the non-warped and warped Vectran wings. In each figure the non-warped point cloud of the Vectran wing is displayed above the deformed shape. The points were individual markers detected by the photogrammetry system. Chord lines were used to connect points at the leading and trailing edges. The numbers and arrows on each figure highlight the change in span-wise angle of attack of the wing. Thus, twist in the wing was calculated. The amount of twist in the wing varied as a function of the wing stiffness. The wing stiffness was based on the inflation pressure, low inflation pressure corresponded to low wing stiffness and higher wing twist. Fig. 6.6 shows the effect of the twisting load on the Vectran wing when the wing

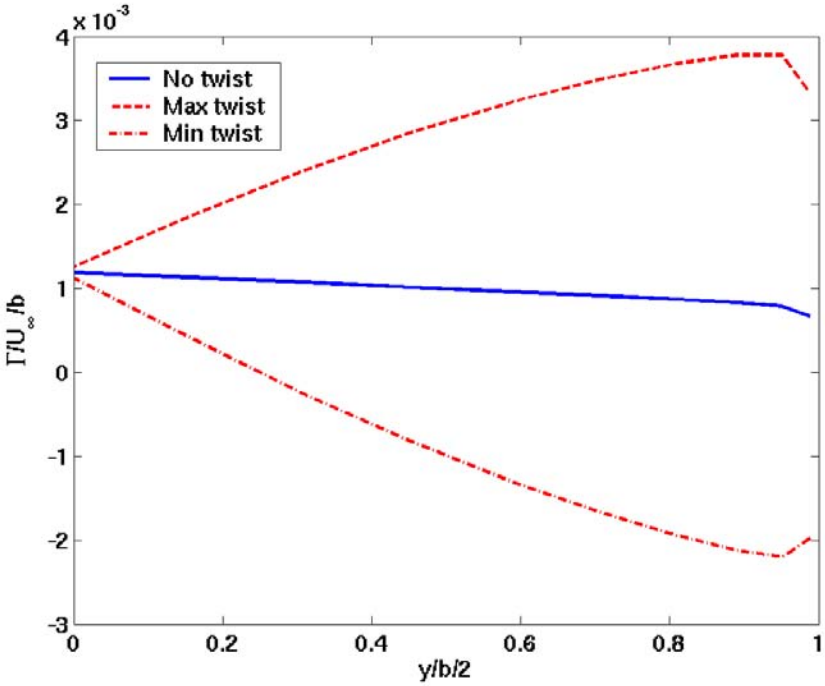

Figure 6.5: Lifting line load distributions for the twisted airfoil.

is inflated to 69 kPa (10 psi) while, Fig. 6.7 shows the effect the same twisting loads have on the wing at 138 kPa (20 psi). As seen in these figures there is a significant decrease in the amount of twist as the inflation pressure is increased. At 69 kPa (Fig. 6.6), the maximum twist at the wingtip is 17°, while at 138 kPa (Fig. 6.7) the maximum twist generated at the wingtip was 10°. This was the maximum amount of twist the warping mechanism could generate based on the inflation pressure. Additional wing twist were also examined in the lifting-line analysis, these included wing twist of 0°, 2.5°, 5°, 10°, 17° of twist. The degree and location of the twist matched the photogrammetry results generated from the deformation forces applied to the Vectran wings.

The Vectran wing profile was based on the NACA 4318 profile. The wings had a span of approximately 1.8 m (6 ft), a taper ratio is 0.65, and an aspect ratio of 5.4. The Vectran wing has a root chord of 0.43 m (17 in), a tip chord length of 0.28 m (11.05 in) and a mean aerodynamic chord length of 0.36 m (14.24 in). The models had a semi-span of 25.5 cm, a mean aerodynamic cord of 10.8 cm, and an aspect ratio of 5.39, matching the Vectran wing.

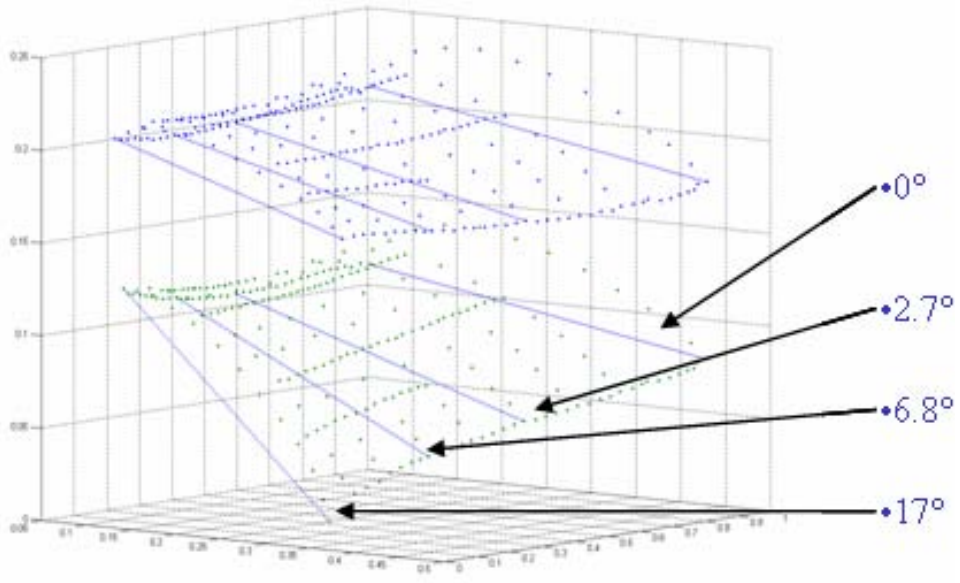

Figure 6.6: Vectran wing twist at 10 psi inflation pressure.

Procedure and Results

As seen in Fig. 6.6 and Fig. 6.7 chord lines were connected from the leading to the trailing edges. The variation in angle of attack (α) over the span of the wings can be seen

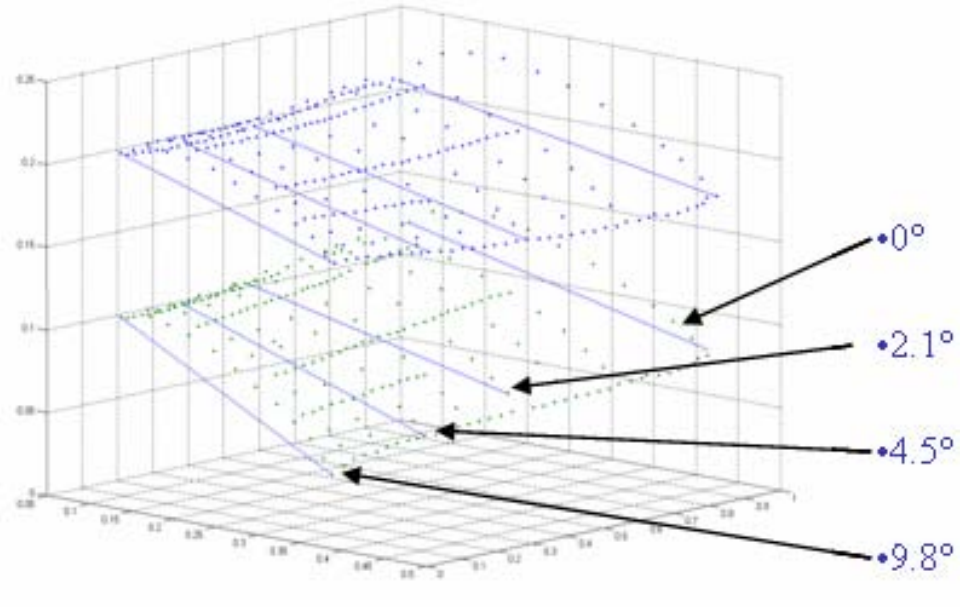

Figure 6.7: Vectran wing twist at 20 psi inflation pressure.

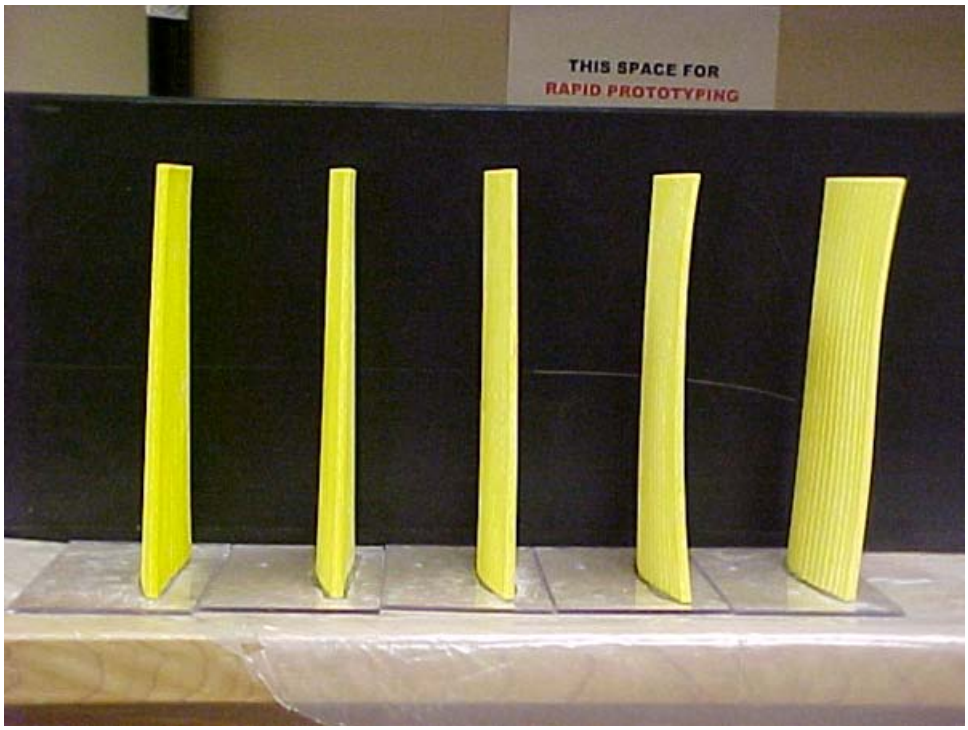

Figure 6.8: Solid models of Vectran Wings.

in Fig. 6.9 *a*. Here, the full span of the wings is shown using the warping mechanism. The mechanism warps one semi-span while not warping the other. Fig. 6.9*a*, shows one semi-span which is non-warped (-0.91 - 0 m) and the adjacent semi-span which is warped (0 - 0.91 m). The warped semi-span displays numerous lines indicating the degree to which the semi-span has been warped and its corresponding inflation pressure. Fig. 6.9*b*, represents a detailed view of the span-wise twist at 69 and 138 kPa (10 and 20 psi) inflation pressures over the warped semi-span. U_∞ is simulated at 15 m/s, which corresponds to a Re of 370,000.

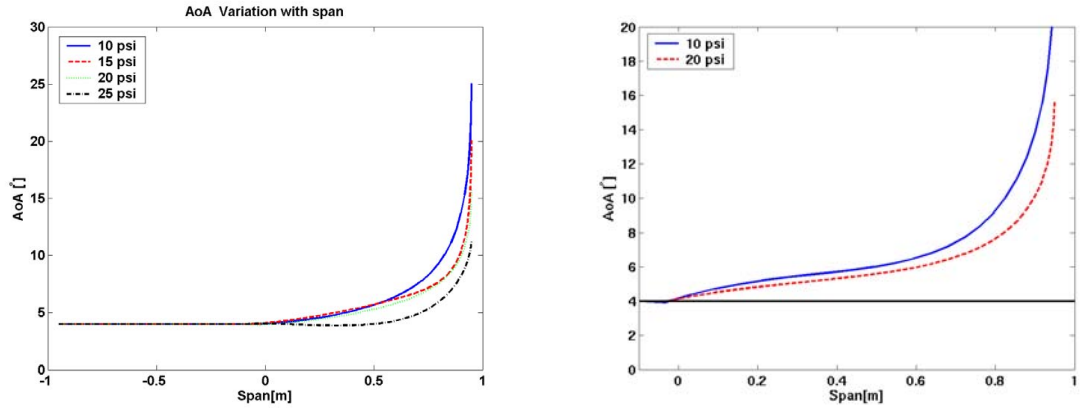

(a) Angle of Attack variation over the span.

(b) Wing twist at 10 and 20 psi.

Figure 6.9: Lifting line prediction for the warped airfoil.

Fig. 6.10 illustrates the predicted circulation from the wing twist at inflation pressures of 69 and 138 kPa (10 and 20 psi). Note that the area under the curve increases as the wing is allowed to twist. This corresponds to an increase in lift generated from the airfoil. As the twist was not linear; higher α deflections were measured toward the wingtip and at lower inflation pressures.

Fig. 6.11 shows the predicted lift generated for all the inflation cases over the span. The twist at each inflation pressure corresponds to the the twists tabulated in Table 5.1. Note that only the starboard wing is warped. The circulation predicted increases toward the wingtip in each case. This is due to higher wing twist at the wingtips. The highest predicted circulation is for the lowest inflation case where twist was 17°. The difference between the area under each curve on both semi-spans gives a prediction of the roll moment coefficient.

Note that the left hand semi-span produces nominal lift while the right hand semi-span produces increased lift as only one semi-span was warped in the positive (increasing alpha) direction. From this, change in roll moment coefficient, ΔC_l can be calculated. The roll

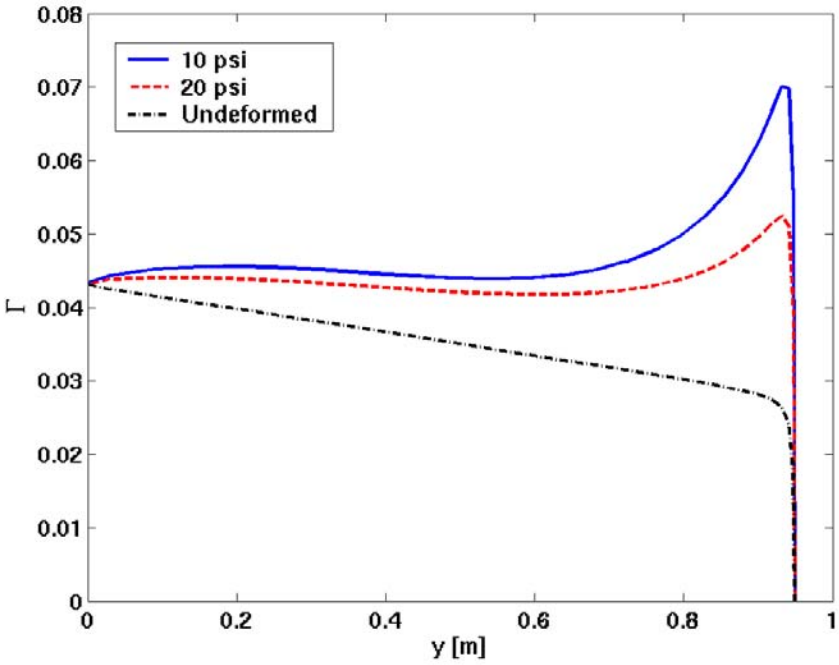

Figure 6.10: Lifting line prediction for 10 and 20 psi warped airfoil.

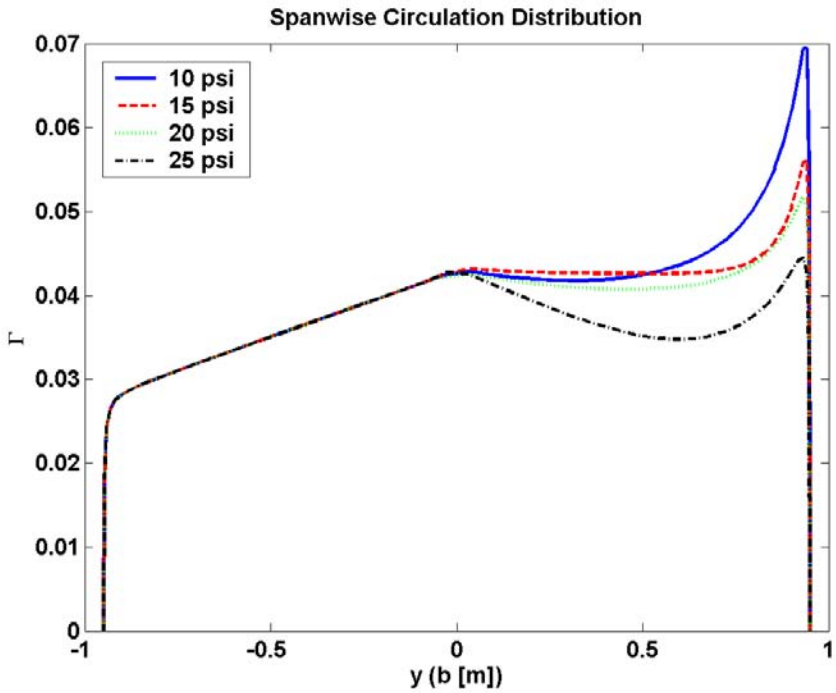

Figure 6.11: Circulation generated by the non-warped and warped semi-spans.

moment is given from Eqn. 6.4, where the change in lift coefficient is given by Eqn. 6.5

$$\Delta M_{ROLL} = \Delta L y \tag{6.4}$$

$$\Delta C_l = \frac{\Delta L}{qSb} = \frac{C_l c y dy}{Sb} \tag{6.5}$$

$$\Delta C_{l\delta_a} = \frac{dC_l}{d\delta_a} = \frac{2C_{l\alpha_w}\tau}{Sb}\int_{y_1}^{y_2} c y dy \tag{6.6}$$

The results were calculated and can be seen in Fig. 6.12. Substantial roll control was available with inflation pressures at or lower than 138 kPa (20 psi). Above this value, roll control dropped significantly. While still non-negligible, adequate roll control may not have been available for gust response and rapid maneuvering. Based on this analysis, flight testing of this mechanism were conducted, detailed in Chapter 7.2.1.

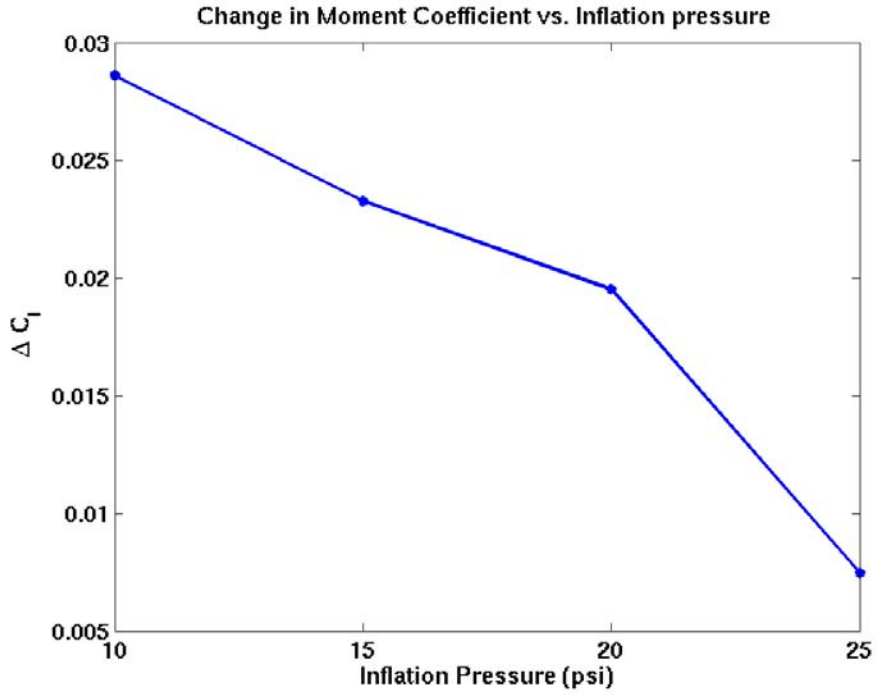

Figure 6.12: Lifting line prediction for rolling moment coefficient.

6.2.2 Lifting line analysis – nylon wings

As seen in Chapter 5, the nylon wings experienced aeroelastic deformation at low inflation pressures, and high dynamic loading conditions. The aeroelastic deformation is plotted in Fig 6.13. Fig. 6.13 details the span-wise change in α from the "No Flow" case

for each dynamic pressure and with an inflation pressure of 13.8 kPa (2 psi). Here the airfoil was initially set at an α value of 8° in Fig. 6.13*a* and an α value of 16° in Fig. 6.13*b*. This change in the α value is plotted relative to the span location in Fig 6.13*a* and *b*. By placing the α variations in a lifting line code, predictions of the change in lift due to the aeroelastic deformation could be made. Fig's. 6.14*a* and *b* shows the predicted lift generated from each semi-span as the aeroelastic effects become prevalent. Note that this was the lift distribution of one semi-span. The area under each of the curves represents the amount of lift generated. As the deformation increased due to dynamic pressure, the lift generated increased due to the wash-in twist.

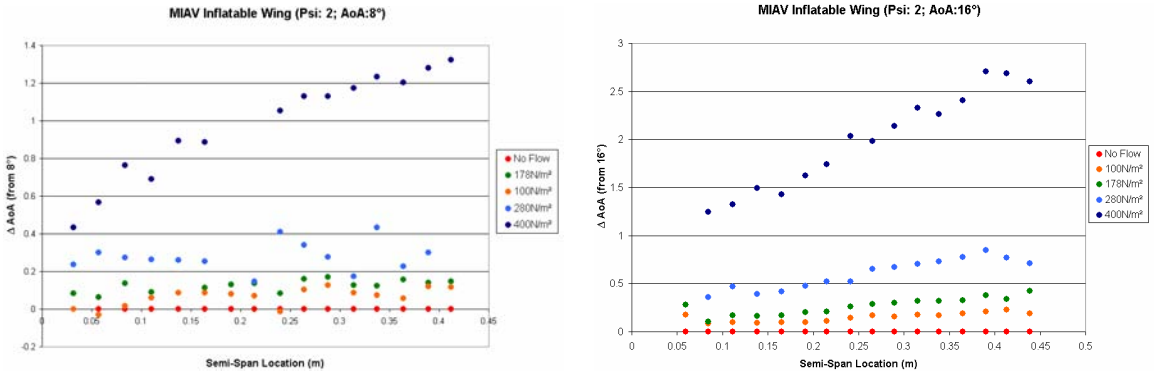

(a) $\alpha = 8°$. (b) $\alpha = 16°$.

Figure 6.13: Change in local angle of attack with increasing dynamic pressure at 13.8 kPa (2 psi).

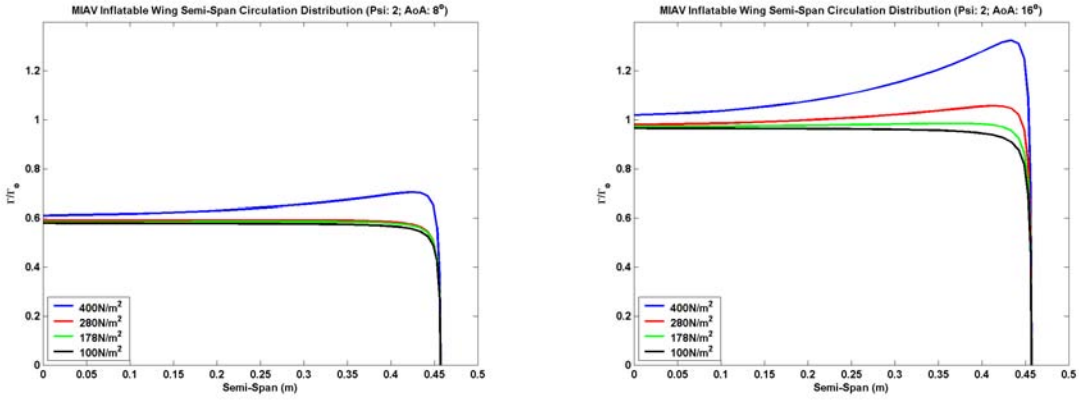

(a) $\alpha = 8°$. (b) $\alpha = 16°$.

Figure 6.14: Nylon Inflatable Wing Semi-Span Circulation Distribution at 13.8 kPa (2 psi).

Table 6.1: Nylon Wing twist at 13.8 kPa (2 psi).

Inflation Pressure [kPa (psi)]	Dynamic Pressure [N/m^2]	Wing mount α [°]	Mid Point α [°]	Wingtip α [°]
13.8 (2)	100	0	0	0
		4	4.1	4.2
		8	8	8.1
		12	12	12
		16	16.1	16.3
13.8 (2)	178	0	0	0
		4	4.2	4.3
		8	8	8.2
		12	12.2	12.4
		16	16.5	16.8
13.8 (2)	280	0	0	0
		4	4.5	4.8
		8	8.3	8.5
		12	12.3	12.7
		16	16.7	17
13.8 (2)	400	0	0.1	0.2
		4	5	5.1
		8	9.1	10.6
		12	14.3	14.5
		16	17.8	18.6

6.2.3 Nylon wing performance – aeroelastic effects

Performance of the nylon wing following aeroelastic deformation is of interest. As can be seen in Fig. 6.13 the nylon wings twist with increasing dynamic pressure. The twist is defined as "wash-in" twist meaning that the α value increases from wing root to wingtip. The nylon wing was placed in the wind tunnel as detailed in Chapter 5.4.2. The wings had a semi-span of 0.45 m and a chord length of 0.33 m. However, due to the constraints of the tunnel test section, the wing was only partially inserted into the tunnel to a distance of 0.45 m (18 in). As in Fig. 6.13 the change in α of the nylon wing was used to examine the aeroelastic effects on the performance of the wing. Unlike Fig. 6.13 not all the span-wise α values were calculated. Here only the α value at the mid point of the semi-span and the α value of the wingtip were calculated. These data can be seen in Tables 6.1, 6.2 and 6.3.

For this investigation, the wing was assumed to twist uniformly from the wing root to the mid-point and from the mid-point to the wingtip. While this was not completely accurate, it was representative of the wing twist. Data were placed into a vortex lattice

Table 6.2: Nylon Wing twist at 27.5 kPa (4 psi).

Inflation Pressure [kPa (psi)]	Dynamic Pressure [N/m^2]	Wing mount α [°]	Mid Point α [°]	Wingtip α [°]
27.5 (4)	100	0	0	0
		4	4	4
		8	8	8.1
		12	12	12
		16	16	16.1
27.5 (4)	178	0	0	0
		4	4	4
		8	8	8.2
		12	12.2	12.3
		16	16.3	16.5
27.5 (4)	280	0	0	0
		4	4.1	4.2
		8	8.3	8.5
		12	12.5	12.8
		16	16.6	16.8
27.5 (4)	400	0	0.1	0.2
		4	4.2	4.3
		8	8.5	8.7
		12	13.1	13.5
		16	16.8	17

Table 6.3: Nylon Wing twist at 41.4 kPa (6 psi).

Inflation Pressure [kPa (psi)]	Dynamic Pressure [N/m^2]	Wing mount α [°]	Mid Point α [°]	Wingtip α [°]
27.5 (4)	100	0	0	0
		4	4	4
		8	8	8
		12	12	12
		16	16	16.1
27.5 (4)	178	0	0	0
		4	4	4
		8	8	8
		12	12.1	12.2
		16	16.3	16.5
27.5 (4)	280	0	0	0
		4	4	4.1
		8	8.1	8.3
		12	12.3	12.5
		16	16.4	16.6
27.5 (4)	400	0	0.1	0.2
		4	4.2	4.3
		8	8.3	8.5
		12	13	13.2
		16	16.5	16.8

code – "Tornado". [104] Tornado is a 3D-vortex lattice program with a flexible wake and runs through Matlab. Tornado's outputs are: 3D forces acting on each panel, as well as aerodynamic coefficients in both body and wind axis. In addition, Tornado derives the stability derivatives with respect to angle of attack, angle of sideslip, angular rates and rudder deflections of the vehicle. Tornado is based on standard vortex lattice theory stemming from potential flow theory. The wake coming off the trailing edge of every lifting surface is flexible and changes shape according to the flight condition. For example: a rolling aircraft will have a "corkscrew" shaped wake, which will influence the aerodynamic coefficients. The classical "horse-shoe" arrangement of other vortex-lattice programs has been replaced with a "vortex-sling" arrangement.

Initially, the wing was created as seen in Fig. 6.15 by specifying geometry. Span, chord length, profile shape, taper ratio, twist, and sweep were specified. One semi-span was created according to the data detailed above and then mirrored. Thus, both semi-spans account for the aeroelastic deformation. The total span of the wing model was 0.9 m. Next the flight conditions were specified including, α, β, roll rate, yaw rate, pitching rate, and flight speed. Fig. 6.15*a*, shows the 3D wing configuration while Fig. 6.15*b* shows the C_p distribution. After processing the data, Tornado computed the results for the specified geometry and flight condition. A sample can be seen in Fig. 6.16.

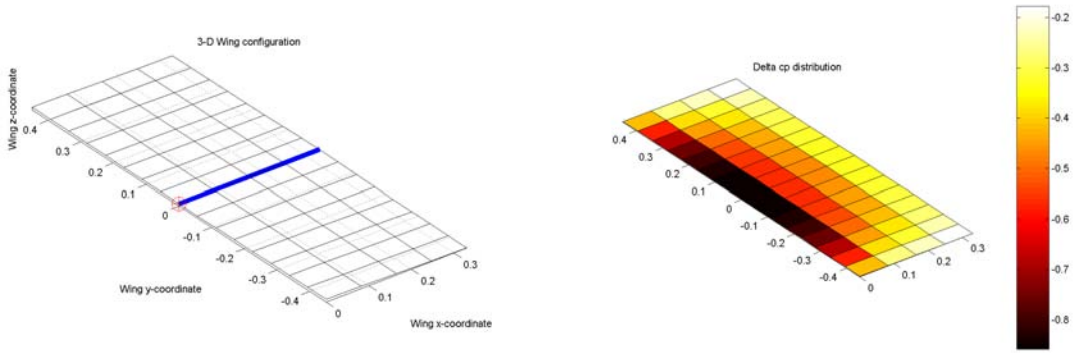

(a) 3D Wing Configuration (4 psi, $\alpha = 16^\circ$, 400 N/m^2).

(b) C_p Distribution (2 psi, $\alpha = 4^\circ$, 178 N/m^2).

Figure 6.15: Modeling the nylon wing using Tornado.

Fig. 6.17 shows C_l relative to C_d for the nylon wing at the three different inflation pressures investigated. As illustrated, there is minimal variation in the ratio of lift to drag. Fig. 6.18 shows the lift to drag ratio relative to α. Here there is slightly more variation in

Tornado Computation Results

JID:	ads19	Downwash matrix condition:	9.5625		
Reference area:	0.29718				
Reference chord:	0.3302	Reference point pos:	0 0 0		
Reference span:	0.9	Center of gravity :	0 0 0		

Net Wind Forces: (N)		Net Body Forces: (N)		Net Body Moments: (Nm)	
Drag:	7.4441	X:	-8.16	Roll:	-1.3739e-015
Side:	-6.18e-017	Y:	-6.18e-017	Pitch:	-7.042
Lift:	74.269	Z:	74.1937	Yaw:	-3.9552e-016

CL	0.89513	CZ	0.89422	Cm	-0.25704
CD	0.08972	CX	-0.098348	Cn	-5.2966e-018
CY	-7.4484e-019	CC	-7.4484e-019	Cl	-1.8399e-017
CD_{treffz}	N/A				

STATE:

alpha:	12	P:	0		
beta:	0	Q:	0	Rudder setting [deg]:	0 0
Airspeed:	21.35	R:	0		
Altitude:	0	PG Correction:	1		
Density:	1.225				

(a) Tornado computational results (2 psi, $\alpha = 12°$, 280 N/m^2).

TORNADO CALCULATION RESULTS, Central difference

JID:	ads7				
Reference area:	0.29718	Alpha:	0	P:	0
Reference chord:	0.3302	Beta:	0	Q:	0
Reference span:	0.9	Airspeed:	21.35	R:	0

CL derivatives :		CD derivatives :		CY derivatives :	
CL-alfa	3.1267	CD-alfa	0.16729	CY-alfa	0
CL-beta	0	CD-beta	-2.9818e-016	CY-beta	0
CL-P	0	CD-P	-1.2722e-014	CY-P	0
CL-Q	5.1047	CD-Q	0.047042	CY-Q	0
CL-R	-2.0356e-013	CD-R	1.9083e-014	CY-R	0

Roll derivatives :		Pitch derivatives :		Yaw derivatives :	
Cl-alfa	1.5334e-015	Cm-alfa	-0.70625	Cn-alfa	-1.0515e-016
Cl-beta	-0.0093717	Cm-beta	1.5903e-015	Cn-beta	0.00043285
Cl-P	-0.27716	Cm-P	2.0356e-013	Cn-P	-0.0074428
Cl-Q	2.754e-015	Cm-Q	-1.9098	Cn-Q	3.4425e-016
Cl-R	-0.069717	Cm-R	-2.0356e-013	Cn-R	0.0038871

(b) Tornado computational results(6 psi, $\alpha = 0°$, 280 N/m^2).

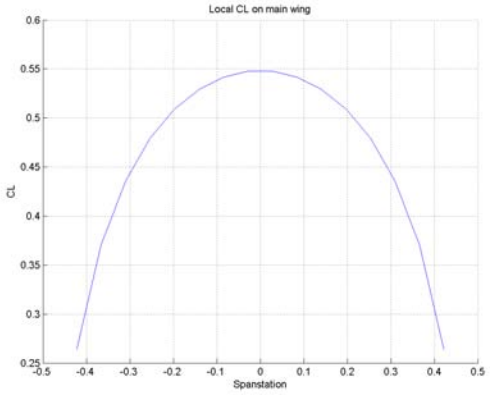

(c) Local C_l on main wing (4 psi, $\alpha = 4°$, 178 N/m^2).

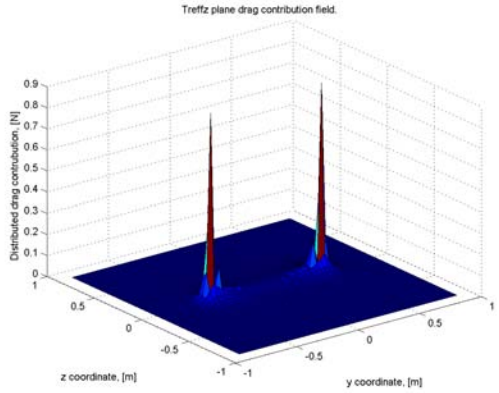

(d) Drag contribution (4 psi, $\alpha = 16°$, 400 N/m^2).

Figure 6.16: Sample results from Tornado.

the data however, it is still not significant.

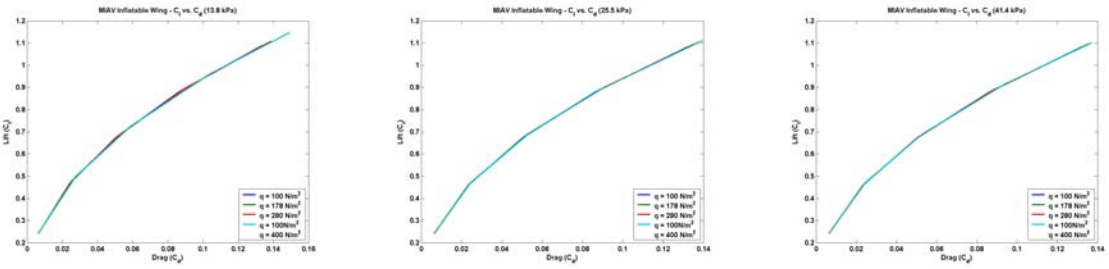

(a) 13.7 kPa (2 psi). (b) 25.5 kPa (4 psi). (c) 41.3 kPa (6 psi).

Figure 6.17: C_l vs. C_d for the nylon wing.

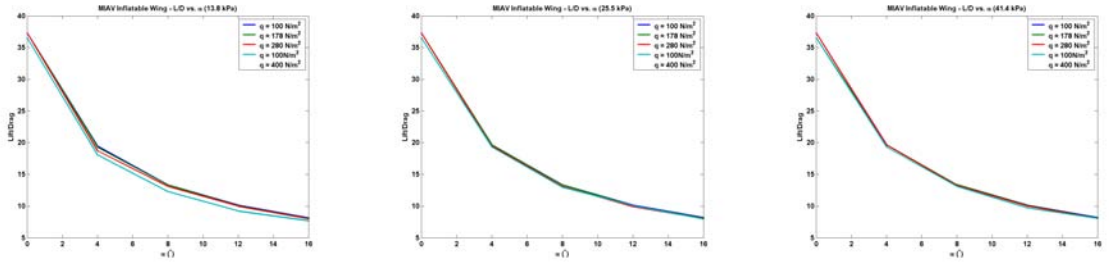

(a) 13.7 kPa (2 psi). (b) 25.5 kPa (4 psi). (c) 41.3 kPa (6 psi).

Figure 6.18: L/D vs. α for the nylon wing.

6.2.4 Modeling – Nylon Wing Warping

As highlighted in Chapter 5.3.1, servos were attached to the nylon inflatable wing as a method of wing warping. The servos warped the trailing edge of the wing thereby changing the chamber of the wing. The warping mechanism as stated in Chapter 5.3.1, used either one servo attached to the wingtip or an additional servo attached to the mid point of the semi-span. The performance of either one or two servos and optimal servo placement is not well understood. The goal of this analysis was to quantify the performance benefits of the servo warping mechanism and to determine optimal servo placement. Much of this research follows the same pattern detailed by Stanford *et al.* [105].

For this analysis "XFLR5" was used. XFLR5 is an analysis software tool for foils and wings operating at low Reynolds numbers and is a windows "friendly" version of XFoil. The algorithms for foil analysis implemented in XFLR5 are exactly the same as those of the original XFoil code. The code has been thoroughly tested against numerous original

XFoil analysis, always with consistent results. The code is broken up into four different applications. These are:

- Two direct design modes which are convenient to compare foils,
- A mixed inverse (QDES) and the full inverse (MDES) foil design routines,
- A foil direct analysis routines (OPER), and
- A wing and plane design routine

Using XFLR5, it was possible to model the warped nylon wing. To do this, the wing geometry and warped airfoil shape were initially specified. The warped airfoil shape and wing geometry can be seen in Fig. 6.19 and Fig. 6.20. In Fig. 6.19 three separate wing profiles can be seen. These represent the warped wing profiles where each of the warped portions are treated like flaps. This is in accordance with the results found in Chapter 5.3.1 – the servos warped the aft $23_c\%$ of the airfoil profile, warping the trailing edge down by 12° and up by 17°. Fig. 6.20 shows a top view of the wing. The span of the wing is divided into 16 evenly spaced segments, 8 for each semi-span. The individual segments on each semi-span can be assigned the profiles created in Fig. 6.19 or twisted relative to one another.

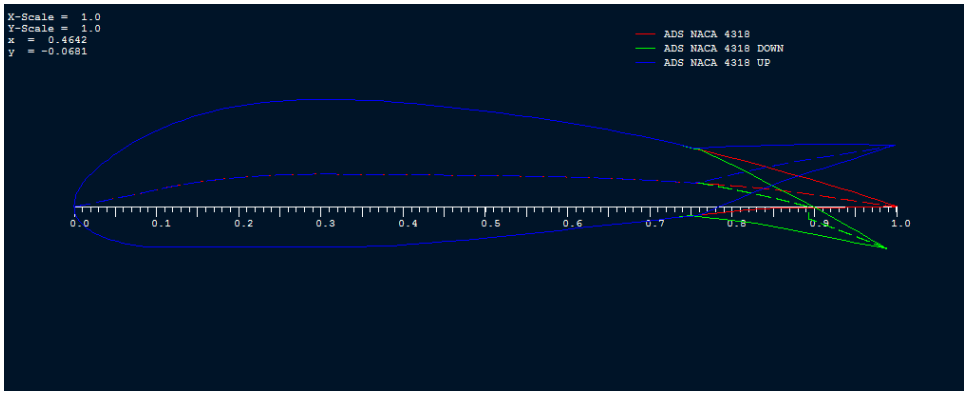

Figure 6.19: Airfoil direct design application – Trailing edge warping of the Nylon wing.

To investigate the effect of servo placement on roll performance, the 16 segmented airfoil sections were warped. The warping was not symmetric about the wing center, i.e. if the 4^{th} segment on the starboard wing was warped down the corresponding D^{th} segment on the port wing was warped up. Nine cases were thus examined, with the servo placement progressing

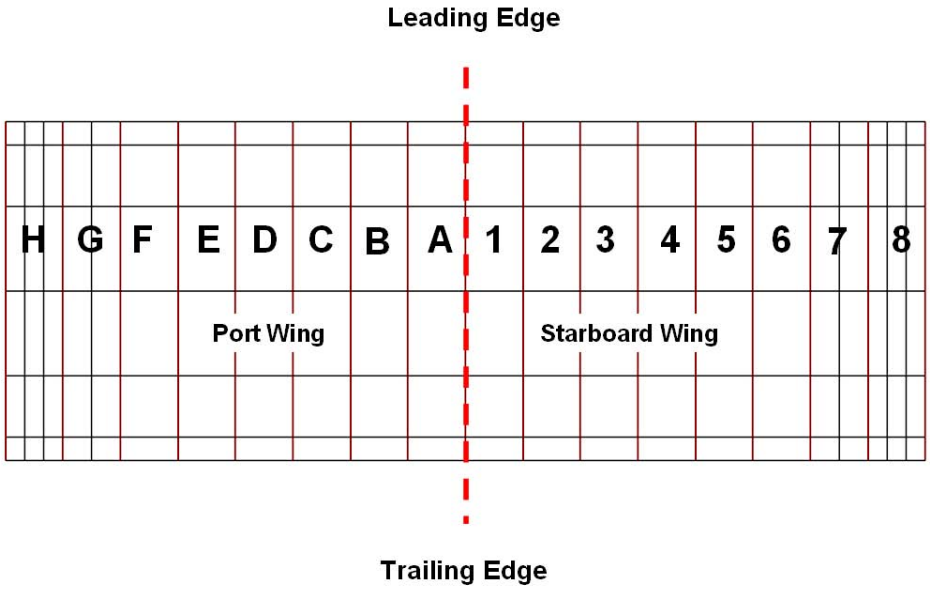

Figure 6.20: Structured mesh of wing panels generated by XFLR5.

Table 6.4: Servo placements investigated.

Case	Starboard Wing	Port Wing
1	Straight	Straight
2	1–Down	A–Up
3	2–Down	B–Up
4	3–Down	C–Up
5	4–Down	D–Up
6	5–Down	E–Up
7	6–Down	F–Up
8	7–Down	G–Up
9	8–Down	H–Up

Table 6.5: Multiple Servo placement investigation.

Case	Starboard Wing	Port Wing
10	7,4–Down	G,D–Up
11	8,5–Down	h,E–Up
12	8,7,6,5–Down	E,F,G,H–Up

through each segment. The cases examined are highlighted in Table 6.4. Fig. 6.21 shows the progression of servo position from the wing root to the wingtip. Note that an individual segment is warped with adjoining segments on each side re-distributing the warped shape.

In addition to the individual servo locations, a few multiple servo locations were tested. These are Tabulated in Table 6.5 and displayed in Fig. 6.22.

To compare results between warped locations, one operating point was selected as a means of comparison. Each wing was set at $\alpha = 4°$, and $U_\infty = 17.05$ m/s. Fig. 6.23*a* shows the angle of attack over the span of the wing. Here the warped segmets have been superimposed to compare the difference in local α across the span. Fig. 6.23*b*, details the local lift coefficient over the span of the wing. The right hand semi-span is warped down increasing the local C_l while the left hand semi-span is warped up decreasing the local C_l. The change in lift coefficient from the straight non-warped case can clearly be seen.

By examining the single servo warping locations (9 designs), the rolling performance at each warping location can be determined. These are summarized in Fig. 6.24. Intuition implies that for a single servo warping the wing, the farther the servo is placed from the wing root, the higher the rolling moment (roll performance). Contrary to this argument, the curve of Fig. 6.24 peaks at an intermediate servo location, rather than at the wingtip.

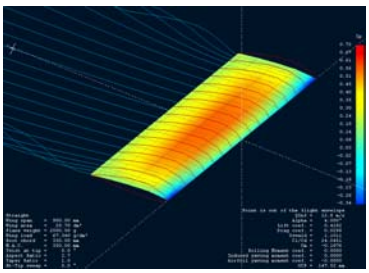

(a) Case 1.

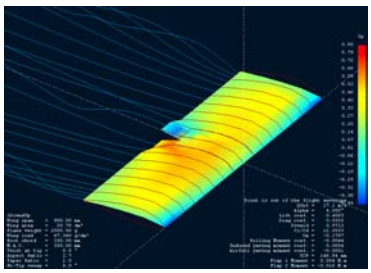

(b) Case 2.

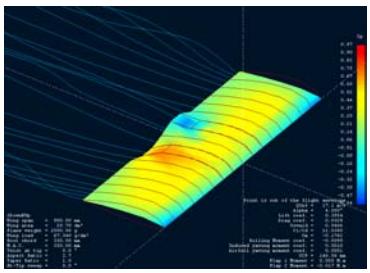

(c) Case 3.

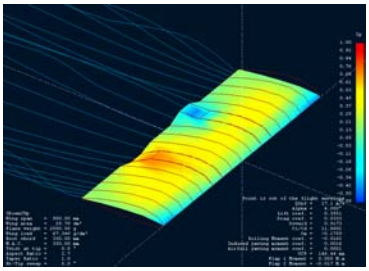

(d) Case 4.

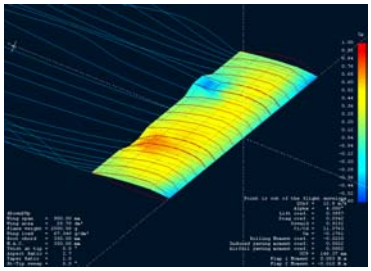

(e) Case 5.

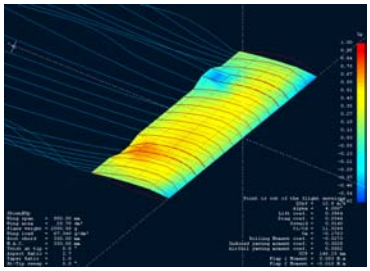

(f) Case 6.

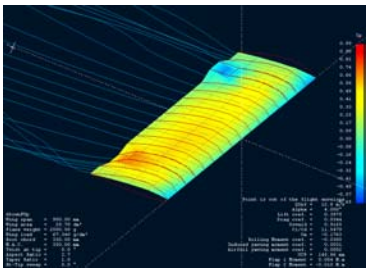

(g) Case 7.

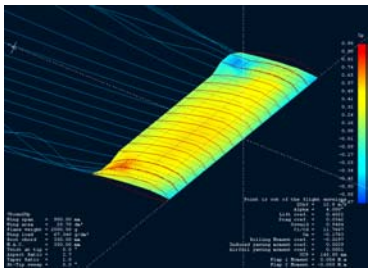

(h) Case 8.

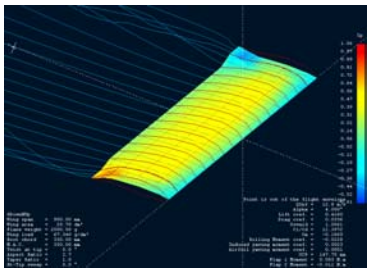

(i) Case 9.

Figure 6.21: Wing Warping Configurations Tested for single servo in multiple locations.

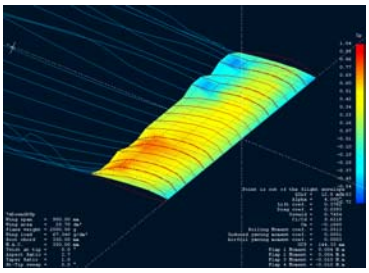

(a) Case 10.

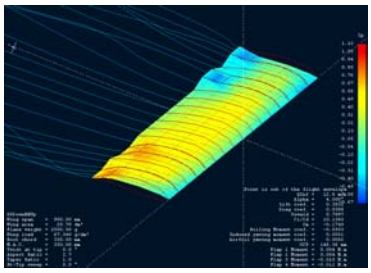

(b) Case 11.

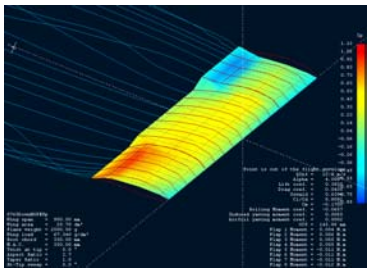

(c) Case 12.

Figure 6.22: Wing Warping Configurations Tested.

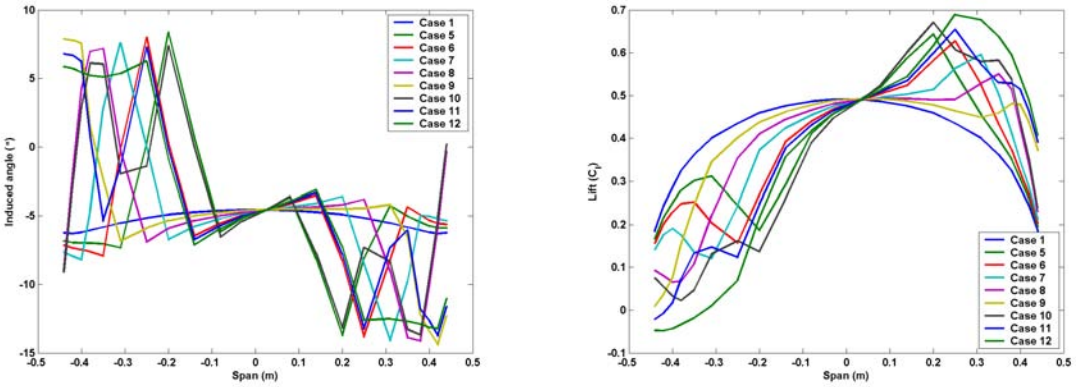

(a) Warp angle vs. span location.

(b) Local lift coefficient vs. span location.

Figure 6.23: Warping Configurations Tested ($\alpha = 4°$, $U_\infty = 17.05$ m/s).

The roll moment coefficient is greatest when the servo is located from 68 – 82% of the semispan and not at the wingtip.

The large displacements used to force the inflatable wing into a rolling maneuver generate significant amounts of asymmetric drag. The lift and drag characteristics of each morphing-mechanism design are given in Fig. 6.25 which shows the lift coefficient C_l vs. the drag coefficient C_d for numerous warped configurations. Fig. 6.26 shows the lift to drag ratio (L/D) as a function of α for the warped configurations.

The servo location has the opposite effect on L/D as compared to the data in Fig. 6.24. The warped wing produces unfavorable L/D ratios as seen in Fig. 6.27. The greatest aerodynamic efficiency (L/D = 14.4) is provided by the unwarped design. Effective servo warping results in non-efficient wing shapes seen in Fig. 6.27. Cases 7 and 8 which provide the maximum rolling moment coefficient, are also some of the weakest in aerodynamic efficiency. It is interesting to note that case 7 and 8 have almost identical rolling moment coefficients (case 7 is slightly higher), however case 8 provides an increase in efficiency of 3.5% over case 7.

Wing warping at multiple servo locations achieved significant improvements in rolling rate coefficient, but had a corresponding drop in the efficiency. This can be seen in Fig. 6.28 where L/D is plotted with respect to rolling moment coefficient. Of the three multiple warped locations examined, case 10 provides the highest efficiency with approximately the same rolling coefficient as case 11. Case 12 has the highest rolling moment coefficient, but is also the least aerodynamically efficient. An important aspect of the multiple servo designs is their superior roll rates compared with single servo designs.

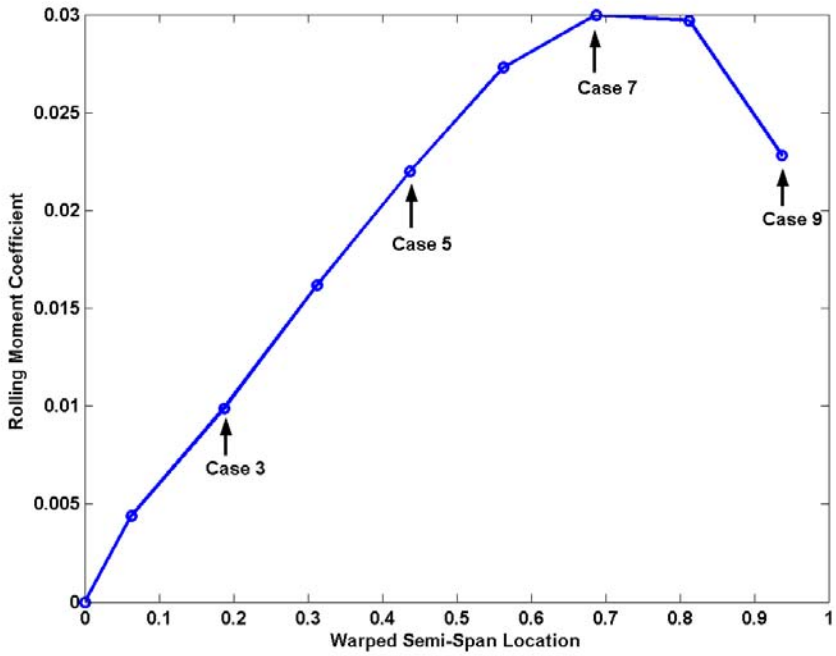

Figure 6.24: Rolling moment coefficient vs. warped span location ($\alpha = 4°$, $U_\infty = 17.05$ m/s).

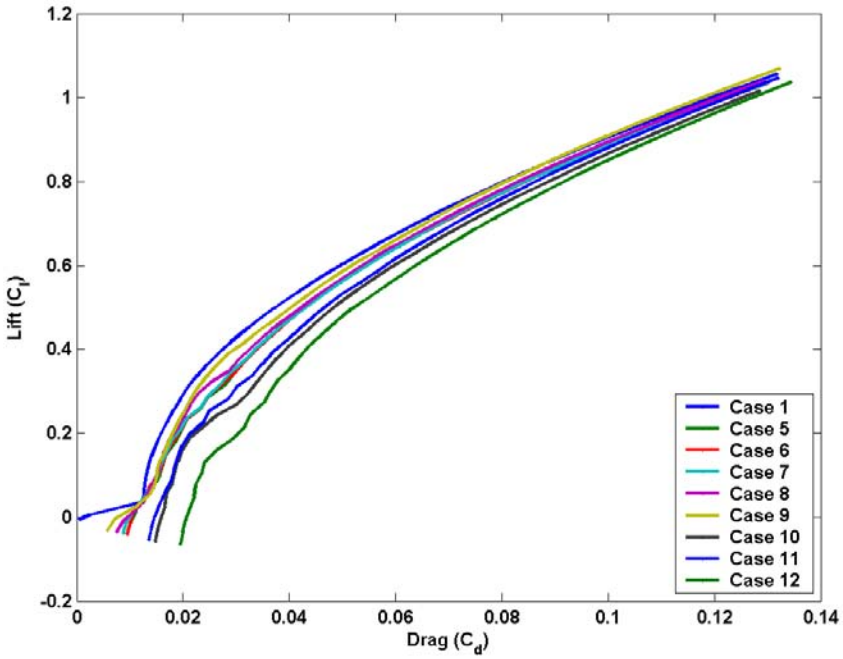

Figure 6.25: C_l vs. C_d ($\alpha = 4°$, $U_\infty = 17.05$ m/s).

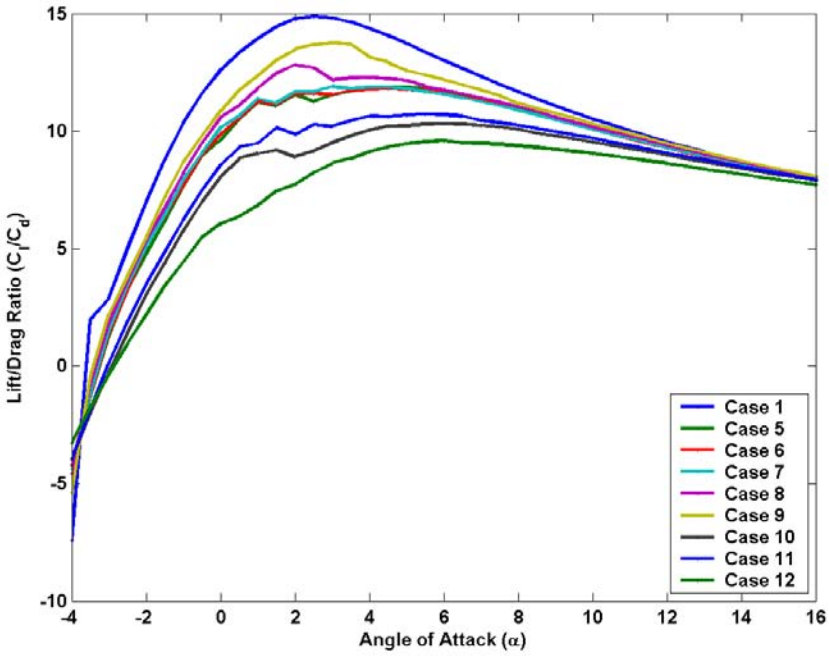

Figure 6.26: L/D vs. α ($\alpha = 4°$, $U_\infty = 17.05$ m/s).

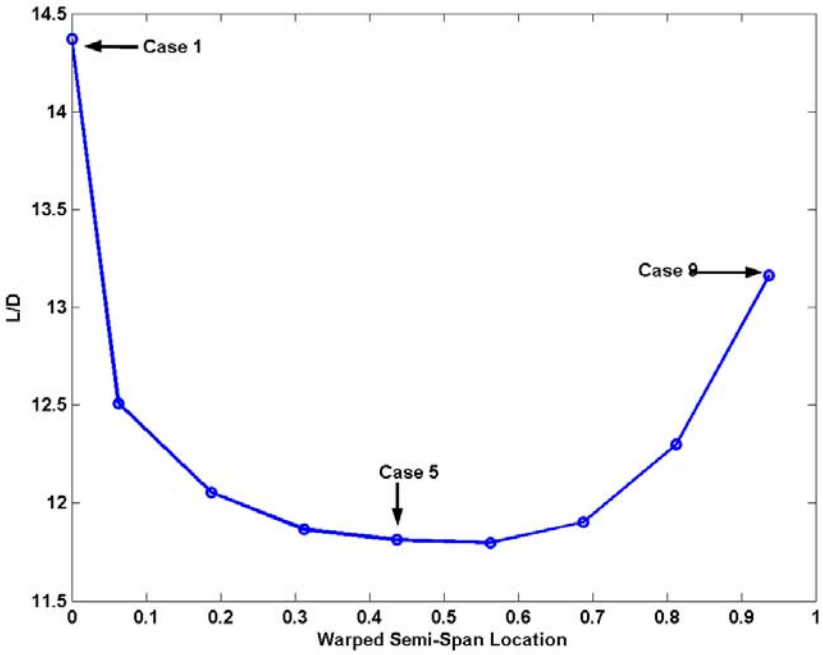

Figure 6.27: L/D vs. warped span location ($\alpha = 4°$, $U_\infty = 17.05$ m/s).

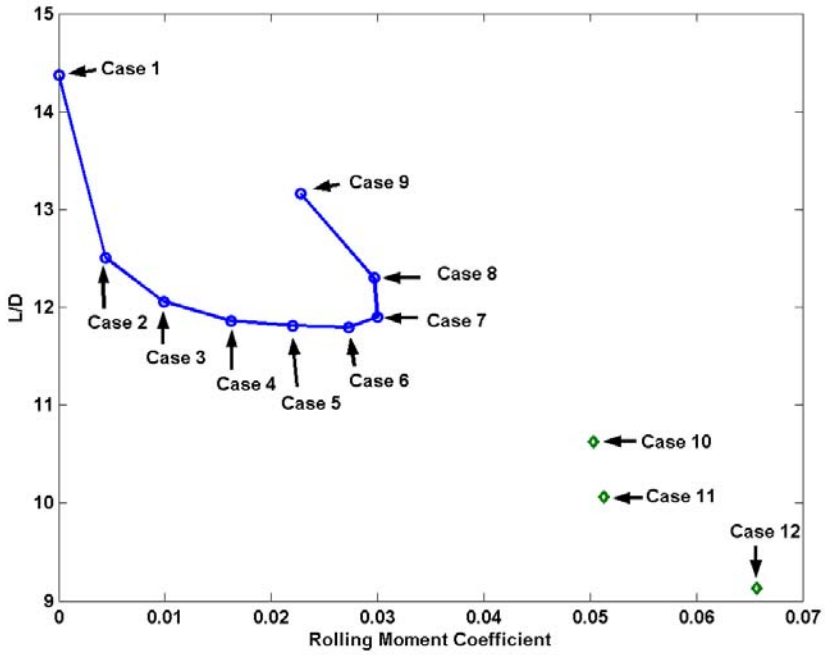

Figure 6.28: L/D vs. Rolling moment coefficient ($\alpha = 4°$, $U_\infty = 17.05$ m/s).

Differential pressure coefficient fields (as predicted by XFLR5) of the non-warped design, the single servo designs, and the multiple servo designs can be seen in Fig. 6.29 and Fig. 6.30. The plots show pressure gradients at the warped locations. This is due to the warping increasing the camber of the wing. As the air flows over the wing, it must rapidly change direction to travel over the warped shape. The downward warping motion on the starboard wing is counteracted by the aerodynamic loading, limiting its effectiveness. The opposite is true on the port wing.

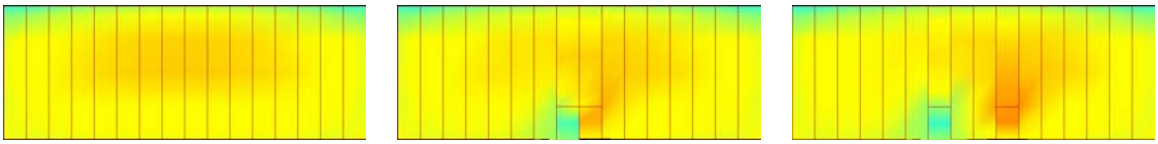

(a) Case 1. (b) Case 2. (c) Case 3.

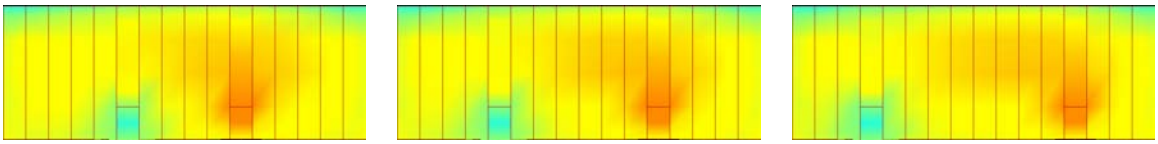

(d) Case 4. (e) Case 5. (f) Case 6.

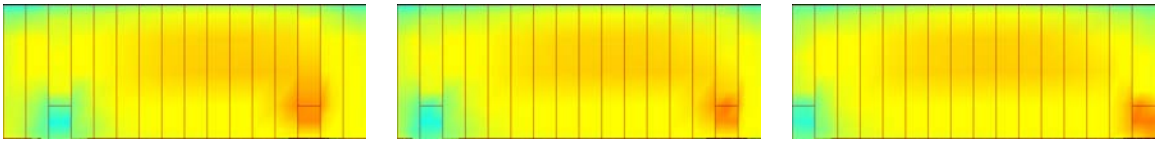

(g) Case 7. (h) Case 8. (i) Case 9.

Figure 6.29: Computed ΔCp for single servo in multiple locations ($\alpha = 4°$, $U_\infty = 17.05$ m/s).

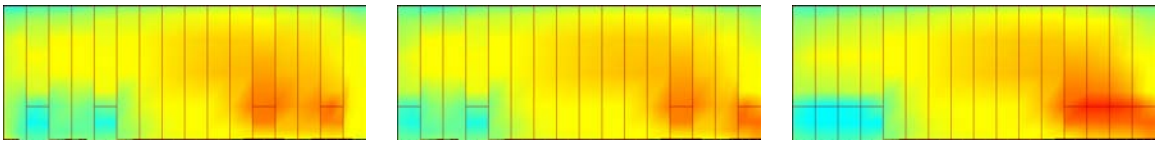

(a) Case 10. (b) Case 11. (c) Case 12.

Figure 6.30: Computed ΔCp for multiple servos ($\alpha = 4°$, $U_\infty = 17.05$ m/s).

Chapter 7

FLIGHT TESTING AND WING DURABILITY

Since 2002, roughly 500 flights of small UAVs have been conducted in support of this research by the University of Kentucky. This includes approximately 300 flights of vehicles using inflatable wings and approximately 200 flights of UAVs using mock-up inflatable wings. Additional flight testing was conducted to test additional equipment through associated research groups (within Big Blue) at the University. Inflatable-rigidizable, Vectran and nylon wings were substantially flight tested in multiple configurations. Wing spans ranged from 1.2 m to 3.7 m (4 ft to 12 ft) and vehicle weights ranged from 2.2 kg to 18 kg (5 lbs to 40 lbs). The following Chapter details some of this testing.

7.1 Inflatable-rigidizable wings

7.1.1 Low altitude flight tests with inflatable-rigidizable wings

Several vehicle configurations were constructed and flown during low altitude flight testing. Two vehicle types were used significantly throughout flight testing. The first consisted of a PVC fuselage with aluminum boom connected to the empenage. A CAD drawing of the configuration is displayed in Fig. 7.1 while Fig. 7.2 shows the actual vehicle. The second vehicle consisted of an entirely composite fuselage providing both weight and strength advantages (Fig. 7.3). In both cases, the wings were mounted to a central plenum which was mounted to the fuselage. Multiple tail configurations were constructed and tested for stability and control characteristics. These included a traditional cruciform tail, T-tail, and V-tail designs. The tail volumes were typically larger than usual to increase control at low speeds during launch. There was no aileron control on the vehicle.

For each test vehicle, several sets of wings were available for flight testing. Multiple sets of inflatable-rigidizable wings were available, including two full-span sets cured in the lab and a set inflated and cured at high altitude. Additionally, simulated inflatable-rigidizable wings were constructed from styrofoam. These wings were constructed with the same profile geometry and planform as their inflatable counterparts, and then weighted to match the final weight of the inflatable-rigidizable wings.

The inflatable-rigidizable wings had a mass of approximately 2.2 kg (4.4 lbs), including

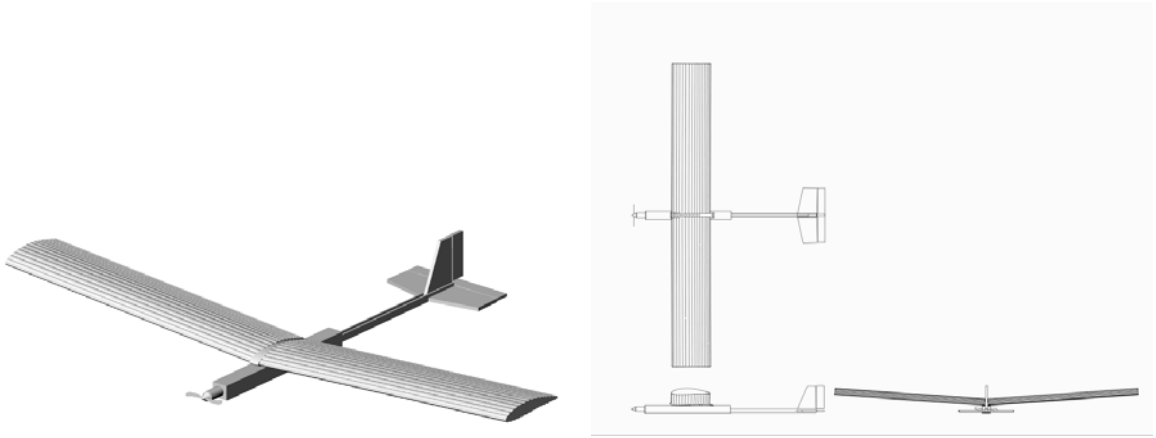

(a) Typical flight model configuration.

(b) Top, Side and Rear view of flight vehicle.

Figure 7.1: PVC fuselage – flight test vehicle.

(a) Pre-flight.

(b) In-flight.

(c) On-board.

Figure 7.2: Flight test vehicle – PVC fuselage with aluminum boom connected to the empenage.

(a) Composite fuselage and empenage.

(b) Flight testing with composite fuselage aircraft.

Figure 7.3: Composite fuselage aircraft.

the aluminum plenum used for inflation and mounting. Note that the chord length is slightly smaller than the E398 upon which it is based due to the blunt trailing edge.

To achieve altitude for the gliding tests, the vehicles were outfitted with an electric motor mounted in a tractor configuration. The motor was a Phasor Jeti 45/3 with a Jeti JES 40-3P Opto Controller and a 16 cell battery providing up to 35 A of current. At an output of 12 V and with a rated motor efficiency of 83%, this provided up to 350 W of power to the propellor. Various sized folding propellers were used as needed. General vehicle parameters are given in Table 7.1.

Table 7.1: Typical vehicle configuration parameters of inflatable-rigidizable wings.

Wing area, S	0.51 m^2
Span, b	1.82 m
Aspect ratio	6.5
Dihedral	7°
Sweep, taper	0
Horizontal tail area	0.045 m^2
Vertical tail area	0.083 m^2
c.g. location	0.42 m
Fuselage mass (nom.)	3.5 kg (7.7 lbs)
Wing mass	0.5–2 kg (1.1–4.4 lbs)
Wing loading	75–110 N/m^2 (1.5–2.2 psf)

On-board equipment

Flight characteristics were recorded using a Micropilot MP-1100, which included an altimeter, Pitot-static tube, accelerometers, rate sensors, and GPS, all logged at 5 Hz. Sample outputs of altitude and position are shown in Figs. 7.4*a* and 7.4*b*, respectively. The flight profile in Fig. 7.4*a* shows the gliding test starting at peak altitude, along with the flare at landing. For many parameters, there were two independent measurements. Additional components that were used as needed include additional accelerometers and airspeed indicators and tail mounted cameras to examine wing behavior such as wing bending and twist.

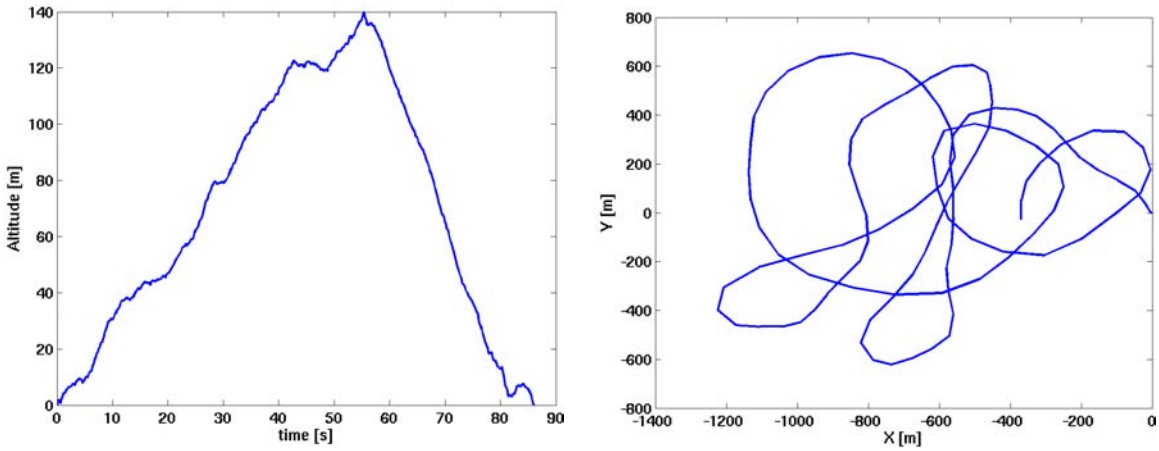

(a) Altitude history from a typical flight test.

(b) Aircraft ground position from a typical flight test.

Figure 7.4: Sample flight test data.

Analysis

Approximately 60 low altitude flight tests of various configurations were conducted using the inflatable-rigidizable wings. These tests were conducted with two goals in mind:

- to evaluate aerodynamic performance of the wings in realistic operating conditions, and
- determine the handling characteristics of the aircraft required for feedback gains in the autopilot system.

While aerodynamic performance closely matched that seen in the wind tunnel, handling characteristics were unique. In general, the vehicles were stable but exhibited Dutch roll at

take-off due to the high wing dihedral. Dutch roll is a type of aircraft motion, consisting of an out-of-phase combination of "yaw" and "roll" from side to side. This yaw-roll coupling is one of the basic flight dynamic modes. The motion is normally damped in most aircraft. However, the combination of the wings placed well above the center of mass and dihedral in the wings, tended to increase the roll restoring force, and therefore increase the Dutch roll tendencies. The Dutch roll characteristics were observed at low speeds.

The initial wing span was chosen based upon manufacturing considerations. Wing loading was in the range of 75–110 N/m^2, which is just slightly higher than that of the Wright Flyer. Using this wing loading and referring to the great flight diagram (Fig. 2.4) [4] we can estimated the cruise velocity. This is shown by Eqn. 7.1 and shown in Fig. 7.5.

$$\mathrm{V}_\infty = \sqrt{\frac{1}{0.38}\frac{W}{S}} \tag{7.1}$$

for the current configuration, this resulted in $V_\infty \approx 16$ m/s, which compared favorably with the test flight data.

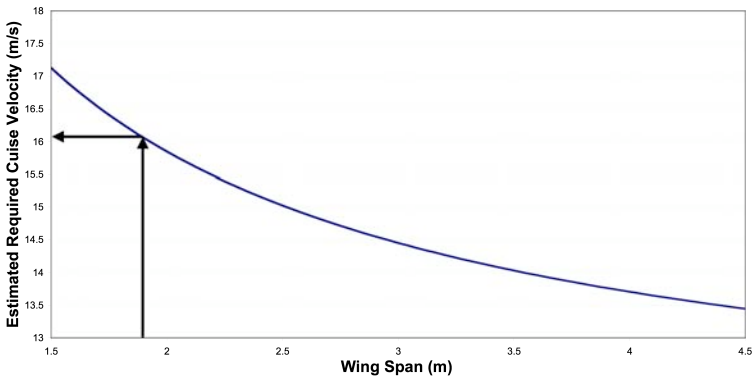

Figure 7.5: Cruise velocity as determined by wing loading.

Flight tests revealed that the aircraft had an equilibrium glide velocity of 15 m/s, a sink rate of 5 m/s and a glide slope angle of 18°. These compared well with the values determined from the wind tunnel tests at a similar Re of 300,000. Note that this was the highest value of Re that the aircraft would experience during flight. The glide slope, while steep, was within expectations.

$$\mathrm{V}_\infty = \sqrt{\frac{2W\cos\theta}{\rho L S}} \tag{7.2}$$

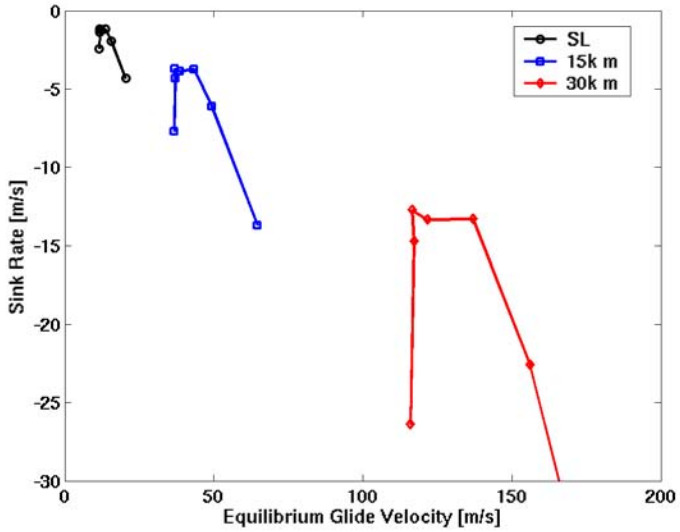

Figure 7.6: Equilibrium glide rate versus sink velocity.

$$V_{sink} = \sqrt{\frac{2W}{\rho L^3/D^2 S}} \tag{7.3}$$

For comparison, Fig. 7.6 shows the sink rate of a glider based upon wind tunnel measurements of the inflatable wing for various altitudes. The equilibrium glide velocity and sink rate are calculated in Eqn. 7.2 and Eqn. 7.3 respectively, where $\theta = \tan^{-1}(D/L)$ for a vehicle weight of 30 N (∼7 lbs). The best glide velocity as a function of altitude for these conditions is shown in Fig. 7.7 along with two other vehicle weights. Compressible effects have been compensated for using the Prandtl-Glauert correction.

Fig. 7.8 shows some of the low altitude flight testing conducted with the inflatable-rigidizable wings on the PVC fuselage. Fig. 7.9 shows low altitude flight testing with composite fuselages.

7.2 Vectran wings

7.2.1 Low altitude flight testing with Vectran Wings

The inflatable Vectran wings have a mass of approximately 3 kg (6.6 lbs), including the aluminum plenum used for inflation and mounting. To achieve altitude, the vehicles were outfitted with an electric power plant mounted in a tractor configuration. The electric motor was an AXI 4120 brushless motor with a Jeti motor controller and 16-20 cell battery

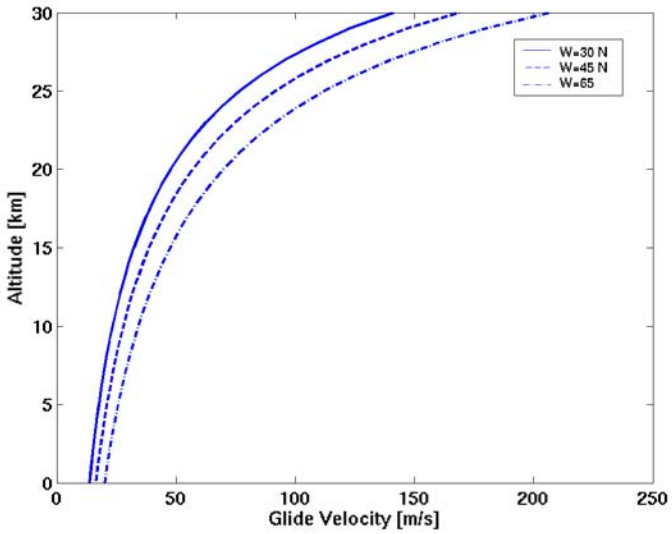

Figure 7.7: Glide velocity.

providing up to 70 A of current. The rated motor efficiency was greater than 82%, which provided up to 549 W of power to the propellor. Various sized folding propellers were used as needed.

Two vehicles types were designed and built that utilized the Vectran inflatable wings. For general flight testing, platforms similar to those used for the inflatable-rigidizable flight tests were used. Table 7.2 details the vehicle specifications and Fig. 7.10 shows the vehicle. Approximately 70 low altitude flight tests have been conducted with the Vectran inflatable wings using this platform. In addition to the general purpose flight test vehicle called "AirCat", composite fuselage vehicles were also designed and built. This vehicle can be seen in Fig. 7.11*a*. An additional vehicle was donated by NASA Ames Research Center for use in this project. The vehicle that was modified to hold the Vectran inflatable wing can be seen in Fig. 7.11*b*.

Warping flight tests

The flight test vehicle (Fig. 7.10) was modified for the wing warping system detailed in Chapter 5.3.1. A typical R/C servo delivering 14.4 kg/cm (200 oz.-in.) of torque at 4.8 V, warped the wings. The warping was achieved through a pulley system attached to the fuselage. The servo was mounted on the tail boom located under the trailing edge of the wing on the fuselage centerline. Nylon lines were run from the servos to attachment points

(a) Preparing for flight.

(b) Hand launching the vehicle.

(c) inflatable-rigidizable wings in flight.

(d) Belly landing after flight.

Figure 7.8: Flight testing with inflatable-rigidizable wings; PVC fuselage.

Table 7.2: Inflatable vehicle configuration parameters.

Wing area, S	0.67 m^2
Span, b	1.82 m (6 ft)
Aspect ratio	5.39
Dihedral	4°
Taper ratio	0.65
Fuselage mass (nom.)	± 5 kg (11 lbs)
Wing mass	3 kg (6 lbs)
Wing loading	65–165 N/m^2 (1.5–4.0 psf)

(a) Preparing for flight.

(b) On-board view of flight.

Figure 7.9: Flight testing with inflatable-rigidizable wings; composite fuselages.

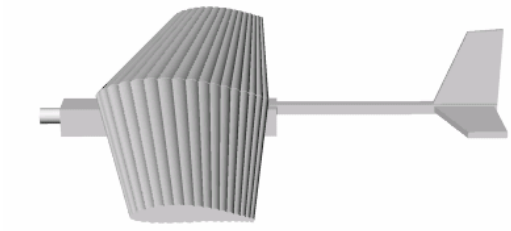

(a) CAD view of the vehicle.

(b) Flight tests vehicle.

Figure 7.10: General purpose flight test vehicle for the Vectran wings.

(a) AIRCAT with Vectran wings.

(b) NASA Ames Vehicle modified for Vectran inflatable Wings.

Figure 7.11: Vectran wing vehicles.

on the pressure surface of the wing at the wingtip. As the servo arm rotated, one semi-span was warped down, while the other semi-span remains non-warped. In this configuration, only one semi-span was warped at a time. Additionally, the wing was warped down only, resulting in a higher than normal lift on the warped semi-span.

Good flight characteristics were observed using the wing warping mechanism, including excellent roll control. Two wing warping configurations were tested in addition to empenage only control[67, 106]. In the first, roll and yaw were coupled though the R/C transmitter and receiver. Qualitative flight stability was greatly improved as compared to the non-warped case using only empenage control. In the second configuration, the vehicle was flown without coupling the roll and yaw (i.e. aileron and rudder inputs were not coupled). Roll control was adequately provided by the wing deformation. Unfortunately, the UAV did not have any onboard sensors, thus roll rate could not be measured and correlated to servo position. Fig. 7.12 shows a series of images form these flight tests.

A roll rate sensor was then developed which is capable of measuring roll rate, pitch rate, longitudinal acceleration, lateral acceleration, and servo position. The output from these sensors during warping flight test flights were used to correlate servo position (and hence wing deformation) to roll rate. Fig. 7.13 shows the servo throw location (hence wing warping) relative to the roll rate of the vehicle during a portion of a warping flight test using the onboard sensors. Fig. 7.13 shows the response of the aircraft to a step input; a nearly constant increase in roll rate (or constant roll acceleration) results, and a steady state roll rate of approximately 160°/s is seen after approximately 3 s. Once the servo input has been removed, the roll rate reverses until the aircraft stabilizes itself. Due to a slight asymmetry in the wings, a constant roll acceleration of approximately -0.75°/s^2 is seen without active

Figure 7.12: Flight test with wing warping of Vectran wings.

input. Results of the flight testing of the UAV and the sensor payload with wing warping were presented elsewhere [107].

To evaluate an aircrafts dynamic stability, a 6-DOF analysis is required. This allows simultaneous rotations in pitch, yaw, and roll. All of these motions interact with each other, requiring cross-derivatives to account for the forces and moments. For initial analysis 1-DOF equations are used. These equations state that the rotational acceleration times the mass moment of inertia equals the sum of the applied moments. The 1-DOF equations are stated in Eqn. 7.6.

$$\text{Pitch} : I_{yy}\dot{q}^{'} = qS_w cC_{m_\alpha}\alpha + qS_w cC_{m_{q^{'}}}q^{'} \tag{7.4}$$

$$\text{Yaw} : I_{zz}\dot{r} = qS_w bC_{n_\beta}\beta + qS_w cC_{n_r}r \tag{7.5}$$

$$\text{Roll} : I_{xx}\dot{p} = qS_w bC_l + qS_w bC_{l_p}p \tag{7.6}$$

These are second-order differential equations since $q^{'}$, r, and p are the derivative with time of pitch, yaw, and roll. If we consider the single degree of freedom equation for roll and neglect roll due to rudder deflection and sideslip, the above equation is simplified to

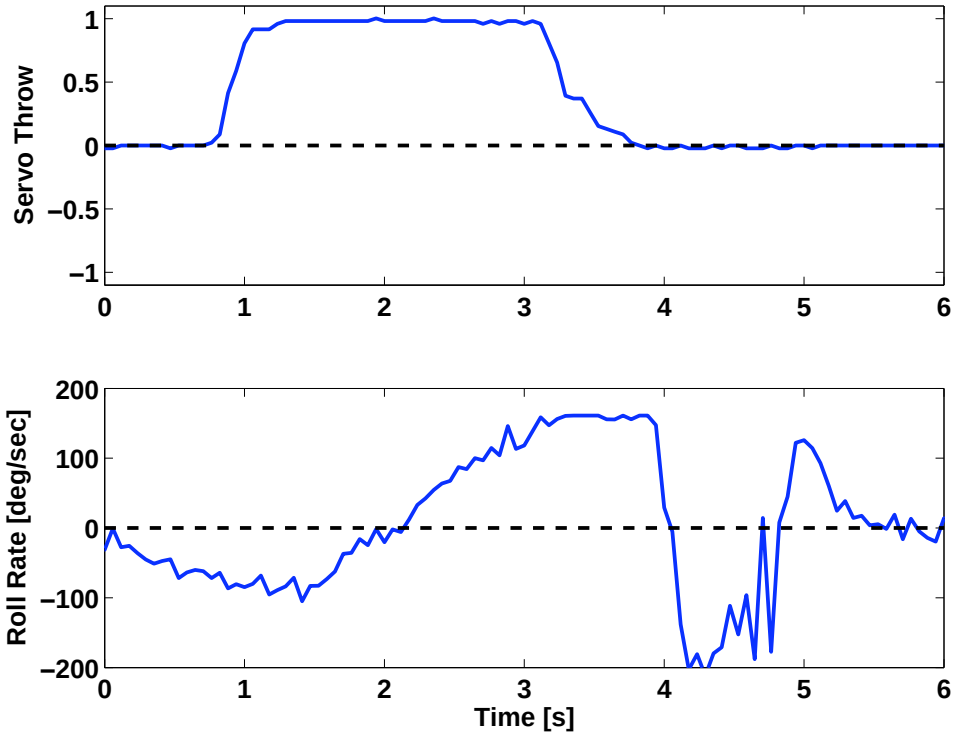

Figure 7.13: Roll response with servo step input.

Eqn. 7.7.

$$0 = \dot{\mathrm{p}}\frac{\mathrm{I_{xx}}}{\mathrm{qSb}} - \mathrm{C_{l_p}}\frac{\mathrm{pb}}{\mathrm{2U}} - \mathrm{C_{l_{\delta_a}}}\delta_\mathrm{a} \tag{7.7}$$

where p is the roll rate in radians/sec, I_{xx} is the moment of inertia in roll, C_{l_p} is the roll damping coefficient, $C_{l_{\delta_a}}$ is the control power coefficient, and δ_a is the effective aileron deflection in radians. For a given flight, flight parameters include q, S, b, U and I_{xx} while measurable variables include p and $\dot{p}$. At initial lateral control input, we can write Eqn. 7.8

$$\dot{\mathrm{p}} = \frac{\mathrm{C_{l_{\delta_a}}}\delta_\mathrm{a}\mathrm{qSb}}{\mathrm{I_{xx}}} \tag{7.8}$$

while at steady state we have Eqn. 7.9

$$\frac{\mathrm{pb}}{\mathrm{2U}} = \frac{-\mathrm{C_{l_{\delta_a}}}\delta_\mathrm{a}}{\mathrm{C_{l_p}}} \tag{7.9}$$

the dimensionless roll-rate, $pb/2U$, is approximately 0.25. With a reported value of $I_{xx} = 0.57$ kg-m^2[29], one can find that $C_{l_{\delta_a}}\delta_a = 0.0013$. Using the laboratory measured value of $\delta_a = 16^\circ$, we estimate values of $C_{l_{\delta_a}} = 0.0047$ and $C_{l_p} = 0.0051$. This compares favorably to the predicted value of $C_{l_{\delta_a}} = 0.0053$ from McCormick [108].

7.2.2 Big Blue – AIRCAT

Students designed and fabricated a multipurpose airframe "AIRCAT" that was used as both a Pax-River (AUVSI Competition) aircraft and the BIG BLUE 3 and 4 vehicle. The aircraft was designed and hand built by students at the University of Kentucky in the mechanical and electrical engineering departments. The vehicle participated in the AUVSI Competition on July 2, 2005. Two AIRCAT vehicles were were built called AIRCAT "I" and "II" seen in Fig. 7.15. AIRCAT I, was used during BIG BLUE 3 and had a composite wing while AIRCAT II was used during BIG BLUE 4 and had the Vectran inflatable wings. The fuselage was based on the NACA 4418 airfoil profile and was constructed from fiberglass and foam insulation. This profile was the same profile used for the Vectran wings. The fuselage was constructed using a female mold as seen in Fig. 7.14*a* and *b*.

Propulsion was initially the Zenoah G-62. This was a small (3.8 in^3) internal combustion engine providing 4.75 Hp and rated for model planes of up to forty pounds. This was later replaced with the BME-50, 50 cm^3, 2 stroke engine, which provided 5 Hp. This change was due to weight saving from 2.2 kg for the Zenoah G-62 to 1.36 kg for the BME-50, while providing similar thrust. Table 7.3 details the two AIRCAT vehicles.

(a) Female mold.

(b) Completed fuselage.

Figure 7.14: Construction of AIRCAT.

(a) AIRCAT I.

(b) AIRCAT II.

Figure 7.15: AIRCAT I and II comparison.

Table 7.3: Inflatable vehicle configuration parameters.

	AIRCAT I	AIRCAT II
Wing area, S	1.18 m^2	0.76 m^2
Span, b	3.96 m	2.74 m
Length	2.44 m	2.44 m
Weight $GTOW$	15.88 kg	17.7 kg
Airspeed	29 kts	47.8 kts
Wing Type	Composite wing	Vectran Inflatable Wing
Wing mass	1.81 kg (4 lbs)	3 kg (6 lbs)
Autopilot	Micropilot MP 2028	Piccolo II
Propulsion	Zenoah G-62	BME-50

On-board Equipment and Flight Testing

A Piccolo II autopilot was used as a recording device for flight testing. The Piccolo is an all in one autopilot/sensor package. This autopilot system has a GPS receiver, an inertial measurement unit, and pressure transducers for pitot and static ports and can communicate with a ground station using UHF 900 MHz radio link. The Piccolo was designed and developed by CloudCap Technologies [109] and offers a programmable and highly integrated package with sensor, GPS, and communications. The radio link communicates to a ground control station which is connected to an operator interface via a serial port. This system was not used to fly the AIRCAT but rather as a sensor package.

Sample outputs of altitude and position are shown in Fig. 7.16 and Fig. 7.17 respectively. The flight path in Fig. 7.16 shows a typical flight test of the AIRCAT vehicle. This shows a typical take-off and landing of the AIRCAT from a paved runway, including the path flown. Fig. 7.17 shows the 3D flight path of the AIRCAT flight. Additional equipment included still and video cameras mounted to the tail and overlooking the inflatable wing. Fig. 7.18 shows some flight testing images of the AIRCAT.

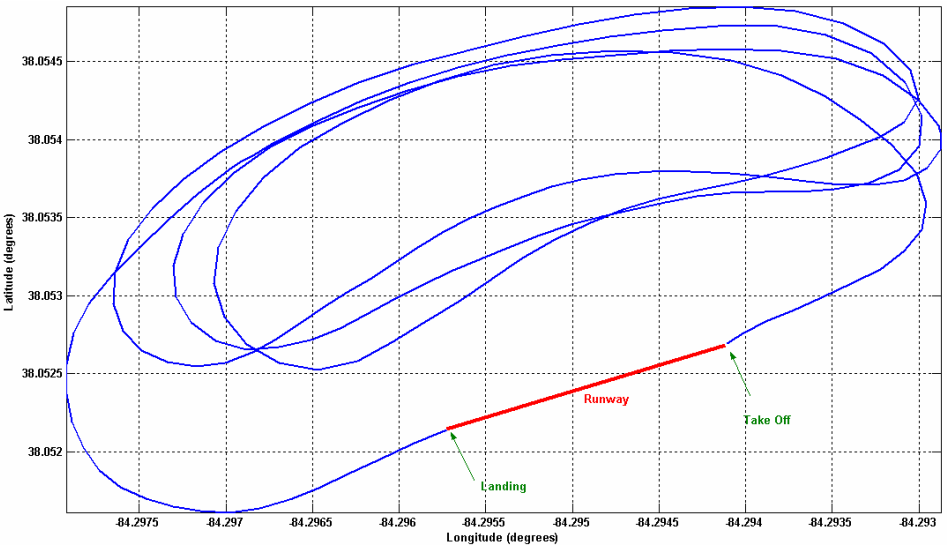

Figure 7.16: 2D Flight Path from AIRCAT Flight.

7.3 Nylon wings

The nylon wings were manufactured by ILC, out of polyurethane coated rip-stop nylon. Two nylon wings were constructed from this material. The first was a straight "yellow"

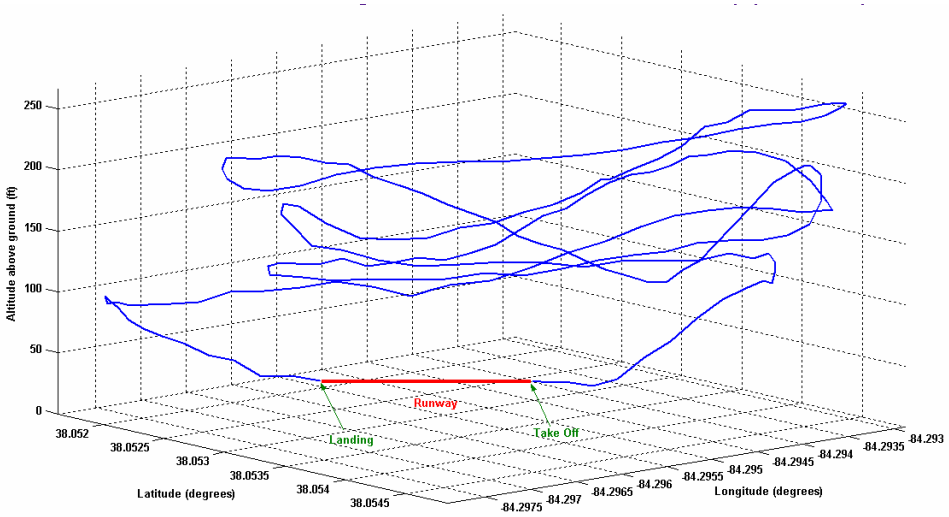

Figure 7.17: 3D Flight Path from AIRCAT Flight.

wing available in varying lengths and the other was a tapered "orange" wing. The tapered wing was produced in semi-spans. Each wing semi-span had a root chord of 48.3 cm (19.5 in) and a tip chord of 34.3 cm (13.5 in) with a semi-span of 91.4 cm. Fig. 7.19*a*, shows the straight yellow nylon wings, while Fig. 7.19*b* shows the orange nylon wings. The tapered wings could be mounted externally to a fuselage via fabricated mounting attachments. The inflation pressure of the wing for flight is a minimum of around 41.4 kPa (6 psi), though the burst pressure was found to be 275.8 kPa (40 psi) in tests.

Three vehicles were designed and built that utilized the nylon inflatable wings. For general flight testing, a platform similar to those used for the inflatable-rigidizable flight testing the Vectran flight testing were used. In addition to the general purpose flight test vehicle, two composite fuselage vehicles were also designed and built. The first was a technology demonstration vehicle, where the majority of the vehicle would be inflatable. The second was the "BIG BLUE *V*" vehicle designed and build by students of the University of Kentucky and Oklahoma State University. These three vehicles can be seen in Fig. 7.20. Unlike the inflatable-rigidizable and Vectran wings the nylon wings do not require a plenum, rather they are either mounted directly to the vehicle as in Fig. 7.20*a*, or mounted independently to the test bed via wing mounts as in Fig. 7.20*b* and *c*.

Figure 7.18: Flight test with Vectran wings on AIRCAT.

(a) "Yellow" Nylon wing.

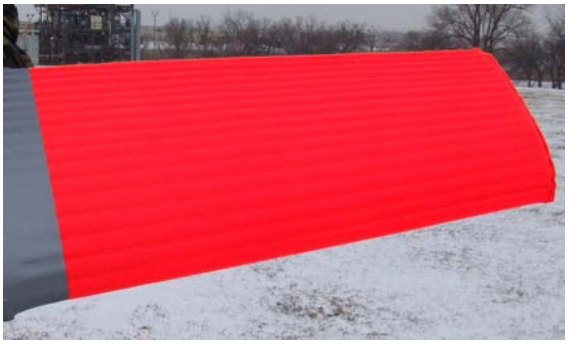

(b) "Orange" Nylon wing.

Figure 7.19: Nylon inflatable wings.

(a) General purpose flight test vehicle.

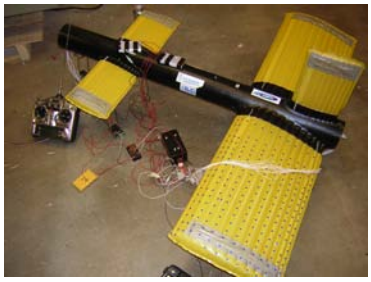

(b) Technology demonstrator.

(c) BIG BLUE V vehicle.

Figure 7.20: Nylon flight test vehicles.

Table 7.4: Nylon technology demonstrator configuration details.

Main wing airfoil	NACA 4318
Main wing chord	33 cm
Main wing α	4.57°
Main wing span	1.22 m (4 ft)
Canard airfoil	NACA 0018
Canard chord	16.5 cm
Canard α	5.83°
Canard span	0.61 m (2 ft)
Center-of-lift separation	61 cm
Fuselage diameter	10.2 cm
Plane weight	3.0 kg
Battery weight	0.74 kg

7.3.1 Technology demonstrator

A technology demonstration vehicle was developed by ILC in conjunction with the University of Kentucky. The goal was to develop a UAV configuration that maximized survivability. The configuration selected was a pusher canard as seen in Fig. 7.21. This configuration was selected as the payload and propulsion components were surrounded by inflatable components, enhancing impact survivability. The packed volume remained low as the inflatable wing could be warped around the solid aft fuselage component. Efficiency was maximized as all wing surfaces provided lift. All the inflatable wings were individually mounted to the fuselage via mounting brackets. The manufacture and assembly of the vehicle could be simplified as the components were interchangeable. Finally, the fuselage volume was sufficiently large to accommodate a range of sensors [32].

The vehicle was sized for a gross take-off weight (GTOW) of 4.49 kg and a 2G load limit. This supported a 0.75 kg sensor mass. The main airfoil was a NACA 4318 with a 1.22 m span and a 33 cm chord, with a fixed angle of attack of 4.6°. The canard and vertical stabilizers were NACA 0018 airfoils with a 0.61 m span and a 16.5 cm chord, with a fixed angle of attack of 5.8°. Operational pressure was 27.6 kPa (4 psi), but the system could be inflated to 75.8 kPa (11 psi). At 55.2 kPa (8 psi), the vehicle was anticipated to weigh 9.49 kg (including added battery mass), and support a 2.80 kg sensor mass. The inflatable components were manufactured from a urethane coated nylon, which was thermally welded in construction and a yellow material was used for visibility in flight test. Table 7.4 details some of the physical characteristics of the vehicle [32].

Nitinol (SMA) wing warping patches were attached to the wingtips for flight control

Figure 7.21: Nylon technology demonstrator.

as detailed in Chapter 5.3.2. The nitinol was used in a boot-lace configuration, where the nitinol was anchored to the wingtip at the trailing edge and run back and forth from trailing to leading edge. The patches were placed on both the pressure and suction wing surfaces. When actuated the constriction in the nitinol caused a localized change in the camber of the wing.

Propulsion was provided by an AXI 2820/12 brushless motor and a Jeti Advanced PLUS motor controller. The drive batteries were four Li-ion polymer cells with a 3150 mAh capacity. The nitinol control warping patches were powered through eight 1500 mAh Li-ion polymer cells, which were controlled through relays. The relays were controlled through a pulse width modulated signal from the RC receiver. The propeller was a 2 blade 11×8 pusher propeller [32].

7.3.2 BIG BLUE 5 vehicle

The fuselage was designed by students at Oklahoma State University according to payload requirements specified by students at the University of Kentucky. The principle payload was the "Piccolo" autopilot system. The wings were constructed in two semi-spans and mounted externally to a fuselage. Mounting attachments were constructed from balsa composite, where approximately 12.7 cm of the wing root was inserted into a wing shaped

cavity. The wings were attached to the wing mount using a light weight low temperature fiberglass tape with a silicon based adhesive. The wing mounts were in turn connected to one another using two carbon fiber tubes running through the fuselage.

The fuselage design is shown in Fig. 7.22. It features a low drag but high volume surface based around a NACA 4318 profile. A center payload hatch allowed easy access to the payload while holes in the bulkheads provide access to the entire fuselage. A carbon fiber rod protruding through the aft portion of the fuselage was for the balloon attachment cable. The fuselage was constructed out of a composite fiberglass – balsa sandwich.

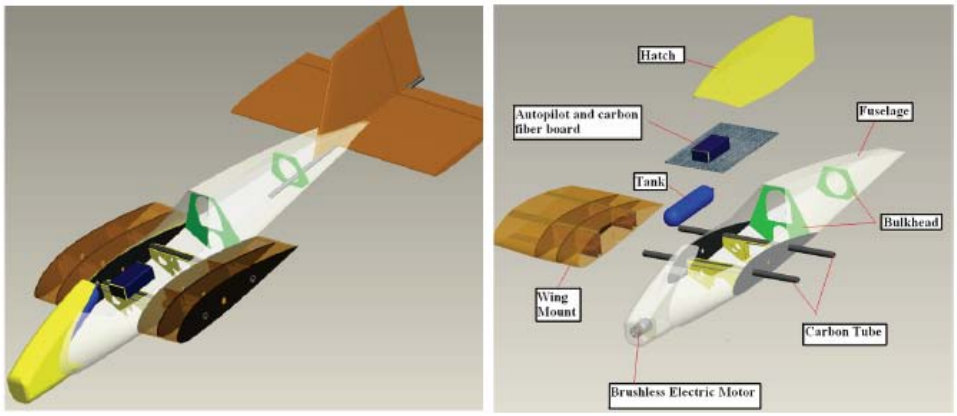

Figure 7.22: BIG BLUE 5 fuselage layout [31].

The piccolo autopilot was successfully used to control this vehicle during flight tests. The Piccolo autopilot controlled the vehicle's non-linear dynamics using nested PID loops to produce the desired airspeed, altitude, and heading rate to track a series of way points. Fig. 7.23 shows an image of the vehicle during the autopilot flight test.

7.3.3 Wing Warping with the general purpose flight test vehicle

Flight test were conducted using high torque servos to warp the nylon wings as detailed in Chapter 5.3.1. Here plexiglass plates were attached to the wing surface and the servo and control horn were then connected to these plates. As the servo was actuated, the wing would bend along one or more of the longitudinal baffles. Fig. 7.24 shows some flight tests of the nylon inflatable wing utilizing this system. This vehicle had a wing span of approximately 1.22 m, and utilized four servos to warp the wing. Vehicle control using this warping technique was adequate.

A second test vehicle was built with an increased wing span. The span was doubled

Figure 7.23: BIG BLUE 5 vehicle.

by joining two 1 m wing sections together with a fiber-glass wing mount. The wing span of the vehicle was thus 1.83 m (6 ft), and the vehicle had a weight of 12.5 lb. Two wing warping servos were used over the span, one at each wingtip. Here the servos were attached to the wing as specified in Chapter 5.3.1. The vehicle can be seen in Fig. 7.25. An on-board wireless video camera was attached to the fuselage, with a view of the port wing and the warping servo. A "snap-shot" of the transmitted video can be seen in Fig. 7.26. This shows an on-board view of the port wing prior to flight and the warping on the inflatable wing.

The goal of this flight test was to examine the effect of increasing the span of the inflatable wing and to examine the flight dynamics of the vehicle using only one wing warping servo per semi-span. For this flight test the inflation pressure was 41.3 kPa (6 psi). Good flight characteristics were observed using the wing warping mechanism, including excellent roll control. The vehicle inherently rolled to the left due to incorrect alignment of the wings in the wing mount. The warping system was capable of overcoming the inherent roll and was able to trim the warping of the wing to counteract the roll generated by the misaligned wings. As seen in Fig. 5.41 the predicted buckling velocity of the inflatable wings was 15 – 17 m/s (33 – 38 mph), at an inflation pressure of 41.3 kPa (6 psi) and a semi-span of ± 1 m. The semi-span wing sections were joined by a rigid wing mount, which was just over 1 ft long. This reduced the inflatable portion of each semi-span to just over 0.75 m. Again referring to Fig. 5.41 the predicted buckling velocity of the inflatable wings was ± 22 – 27 m/s (49 – 60 mph) Due to pilot error during the flight, the vehicle was put into a

(a) Take-off. (b) In-flight.

Figure 7.24: Flight test of the Nylon wings with servo actuators.

Figure 7.25: 2.44 m span Nylon wing flight test vehicle.

sharp banking dive. During the attempt to recover from the dive, the port wing buckled as seen in Fig. 7.27 and Fig. 7.28. The buckling was sudden and was caused by a combination of high flight speed and wing warping. The flight speed was estimated to be ± 25 m/s (56 mph). Additionally, it was determined that the wing inflation pressure was 31 kPa (4.5 psi) during the flight.

Fig. 7.27 shows a sequence of images from a ground based video camera of the wing buckling. Note that the vehicle is rolling to the right by warping the port wing which buckles. Here images are displayed at an interval of 0.033 s. Fig. 7.28 shows an on-board view of the port wing buckling. Note that the servo is warping the port wing down in order to roll the vehicle to the right. This in combination with the flight speed caused the wing

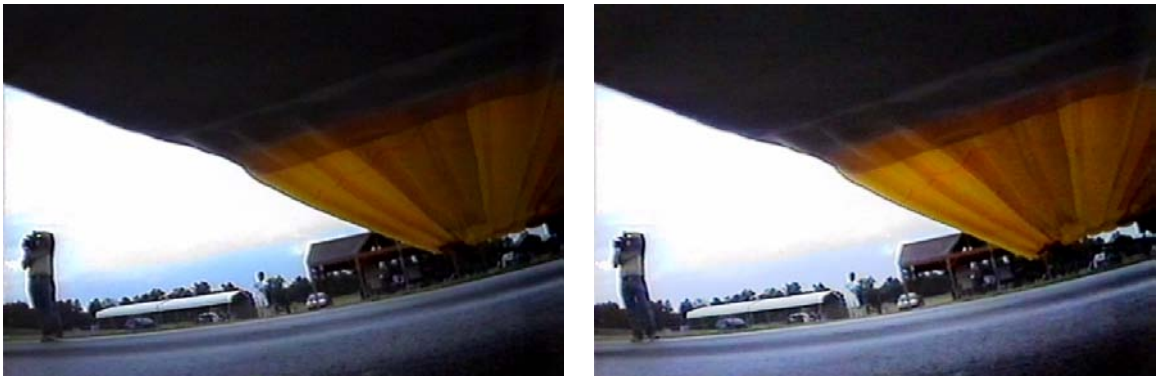

(a) Neutral (b) Warped down

Figure 7.26: On-board view of port wing prior to flight.

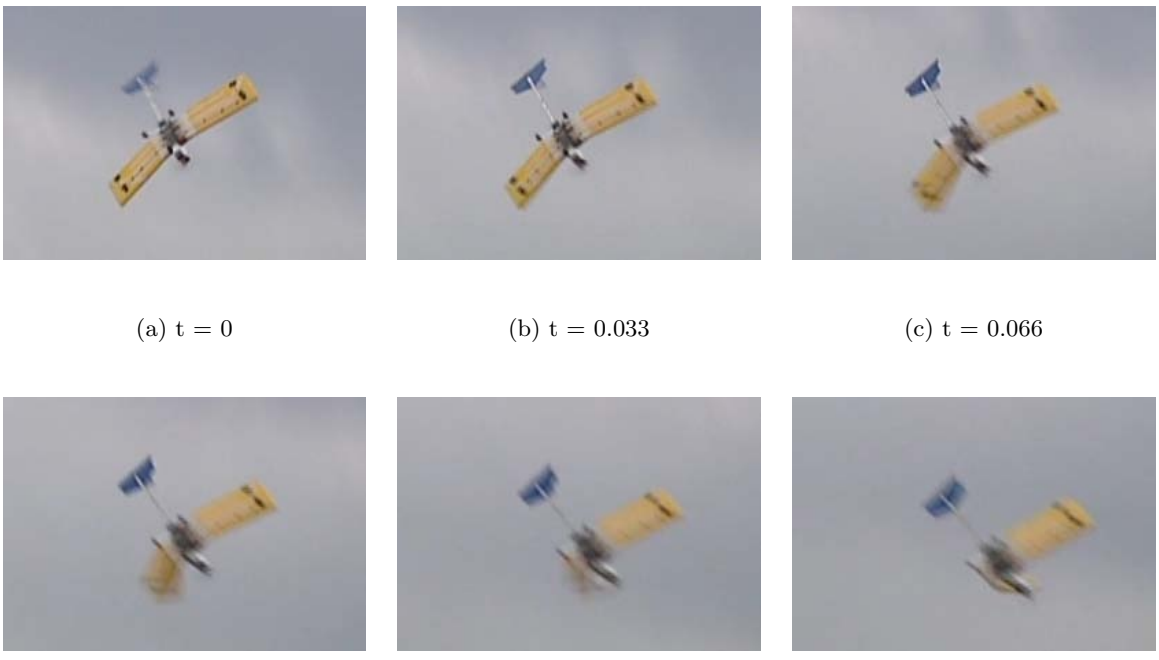

(a) t = 0 (b) t = 0.033 (c) t = 0.066

(d) t = 0.1 (e) t = 0.133. (f) t = 0.166.

Figure 7.27: Ground view of port wing buckling.

to buckle.

(a) t = 0 (b) t = 0.033 (c) t = 0.066

(d) t = 0.1 (e) t = 0.133 (f) t = 0.166

Figure 7.28: On-board view of port wing buckling.

7.4 Repeated Wing Deployment

The repeated inflation and deflation of inflatable wings has been shown to be reliable, repeatable, and fast [32]. Deployment has been achieved within 0.77 sec, and was repeated multiple times (100 times) without damage. This is shown in Fig. 7.29. Additionally, the wings were shown to be exceedingly durable, with extreme loading demonstrations displaying their resilience. In Fig. 7.30 the Vectran wings are impacted by a 22 kg sand bag, and in Fig. 7.31 the nylon wings are impacted by a 1.8 kg sand bag [32]. The inflatable wings were undamaged during this testing. The wings deform due to the impact and snap back into the their original position. Typical wings would suffer substantial permanent damage due to these sorts of impacts.

7.5 Survivability

One of the unforeseen benefits of the inflatable wings has been there unrivaled performance in crash survivability; the wings "bounce". Fig. 7.32 shows the comparison of damage rates of various components during flight tests. While damage was determined

Figure 7.29: Rapid deployment testing of Vectran wing [32].

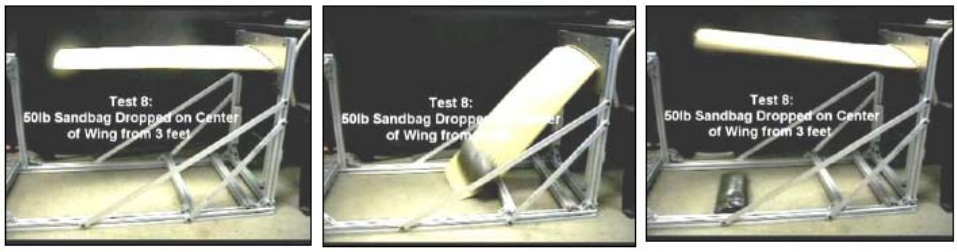

Figure 7.30: Vectran Wing – Snap back testing [32].

Figure 7.31: Nylon Wing – Snap back testing [32].

using a broad definition including adjustment, repair, or replacement of component parts in the field prior to subsequent flight tests, the results show that the inflatable wings were extremely damage resistant. The inflatable wings have even survived serious crashes that have resulted in the near total destruction of the vehicle. Thus, vehicles requiring high damage tolerance may benefit from such wings.

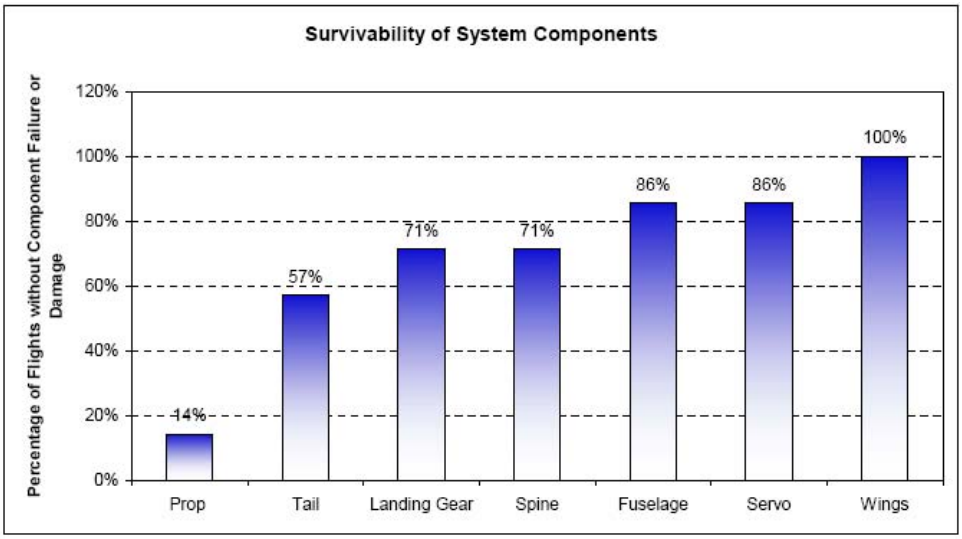

Figure 7.32: Survivability of inflatable wings and other small UAV components from flight test data.

Inflatable structures have shown to be very resilient to damage from sudden deflection, and return to their original design shape after an event. In this way they can expand the flight envelope by surviving gust loads encountered in rough weather or off-nominal flight conditions, while reducing system mass by allowing lower design margins. This is not surprising as inflatable structure have been been demonstrated reliable in a myriad of applications such as the F-111 escape system impact airbags, Mars Pathfinder and MER airbags, and automotive impact attenuation systems. Performance in these applications include landing on unprepared landing sites populated with jagged rocks, or other sharp objects. Testing of inflatable UAV wings in this manner has shown a 100% survivability rate after numerous ($\geq$100) crash incidences. As an example, Fig. 7.33 and Fig. 7.34 show two crash incidence using the nylon inflatable wing. Fig. 7.33 shows the BIG BLUE V vehicle crashing into a tree and wire fence. The inflatable wings can be seen deforming and absorbing the impact. Note that the vehicle and wings "bounced" off the tree. The wings were unscathed and the vehicle had only minor damage following the impact. Fig. 7.34

shows a crash of the general purpose flight test vehicle during wing warping flight tests. Here the vehicle impacts the ground at a speed in excess of 25 m/s ($\geq$56 mph). While the vehicle was completely distroyed, the wings "bounced" off the ground, seperating from the vehicle and were not damaged.

Figure 7.33: BIG BLUE *V* vehicle crashing into a tree.

Figure 7.34: Crash of the general purpose flight test vehicle.

An added benefit in creating a highly survivable inflatable UAV is the reduced capabilities burden on the pilot. A UAV that affords the user to be less proficient at piloting, especially in the launch or landing [32]. Evaluation of the logistics chain for UAV operation indicates that survivability will have a major role in system cost and mission effectiveness associated with time available to fly. Keeping repair items in inventory, transporting inventory to operations sites, the ability to field repair, training for repair, etc., will greatly impact system cost, and can even become the driver in total system cost in some cases in comparison to the base cost of the vehicle[32]. Engineered inflatable structures are very resistant to impact, and even if punctured, can be patched with a simple operation that is familiar to most people because it is similar to patching a bicycle tire inner tube. The simplicity of this operation as compared to the complexity of repairing a damaged rigid composite component is significant. Perhaps the most significant benefit in creating a highly survivable inflatable UAV is the reduced capabilities burden on the pilot. A UAV that affords the user to be less proficient at piloting, especially in the launch or landing phase of operation will be a strong factor in increasing user acceptance[32]. This benefit will allow inexperienced pilots and launch crews to make as many attempts as necessary at launch and landing without damaging the aircraft, and limits their need for training. Extended survivability margin in launch and landing will also extend the mission envelope

into more difficult weather by eliminating the potential for damage with crash landings. Packing efficiency is also an important benefit of inflatable structures. Numerous mission scenarios dictate remote operation of the vehicle. The "back-pack UAV" that can be easily transported and is very pack tolerant in rough handling, can extend mission operations for military and civilian needs. The ability to pull a tightly packaged UAV from a back-pack, rapidly inflate it with a simple hand pump or possibly a CO^2 cannister.

Chapter 8

CONCLUDING REMARKS

8.1 Overview

The use of inflatable wings on UAVs has been investigated in this research. Initially, the concept was novel. The benefits could clearly be seen for some applications , but as the technology was unproven and thus a risk, was not widely used. Primarily, inflatable wing UAVs were seen as a niche technology to be used in situations where space was constrained for some portion of the mission. In order to expand the scope and use of UAVs with inflatable wings, the risks and benefits of inflatable wing technology were explored within this research. This was explored through aeroelastic and aerodynamic investigations of the inflatable wings as well as substantial flight testing. The inflatable wings have proved to be extremely durable and reliable. Inflatable wings have many exciting possibilities; we have only scratched the surface of what is possible.

8.2 Aeroelasticity

The inflatable wings developed within this research have proved to be remarkably resilient to aeroelastic deformation at the nominal design inflation pressure of the wings. For the flight envelope that each of the wings was designed to operate within the deformation of the wings was minimal and the UAVs operated with the same performance as those of solid structural wings. Confidence was so high that the inflation pressures of the wings was lowered to enable the shape of the wings to be manipulated – wing warping.

Initial point and distributed loading of the Vectran wings demonstrated the low bending deformation of the wings. At the extremely low inflation pressures the wing tip deflection was less than 3% of the span and appeared to be monotonically decreasing with increasing inflation pressure. Thus at the design inflation pressure minimal bending deformation of the wings was seen.

The nylon wings were investigated in the wind tunnel at the expected flight velocity. At nominal design inflation pressures the nylon wings did not deform significantly. While some deformation was noted, it was minimal and not sufficient to adversely impact the performance of the UAV using them. As the inflation was dropped below the design point,

bending increased. This was expected, but was still remarkable low given that the wings were tested to inflation pressures one-third that of the design inflation pressure. This is some risk abatement for UAVs employing inflatable wings as the vehicle can still operate at off design inflation pressures. As stated, in all cases "wash-in" torsion and bending of the wings was observed. Torsion and bending were coupled. Thus the angle of attack of the increased toward the wing tip as the wing bent up. This could potentially cause vehicle controll issues as the wing tip stall before the root. At extremely high loading conditions (or low inflation pressures) this can also cause the wing to buckle. Thus, vehicles operating with inflatable wings should avoid extreme maneuvers in these conditions. That said, the conditions in tunnel testing and maneuvers during flight testing required to force the wing to buckle were extreme and off design. Operation of the nylon wing at extremely low inflation pressures was possible (within the operating envelope), but not recommended.

The buckling airspeed for collapse was modeled. Good agreement between the actual buckling velocities and the predicted buckling velocities was found. This was expanded to include predictions for of the buckling velocity, as the semi-span length was increased. As expected the buckling velocity reduces as the semi-span increases. This will aid in the design of future UAVs employing inflatable wing technology.

Free vibration analysis of the nylon inflatable wings determined potential made shapes. The first bending mode of the inflatable wing was found to be $\approx$8.3 Hz with an associated damping ratio of 10%. This damping ratio is remarkable high as typical metalic structures have damping ratios of 3-4%. This indicates the the wings are highly damped structures. Forced vibration of the nylon wings found broadband frequency content observed at $\approx$10 Hz. The broadband content did not change frequency over the range of α and Re values. This was assumed to be assosiated with the first bending mode observed in the free vibration.

8.3 Aerodynamics

The wing surface perturbations were of concern as they could potential adversely impact the UAVs performance. The bumpy airfoil profile is a byproduct of the internal design and the manufacturing process. It was shown that the extent of the influence of the bumps was dependent on the Re. It was shown that the trend increased the L/D ratio at low Re values $\leq 10^5$ and reduced the L/D ratio at Re values $\geq 10^5$. The conclusion is that at low Re values the bumps improve performance and at high Re values the performance is diminished. Three options are thus available; accept the adverse performance at high Re values, put a smooth coating layer over the outer surface to eliminate the bumps, or focus

on producing a slender low Re inflatable airfoil profile. It is my opinion that skinning the airfoil simply adds weight and complexity to the system and thus was not utilized within this research. Obtaining a more slender airfoil will be problematic due to the manufacturing constraints. UAVs with specific performance goals may these options appealing.

Aerodynamic analysis of wing warping data indicated that substantial roll control was available when the inflatable wings were warped. This was confirmed when scaled models were constructed of the warped inflatable wings and analyzed in the tunnel. PIV measurements of the circulation revealed that the warped wing model generated approximately four-times the amount of lift as the non-warped case. Thus, it was determined that roll authority was possible through manipulating the wing in this manner. However, the current warping strategies may not be sufficient to provide adequate roll control for gust response and rapid maneuvering. The most promising and simple solution was wing warping through conventional servos attached to the trailing edge of the wing. The analysis indicated that the optimal servo location for roll performance was between 68 - 82% of the semi-span. Other warping techniques were investigated however they did not the easy implementation, performance and simplicity of conventional servos. Removing the servos form the surface of the airfoil will improve performance and reduce drag. This could be accomplished through creating a cavity into which the servo is positioned. However, this would add manufacturing complexity.

8.4 Flight Testing

Substantial flight testing of the inflatable wings was conducted during this research. Each inflatable wing design was flight tested in multiple configurations. Approximately 500 flights of small UAVs have been conducted in support of this research. This includes approximately 300 flights of vehicles using inflatable wings and approximately 200 flights of UAVs using mock-up inflatable wings. This covers a large range of wing spans (4 – 12 ft), weights (5 – 40 lbs), flight durations and weather conditions. In addition this also includes flight testing of wing warping.

Three different wing warping techniques were ultimately examined: a tensile force on the surface of the wing, from the wing root to the wingtip; a chord-wise tensile force between the leading and trailing edges; and a mechanical force applied to the trailing edge.

The Vectran and nylon wings were warped in laboratory tests using nitinol actuators. When measured from leading to trailing edge at the wingtip, the wing twist generated by the nitinol caused an effective increase in α of 3°. If the deflection is measured from the first

deformation point (approximately 0.75c), the effective flap deflection was approximately 16°. This technique showed promise and was used on a nylon wing during flight testing. The technique was not successful during this testing as the convective cooling of the scrubbing airflow did not enable the nitinol to operate correctly. Another issue during testing was control. The response rate of the nitinol was slow and thus a risk. Potentially other SMA materials could be used but were not extensively examined.

Mechanical trailing edge warping (using the servo and pulley system) provided excellent roll control of the Vectran wings. Qualitative flight stability was greatly improved from the empenage only control. Roll control was adequately provided by the wing deformation, resulting in controlled steady state roll rates. While effective, this warping techniques was not a long term solution.

As highlighted above the most practical solution was wing warping of the inflatable wing with mechanical servos. The actuated servo bend the wing chord-wise along one or more longitudinal baffles. This mechanism provided adequate roll control to the vehicle and was capable of trimming out any inherent roll. This method was easy to implement and was reliable. However, as stated above, the disadvantage is that the solid mechanical servos were adhered to the surface of the wing. This complicates one of the main benefits of inflatable wings – minimal packed-volume. Additionally, the servos adhered to the wing surface adversely affect the airflow over the airfoil.

One suggestion for possible future work is to control the wing shape pneumatically. Currently, the inflatable wings have a common or open internal volume. Thus the internal pressure is distributed evenly within the wing. The span-wise baffles could be capped at each end allowing each baffled segment to have an independent inflation pressure. This could be used to alter the outer airfoil profile, or to create span-wise stiff or weak points. Span-wise stiff or weak baffles can be used the create flaps and changes to the outer profile could be optimized for the flight regime.

Another suggestion, which was not investigated within this research, is the deployment of inflatable wings from the wing tips of conventional wings. Deployable wing extensions would be ideally suited for inflatable wings as packed space is of concern. Here traditional wings could be fitted with inflatable wing extensions to provide additional span when needed. This would require the development of some form of wing retracting and/or deflating device.

8.5 Survivability

The inflatable wings have proved to be very durable, which will help in their long term acceptance due to this high damage tolerance. All the inflatable wings used within this research have survived multiple crash landings. Even crashes where the entire vehicle has been destroyed, the wing have remained intact and undamaged. Minor repairs have been made to the internal bladders of the Vectran wings however these repairs were made due to human error and negligence. The repairs are simple, similar to that of a flat bicycle tire. The inflatable wings can absorb sudden impact loads with no adverse affect to the inflatable structure. The wings simply deforms due to the impact and then returns to its original position.

Appendix A

AEROELASTIC EFFECTS AND WING WARPING – Matlab Scripts

Appendix A.1 is a Matlab scrip used to plot photogrametry data. The raw image data is processed using PhotoModeler Pro, and then is inserted into this code in order to generate Figures of the wing deformation. Appendix A.2 was used to obtain the Reciprocity, phase, frequency and coherence. Data is inserted into this scrip after the "Free Vibration" testing. Appendix A.3 was used to obtain the time history and frequency spectrum plots from data obtained during the "Forced Vibration" testing.

A.1 Photogrametry Reader

```
% AndrewWing.m
%
% Andrew Simpson
% 1/25/2005
%
clear all;
close all;
%
% [ID, X, Y, Z] in meters
Run1=[]
Run2=[];
Run3=[];
Run4=[];
Run5=[];

figure('color','w')
Hold on;

plot3(Run5(:,2),Run5(:,3),Run5(:,4),'.',Run2(:,2),Run2(:,3),
Run2(:,4),'.',Run3(:,2),Run3(:,3),Run3(:,4),'.',Run4(:,2),
Run4(:,3),Run4(:,4),'.',Run5(:,2),Run5(:,3),Run5(:,4),'.')
grid on;
title('Aeroelasticity');
%
% Generate Surfaces from http://www.mathworks.com/support/
% For Tip Up
x1 = Run1(:,2);
y1 = Run1(:,3);
z1 = Run1(:,4);
% Load the data and extract the (x,y,z) information:
%load sample.mat
% Determine the minimum and the maximum x and y values:
xmin1 = min(x1); ymin1 = min(y1);
xmax1 = max(x1); ymax1 = max(y1);
% Define the resolution of the grid:
xres1=20;
yres1=20;
% Define the range and spacing of the x- and y-coordinates,
% and then fit them into X and Y
xv1 = linspace(xmin1, xmax1, xres1);
yv1 = linspace(ymin1, ymax1, yres1);
```

```
[Xinterp1,Yinterp1] = meshgrid(xv1,yv1);
% Calculate Z in the X-Y interpolation space, which is an
% evenly spaced grid:
Zinterp1 = griddata(x1,y1,z1,Xinterp1,Yinterp1);

 x2 = Run2(:,2);
 y2 = Run2(:,3);
 z2 = Run2(:,4);
% Load the data and extract the (x,y,z) information:
%load sample.mat
% Determine the minimum and the maximum x and y values:
xmin2 = min(x2); ymin2 = min(y2);
xmax2 = max(x2); ymax2 = max(y2);
% Define the resolution of the grid:
xres2=20;
yres2=20;
% Define the range and spacing of the x- and y-coordinates,
% % and then fit them into X and Y
xv2 = linspace(xmin2, xmax2, xres2);
yv2 = linspace(ymin2, ymax2, yres2);
[Xinterp2,Yinterp2] = meshgrid(xv2,yv2);
% Calculate Z in the X-Y interpolation space, which is an
% evenly spaced grid:
Zinterp2 = griddata(x2,y2,z2,Xinterp2,Yinterp2);

 x3 = Run3(:,2);
 y3 = Run3(:,3);
 z3 = Run3(:,4);
% Load the data and extract the (x,y,z) information:
%load sample.mat
% Determine the minimum and the maximum x and y values:
xmin3 = min(x3); ymin3 = min(y3);
xmax3 = max(x3); ymax3 = max(y3);
% Define the resolution of the grid:
xres3=20;
yres3=20;
% Define the range and spacing of the x- and y-coordinates,
% % and then fit them into X and Y
xv3 = linspace(xmin3, xmax3, xres3);
yv3 = linspace(ymin3, ymax3, yres3);
[Xinterp3,Yinterp3] = meshgrid(xv3,yv3);
% Calculate Z in the X-Y interpolation space, which is an
% evenly spaced grid:
Zinterp3 = griddata(x3,y3,z3,Xinterp3,Yinterp3);


 x4 = Run4(:,2);
 y4 = Run4(:,3);
 z4 = Run4(:,4);
% Load the data and extract the (x,y,z) information:
%load sample.mat
% Determine the minimum and the maximum x and y values:
xmin4 = min(x4); ymin4 = min(y4);
xmax4 = max(x4); ymax4 = max(y4);
% Define the resolution of the grid:
xres4=20;
yres4=20;
% Define the range and spacing of the x- and y-coordinates,
% % and then fit them into X and Y
xv4 = linspace(xmin4, xmax4, xres4);
yv4 = linspace(ymin4, ymax4, yres4);
[Xinterp4,Yinterp4] = meshgrid(xv4,yv4);
% Calculate Z in the X-Y interpolation space, which is an
% evenly spaced grid:
Zinterp4 = griddata(x4,y4,z4,Xinterp4,Yinterp4);
```

```
 x5 = Run5(:,2);
 y5 = Run5(:,3);
 z5 = Run5(:,4);
% Load the data and extract the (x,y,z) information:
%load sample.mat
% Determine the minimum and the maximum x and y values:
xmin5 = min(x5); ymin5 = min(y5);
xmax5 = max(x5); ymax5 = max(y5);
% Define the resolution of the grid:
xres5=20;
yres5=20;
% Define the range and spacing of the x- and y-coordinates,
% % and then fit them into X and Y
xv5 = linspace(xmin5, xmax5, xres5);
yv5 = linspace(ymin5, ymax5, yres5);
[Xinterp5,Yinterp5] = meshgrid(xv5,yv5);
% Calculate Z in the X-Y interpolation space, which is an
% evenly spaced grid:
Zinterp5 = griddata(x5,y5,z5,Xinterp5,Yinterp5);

% Generate the mesh plot (CONTOUR can also be used):
figure('color','w')
hold on;
h(1)=surf(Xinterp1,Yinterp1,Zinterp1)
colormap(hsv)
h(2)=surf(Xinterp2,Yinterp2,Zinterp2)
colormap(autumn(128))
h(3)=surf(Xinterp3,Yinterp3,Zinterp3)
colormap(hsv)
h(4)=surf(Xinterp4,Yinterp4,Zinterp4)
colormap(hsv)
h(5)=surf(Xinterp5,Yinterp5,Zinterp5)
colormap(hsv)
xlabel X; ylabel Y; zlabel Z;
grid on;
axis([-0.45 -0.1 -0.1 0.4 0.2 0.45]);
xlabel('X Position (m)');
ylabel('Y Position (m)');
zlabel('Height (m)');
title('MIAV - Inflatable Wing (2-8)');
```

A.2 Reciprocity File

```
load test10_frf_chan2.txt;
load test9_frf_chan3.txt;
load test10_coh_chan2.txt;
load test9_coh_chan3.txt;

freqch2=test10_frf_chan2(:,1);
realch2=test10_frf_chan2(:,2);
imagch2=test10_frf_chan2(:,3);
cohch2=test10_coh_chan2(:,2);

imagch2=imagch2*j;
magch2=abs(realch2+imagch2);
phasech2=angle(realch2+imagch2);

freqch3=test9_frf_chan3(:,1);
realch3=test9_frf_chan3(:,2);
imagch3=test9_frf_chan3(:,3);
cohch3=test9_coh_chan3(:,2);

imagch3=imagch3*j;
```

```
magch3=abs(realch3+imagch3);
phasech3=angle(realch3+imagch3);

subplot(3,1,1),plot(freqch2,magch2)
hold on
subplot(3,1,2),plot(freqch2,phasech2)
hold on
subplot(3,1,3),plot(freqch2,cohch2)
hold on
subplot(3,1,1),plot(freqch3,magch3,'r')
ylabel('Magnitude')
Title('MIAV Reciprocity Function (6psi)')
subplot(3,1,2),plot(freqch3,phasech3,'r')
ylabel('Phase')
subplot(3,1,3),plot(freqch3,cohch3,'r')
xlabel('Frequency, Hz')
ylabel('Coherence')
legend('midpoint','trailing edge')
print -dpng test1_chans
```

A.3 Time History and Frequency Spectrum plots

```
function bdlook3(bdata,xdata,line,dtype)

% this is a function to look at the plots from the bridge data
% (with any number of columns)
% they can be time history or averaged fft or cepstrum plots
%
% bdlook3(bdata,xdata,line,dtype)
% bdata is a matrix of 24 columns, one for each cable of the set
% xdata is the time vector (or frequency or time) for the x-axis
% line is a string variable with the line designation (as, an, bs, etc.)
% dtype is a string variable with the type of data (time record, avg fft, etc.)
% (including a comma and a space after it)
%
% they are displayed on pages of eight plots each




szdata=size(bdata);
npage=ceil(szdata(2)/8);

for i=1:npage-1
   eval([ 'figure(i)' ])

   for ii=1:8
      iii=(i-1)*8+ii;
      eval(['subplot(42' num2str(ii) '),plot(xdata,bdata(:,' num2str(iii) '))'])
      eval(['title( [dtype line num2str(iii)] )' ])
   end

end

remain=szdata(2)-((npage-1)*8);
i=npage;
   eval([ 'figure(i)' ])

   for ii=1:remain
      iii=(i-1)*8+ii;
      eval(['subplot(42' num2str(ii) '),plot(xdata,bdata(:,' num2str(iii) '))'])
      eval(['title( [dtype line num2str(iii)] )' ])
   end
```

```
function bdlook3(bdata,xdata,line,dtype)

% this is a function to look at the plots from the bridge data
% (with any number of columns)
% they can be time history or averaged fft or cepstrum plots
%
% bdlook3(bdata,xdata,line,dtype)
% bdata is a matrix of 24 columns, one for each cable of the set
% xdata is the time vector (or frequency or time) for the x-axis
% line is a string variable with the line designation (as, an, bs, etc.)
% dtype is a string variable with the type of data (time record, avg fft, etc.)
% (including a comma and a space after it)
%
% they are displayed on pages of eight plots each




szdata=size(bdata);
npage=ceil(szdata(2)/8);

for i=1:npage-1
   eval([ 'figure(i)' ])

   for ii=1:8
      iii=(i-1)*8+ii;
      eval(['subplot(42' num2str(ii) '),plot(xdata,bdata(:,' num2str(iii) '))'])
      eval(['title( [dtype line num2str(iii)] )' ])
   end

end

remain=szdata(2)-((npage-1)*8);
i=npage;
   eval([ 'figure(i)' ])

   for ii=1:remain
      iii=(i-1)*8+ii;
      eval(['subplot(42' num2str(ii) '),plot(xdata,bdata(:,' num2str(iii) '))'])
      eval(['title( [dtype line num2str(iii)] )' ])
   end
```

Appendix B

AERODYNAMICS AND MODELING – Matlab Scripts

Appendix B.1 was used to process wake traverse data. Three velocity components were read by this script and lift and drag were calculated. The script then plots C_l and C_d versus α°, C_l versus C_d (drag polar), and L/D versus α°.

Appendix B.2 was used to process the images captured during the PIV process. The file calculates the circulation (via vorticity) from the trailing edge of the wing. This can then be transformed into a value for Lift.

Appendix B.3 was a lifting line script.

B.1 Wake Traverse Data Reader

```
function    wakesurvey

% BIG BLUE wing Tests
% 7 Hole Probe Data Reducer
% Reads in AAV (average velocity) files
% and returns aerodynamic variables

span=24*.0254; % in meters
rho=1.23; % density in kg/m^3
chord=11.0401*.0254;
area=span*chord;

%airfoil='e';
%run=1;

%%%%%%%%%%%%%%% re200k
Re=200000;

Uinfideal=(Re.*0.000017775)/(rho*chord)
Winfideal=(Re.*0.000017775)/(rho*chord)

file1='/Documents and Settings/aeroprobedata/re200k/text/re200k_AoA-6.txt';
file2='/Documents and Settings/aeroprobedata/re200k/text/re200k_AoA-4.txt';
file3='/Documents and Settings/aeroprobedata/re200k/text/re200k_AoA-2.txt';
file4='/Documents and Settings/aeroprobedata/re200k/text/re200k_AoA0.txt';
file5='/Documents and Settings/aeroprobedata/re200k/text/re200k_AoA2.txt';
file6='/Documents and Settings/aeroprobedata/re200k/text/re200k_AoA4.txt';
file7='/Documents and Settings/aeroprobedata/re200k/text/re200k_AoA6.txt';
file8='/Documents and Settings/aeroprobedata/re200k/text/re200k_AoA8.txt';
file9='/Documents and Settings/aeroprobedata/re200k/text/re200k_AoA10.txt';
file10='/Documents and Settings/aeroprobedata/re200k/text/re200k_AoA12.txt';
file11='/Documents and Settings/aeroprobedata/re200k/text/re200k_AoA14.txt';
file12='/Documents and Settings/aeroprobedata/re200k/text/re200k_AoA16.txt';
file13='/Documents and Settings/aeroprobedata/re200k/text/re200k_AoA18.txt';
file14='/Documents and Settings/aeroprobedata/re200k/text/re200k_AoA20.txt';
%filebase=strcat(airfoil,'run',num2str(run));
%file=strcat(filebase,'_Prb0.aav');
```

```
%%%%%%%%%% re250,0000
Re2=250000;

Uinfideal2=(Re2.*0.000017775)/(rho*chord)
Winfideal2=(Re2.*0.000017775)/(rho*chord)

file15='/Documents and Settings/aeroprobedata/re250k/text/re250k_AoA-6.txt';
file16='/Documents and Settings/aeroprobedata/re250k/text/re250k_AoA-4.txt';
file17='/Documents and Settings/aeroprobedata/re250k/text/re250k_AoA-2.txt';
file18='/Documents and Settings/aeroprobedata/re250k/text/re250k_AoA0.txt';
file19='/Documents and Settings/aeroprobedata/re250k/text/re250k_AoA2.txt';
file20='/Documents and Settings/aeroprobedata/re250k/text/re250k_AoA4.txt';
file21='/Documents and Settings/aeroprobedata/re250k/text/re250k_AoA6.txt';
file22='/Documents and Settings/aeroprobedata/re250k/text/re250k_AoA8.txt';
file23='/Documents and Settings/aeroprobedata/re250k/text/re250k_AoA10.txt';
file24='/Documents and Settings/aeroprobedata/re250k/text/re250k_AoA12.txt';
file25='/Documents and Settings/aeroprobedata/re250k/text/re250k_AoA14.txt';
file26='/Documents and Settings/aeroprobedata/re250k/text/re250k_AoA16.txt';
file27='/Documents and Settings/aeroprobedata/re250k/text/re250k_AoA18.txt';
file28='/Documents and Settings/aeroprobedata/re250k/text/re250k_AoA20.txt';
%filebase=strcat(airfoil,'run',num2str(run));
%file=strcat(filebase,'_Prb0.aav');

%%%%%%re200k
[x,y,z,u1,v1,w1,po,ps,pvread,valid]=textread(file1,'%n%n%n%n%n%n%n%n%n',
'headerlines',1);
[x,y,z,u2,v2,w2,po,ps,pvread,valid]=textread(file2,'%n%n%n%n%n%n%n%n%n',
'headerlines',1);
[x,y,z,u3,v3,w3,po,ps,pvread,valid]=textread(file3,'%n%n%n%n%n%n%n%n%n',
'headerlines',1);
[x,y,z,u4,v4,w4,po,ps,pvread,valid]=textread(file4,'%n%n%n%n%n%n%n%n%n',
'headerlines',1);
[x,y,z,u5,v5,w5,po,ps,pvread,valid]=textread(file5,'%n%n%n%n%n%n%n%n%n',
'headerlines',1);
[x,y,z,u6,v6,w6,po,ps,pvread,valid]=textread(file6,'%n%n%n%n%n%n%n%n%n',
'headerlines',1);
[x,y,z,u7,v7,w7,po,ps,pvread,valid]=textread(file7,'%n%n%n%n%n%n%n%n%n',
'headerlines',1);
[x,y,z,u8,v8,w8,po,ps,pvread,valid]=textread(file8,'%n%n%n%n%n%n%n%n%n',
'headerlines',1);
[x,y,z,u9,v9,w9,po,ps,pvread,valid]=textread(file9,'%n%n%n%n%n%n%n%n%n',
'headerlines',1);
[x,y,z,u10,v10,w10,po,ps,pvread,valid]=textread(file10,'%n%n%n%n%n%n%n%n%n',
'headerlines',1);
[x,y,z,u11,v11,w11,po,ps,pvread,valid]=textread(file11,'%n%n%n%n%n%n%n%n%n',
'headerlines',1);
[x,y,z,u12,v12,w12,po,ps,pvread,valid]=textread(file12,'%n%n%n%n%n%n%n%n%n',
'headerlines',1);
[x,y,z,u13,v13,w13,po,ps,pvread,valid]=textread(file13,'%n%n%n%n%n%n%n%n%n',
'headerlines',1);
[x,y,z,u14,v14,w14,po,ps,pvread,valid]=textread(file14,'%n%n%n%n%n%n%n%n%n',
'headerlines',1);

%%%%%re250k
[x,y,z,u15,v15,w15,po,ps,pvread,valid]=textread(file15,'%n%n%n%n%n%n%n%n%n',
'headerlines',1);
[x,y,z,u16,v16,w16,po,ps,pvread,valid]=textread(file16,'%n%n%n%n%n%n%n%n%n',
'headerlines',1);
[x,y,z,u17,v17,w17,po,ps,pvread,valid]=textread(file17,'%n%n%n%n%n%n%n%n%n',
'headerlines',1);
[x,y,z,u18,v18,w18,po,ps,pvread,valid]=textread(file18,'%n%n%n%n%n%n%n%n%n',
'headerlines',1);
[x,y,z,u19,v19,w19,po,ps,pvread,valid]=textread(file19,'%n%n%n%n%n%n%n%n%n',
'headerlines',1);
[x,y,z,u20,v20,w20,po,ps,pvread,valid]=textread(file20,'%n%n%n%n%n%n%n%n%n',
'headerlines',1);
```

```
[x,y,z,u21,v21,w21,po,ps,pvread,valid]=textread(file21,'%n%n%n%n%n%n%n%n%n',
'headerlines',1);
[x,y,z,u22,v22,w22,po,ps,pvread,valid]=textread(file22,'%n%n%n%n%n%n%n%n%n',
'headerlines',1);
[x,y,z,u23,v23,w23,po,ps,pvread,valid]=textread(file23,'%n%n%n%n%n%n%n%n%n',
'headerlines',1);
[x,y,z,u24,v24,w24,po,ps,pvread,valid]=textread(file24,'%n%n%n%n%n%n%n%n%n',
'headerlines',1);
[x,y,z,u25,v25,w25,po,ps,pvread,valid]=textread(file25,'%n%n%n%n%n%n%n%n%n',
'headerlines',1);
[x,y,z,u26,v26,w26,po,ps,pvread,valid]=textread(file26,'%n%n%n%n%n%n%n%n%n',
'headerlines',1);
[x,y,z,u27,v27,w27,po,ps,pvread,valid]=textread(file27,'%n%n%n%n%n%n%n%n%n',
'headerlines',1);
[x,y,z,u28,v28,w28,po,ps,pvread,valid]=textread(file28,'%n%n%n%n%n%n%n%n%n',
'headerlines',1);

[ny1,dum]=size(u1);
[ny2,dum]=size(u2);
[ny3,dum]=size(u3);
[ny4,dum]=size(u4);
[ny5,dum]=size(u5);
[ny6,dum]=size(u6);
[ny7,dum]=size(u7);
[ny8,dum]=size(u8);
[ny9,dum]=size(u9);
[ny10,dum]=size(u10);
[ny11,dum]=size(u11);
[ny12,dum]=size(u12);
[ny13,dum]=size(u13);
[ny14,dum]=size(u14);
%mag=sqrt(u.^2+v.^2+w.^2)

[ny15,dum]=size(u15);
[ny16,dum]=size(u16);
[ny17,dum]=size(u17);
[ny18,dum]=size(u18);
[ny19,dum]=size(u19);
[ny20,dum]=size(u20);
[ny21,dum]=size(u21);
[ny22,dum]=size(u22);
[ny23,dum]=size(u23);
[ny24,dum]=size(u24);
[ny25,dum]=size(u25);
[ny26,dum]=size(u26);
[ny27,dum]=size(u27);
[ny28,dum]=size(u28);
%mag=sqrt(u.^2+v.^2+w.^2)


xlin1=linspace(0,548,ny1);
xlin2=linspace(0,548,ny2);
xlin3=linspace(0,548,ny3);
xlin4=linspace(0,551,ny4);
xlin5=linspace(0,548,ny5);
xlin6=linspace(0,548,ny6);
xlin7=linspace(0,548,ny7);
xlin8=linspace(0,548,ny8);
xlin9=linspace(0,548,ny9);
xlin10=linspace(0,548,ny10);
xlin11=linspace(0,548,ny11);
xlin12=linspace(0,548,ny12);
xlin13=linspace(0,548,ny13);
xlin14=linspace(0,548,ny14);
```

```
xlin15=linspace(0,548,ny15);
xlin16=linspace(0,548,ny16);
xlin17=linspace(0,548,ny17);
xlin18=linspace(0,553,ny18);
xlin19=linspace(0,553,ny19);
xlin20=linspace(0,553,ny20);
xlin21=linspace(0,553,ny21);
xlin22=linspace(0,553,ny22);
xlin23=linspace(0,553,ny23);
xlin24=linspace(0,548,ny24);
xlin25=linspace(0,548,ny25);
xlin26=linspace(0,548,ny26);
xlin27=linspace(0,548,ny27);
xlin28=linspace(0,548,ny28);

[nx1,dum]=size(w1);
[nx2,dum]=size(w2);
[nx3,dum]=size(w3);
[nx4,dum]=size(w4);
[nx5,dum]=size(w5);
[nx6,dum]=size(w6);
[nx7,dum]=size(w7);
[nx8,dum]=size(w8);
[nx9,dum]=size(w9);
[nx10,dum]=size(w10);
[nx11,dum]=size(w11);
[nx12,dum]=size(w12);
[nx13,dum]=size(w13);
[nx14,dum]=size(w14);
%mag=sqrt(u.^2+v.^2+w.^2)

[nx15,dum]=size(w15);
[nx16,dum]=size(w16);
[nx17,dum]=size(w17);
[nx18,dum]=size(w18);
[nx19,dum]=size(w19);
[nx20,dum]=size(w20);
[nx21,dum]=size(w21);
[nx22,dum]=size(w22);
[nx23,dum]=size(w23);
[nx24,dum]=size(w24);
[nx25,dum]=size(w25);
[nx26,dum]=size(w26);
[nx27,dum]=size(w27);
[nx28,dum]=size(w28);
%mag=sqrt(u.^2+v.^2+w.^2)

uinf1=u1(1:200);
uinf2=u1(348:548);
Uinf1=(sum(uinf1)+sum(uinf2))./400 ;
ud1=Uinf1.^2-u1.^2;
%us1=u1.*(Uinf-u1);
%ud=Uinf-mag;
%us=mag.*(Uinf-mag);
%udo1=1-u1./Uinf;
wake1=trapz(xlin1,ud1)/1000;
drag1=0.5*rho*span*wake1
cd1=drag1/(0.5*rho*Uinfideal.^2*area)

uinf1=u2(1:200);
uinf2=u2(348:548);
Uinf2=(sum(uinf1)+sum(uinf2))./400;
ud2=Uinf2.^2-u2.^2;
%us2=u2.*(Uinf-u2);
%ud=Uinf-mag;
%us=mag.*(Uinf-mag);
%udo2=1-u2./Uinf;
wake2=trapz(xlin2,ud2)/1000;
drag2=0.5*rho*span*wake2
```

```
cd2=drag2/(0.5*rho*Uinfideal.^2*area)

uinf1=u3(1:200);
uinf2=u3(348:548);
Uinf3=(sum(uinf1)+sum(uinf2))./400;
ud3=Uinf3.^2-u3.^2;
%us3=u3.*(Uinf-u3);
%ud=Uinf-mag;
%us=mag.*(Uinf-mag);
%udo3=1-u3./Uinf;
wake3=trapz(xlin3,ud3)/1000;
drag3=0.5*rho*span*wake3
cd3=drag3/(0.5*rho*Uinfideal.^2*area)

uinf1=u4(1:150);
uinf2=u4(348:548);
Uinf4=(sum(uinf1)+sum(uinf2))./350;
ud4=Uinf4.^2-u4.^2;
%us4=u4.*(Uinf-u4);
%ud=Uinf-mag;
%us=mag.*(Uinf-mag);
%udo4=1-u3./Uinf;
wake4=trapz(xlin4,ud4)/1000;
drag4=0.5*rho*span*wake4
cd4=drag4/(0.5*rho*Uinfideal.^2*area)

uinf1=u5(1:150);
uinf2=u5(348:548);
Uinf5=(sum(uinf1)+sum(uinf2))./350;
ud5=Uinf5.^2-u5.^2;
%us4=u4.*(Uinf-u4);
%ud=Uinf-mag;
%us=mag.*(Uinf-mag);
%udo4=1-u3./Uinf;
wake5=trapz(xlin5,ud5)/1000;
drag5=0.5*rho*span*wake5
cd5=drag5/(0.5*rho*Uinfideal.^2*area)

uinf1=u6(1:150);
uinf2=u6(348:548);
Uinf6=(sum(uinf1)+sum(uinf2))./350;
ud6=Uinf6.^2-u6.^2;
%us4=u4.*(Uinf-u4);
%ud=Uinf-mag;
%us=mag.*(Uinf-mag);
%udo4=1-u3./Uinf;
wake6=trapz(xlin6,ud6)/1000;
drag6=0.5*rho*span*wake6
cd6=drag6/(0.5*rho*Uinfideal.^2*area)

uinf1=u7(1:150);
uinf2=u7(348:548);
Uinf7=(sum(uinf1)+sum(uinf2))./350;
ud7=Uinf7.^2-u7.^2;
%us4=u4.*(Uinf-u4);
%ud=Uinf-mag;
%us=mag.*(Uinf-mag);
%udo4=1-u3./Uinf;
wake7=trapz(xlin7,ud7)/1000;
drag7=0.5*rho*span*wake7
cd7=drag7/(0.5*rho*Uinfideal.^2*area)

uinf1=u8(1:150);
uinf2=u8(348:548);
Uinf8=(sum(uinf1)+sum(uinf2))./350;
ud8=Uinf8.^2-u8.^2;
%us4=u4.*(Uinf-u4);
%ud=Uinf-mag;
%us=mag.*(Uinf-mag);
```

```
%udo4=1-u3./Uinf;
wake8=trapz(xlin8,ud8)/1000;
drag8=0.5*rho*span*wake8
cd8=drag8/(0.5*rho*Uinfideal.^2*area)

uinf1=u9(1:150);
uinf2=u9(348:548);
Uinf9=(sum(uinf1)+sum(uinf2))./350;
ud9=Uinf9.^2-u9.^2;
%us4=u4.*(Uinf-u4);
%ud=Uinf-mag;
%us=mag.*(Uinf-mag);
%udo4=1-u3./Uinf;
wake9=trapz(xlin9,ud9)/1000;
drag9=0.5*rho*span*wake9
cd9=drag9/(0.5*rho*Uinfideal.^2*area)

uinf1=u10(1:150);
uinf2=u10(348:548);
Uinf10=(sum(uinf1)+sum(uinf2))./350;
ud10=Uinf10.^2-u10.^2;
%us4=u4.*(Uinf-u4);
%ud=Uinf-mag;
%us=mag.*(Uinf-mag);
%udo4=1-u3./Uinf;
wake10=trapz(xlin10,ud10)/1000;
drag10=0.5*rho*span*wake10
cd10=drag10/(0.5*rho*Uinfideal.^2*area)

uinf1=u11(1:150);
uinf2=u11(348:548);
Uinf11=(sum(uinf1)+sum(uinf2))./350;
ud11=Uinf11.^2-u11.^2;
%us4=u4.*(Uinf-u4);
%ud=Uinf-mag;
%us=mag.*(Uinf-mag);
%udo4=1-u3./Uinf;
wake11=trapz(xlin11,ud11)/1000;
drag11=0.5*rho*span*wake11
cd11=drag11/(0.5*rho*Uinfideal.^2*area)

uinf1=u12(1:150);
uinf2=u12(348:548);
Uinf12=(sum(uinf1)+sum(uinf2))./350;
ud12=Uinf12.^2-u12.^2;
%us4=u4.*(Uinf-u4);
%ud=Uinf-mag;
%us=mag.*(Uinf-mag);
%udo4=1-u3./Uinf;
wake12=trapz(xlin12,ud12)/1000;
drag12=0.5*rho*span*wake12
cd12=drag12/(0.5*rho*Uinfideal.^2*area)

uinf1=u13(1:150);
uinf2=u13(348:548);
Uinf13=(sum(uinf1)+sum(uinf2))./350;
ud13=Uinf13.^2-u13.^2;
%us4=u4.*(Uinf-u4);
%ud=Uinf-mag;
%us=mag.*(Uinf-mag);
%udo4=1-u3./Uinf;
wake13=trapz(xlin13,ud13)/1000;
drag13=0.5*rho*span*wake13
cd13=drag13/(0.5*rho*Uinfideal.^2*area)

uinf1=u14(1:150);
uinf2=u14(348:548);
Uinf14=(sum(uinf1)+sum(uinf2))./350;
ud14=Uinf14.^2-u14.^2;
```

```
%us4=u4.*(Uinf-u4);
%ud=Uinf-mag;
%us=mag.*(Uinf-mag);
%udo4=1-u3./Uinf;
wake14=trapz(xlin14,ud14)/1000;
drag14=0.5*rho*span*wake14
cd14=drag14/(0.5*rho*Uinfideal.^2*area)

%%%%%%%%%%%%%%lift re200k%%%%%%%%%%%%%%%%%%%
% vinf1=v1(1:200);
% vinf2=v1(348:548);
% Vinf1=(sum(vinf1)+sum(vinf2))./400
% vd1=Vinf1-v1;
wd1=(Winfideal-w1).*v1;
%us1=u1.*(Uinf-u1);
%ud=Uinf-mag;
%us=mag.*(Uinf-mag);
%udo1=1-u1./Uinf;
wake1=trapz(xlin1,wd1)/1000;
lift1=rho*span*wake1
cl1=lift1/(0.5*rho*Winfideal.^2*area)

% vinf1=v2(1:200);
% vinf2=v2(348:548);
% Vinf2=(sum(vinf1)+sum(vinf2))./400
% vd2=Vinf2-v2;
wd2=(Winfideal-w2).*v2;
%us1=u1.*(Uinf-u1);
%ud=Uinf-mag;
%us=mag.*(Uinf-mag);
%udo1=1-u1./Uinf;
wake2=trapz(xlin2,wd2)/1000;
lift2=rho*span*wake2
cl2=lift2/(0.5*rho*Winfideal.^2*area)

% vinf1=v3(1:200);
% vinf2=v3(348:548);
% Vinf3=(sum(vinf1)+sum(vinf2))./400
% vd3=Vinf3-v3;
wd3=(Winfideal-w3).*v3;
%us1=u1.*(Uinf-u1);
%ud=Uinf-mag;
%us=mag.*(Uinf-mag);
%udo1=1-u1./Uinf;
wake3=trapz(xlin3,wd3)/1000;
lift3=rho*span*wake3
cl3=lift3/(0.5*rho*Winfideal.^2*area)

% vinf1=v4(1:200);
% vinf2=v4(348:548);
% Vinf4=(sum(vinf1)+sum(vinf2))./400
% vd4=Vinf4-v4;
wd4=(Winfideal-w4).*v4;
%us1=u1.*(Uinf-u1);
%ud=Uinf-mag;
%us=mag.*(Uinf-mag);
%udo1=1-u1./Uinf;
wake4=trapz(xlin4,wd4)/1000;
lift4=rho*span*wake4
cl4=lift4/(0.5*rho*Winfideal.^2*area)

% vinf1=v5(1:200);
% vinf2=v5(348:548);
% Vinf5=(sum(vinf1)+sum(vinf2))./400
% vd5=Vinf5-v5;
wd5=(Winfideal-w5).*v5;
%us1=u1.*(Uinf-u1);
%ud=Uinf-mag;
%us=mag.*(Uinf-mag);
```

```
%udo1=1-u1./Uinf;
wake5=trapz(xlin5,wd5)/1000;
lift5=rho*span*wake5
cl5=lift5/(0.5*rho*Winfideal.^2*area)

% vinf1=v6(1:200);
% vinf2=v6(348:548);
% Vinf6=(sum(vinf1)+sum(vinf2))./400
% vd6=Vinf6-v6;
wd6=(Winfideal-w6).*v6;
%us1=u1.*(Uinf-u1);
%ud=Uinf-mag;
%us=mag.*(Uinf-mag);
%udo1=1-u1./Uinf;
wake6=trapz(xlin6,wd6)/1000;
lift6=rho*span*wake6
cl6=lift6/(0.5*rho*Winfideal.^2*area)

% vinf1=v7(1:200);
% vinf2=v7(348:548);
% Vinf7=(sum(vinf1)+sum(vinf2))./400
% vd7=Vinf7-v7;
wd7=(Winfideal-w7).*v7;
%us1=u1.*(Uinf-u1);
%ud=Uinf-mag;
%us=mag.*(Uinf-mag);
%udo1=1-u1./Uinf;
wake7=trapz(xlin7,wd7)/1000;
lift7=rho*span*wake7
cl7=lift7/(0.5*rho*Winfideal.^2*area)

% vinf1=v8(1:200);
% vinf2=v8(348:548);
% Vinf8=(sum(vinf1)+sum(vinf2))./400
% vd8=Vinf8-v8;
wd8=(Winfideal-w8).*v8;
%us1=u1.*(Uinf-u1);
%ud=Uinf-mag;
%us=mag.*(Uinf-mag);
%udo1=1-u1./Uinf;
wake8=trapz(xlin8,wd8)/1000;
lift8=rho*span*wake8
cl8=lift8/(0.5*rho*Winfideal.^2*area)

% vinf1=v9(1:200);
% vinf2=v9(348:548);
% Vinf9=(sum(vinf1)+sum(vinf2))./400
% vd9=Vinf9-v9;
wd9=(Winfideal-w9).*v9;
%us1=u1.*(Uinf-u1);
%ud=Uinf-mag;
%us=mag.*(Uinf-mag);
%udo1=1-u1./Uinf;
wake9=trapz(xlin9,wd9)/1000;
lift9=rho*span*wake9
cl9=lift9/(0.5*rho*Winfideal.^2*area)

% vinf1=v10(1:200);
% vinf2=v10(348:548);
% Vinf10=(sum(vinf1)+sum(vinf2))./400
% vd10=Vinf10-v10;
wd10=(Winfideal-w10).*v10;
%us1=u1.*(Uinf-u1);
%ud=Uinf-mag;
%us=mag.*(Uinf-mag);
%udo1=1-u1./Uinf;
wake10=trapz(xlin10,wd10)/1000;
lift10=rho*span*wake10
cl10=lift10/(0.5*rho*Winfideal.^2*area)
```

```
% vinf1=v11(1:200);
% vinf2=v11(348:548);
% Vinf11=(sum(vinf1)+sum(vinf2))./400
% vd11=Vinf11-v11;
wd11=(Winfideal-w11).*v11;
%us1=u1.*(Uinf-u1);
%ud=Uinf-mag;
%us=mag.*(Uinf-mag);
%udo1=1-u1./Uinf;
wake11=trapz(xlin11,wd11)/1000;
lift11=rho*span*wake11
cl11=lift11/(0.5*rho*Winfideal.^2*area)

% vinf1=v12(1:200);
% vinf2=v12(348:548);
% Vinf12=(sum(vinf1)+sum(vinf2))./400
% vd12=Vinf12-v12;
wd12=(Winfideal-w12).*v12;
%us1=u1.*(Uinf-u1);
%ud=Uinf-mag;
%us=mag.*(Uinf-mag);
%udo1=1-u1./Uinf;
wake12=trapz(xlin12,wd12)/1000;
lift12=rho*span*wake12
cl12=lift12/(0.5*rho*Winfideal.^2*area)

% vinf1=v13(1:200);
% vinf2=v13(348:548);
% Vinf13=(sum(vinf1)+sum(vinf2))./400
% vd13=Vinf13-v13;
wd13=(Winfideal-w13).*v13;
%us1=u1.*(Uinf-u1);
%ud=Uinf-mag;
%us=mag.*(Uinf-mag);
%udo1=1-u1./Uinf;
wake13=trapz(xlin13,wd13)/1000;
lift13=rho*span*wake13
cl13=lift13/(0.5*rho*Winfideal.^2*area)

% vinf1=v14(1:200);
% vinf2=v14(348:548);
% Vinf14=(sum(vinf1)+sum(vinf2))./400
% vd14=Vinf14-v14;
wd14=(Winfideal-w14).*v14;
%us1=u1.*(Uinf-u1);
%ud=Uinf-mag;
%us=mag.*(Uinf-mag);
%udo1=1-u1./Uinf;
wake14=trapz(xlin14,wd14)/1000;
lift14=rho*span*wake14
cl14=lift14/(0.5*rho*Winfideal.^2*area)

%%%%%%%%%%%%%%%%%%%%%%%%drag re250k%%%%%%%%%%%%%%%%%%%
uinf1=u15(1:200);
uinf2=u15(348:548);
Uinf15=(sum(uinf1)+sum(uinf2))./400 ;
ud15=Uinf15.^2-u15.^2;
%us1=u1.*(Uinf-u1);
%ud=Uinf-mag;
%us=mag.*(Uinf-mag);
%udo1=1-u1./Uinf;
wake15=trapz(xlin1,ud15)/1000;
drag15=0.5*rho*span*wake15
cd15=drag15/(0.5*rho*Uinfideal2.^2*area)

uinf1=u16(1:200);
uinf2=u16(348:548);
Uinf16=(sum(uinf1)+sum(uinf2))./400;
```

```
ud16=Uinf16.^2-u16.^2;
%us2=u2.*(Uinf-u2);
%ud=Uinf-mag;
%us=mag.*(Uinf-mag);
%udo2=1-u2./Uinf;
wake16=trapz(xlin16,ud16)/1000;
drag16=0.5*rho*span*wake16
cd16=drag16/(0.5*rho*Uinfideal2.^2*area)

uinf1=u17(1:200);
uinf2=u17(348:548);
Uinf17=(sum(uinf1)+sum(uinf2))./400;
ud17=Uinf17.^2-u17.^2;
%us3=u3.*(Uinf-u3);
%ud=Uinf-mag;
%us=mag.*(Uinf-mag);
%udo3=1-u3./Uinf;
wake17=trapz(xlin17,ud17)/1000;
drag17=0.5*rho*span*wake17
cd17=drag17/(0.5*rho*Uinfideal2.^2*area)

uinf1=u18(1:200);
uinf2=u18(348:548);
Uinf18=(sum(uinf1)+sum(uinf2))./400;
ud18=Uinf18.^2-u18.^2;
%us4=u4.*(Uinf-u4);
%ud=Uinf-mag;
%us=mag.*(Uinf-mag);
%udo4=1-u3./Uinf;
wake18=trapz(xlin18,ud18)/1000;
drag18=0.5*rho*span*wake18
cd18=drag18/(0.5*rho*Uinfideal2.^2*area)

uinf1=u19(1:200);
uinf2=u19(348:548);
Uinf19=(sum(uinf1)+sum(uinf2))./400;
ud19=Uinf19.^2-u19.^2;
%us4=u4.*(Uinf-u4);
%ud=Uinf-mag;
%us=mag.*(Uinf-mag);
%udo4=1-u3./Uinf;
wake19=trapz(xlin19,ud19)/1000;
drag19=0.5*rho*span*wake19
cd19=drag19/(0.5*rho*Uinfideal2.^2*area)

uinf1=u20(1:150);
uinf2=u20(298:548);
Uinf20=(sum(uinf1)+sum(uinf2))./400;
ud20=Uinf20.^2-u20.^2;
%us4=u4.*(Uinf-u4);
%ud=Uinf-mag;
%us=mag.*(Uinf-mag);
%udo4=1-u3./Uinf;
wake20=trapz(xlin20,ud20)/1000;
drag20=0.5*rho*span*wake20
cd20=drag20/(0.5*rho*Uinfideal2.^2*area)

uinf1=u21(1:150);
uinf2=u21(298:548);
Uinf21=(sum(uinf1)+sum(uinf2))./400;
ud21=Uinf21.^2-u21.^2;
%us4=u4.*(Uinf-u4);
%ud=Uinf-mag;
%us=mag.*(Uinf-mag);
%udo4=1-u3./Uinf;
wake21=trapz(xlin21,ud21)/1000;
drag21=0.5*rho*span*wake21
cd21=drag21/(0.5*rho*Uinfideal2.^2*area)
```

```
uinf1=u22(1:150);
uinf2=u22(348:548);
Uinf22=(sum(uinf1)+sum(uinf2))./350;
ud22=Uinf22.^2-u22.^2;
%us4=u4.*(Uinf-u4);
%ud=Uinf-mag;
%us=mag.*(Uinf-mag);
%udo4=1-u3./Uinf;
wake22=trapz(xlin22,ud22)/1000;
drag22=0.5*rho*span*wake22
cd22=drag22/(0.5*rho*Uinfideal2.^2*area)

uinf1=u23(1:150);
uinf2=u23(348:548);
Uinf23=(sum(uinf1)+sum(uinf2))./350;
ud23=Uinf23.^2-u23.^2;
%us4=u4.*(Uinf-u4);
%ud=Uinf-mag;
%us=mag.*(Uinf-mag);
%udo4=1-u3./Uinf;
wake23=trapz(xlin23,ud23)/1000;
drag23=0.5*rho*span*wake23
cd23=drag23/(0.5*rho*Uinfideal2.^2*area)

uinf1=u24(1:150);
uinf2=u24(348:548);
Uinf24=(sum(uinf1)+sum(uinf2))./350;
ud24=Uinf24.^2-u24.^2;
%us4=u4.*(Uinf-u4);
%ud=Uinf-mag;
%us=mag.*(Uinf-mag);
%udo4=1-u3./Uinf;
wake24=trapz(xlin24,ud24)/1000;
drag24=0.5*rho*span*wake24
cd24=drag24/(0.5*rho*Uinfideal2.^2*area)

uinf1=u25(1:150);
uinf2=u25(348:548);
Uinf25=(sum(uinf1)+sum(uinf2))./350;
ud25=Uinf25.^2-u25.^2;
%us4=u4.*(Uinf-u4);
%ud=Uinf-mag;
%us=mag.*(Uinf-mag);
%udo4=1-u3./Uinf;
wake25=trapz(xlin25,ud25)/1000;
drag25=0.5*rho*span*wake25
cd25=drag25/(0.5*rho*Uinfideal2.^2*area)

uinf1=u26(1:150);
uinf2=u26(348:548);
Uinf26=(sum(uinf1)+sum(uinf2))./350;
ud26=Uinf26.^2-u26.^2;
%us4=u4.*(Uinf-u4);
%ud=Uinf-mag;
%us=mag.*(Uinf-mag);
%udo4=1-u3./Uinf;
wake26=trapz(xlin26,ud26)/1000;
drag26=0.5*rho*span*wake26
cd26=drag26/(0.5*rho*Uinfideal2.^2*area)

uinf1=u27(1:150);
uinf2=u27(348:548);
Uinf27=(sum(uinf1)+sum(uinf2))./350;
ud27=Uinf27.^2-u27.^2;
%us4=u4.*(Uinf-u4);
%ud=Uinf-mag;
%us=mag.*(Uinf-mag);
%udo4=1-u3./Uinf;
wake27=trapz(xlin27,ud27)/1000;
```

```
drag27=0.5*rho*span*wake27
cd27=drag27/(0.5*rho*Uinfideal2.^2*area)

uinf1=u28(1:150);
uinf2=u28(348:548);
Uinf28=(sum(uinf1)+sum(uinf2))./350;
ud28=Uinf28.^2-u28.^2;
%us4=u4.*(Uinf-u4);
%ud=Uinf-mag;
%us=mag.*(Uinf-mag);
%udo4=1-u3./Uinf;
wake28=trapz(xlin28,ud28)/1000;
drag28=0.5*rho*span*wake28
cd28=drag28/(0.5*rho*Uinfideal2.^2*area)

%%%%%%%%%% re250k lift %%%%%%%%%%%%%%%%%%%%%%%%%%%%%%%%
% vinf1=v1(1:200);
% vinf2=v1(348:548);
% Vinf1=(sum(vinf1)+sum(vinf2))./400
% vd1=Vinf1-v1;
wd15=(Winfideal2-w15).*v15;
%us1=u1.*(Uinf-u1);
%ud=Uinf-mag;
%us=mag.*(Uinf-mag);
%udo1=1-u1./Uinf;
wake15=trapz(xlin15,wd15)/1000;
lift15=rho*span*wake15
cl15=lift15/(0.5*rho*Winfideal2.^2*area)

% vinf1=v2(1:200);
% vinf2=v2(348:548);
% Vinf2=(sum(vinf1)+sum(vinf2))./400
% vd2=Vinf2-v2;
wd16=(Winfideal2-w16).*v16;
%us1=u1.*(Uinf-u1);
%ud=Uinf-mag;
%us=mag.*(Uinf-mag);
%udo1=1-u1./Uinf;
wake16=trapz(xlin16,wd16)/1000;
lift16=rho*span*wake16
cl16=lift16/(0.5*rho*Winfideal2.^2*area)

% vinf1=v3(1:200);
% vinf2=v3(348:548);
% Vinf3=(sum(vinf1)+sum(vinf2))./400
% vd3=Vinf3-v3;
wd17=(Winfideal2-w17).*v17;
%us1=u1.*(Uinf-u1);
%ud=Uinf-mag;
%us=mag.*(Uinf-mag);
%udo1=1-u1./Uinf;
wake17=trapz(xlin17,wd17)/1000;
lift17=rho*span*wake17
cl17=lift17/(0.5*rho*Winfideal2.^2*area)

% vinf1=v4(1:200);
% vinf2=v4(348:548);
% Vinf4=(sum(vinf1)+sum(vinf2))./400
% vd4=Vinf4-v4;
wd18=(Winfideal2-w18).*v18;
%us1=u1.*(Uinf-u1);
%ud=Uinf-mag;
%us=mag.*(Uinf-mag);
%udo1=1-u1./Uinf;
wake18=trapz(xlin18,wd18)/1000;
%lift18=rho*span*wake18
%cl18=lift18/(0.5*rho*Winfideal.^2*area)
lift18=6.6797
cl18=0.3828
```

```
% vinf1=v5(1:200);
% vinf2=v5(348:548);
% Vinf5=(sum(vinf1)+sum(vinf2))./400
% vd5=Vinf5-v5;
wd19=(Winfideal2-w19).*v19;
%us1=u1.*(Uinf-u1);
%ud=Uinf-mag;
%us=mag.*(Uinf-mag);
%udo1=1-u1./Uinf;
wake19=trapz(xlin19,wd19)/1000;
lift19=rho*span*wake19
cl19=lift19/(0.5*rho*Winfideal2.^2*area)

% vinf1=v6(1:200);
% vinf2=v6(348:548);
% Vinf6=(sum(vinf1)+sum(vinf2))./400
% vd6=Vinf6-v6;
wd20=(Winfideal2-w20).*v20;
%us1=u1.*(Uinf-u1);
%ud=Uinf-mag;
%us=mag.*(Uinf-mag);
%udo1=1-u1./Uinf;
wake20=trapz(xlin20,wd20)/1000;
lift20=rho*span*wake20
cl20=lift20/(0.5*rho*Winfideal2.^2*area)

% vinf1=v7(1:200);
% vinf2=v7(348:548);
% Vinf7=(sum(vinf1)+sum(vinf2))./400
% vd7=Vinf7-v7;
wd21=(Winfideal2-w21).*v21;
%us1=u1.*(Uinf-u1);
%ud=Uinf-mag;
%us=mag.*(Uinf-mag);
%udo1=1-u1./Uinf;
wake21=trapz(xlin21,wd21)/1000;
lift21=rho*span*wake21
cl21=lift21/(0.5*rho*Winfideal2.^2*area)

% vinf1=v8(1:200);
% vinf2=v8(348:548);
% Vinf8=(sum(vinf1)+sum(vinf2))./400
% vd8=Vinf8-v8;
wd22=(Winfideal2-w22).*v22;
%us1=u1.*(Uinf-u1);
%ud=Uinf-mag;
%us=mag.*(Uinf-mag);
%udo1=1-u1./Uinf;
wake22=trapz(xlin22,wd22)/1000;
lift22=rho*span*wake22
cl22=lift22/(0.5*rho*Winfideal2.^2*area)

% vinf1=v9(1:200);
% vinf2=v9(348:548);
% Vinf9=(sum(vinf1)+sum(vinf2))./400
% vd9=Vinf9-v9;
wd23=(Winfideal2-w23).*v23;
%us1=u1.*(Uinf-u1);
%ud=Uinf-mag;
%us=mag.*(Uinf-mag);
%udo1=1-u1./Uinf;
wake23=trapz(xlin23,wd23)/1000;
lift23=rho*span*wake23
cl23=lift23/(0.5*rho*Winfideal2.^2*area)

% vinf1=v10(1:200);
% vinf2=v10(348:548);
% Vinf10=(sum(vinf1)+sum(vinf2))./400
```

```
% vd10=Vinf10-v10;
wd24=(Winfideal2-w24).*v24;
%us1=u1.*(Uinf-u1);
%ud=Uinf-mag;
%us=mag.*(Uinf-mag);
%udo1=1-u1./Uinf;
wake24=trapz(xlin24,wd24)/1000;
lift24=rho*span*wake24
cl24=lift24/(0.5*rho*Winfideal2.^2*area)

% vinf1=v11(1:200);
% vinf2=v11(348:548);
% Vinf11=(sum(vinf1)+sum(vinf2))./400
% vd11=Vinf11-v11;
wd25=(Winfideal2-w25).*v25;
%us1=u1.*(Uinf-u1);
%ud=Uinf-mag;
%us=mag.*(Uinf-mag);
%udo1=1-u1./Uinf;
wake25=trapz(xlin25,wd25)/1000;
lift25=rho*span*wake25
cl25=lift25/(0.5*rho*Winfideal2.^2*area)

% vinf1=v12(1:200);
% vinf2=v12(348:548);
% Vinf12=(sum(vinf1)+sum(vinf2))./400
% vd12=Vinf12-v12;
wd26=(Winfideal2-w26).*v26;
%us1=u1.*(Uinf-u1);
%ud=Uinf-mag;
%us=mag.*(Uinf-mag);
%udo1=1-u1./Uinf;
wake26=trapz(xlin26,wd26)/1000;
lift26=rho*span*wake26
cl26=lift26/(0.5*rho*Winfideal2.^2*area)

% vinf1=v13(1:200);
% vinf2=v13(348:548);
% Vinf13=(sum(vinf1)+sum(vinf2))./400
% vd13=Vinf13-v13;
wd27=(Winfideal2-w27).*v27;
%us1=u1.*(Uinf-u1);
%ud=Uinf-mag;
%us=mag.*(Uinf-mag);
%udo1=1-u1./Uinf;
wake27=trapz(xlin27,wd27)/1000;
lift27=rho*span*wake27
cl27=lift27/(0.5*rho*Winfideal2.^2*area)

% vinf1=v14(1:200);
% vinf2=v14(348:548);
% Vinf14=(sum(vinf1)+sum(vinf2))./400
% vd14=Vinf14-v14;
wd28=(Winfideal2-w28).*v28;
%us1=u1.*(Uinf-u1);
%ud=Uinf-mag;
%us=mag.*(Uinf-mag);
%udo1=1-u1./Uinf;
wake28=trapz(xlin28,wd28)/1000;
lift28=rho*span*wake28
cl28=lift28/(0.5*rho*Winfideal2.^2*area)
%%%%%%%%%%%%%%%%%%plotting

x=linspace(-6,20,14);

drag=[drag1,drag2,drag3,drag4,drag5,drag6,drag7,drag8,drag9,drag10,
drag11,drag12,drag13,drag14];
drag_2=[drag15,drag16,drag17,drag18,drag19,drag20,drag21,drag22,
drag23,drag24,drag25,drag16,drag27,drag28];
```

```
cd=[cd1,cd2,cd3,cd4,cd5,cd6,cd7,cd8,cd9,cd10,cd11,cd12,cd13,cd14];
cd_2=[cd15,cd16,cd17,cd18,cd19,cd20,cd21,cd22,cd23,cd24,cd25,cd26,
cd27,cd28];

lift=[lift1,lift2,lift3,lift4,lift5,lift6,lift7,lift8,lift9,lift10,
lift11,lift12,lift13,lift14];
lift_2=[lift15,lift16,lift17,lift18,lift19,lift20,lift21,lift22,
lift23,lift24,lift25,lift26,lift27,lift28];

cl=[cl1,cl2,cl3,cl4,cl5,cl6,cl7,cl8,cl9,cl10,cl11,cl12,cl13,cl14];
cl_2=[cl15,cl16,cl17,cl18,cl19,cl20,cl21,cl22,cl23,cl24,cl25,cl26,
cl27,cl28];

figure(1)
plot(x,cd,'b')
xlabel('{\alpha}^o'),ylabel('C_l      C_d'),title('BIG BLUE I Wing')
hold on
plot(x,cl,'bo-')
hold on
plot(x,cd_2,'r-.')
hold on
plot(x,cl_2,'ro-.')
hold off
legend('C_l  Re 2.0\cdot10^5','C_d Re 2.0\cdot10^5','C_l  Re 2.5\cdot10^5',
'C_d Re 2.5\cdot10^5',2)


L_D=cl./cd;
L_D_2=cl_2./cd_2;
figure(2)
plot(x,L_D,'b')
xlabel('{\alpha}^o'),ylabel('L/D'),title('BIG BLUE I Wing: L/D vs.{\alpha}^o')
hold on
plot(x,L_D_2,'r-.')
hold off
legend('Re 2.0\cdot10^5','Re 2.5\cdot10^5',4)

figure(3)
plot(cd,cl,'b')
xlabel('C_d'),ylabel('C_l'),title('BIG BLUE I Wing: Drag Polar')
hold on
plot(cd_2,cl_2,'r-.')
hold off
legend('Re 2.0\cdot10^5','Re 2.5\cdot10^5',4)

end
```

B.2 Vorticity Data from PIV

```
function [lift]=airfoil_piv(run,boxoff)
% program to average turbine data sets

ntot=50;   %number of tensor files (62)
ren=50; % Reynolds number, in 1k
% date='11.04.05';


run='0-4';
boxoff=1;

%set base path of files
% basepath=strcat('Re',int2str(ren),'k',date)
basepath=strcat('F:\Research\PIV FASM WING MODEL\processed re100000')
tecid=fopen('tecplot','w');
tecflag=0; %set to 1 to output tec data file
plotflag=0; %set to 1 to show all plots on screen
```

```
%conversion info - spatial and temporal scales to give units in cm/s
scale=110;  %pixels/cm
if ren == 100,
    pulse=45;  %pulse timer in microseconds for high Re cases (was 10)
    uf=13.04; %m/s
else
    pulse=90; %pulse timer in microseconds for low Re cases;
    uf=6.52; %m/s
end

%chord length
chord=10.8; %MAC IN cm

umean=uf*100; % cm/s
re=umean*chord/0.151;
re=uf*(chord/100)*1.229/.0000173;
fprintf('\n Freestream velocity is %6.2f cm/s\n Re based on this is %

%conversion factors to cm/s
convel=(scale*pulse/1000000);
convor=(pulse/1000000);

%check array size
k=1; [ny,nx]=tensfunc2(run,k,basepath)

dx=1008./nx./scale;
dy=1018./ny./scale;

uav=zeros(ntot,nx,ny);
vav=zeros(ntot,nx,ny);
vortav=zeros(ntot,nx,ny);
contav=zeros(ntot,nx,ny);
un=zeros(nx,ny);
vn=zeros(nx,ny);
vorn=zeros(nx,ny);
conn=zeros(nx,ny);
corn=zeros(nx,ny);
rfp=zeros(nx,ny);
sep=zeros(nx,ny);
urms=zeros(nx,ny);
dvdxn=zeros(1,ny);

%read in data files
for i=1:ntot,
   % i=38;
   [u,v,vort,cont,corr,dvdx]=tensfunc(run,i,basepath); %miner(
   un=u+un;
   vn=v+vn;
   vorn=vort+vorn;
   conn=cont+conn;
   corn=corr+corn;
   uav(i,:,:)=u;
   vav(i,:,:)=v;
   vortav(i,:,:)=vort;
   contav(i,:,:)=cont;
   dvdxn=dvdxn+dvdx(nx,:);
   neg_pixels=0;
   for j=1:nx
      for k=1:ny
         if u(j,k) < 0,
            neg_pixels=neg_pixels+1;
            rfp(j,k)=rfp(j,k)+1;
         end
      end
   end
end

%%%%%%%%%%%%%% PROCESSING %%%%%%%%%%%%%%%%%%%%%
```

```
%set edge regions to zero if need be
% un(:,1)=0; vn(:,1)=0; vorn(:,1)=0; rfp(:,1)=0;
% un(:,2)=0; vn(:,2)=0; vorn(:,2)=0;
% un(1,:)=0; vn(1,:)=0; vorn(1,:)=0;
% un(:,ny-1)=0; vn(:,ny-1)=0; vorn(:,ny-1)=0;
% un(:,ny)=0; vn(:,ny)=0; vorn(:,ny)=0;
%set edges for individual arrays
uav(:,:,1)=0; uav(:,:,2)=0;
uav(:,:,3)=0; uav(:,:,4)=0;uav(:,1,:)=0;
uav(:,:,ny)=0; uav(:,:,ny-1)=0;
vav(:,:,1)=0; vav(:,:,2)=0;
vav(:,:,3)=0; vav(:,:,4)=0;vav(:,1,:)=0;
vav(:,:,ny)=0; vav(:,:,ny-1)=0;
vortav(:,:,1)=0; vortav(:,:,2)=0;
vortav(:,:,3)=0; vortav(:,:,4)=0;vortav(:,1,:)=0;
vortav(:,:,ny)=0; vortav(:,:,ny-1)=0;

% eliminate values nearest blade surface
for kk=1:ny
    flag=0;
    for k=nx:-1:1
        if un(k,kk)~=0
            %k,kk
            if flag==0
                un(k,kk)=0;
                vn(k,kk)=0;
                rfp(k,kk)=0;
            end
            flag=1;
        end
    end
end

%calculate averages
un=un/ntot;
vn=vn/ntot;
vorn=vorn/ntot;
conn=conn/ntot;
corn=corn/ntot;
dvdxn=dvdxn/ntot;
rfp=rfp/ntot;

%scale data
un=un/convel;
vn=vn/convel;
vorn=vorn/convor;
vortav=vortav/convor;

% play with FFT
% ctf=fft2(un);
% size(ctf);
% nfft=length(ctf);
% power=abs(ctf(1:nfft/2)).^2;
% freq=(1:nfft/2)/(nfft/2)*0.5;

%plot(ctf,'ro')
%plot(1./freq,power)

fprintf('\nThinking....')

%calculate rms turbulence
for j=1:nx
    fprintf('.')
    for k=1:ny
        dum1=0; dum2=0; dum3=0;
        for i=1:ntot
            dum1=sqrt(un(j,k)^2+vn(j,k)^2);
            dum2=sqrt(uav(i,j,k)^2+vav(i,j,k)^2);
```

```
            dum3=(dum1-dum2)^2+dum3;
        end
        urms(j,k)=sqrt(dum3)/ntot;
    end
end

%skin friction coef.
mu=0.0000185;
shear=mu*dvdxn;
cf=shear/(0.5*1.23*uf^2);
%cf=cf(1,12:82);
%size(cf)

%% PLOTTING

fprintf('\nPlotting\n')

offset=-10;
xllim=offset;
yllim=offset;
xulim=nx-offset;
yulim=ny-(offset);
%yllim=20;
%yulim=50;

%new colormap
jet2=abs(jet-1);

mag=sqrt(un.^2+vn.^2);
%mag=un;


%[xs,ys]=meshgrid(nx,ny);
xs=[1:nx]*dx;
ys=[1:ny]*dy;

%% PLOTS

if plotflag==1 %plots figures 1 through 6 if plotflag=1

    figure(2);
    colormap jet;
    contourf(xs,ys,vorn,50),axis off, axis equal,title('Vorticity')
    ,axis ij,shading flat;
    xlabel('x [cm]'),ylabel('y [cm]')
    colorbar; %gtext('s^{-1}');

    figure(3);
    colormap jet;
    contourf(xs,ys,urms,50),axis off, axis equal,
    title('RMS Velocity Variation'),axis ij;,shading flat;
    xlabel('x [cm]'),ylabel('y [cm]')
    colorbar;
    %patch(x,y,'k');

    figure(4);
    colormap jet;
    contourf(xs,ys,conn,50),axis off, axis equal,
    title('Continuity (as a check of 3-D effects): Run 4'),axis ij
    ,shading flat;
    xlabel('x [cm]'),ylabel('y [cm]')
    colorbar;

    figure(5);
    colormap jet;
    contourf(xs,ys,corn,[0 .1 .2 .3 .4 .5 .6 .7 .8 .9 1.0]),axis off
    , axis equal,
    title('Average PIV Correlation: Run 4'),axis ij;
    xlabel('x [cm]'),ylabel('y [cm]')
```

```
    colorbar;

    figure(6);
    quiver(xs,ys,un,vn,2),axis equal,title('Velocity'),axis ij
    xlabel('x [cm]'),ylabel('y [cm]')

end

figure(7);
colormap jet;
contourf(vorn,50), axis equal,
title('Velocity & Vorticity Magnitude (Indexed)'),axis ij,shading flat;
colorbar; %gtext('m/s');
hold on;
quiver(un,vn,5,'w'),axis equal,axis ij
hold off;



%%%%% Cirulation Sequence %%%%%

gamma_vor=0;
gamma_vel=0;

%find center of vortex
fprintf('\nSelect vortex center');
[xcen,ycen]=ginput(1);
xcen=round(xcen)
ycen=round(ycen)

boxwidth=min([nx-xcen-boxoff,xcen-1-boxoff,ny-ycen-boxoff,ycen-1-boxoff])

radius=dx.*[0:boxwidth];

fprintf('\nCirculation routines .');

for iter=1:boxwidth

    cbox=iter;

    hold on;
    plot([xcen-cbox,xcen-cbox],[ycen-cbox,ycen+cbox],'y-')
    plot([xcen+cbox,xcen+cbox],[ycen-cbox,ycen+cbox],'y-')
    plot([xcen-cbox,xcen+cbox],[ycen-cbox,ycen-cbox],'y-')
    plot([xcen-cbox,xcen+cbox],[ycen+cbox,ycen+cbox],'y-')
    plot([xcen],[ycen],'c.','markersize',20)
    hold off;

    %circulation via vorticity
    fprintf('.');
    vor_gamma=0.0;
    for p=xcen-cbox:xcen+cbox
        for q=ycen-cbox:ycen+cbox
            vor_gamma = vor_gamma + vorn(q,p);
        end
    end
    vor_gamma;

    gamma_vor=(sum(sum(vorn(ycen-cbox:ycen+cbox, xcen-cbox:xcen+cbox))
    ))*dx.^2;

    %fprintf('. . . gamma_vor is %1.0f, ',gamma_vor);

    %circulation via velocity
    fprintf('.');
    for i=xcen-cbox:xcen+cbox
        gamma_vel=un(ycen+cbox,i)+gamma_vel;
        gamma_vel=-un(ycen-cbox,i)+gamma_vel;
    end
```

```
    for j=ycen-cbox:ycen+cbox
        gamma_vel=vn(j,xcen-cbox)+gamma_vel;
        gamma_vel=-vn(j,xcen+cbox)+gamma_vel;
    end
    gamma_vel=gamma_vel*dx;

    gamma_itervor(iter)=gamma_vor;
    gamma_itervel(iter)=gamma_vel;
    % gamma_voriter(iter)=vor_gamma
end

gamma_itervor=[0,gamma_itervor];
gamma_itervel=[0,gamma_itervel];

gamma_vormax=max(gamma_itervor);
gamma_velmax=max(gamma_itervel);

fprintf('\n\nMax gamma_vel is %3.0f cm^2/s\n', gamma_velmax);
fprintf('Max gamma_vor is %3.0f cm^2/s\n', gamma_vormax);

lift=gamma_velmax * .0012 * umean;

fprintf('Lift is %3.0f \n',lift);

figure(8)
plot(radius,gamma_itervor,'ro-')
hold on
plot(radius,gamma_itervel,'bs-')
% plot(gamma_voriter,'gs-')
xlabel('r [cm]'),ylabel('\Gamma [cm^2/s]')
legend('\Gamma=\int\omega\cdotdA','\Gamma=\intu\cdotdl',0)
hold off



%%%% TECPLOT ROUTINE %%%%%

Imax=ny; Jmax=nx;

if tecflag==1
    fprintf(tecid,'variables = "i", "j", "x", "y", "u", "v", "vorn"\n');
    fprintf(tecid,'zone i=%i j=%i f=point \n',Imax,Jmax);
    for j=1:Jmax
        for i=1:Imax
            fprintf(tecid,'%f %f %f %f %f %f\n',j,i,xs(j),ys
        end
    end
    fclose(tecid);
end

fprintf('\nDone with airfoil_piv\n\n');
%HERE=vorn(8,10)
return;
%end of main routine

%%%%%%%%%%%%%%%%%%%%%%%%%%%%%%%%%%%%%%%%%%%%%%%%%%%%%%%%%%%%%%%%%%%%%%%%%%%
%%%%%%%%%%%%%%%%%%%%%%%%%%%%%%%%%%%%%%%%%%%%%%%%%%%%%%%%%%%%%%%%%%%%%%%%%%%

function [e1,e2,vorticity,continuity,corr,dvdx]=tensfunc
(run,batch,basepath)
% MATLAB Script to read WALPT data and image files.
% Jamey Jacob, Jan. 18 2000
% Version 1.1, last modified Feb. 15, 2000
% Miner version May 30, 2001 - only data read
%
% For use with MATLAB release 11 (5.3)
% Ticker will not work with older versions (see "movie")
% jdjacob@uky.edu
```

```
%run=int2str(run);
%alf=int2str(alf);
%ren=int2str(ren);
bat=int2str(batch);

% file and path names

%set extension
if batch < 10
    bat=strcat('.00',bat);
else
    if batch < 100
        bat=strcat('.0',bat);
    else
        bat=strcat('.',bat);
    end
end
%set tensor file name
lptfile=strcat('run',run,bat);

%SET PATHS AND FILE NAMES
if ispc==1
    path=strcat(basepath,'\');
else
    path=strcat(basepath,'/');
end
rdfile=strcat(path,lptfile);

% read data file into header and tensor arrays

fprintf(' Reading single tensor file %s in %s\n',lptfile,path)

if ispc==1
    fid=fopen(rdfile,'r');
else
    fid=fopen(rdfile,'r','ieee-le');
end
header=fread(fid,64,'int16');
version=header(1);                % walpt version number
nxc =header( 2) ; nyc =header( 3); % camera size
nxuv=header( 4) ; nyuv=header( 5); % velocity array size
nxw =header( 6) ; nyw =header( 7); % window sizes in pixels
nxs =header( 8) ; nys =header( 9); % step sizes in pixels
nxf =header(10) ; nyf =header(11); % flow region size in pixels
xf  =header(12) ; yf  =header(13); % flow region offset in pixels
nbits=header(14);                 % pixel depth of original
% utensor=[nxuv,nyuv,7]
% read tensor components from file in succession
e1=fread(fid,[nxuv,nyuv],'float'); % u
e2=fread(fid,[nxuv,nyuv],'float'); % v
e3=fread(fid,[nxuv,nyuv],'float'); % du/dx
e4=fread(fid,[nxuv,nyuv],'float'); % dv/dx
e5=fread(fid,[nxuv,nyuv],'float'); % du/dy
e6=fread(fid,[nxuv,nyuv],'float'); % dv/dy
e7=fread(fid,[nxuv,nyuv],'float'); % correlation
st=fclose(fid);

%rotate fields
e1=e1.';
e2=e2.';
e3=e3.';
e4=e4.';
e5=e5.';
e6=e6.';
e7=e7.';

% Check and replace the "missing" 1000 in velocity
% fields with zeros (option XXXX in walpt).
```

```
% (This option is for use with IDL or similar programs.)

for i=1:nyuv
    for j=1:nxuv
        if e1(i,j) > 999
            e1(i,j) = 0;
        end
        if e2(i,j) > 999
            e2(i,j) = 0;
        end
    end
end

%Items to return
corr=e7;

% Calculate vorticity,continuity

vorticity=e5-e4;    %du/dy-dv/dx
continuity=e3+e6;   %du/dx+dv/dy

%return velocity gradient for wall skin friction calculation
%(in this case, dv/dx)

dvdx=e4;

return

%%%%%%%%%%%%%%%%%%%%%%%%%%%%%%%%%%%%%%%%%%%%%%%%%%%%%%%%%%%%%%%%%%%

function [nx,ny]=tensfunc2(run,batch,basepath)
%reads tensor file and returns array size

%run=int2str(run);
%alf=int2str(alf);
%ren=int2str(ren);
bat=int2str(batch);

% file and path names

%set extension
if batch < 10
    bat=strcat('.00',bat);
else
    if batch < 100
        bat=strcat('.0',bat);
    else
        bat=strcat('.',bat);
    end
end
%set tensor file name
lptfile=strcat('run',run,bat);

%SET PATHS AND FILE NAMES
if ispc==1
    path=strcat(basepath,'\');
else
    path=strcat(basepath,'/');
end
rdfile=strcat(path,lptfile);
lptima1=strcat('image1.lpt');lptima2=strcat('image2.lpt');
%imfile1=strcat(path,'image','1-',reg,'-',cdnstr,'.lpt')
%imfile2=strcat(path,'image','2-',reg,'-',cdnstr,'.lpt');
%imfile2=strcat(path,lptima2);

% read data file into header and tensor arrays

fprintf(' Reading tensor file %s in %s to determine array

if ispc==1
```

```
    fid=fopen(rdfile,'r');
else
    fid=fopen(rdfile,'r','ieee-le');
end
header=fread(fid,64,'int16');
version=header(1);                  % walpt version number
nxc =header( 2) ; nyc =header( 3); % camera size
nxuv=header( 4) ; nyuv=header( 5); % velocity array size
nxw =header( 6) ; nyw =header( 7); % window sizes in pixels
nxs =header( 8) ; nys =header( 9); % step sizes in pixels
nxf =header(10) ; nyf =header(11); % flow region size in pixels
xf  =header(12) ; yf  =header(13); % flow region offset in pixels
nbits=header(14);                   % pixel depth of original flow images
% utensor=[nxuv,nyuv,7]
% read tensor components from file in succession
e1=fread(fid,[nxuv,nyuv],'float'); % u
e2=fread(fid,[nxuv,nyuv],'float'); % v
e3=fread(fid,[nxuv,nyuv],'float'); % du/dx
e4=fread(fid,[nxuv,nyuv],'float'); % dv/dx
e5=fread(fid,[nxuv,nyuv],'float'); % du/dy
e6=fread(fid,[nxuv,nyuv],'float'); % dv/dy
e7=fread(fid,[nxuv,nyuv],'float'); % correlation
st=fclose(fid);

nx=nxuv;
ny=nyuv;

%open up image to check IPX routine
% fid=fopen(imfile1,'r');
% image1=fread(fid,[nxc,nyc],'int16');
% st=fclose(fid);
% fid=fopen(imfile2,'r');
% image2=fread(fid,[nxc,nyc],'int16');
% st=fclose(fid);

% 'ticker'
% figure(10);shg;newplot;
% colormap(hot) %also try gray
% imagesc(image1.'),axis off,axis equal
% figure(11);shg;newplot;
% colormap(gray)
% imagesc(image2.'),axis off,axis equal

return
```

B.3 Lifting Line Code

```
% LIFTLINE.M
%Code written by Dr. J.D. Jacob, Modified by  A.D. Simpson
%Calcuations of aerodynamic characteristics of finite wings
% using Prandtl-Glauert's
%lifting line method; points on wing are determined using
%a Chebyshev


close('all'); clear;
% INPUT SECTION
% -------------------------------------------------------------
% no. of points on the wing
n=50;

%velocity, density (SI)
Vinf=15; %(in m/s)
rho=1.23;
```

```
%span, root chord, tip chord in m
b=1.898396;
cr=.4318;
ct=.28067;

%assume wing is trapezoidal
S=.5*b*(cr+ct); lambda=ct/cr; AR=b^2/S;

%distribution of theta pts along wing
theta0=linspace(0,pi,n); y0=-b/2*cos(theta0);

%chord distribution along wing
c=interp1([-b/2,0,b/2],[ct,cr,ct],y0);

%a (dCl/dalpha) of lift gradient of each wing section
Clalpha=0.0954 %2*pi; %%% CHANGE THIS
Clalpha=Clalpha*ones(n,1);

%zero lift AoA (degrees)
alpha0=-4; %%% CHANGE THIS
alpha0=alpha0*ones(n,1)/180*pi;

%AoA of wing root (degrees) - reference angle of wing
alphar=4;

%wing twist (degrees) - downwash, positive twist is negative down
e=zeros(n,1);
e(n/2:n,1)=-0; %%%this puts in a 5 degree twist up(positive)
%on the right semi-span
for i=n/2:n
    j=(i-n/2)./(n/2);%ADS
    e(i,1) =-(6.702*j^6 + 5.4939*j^5 - 2.5777*j^4 + 3.2565*j^3
    + 6.4152*j^2 + 1.7885*j - 0.0038);%ADS
end


%wing twist (degrees) - downwash, positive twist is negative down%ADS
v=zeros(n,1);%ADS
v(n/2:n,1)=-0; %%% this puts in a 5
for i=n/2:n%ADS
    j=(i-n/2)./(n/2);%ADS
    v(i,1) =-(13.278*j^6 + 8.8719*j^5 - 12.867*j^4 - 3.551*j^3
     + 7.6162*j^2 + 2.7194*j + 0.0201);%ADS
end%ADS


%wing twist (degrees) - downwash, positive twist is negative down%ADS
g=zeros(n,1);%ADS
g(n/2:n,1)=-0; %%% this puts in a 5 degree %ADS
for i=n/2:n%ADS
    j=(i-n/2)./(n/2);%ADS
    g(i,1) =-(4.6476*j^6 + 2.5358*j^5 - 3.9715*j^4 + 1.7691*j^3 +
    5.2319*j^2 + 1.6512*j -   0.0513);%ADS
end%ADS


%wing twist (degrees) - downwash, ADS
h=zeros(n,1);%ADS
h(n/2:n,1)=-0; %%% this puts in a 5 degree twist up%ADS
for i=n/2:n%ADS
    j=(i-n/2)./(n/2);%ADS
    h(i,1) =-(-7.7188*j^6 - 2.1877*j^5 + 13.52*j^4 + 6.6928*j^3
     - 2.1969*j^2 - 0.8213*j + 0.0709);%ADS
end%ADS


% ------------------------------------------------
% END OF THE INPUT SECTION
```

```
%angle of attack of each section (in degrees)
alpha=(alphar-e)/180*pi;
alpha1=(alphar-v)/180*pi;%ADS
alpha2=(alphar-g)/180*pi;%ADS
alpha3=(alphar-h)/180*pi;%ADS

%system of A*An=Anoto of n-2 equations
Anoto=(alpha(2:n-1)-alpha0(2:n-1));
Anoto1=(alpha1(2:n-1)-alpha0(2:n-1));%ADS
Anoto2=(alpha2(2:n-1)-alpha0(2:n-1));%ADS
Anoto3=(alpha3(2:n-1)-alpha0(2:n-1));%ADS


for i=2:n-1
for j=2:n-1
 A(i-1,j-1)=4*b*sin((j-1)*theta0(i))/Clalpha(i)/c(i)+(j-1)
 *sin((j-1)*theta0(i))/sin(theta0(i));
end;
end;
An=A\Anoto;

for i=2:n-1%ADS
for j=2:n-1%ADS
 A1(i-1,j-1)=4*b*sin((j-1)*theta0(i))/Clalpha(i)/c(i)+
 (j-1)*sin((j-1)*theta0(i))/sin(theta0(i));%ADS
end;%ADS
end;%ADS
An1=A1\Anoto1;%ADS

for i=2:n-1%ADS
for j=2:n-1%ADS
 A2(i-1,j-1)=4*b*sin((j-1)*theta0(i))/Clalpha(i)/c(i)+
 (j-1)*sin((j-1)*theta0(i))/sin(theta0(i));%ADS
end;%ADS
end;%ADS
An2=A2\Anoto2;%ADS

for i=2:n-1%ADS
for j=2:n-1%ADS
 A3(i-1,j-1)=4*b*sin((j-1)*theta0(i))/Clalpha(i)/c(i)+
 (j-1)*sin((j-1)*theta0(i))/sin(theta0(i));%ADS
end;%ADS
end;%ADS
An3=A3\Anoto3;%ADS


% calculation of the vorticity Gamma on the wing
for i=2:n-1
Gamma(i)=2*b*Vinf*sum(An(:).*sin((1:n-2)*theta0(i))');
end;
Gamma(n)=0;Gamma(1)=0;

% calculation of the vorticity Gamma on the wing%ADS
for i=2:n-1%ADS
Gamma1(i)=2*b*Vinf*sum(An1(:).*sin((1:n-2)*theta0(i))');%ADS
end;%ADS
Gamma1(n)=0;Gamma1(1)=0;%ADS

% calculation of the vorticity Gamma on the wing%ADS
for i=2:n-1%ADS
Gamma2(i)=2*b*Vinf*sum(An2(:).*sin((1:n-2)*theta0(i))');%ADS
end;%ADS
Gamma2(n)=0;Gamma2(1)=0;%ADS

% calculation of the vorticity Gamma on the wing%ADS
for i=2:n-1%ADS
Gamma3(i)=2*b*Vinf*sum(An3(:).*sin((1:n-2)*theta0(i))');%ADS
```

```
end;%ADS
Gamma3(n)=0;Gamma3(1)=0;%ADS


% calculation of the aerodynamical characteristics  wing%ADS
Cl3=2*Gamma3/c/Vinf;%ADS
l3=rho*Vinf*Gamma3; % N/m%ADS

% calculation of the aerodynamical characteristics  wing%ADS
Cl2=2*Gamma2/c/Vinf;%ADS
l2=rho*Vinf*Gamma2; % N/m%ADS

% calculation of the aerodynamical characteristics wing%ADS
Cl1=2*Gamma1/c/Vinf;%ADS
l1=rho*Vinf*Gamma1; % N/m%ADS

% calculation of the aerodynamical characteristics  wing
Cl=2*Gamma/c/Vinf;
l=rho*Vinf*Gamma; % N/m

%calculation of total lift and drag coef.
%CL is a f'n of A1 only, CD is a f'n of all An
CL=An(1)*pi*AR;
for i=2:n-1
alphai(i)=sum((1:n-2)'.*An.*sin((1:n-2)'
*theta0(i))./sin(theta0(i)));
end;
alphai(1)=sum((1:n-2)'.*An.*(1:n-2)');
alphai(n)=sum((1:n-2)'.*An.*(1:n-2)');
d=l.*alphai;
Cdi=d./(.5*rho*Vinf^2*c);

CDi=pi*AR*sum((1:n-2)'.*(An.^2));

CL1=An1(1)*pi*AR;

L=CL*.5*rho*Vinf^2*S
Di=CDi*.5*rho*Vinf^2*S;

L1=CL1*.5*rho*Vinf^2*S

fprintf('\n C_L is %4.2f and C_Di is %4.3f\n',CL,CDi)
fprintf(' Lift is %6.2f N and Induced Drag is %6.2f N\n',L,Di)

%PLOTS
%planform
figure(1); patch([-b/2 0 b/2 b/2 0 -b/2],[-ct/2 -cr/2
-ct/2 +ct/2 +cr/2 +ct/2],'b')
,axis equal;
ylabel('x (c [m])');xlabel('y (b [m])');

%twist
figure(2); plot(y0,alpha,'b-'); ylabel('AoA');xlabel('Span[m]');
hold on
plot(y0,alpha1,'r--')
hold on
plot(y0,alpha2,'g:')
hold on
plot(y0,alpha3,'k-.')
legend('10 psi','15 psi','20 psi','25 psi',0);
hold off

%twist
figure(3); plot(y0,alpha*180/pi,'b-'); ylabel('AoA [
^\circ]');xlabel('Span[m]');
hold on
plot(y0,alpha1*180/pi,'r--')
plot(y0,alpha2*180/pi,'g:')
plot(y0,alpha3*180/pi,'k-.')
```

```
legend('10 psi','15 psi','20 psi','25 psi',0);
hold off

figure(4);
plot(y0,Gamma,'b-'); ylabel('\Gamma');xlabel('y (b [m])');
title('Spanwise Circulation Distribution')
  hold on%ADS
  plot(y0,Gamma1,'r--')%ADS
%   plot(-y0,Gamma1,'k-.')
  plot(y0,Gamma2,'g:')%ADS
  plot(y0,Gamma3,'k-.')%ADS
  %legend('10 psi','20 psi',0);
  legend('10 psi','15 psi','20 psi','25 psi')
  hold off



  figure(5);
  fill(y0,Gamma,'r'); ylabel('\Gamma');xlabel('y (b [m])');
  title('Spanwise Circulation Distribution')
  hold on%ADS
  fill(y0,Gamma1,'y')%ADS
  fill(y0,Gamma2,'g')%ADS
  fill(y0,Gamma3,'b')%ADS
%   plot(y0,Gamma1,'k-')%ADS
  legend('10 psi','15 psi','20 psi','25 psi');
  hold off

% ADS  from here down;

A=-0.94+1/100:1/100:0% ADS
NoTwist = trapz(squeeze(y0(:,1:25)),squeeze(Gamma(:,1:25)))  % ADS
AA=1/100:1/100:0.94% ADS
Twist = trapz(squeeze(y0(:,26:50)),squeeze(Gamma(:,26:50)))  % ADS

B=-0.94+1/100:1/100:0% ADS
NoTwist1 = trapz(squeeze(y0(:,1:25)),squeeze(Gamma1(:,1:25)))  % ADS
BB=1/100:1/100:0.94% ADS
Twist1 = trapz(squeeze(y0(:,26:50)),squeeze(Gamma1(:,26:50)))  % ADS

C=-0.94+1/100:1/100:0% ADS
NoTwist2 = trapz(squeeze(y0(:,1:25)),squeeze(Gamma2(:,1:25)))  % ADS
CC=1/100:1/100:0.94% ADS
Twist2 = trapz(squeeze(y0(:,26:50)),squeeze(Gamma2(:,26:50)))  % ADS

D=-0.94+1/100:1/100:0% ADS
NoTwist3 = trapz(squeeze(y0(:,1:25)),squeeze(Gamma3(:,1:25)))  % ADS
DD=1/100:1/100:0.94% ADS
Twist3 = trapz(squeeze(y0(:,26:50)),squeeze(Gamma3(:,26:50)))  % ADS
%
Twist=((Twist-NoTwist)/NoTwist)*100
Twist11=((Twist1-NoTwist)/NoTwist)*100
Twist22=((Twist2-NoTwist)/NoTwist)*100
Twist33=((Twist3-NoTwist)/NoTwist)*100

Tw = [Twist Twist11 Twist22 Twist33]
Pr =[10 15 20 25]
figure(6);
plot(Pr,Tw,'b*-'); ylabel('% Increase in \Gamma');xlabel('Inflation Pressure (psi)');
title('Change in \Gamma due to deformation vs. Inflation pressure ')

% Tw = [Twist Twist11 Twist22 Twist33]
% Pr =[10 15 20 25]
% plot(Pr,Tw,'r*');
 %%%%%%%%%%%%%%%%%%%%%%%%%%%%%%%

RollMoment = y0(:,1:25)*trapz(squeeze(y0(:,1:25)),squeeze
(Gamma(:,1:25)))  % ADS
```

```
RollMomentDef = y0(:,26:50)*trapz(squeeze(y0(:,26:50)),squeeze
(Gamma(:,26:50)))  % ADS

RollMoment1a = y0(:,1:25)*trapz(squeeze(y0(:,1:25)),squeeze
(Gamma1(:,1:25)))  % ADS
RollMomentDef1a = y0(:,26:50)*trapz(squeeze(y0(:,26:50)),squeeze
(Gamma1(:,26:50)))  % ADS
%
RollMoment2a = y0(:,1:25)*trapz(squeeze(y0(:,1:25)),squeeze
(Gamma2(:,1:25)))  % ADS
RollMomentDef2a = y0(:,26:50)*trapz(squeeze(y0(:,26:50)),squeeze
(Gamma2(:,26:50)))  % ADS
%
RollMoment3a = y0(:,1:25)*trapz(squeeze(y0(:,1:25)),squeeze
(Gamma3(:,1:25)))  % ADS
RollMomentDef3a = y0(:,26:50)*trapz(squeeze(y0(:,26:50)),squeeze
(Gamma3(:,26:50)))  % ADS

%%%%%%%%%%%%%%%%%%%

RollMoment = trapz(y0(:,1:25)*trapz(squeeze(y0(:,1:25)),squeeze(
Gamma(:,1:25))))  % ADS
RollMomentDef = trapz(y0(:,26:50)*trapz(squeeze(y0(:,26:50)),squeeze
(Gamma(:,26:50))))  % ADS

RollMoment1 = trapz(y0(:,1:25)*trapz(squeeze(y0(:,1:25)),squeeze
(Gamma1(:,1:25))))  % ADS
RollMomentDef1 = trapz(y0(:,26:50)*trapz(squeeze(y0(:,26:50)),squeeze
(Gamma1(:,26:50))))  % ADS
%
RollMoment2 = trapz(y0(:,1:25)*trapz(squeeze(y0(:,1:25)),squeeze
(Gamma2(:,1:25))))  % ADS
RollMomentDef2 = trapz(y0(:,26:50)*trapz(squeeze(y0(:,26:50)),squeeze
(Gamma2(:,26:50))))  % ADS
%
RollMoment3 = trapz(y0(:,1:25)*trapz(squeeze(y0(:,1:25)),squeeze
(Gamma3(:,1:25))))  % ADS
RollMomentDef3 = trapz(y0(:,26:50)*trapz(squeeze(y0(:,26:50)),squeeze
(Gamma3(:,26:50))))  % ADS


Cm = 2*RollMoment/S/Vinf
CmDef = 2*RollMomentDef/S/Vinf
CmDef1 = 2*RollMomentDef1/S/Vinf
CmDef2 = 2*RollMomentDef2/S/Vinf
CmDef3 = 2*RollMomentDef3/S/Vinf

CM = CmDef - (-Cm)
CM1 = CmDef1  - (-Cm)
CM2 = CmDef2  - (-Cm)
CM3 = CmDef3  - (-Cm)

DeltaCM = [CM CM1 CM2 CM3]

figure(7);
plot(Pr,DeltaCM,'b*-');ylabel(' \Delta Cm');xlabel
('Inflation Pressure (psi)');
title('Change in Moment Coefficient vs. Inflation pressure ')
% plot(Pr,Tw,'b*-');

% ADS3 - ADS1
% ADS5 = ADS2 - ADS1% ADS
% ADS6 = ADS4 - ADS3% ADS

% X = 0:pi/100:pi;
% Y = sin(X);
% Z  = Trapz(X,Y)
```

BIBLIOGRAPHY

[1] http://www.cradleofaviation.org. October 30, 2007.

[2] P.B.S. Lissaman. Low-reynolds-number airfoils. *Annual Rev. of Fluid Mech.*, 15:223–239, 1983.

[3] T.J. Mueller and J.D. DeLaurier. Aerodynamics of small vehicles. *Annual Rev. of Fluid Mech.*, 35:89–111, 2003.

[4] H. Tennekes. *The Simple Science of Flight: From Insects to Jumbo Jets.* The MIT Press, Cambridge MA, 1 edition, 1997.

[5] http://www.aiaa.org/images/PDF/WilsonChart.pdf. October 30, 2007.

[6] Jr. John D. Anderson. *Fundamentals of Aerodynamics.* McGraw-Hill, New York, 3 edition, 2001.

[7] H.P. Horton. Laminar separation bubbles in two and three-dimensional incompressible flow. Master's thesis, University of London, London, England, 1968.

[8] H.v.W. Nachtigall and J. Wieser. Profilmessungen am taubenflugel. *Zeit. Vergl. Physiol*, 52:333–346, 1966.

[9] C. J. Pennycuick. A wind-tunnel study of gliding flight in the pigeon columba livi. *Journal of Experimental Biology*, 49:509–526, 1968.

[10] http://www.centennialofflight.gov/media/photo/congress/display/congress1.htm. October 30, 2007.

[11] Jr. John D. Anderson. *Aircraft Performance and Design.* McGraw-Hill, New York, 1999.

[12] G. Brown, R. Haggard, and B. Norton. Inflatable structures for deployable wings. AIAA Paper 2001–2068, AIAA Aerodynamic Decelerator Systems Technology Conference and Seminar, Boston, MA, May 2001.

[13] USPTO - United States Patent, Patent 1,905,298, 1933.

[14] USPTO - United States Patent, Patent 3,106,373, 1963.

[15] USPTO - United States Patent, Patent 3,957,232, 1976.

[16] USPTO - United States Patent, Patent 4,725,021, 1988.

[17] B.W. Cocke Jnr. Wind tunnel investigation of the aerodynamic and structural deflection characteristics of the goodyear inflatoplane. NACA-RM-L58E09P, NASA, Langley Aeronautical Laboratory, Langley Field, Va., September 1958.

[18] D. Cadogan, T. Smith, R. Lee, S. Scarborough, and D. Graziosi. Inflatable and rigidizable wing components for unmanned aerial vehicles. AIAA Paper 2003–6630, 44th AIAA/ASME/ASCE/AHS/ASC Structures, Structural Dynamics and Materials Conference, Norfolk, VA, April 2003.

[19] J. Murray, J. Pahle, S. Thornton, T. Frackowiak, J. Mello, and B. Norton. Ground and flight evaluation of a small-scale inflatable-winged aircraft. AIAA Paper 2002–0820, 40th AIAA Aerospace Sciences Meeting & Exhibit, 2002.

[20] http://www.prospective concepts.ch. October 30, 2007.

[21] M. Usui. Aeromechanics of low reynolds number inflatable/rigidizable wings. Master's thesis, University of Kentucky, Lexington, Kentucky, May 2004.

[22] J. Kearns, M. Usui, S. Smith, S. Scarborough, T. Smith, and D. Cadogan. Development of uv-curable inflatable wings for low density flight applications. AIAA Paper 2004-1503, 45th AIAA Gossamer Spacecraft Forum, Palm Springs, CA, April 2004.

[23] A.D. Simpson, M. Usui, S.W. Smith, and J.D. Jacob. Development and flight testing of a uav with inflatable-rigidizable wings. AIAA Paper 2004-1373, 42nd AIAA Aerospace Sciences Meeting and Exhibit, Reno, NV, January 2004.

[24] A.D Simpson, M. Usui, S.W. Smith, and J.D. Jacob. Aeromechanics of inflatable wings. AIAA Paper 2004-2233, 34th Fluid Dynamics Conference, Portland, OR, June 2004.

[25] http://www.engr.uky.edu/bigblue/. October 30, 2007.

[26] Johnathan M. Rowe. Modeling inflatable airfoils. Master's thesis, University of Kentucky, Lexington, Kentucky, August 2007.

[27] J.D. Jacob and S.W. Smith. Design of hale aircraft using inflatable wings. AIAA Paper 2008-167, 46th AIAA Aerospace Sciences Meeting and Exhibit, Reno, NV, January 2008.

[28] J.T. Black. Design and analysis methodologies for inflated beams. Master's thesis, University of Kentucky, Lexington, Kentucky, December 2006.

[29] D. Cadogan, T. Smith, F. Uhelsky, and M. Mackusick. Morphing inflatable wing development for compact package unmanned aerial vehicles. AIAA Paper 2004–1807, 45th AIAA/ASME/ASCE/AHS/ASC Structures, Structural Dynamics and Materials Conference, Palm Springs, CA, April 2004.

[30] T.C.S. Rendall, C.W.C. Chang, P. Marzocca, E. Bollt, and P. Zamankhan. Aeroelastic behavior of a non-rigidizable inflatable uav wing. AIAA Paper 2006-2161, AIAA Structures, Structural Dynamics and Materials Conference, Newport, Rhode Island, May 2006.

[31] J Chandler and J.D. Jacob. Design and flight testing of a mars aircraft prototype using inflatable wings. 58th International Astronautical Congress, Hyderabad, India, September 27, 2007, September 2007.

[32] D.P. Cadogan, S.E. Scarborough, D. Gleeson, A. Dixit, J.D. Jacob, and A.D. Simpson. Recent development and testing of inflatable wings. AIAA Paper 2006-2139, AIAA, 47th AIAA/ASME/ASCE/AHS/ASC Structures, Structural Dynamics, and Materials Conference and 14th AIAA/ASME/AHS Adaptive Structures Conference, Newport, Rhode Island, May 2006.

[33] http://www.nasm.si.edu/research/aero/aircraft/langleyA.htm. October 30, 2007.

[34] L.R. Newcome. *Unmanned Aviation: A Brief History of Unmanned Aerial Vehicles.* AIAA, Reston, Virginia, 2004.

[35] Office of the Under Secretary of Defense for Acquisition. Defense science board study on unmanned aerial vehicles and uninhabited combat aerial vehicles. Technical report, Technology and Logistics, Washington, DC, February 2004.

[36] Office of the Secretary of Defense. Unmanned aerial vehicles roadmap 2002-2027. Technical report, Washington, DC, December 2002.

[37] A.L. Money and D.R. Oliver. Unmanned aerial vehicles roadmap 2000-2025. Technical report, Office of the Secretary of Defense, Washington, DC, April 2001.

[38] J.H. McMasters and M.L. Henderson. Low-speed single element airfoil synthesis. *Technical Soaring*, 6:1–21, 1980.

[39] M. Gad-El-Hak. Flow control: The future. *Journal of Aircraft*, 38:402–418, 2001.

[40] M. Gad-El-Hak. Control of low-speed airfoil aerodynamics. *AIAA Journal*, 28:1537–1552, 1990.

[41] E.N. Jacobs. Airfoil section characteristics as affected by protuberances. NACA TR–446, 1932.

[42] E.N. Jacobs. Wing characteristics as affected by protuberances of short span. NACA TR–449, 1932.

[43] K.B.M.Q. Zaman and M.G. Potapczuk. The low-frequency oscillation in the flow over a naca 0012 airfoil with an iced leading edge. In T.J. Mueller, editor, *Low Reynolds Number Aerodynamics*, pages 271–282. Springer-Verlag, New York, 1989.

[44] M. B. Bragg, M. J. Cummings, and C. M. Henze. Boundary-layer and heat-transfer measurements on an airfoil with simulated ice-roughness. AIAA Paper 1996–0866, 34th AIAA Aerospace Sciences Meeting, Reno, NV, January 1996.

[45] Michael F. Kerho and Michael B. Bragg. Airfoil boundary layer development and transition with large leading-edge roughness. *AIAA Journal*, 35(1):75–84, 1997.

[46] A. D. Young. Boundary layers. In *Low Reynolds Number Aerodynamics.* AIAA Press, Washington DC, 1989.

[47] A. Braslow, R. Hicks, and R. Harris. Use of grit-type boundary-layer-transition trips on wind tunnel models. NASA TN D-3579, 1966.

[48] M.L.Rasmussen and D.E. Smith. Lifting-line theory for arbitrarily shaped wings. *Journal of Aircraft*, 36:340–348, 1999.

[49] J. Bowman, B. Sanders, and T. Weisshaar. Evaluating the impact of morphing technologies on aircraft performance. AIAA Paper 2002-1631, 43rd AIAA/ASME/ASCE/AHS/ASC Structures, Structural Dynamics, and Materials Conference, Denver, Colorado, April 2002.

[50] J.D. Jacob. On the fluid dynamics of adaptive airfoils. In *Proc. ASME International Mechanical Engineering and Exposition.*, Anaheim, CA, 1998. ASME.

[51] P. B. S. Lissaman. Low-reynolds-number airfoils. *Annual Review of Fluid Mechanics.*, 15:223–239, 1983.

[52] M. Drela. Xfoil: An analysis and design system for low reynolds number airfoils. In T.J. Mueller, editor, *Low Reynolds Number Aerodynamics.* Springer-Verlag, New York, 1989.

[53] K.Y. Billah and R.H. Scanlan. Resonance, tacoma narrows bridge failure, and undergraduate physics. *American Journal of Physics*, 59(2), 1992.

[54] H. Schlicting. *Boundary Layer Theory.* Mcgraw-Hill Book Co., New York, 1960.

[55] A. Natarajan. Aeroelasticity of morphing wings using neural networks. Master's thesis, Virginia Polytechnic Institute and State University, Blacksburg, Virginia, July 2002.

[56] E.H. Dowell, E.F. Crawley, H.C Curtiss, D.A. Peters, R.H. Scanlan, and s. Fernando. *A Modern Course in Aeroelasticity.* Kluwer Academic Publishers, 1995.

[57] A.H. Nayfeh and B. Balachandran. *Applied Nonlinear Dynamics: Analytical, Computational, and Experimental Methods.* Wiley-Interscience, New York, 1995.

[58] N.S. Khot, F.E. Eastep, and R.M. Kolonay. Method for enhancement of the rolling maneuver of a flexible wing. *Journal of Aircraft*, 34, 1997.

[59] R.L. Bisplinghoff, H. Ashley, and R.L. Halfman. *Aeroelasticity.* Addison-Wessley Inc, Massachusetts, 1957.

[60] J.D. Anderson Jr. *A history of Aerodynamics and Its Impact on Flying Machines.* Cambridge University Press, New York, 1997.

[61] F.H. Gern, D.J. Inman, and R.K. Kapania. Aeroelastic modeling of general planform wings with morphing airfoils. *AIAA Journal*, 40(4):628637, 2002.

[62] B. Sanders, F.E. Eastep, and E. Foster. Aerodynamic and aeroelastic characteristics of wings with conformal control surfaces for morphing aircraft. *Journal of Aircraft*, 40:94–99, 2003.

[63] M. Amprikidis and J.E. Cooper. Development of smart spars for active aeroelastic structures. AIAA Paper 2003–1799, 44th AIAA/ASME/ASCE/AHS/ASC Structures, Structural Dynamics and Materials Conference, Norfolk, Virginia, April 2003.

[64] J.S. Bae, T.M. Seigler, and D.J. Inman. Aerodynamic and aeroelastic characteristics of a variable-span morphing wing. *Journal of Aircraft*, 40:528–534, 2005.

[65] C.H. Jenkins. Gossamer spacecraft: Membrane/inflatable structures technologies for space applications. Technical report, AIAA, Washington, DC, October 2001.

[66] D.P. Cadogan and S.E. Scarborough. Rigidizable materials for use in gossamer space inflatable structures. AIAA Paper 2001-1417, 42nd AIAA/ASME/ ASCE/AHS/ASC Structures, Structural Dynamics, and Materials Conference and Exhibit AIAA Gossamer Spacecraft Forum, April 2001.

[67] A.D Simpson, A. Santhanakrishnan, J.D. Jacob, S.W. Smith, J. Lumpp, and D. Cadogan. Flying on air: Uav flight testing with inflatable wing technology. AIAA Paper 2004-6570, 3rd "'Unmanned Unlimited"' Technical Conference, Workshop and Exhibit, Chicago, Il, September 2004.

[68] E. Stanewsky. Adaptive wing and flow control technology. *Progress in Aerospace Sciences*, 37:583–667, 2001.

[69] S.L. Veldman. New ultra-lightweight stiff panels for space apertures. Master's thesis, Technische Universiteit Delft, Delft, The Netherlands, June 2005.

[70] P. Crimi. Divergence of an inflated wing. *Journal of Aircraft*, 37:186–187, 2000.

[71] J.A. Main, P.S. Peterson, and A.M. Strauss. Beam-type bending of space-based inflated membrane structures. *Journal of Aerospace Engineering*, 8:120–125, 1995.

[72] J.M. Gere and S.P. Timoshenko. *Mechanics of Materials.* PWS Pub. Co., Park Plaza, Boston, 4th edition, 1997.

[73] J.K. Lin, G.H. Sapna, D.P. Cadogan, and S.E. Scarborough. Inflatable rigidizable isogrid boom development. AIAA Paper 2002-1297, 43rd AIAA/ASME/ ASCE/AHS/ASC Structures, Structural Dynamics, and Materials Conference and Exhibit AIAA Gossamer Spacecraft Forum, April 2002.

[74] R. Allred, A. Hoyt, L. Harrah, P. McElroy, S. Scarborough, and D. Cadogan. Light curing rigidizable inflatable wing. AIAA Paper 2004-1809, 45th AIAA/ASME/ASCE/AHS/ASC Structures, Structural Dynamics and Materials Conference, Palm Springs, CA, April 2004.

[75] D. Hall. Airplane for mars exploration: Conceptual design of the full-scale vehicle; design, construction and test of performance and deployment models. Technical report, Final Report, David Hall Consulting, May 1997.

[76] S.C. Smith, A. Hahn, W. Johnson D. Kinnery, J. Pollitt, and J. Reuther. The design of the canyon flyer, an airplane for mars exploration. AIAA Paper 2000-0514, 38th AIAA Aerospace Sciences Meeting, Reno, NV, January 2000.

[77] J. Murray and P. Tartabini. Development of a mars airplane entry, descent, and flight trajectory. NASA/ tm-2001-209035, January 2001.

[78] M. Guynn, M. Croom, S. Smith, R. Parks, and P. Gelhausen. Evolution of a mars airplane concept for the ares mars scout mision. AIAA Paper 2003-6578, 2nd AIAA "Unmanned Unlimited" Systems, Technologies,and Operations Aerospace Conference, San Diego, CA, September 2003.

[79] G.A. Landis, A. Colozza, and C.M. LaMarre. Atmospheric flight on venus. AIAA Paper 2002-0819, AIAA, 40th AIAA Aerospace Sciences Meeting & Exhibit, January 2002.

[80] http://mars.jpl.nasa.gov/technology/airplanes/. October 30, 2007.

[81] M. Usui, J.D. Jacob, S. Smith, S. Scarborough, and D. Cadogan. Second generation inflatable/rigidizable wings for low-density applications. AIAA Paper 2005-1883, 46th AIAA Gossamer Spacecraft Forum, Austin, TX, April 2005.

[82] S. Batill and T. Mueller. Visualization of transition in the flow over and airfoil using the smoke wire technique. *AIAA Journal*, 19:340–345, 1981.

[83] T. Mueller. *Low Reynolds Number Aerodynamics.* Springer, Verlag, 1989.

[84] A. Santhanakrishnan and J.D. Jacob. Effect of regular surface perturbations on flow over an airfoil. AIAA Paper 2005-5145, 35th AIAA Fluid Dynamics Conference and Exhibit, Toronto, Canada, June 2005.

[85] S.W. Smith and J.A. Main. Modeling the deployment of inflating space structures. *AIAA Journal*, pages 203–241, 2001.

[86] J.E. Campbell, S.W. Smith, J.A. Main, and J. Kearns. Staged microgravity deployment of a pressurizing scale model spacecraft. AIAA Paper 2002-1455, Proceedings of the AIAA SDM Gossamer Spacecraft Forum, Denver, CO, April 2002.

[87] A.L. Welch and S.W. Smith. Experimental results regarding two-dimensional deployment of inflatable beams. AIAA Paper 2003-1976, Proceedings of the AIAA SDM Gossamer Spacecraft Forum, Norfolk, Virginia, April 2004.

[88] T.C.S. Rendall, C.P. Cormier, P. Marzocca, and R. Jha. Static, buckling and dynamic behavior of inflatable beams. AIAA Paper 2006-1701, AIAA Structures, Structural Dynamics and Materials Conference, Newport, Rhode Island, May 2006.

[89] Michiko Usui, Andrew Simpson, Suzanne Smith, and Jamey D. Jacob. Development and flight testing of a uav with inflatable-rigidizable wings. AIAA Paper 2004-1373, 42nd AIAA Aerospace Sciences Meeting, Reno, NV, January 2004.

[90] J. Rowe, S.W. Smith, A.D. Simpson, and J.D. Jacob. Development of a finite element model of warping inflatable wings. AIAA Paper 2006-1697, AIAA, 47th AIAA/ASME/ASCE/AHS/ASC Structures, Structural Dynamics, and Materials Conference and 14th AIAA/ASME/AHS Adaptive Structures Conference, Newport, Rhode Island, May 2006.

[91] J. Breuer, W. Ockels, and R. Luchsinger. An inflatable wing using the principle of tensairity. AIAA Paper 2007-2117, 48th AIAA/ASME/ASCE/AHS/ASC Structures, Structural Dynamics, and Materials Conference, HI, April 2007.

[92] P.R. Wolf. *Elements of Photogrammetry.* McGraw-Hill, New York, New York, 2nd edition, 1983.

[93] E.M. Mikhail, J.S. Bethel, and J.C. McGlone. *Introduction to Modern Photogrammetry.* John Wiley and Sons, New York, 2001. ISBN 0471309249.

[94] R.S. Pappa, L.R.Giersch, and J.M Quagliaroli. Photogrammetry of a 5m inflatable space antenna with consumer-grade digital cameras. *Experimental Techniques, Society for Experimental Mechanics*, 25, 2001.

[95] L.R. Giersch. Pathfinder photogrammetry research for ultra-lightweight and inflatable space structures. Nasa contractor report, nasa/cr-2001-211244, November 2001.

[96] K.B. Atkinson. *Close Range Photogrammetry and Machine Vision.* Whittles Publishing, Caithness, Scotland, 2001. ISBN 1870325737.

[97] Eos Systems Inc. Photomodeler pro users manual. Version 5, Vancouver, B.C., Canada, 2003.

[98] S. Batill and T. Mueller. Visualization of transition in the flow over an airfoil using the smoke wire technique. *AIAA Journal*, 19:340–345, 1981.

[99] J. Kudva, K. Appa, C.A. Martin, A.P. Jardine, G. Sendeckyj, T. Harris, A. McGowan, and R. Lake. Design, fabrication, and testing of the darpa / wright lab smart wing wind tunnel model. AIAA Paper 1997-1198, Proceedings of the AIAA 38th Structures and Structural Dynamics Conference, Kissimmee, Fl, April 1997.

[100] N. Pern and J.D. Jacob. Characterization of zero mass flux flow control for separation control of an adaptive airfoil. AIAA Paper 2006–3032, 36th AIAA Fluid Dynamics Conference and Exhibit, San Francisco, Ca, June 2006.

[101] R.W. Lynch and W.A. Rodgers. Aeroelastic tailoring of composite materials to improve performance. pp. 61-68, 17th AIAA/ASME/SAE Structures, Structural Dynamics and Materials Conference, King of Prussia, Pa, May 1976.

[102] G.W. Brune. Quantitative low-speed wake surveys. *AIAA Journal*, 31:249–255, 1994.

[103] M. Sholl and O. Savas. A fast lagrangian piv method for study of general high-gradient flows. AIAA Paper 1997–0493, 35th AIAA Aerospace Sciences Meeting, Reno, NV, January 1997.

[104] http://www.ave.kth.se/divisions/aero/. October 30, 2007.

[105] Bret Stanford, Mujahid Abdulrahim, Rick Lind, and Peter Ifju. Investigation of membrane actuation for roll control of a micro air vehicle. *Journal of Aircraft*, 44:741–749, 2007.

[106] A.D. Simpson, N. Coulombe, J.D. Jacob, and S.W. Smith. Morphing of inflatable wings. AIAA Paper 2005-2110, 46th 13th AIAA/ASME/AHS Adaptive Structures Conference Austin, Tx, April 2005.

[107] A.D. Simpson and J.D. Jacob. Aerodynamic control of an inflatable wing using wing warping. AIAA Paper 2005-5133, 35th Fluid Dynamics Conference, Toronto, Canada, April 2005.

[108] B. McCormick. *Aerodynamics, Aeronautics, and Flight Mechanics.* Wiley, New York, 1979.

[109] http://www.cloudcaptech.com/. October 30, 2007.

VITA

Andrew was born in Durban, KwaZulu-Natal, South Africa in 1978. He graduated with his B.S. from the University of Natal in the School of Bioresources Engineering and Environmental Hydrology in 2000. He decided to continue his education through pursuing M.S. in Biosystems and Agricultural Engineering from the University of Kentucky. Following this he join Dr. Jamey Jacob as a Ph.D student in the Fluid Mechanics Laboratory. As a Ph.D student he has served as a Research Assistant at the Fluid Mechanics Laboratory and as a Teaching Assistant for the Department of Mechanical Engineering. He has instructed undergraduate courses for the Department of Mechanical Engineering. He has presented numerous talks on his research at international level conferences (ASME, AIAA and APS).

Awards

- Best Presentation, *Deformation and Buckling of Inflatable Wings Under Dynamic Loads*, 2007 AIAA 32nd Annual Dayton-Cincinnati Aerospace Science Symposium

Publications:

Journal Publications

- Jacob, J.D., A.D. Simpson, and S.W. Smith, "Design and Flight Testing of Inflatable Wings with Wing Warping," *SAE Transactions Journal of Aerospace*, 2005, 2005-01-3392, pp. 1306-1315.

Conference Papers

- Simpson, A.D., J.M. Rowe, S.W. Smith and J.D. Jacob, "Aeroelastic Deformation and Buckling of Inflatable Wings Under Dynamic Loads," AIAA-2007-2239, *48th AIAA/ASME/ASCE/AHS/ASC Structures, Structural Dynamics, and Materials Conference*, Honolulu, Hawaii, April 23-26, 2007.

- Simpson, A.D., S.W. Smith and J.D. Jacob, "Aeroelastic Behavior of Inflatable Wings: Wind Tunnel and Flight Testing," AIAA-2007-1069, *45th Aerospace Sciences Meetin*g, Reno, Nevada, Jan 8-11, 2007.

- Simpson, A., J.D. Jacob and S.W. Smith, "Flight Control of a UAV with Inflatable Wings with Wing Warping," AIAA-2006-2831, *24th AIAA Applied Aerodynamics Conference*, San Francisco, California, June 5-8, 2006.

- Rowe, J.M., S.W. Smith, A.D. Simpson, J.D. Jacob and S.E. Scarborough, "Development of a Finite Element Model of Warping Inflatable Wings," AIAA-2006-1697, *7th SDM Gossamer Spacecraft Forum*, Newport, Rhode Island, May 1-4, 2006.

- Jacob, J.D., A.D. Simpson and S.W. Smith, "Design and Flight Testing of Inflatable Wings with Wing Warping," WAC-2005-01-3392, *SAE World Aerospace Congress*, Fort Worth, Texas, Oct. 3-6, 2005.

- Simpson, A.D., J.D. Jacob and S.W. Smith, "Inflatable and Warpable Wings for Meso-Scale UAVs," AIAA-2005-7161, *AIAA Infotech@Aerospace Conference*, Arlington, Virginia, September 26-29, 2005

- Simpson, A., N. Coulombe, J.D. Jacob, and S.W. Smith, "Morphing of Inflatable Wings." AIAA 2005-2110, *AIAA SDM Adaptive Structures Conference*, Austin, TX, April, 2005.

- Simpson, A.D., et. al., "BIG BLUE: A High-Altitude UAV Demonstrator of Mars Airplane Technology," *IEEE Aerospace Conference*, Big Sky, MT, March 6-10, 2005. (presented by W. Deiter)

- Simpson A., J.D. Jacob, S.W. Smith, O. Rawashdeh, J.E. Lumpp and W.T. Smith, "BIG BLUE II: Mars Aircraft Prototype with Inflatable-Rigidizable Wings" AIAA-2005-0813, *AIAA Aerospace Sciences Meeting*, Reno, NV, Jan 10-13, 2005.

- Simpson, A.D., Santhanakrishnan, A., Jacob, J.D., Smith, S.W., Lumpp, J., Cadogan, D., "Flying on Air: UAV Flight Testing with Inflatable Wing Technology," AIAA 2004-6570, *AIAA 3rd Unmanned Unlimited Technical Conference Workshop and Exhibit*, Chicago, IL, September 20-23, 2004.

- Simpson, A.D., M. Usui, S.W. Smith and J.D. Jacob, "Aeromechanics of Inflatable Airfoils," AIAA-2004-2233, *AIAA 34th Fluid Dynamics Conference*, Portland, OR, June 2004.

- Usui, M., A. Simpson, S.W. Smith and J.D. Jacob, "Development and Flight Testing of a UAV with Inflatable-Rigidizable Wings," AIAA-2004-1373, *AIAA Aerospace Sciences Conference*, Reno NV, January 5-8, 2004.

Conference Presentations

- Simpson, A.D., Smith, S.W., Jacob, J.D., "Aeroelastic Deformation and Buckling of Inflatable Wings under Dynamic Loads." *59th Annual Meeting of the Division of Fluid Dynamics*, November 19-21, 2006; Tampa Bay, FL

- Simpson, A.D., Smith, S.W., Jacob, J.D., "Wing Warping, Roll Control and Aerodynamic Optimization of Inflatable Wings." *58th Annual Meeting of the Division of Fluid Dynamic*s, November 20-22, 2005; Chicago, IL

- Simpson, A.D., Smith, S.W., Jacob, J.D., "Deformation and Buckling of Inflatable Wings Under Dynamic Loads." *32nd Annual Dayton-Cincinnati Aerospace Science Symposium*, Dayton, OH, 2007

- Simpson, A.D., Smith, S.W., Jacob, J.D., "Warping, Control and Aerodynamic Optimization of Inflatable Wings." *31st Annual Dayton-Cincinnati Aerospace Sciences Symposium*, Dayton, OH, 2006

- Simpson, A.D., Smith, S.W., Jacob, J.D., "Wing Warping with Inflatable Airfoils." *30th Annual Dayton-Cincinnati Aerospace Sciences Symposium,* Dayton, OH, 2005

Andrew D. Simpson

02/22/2008